

①

# Study of Plasma-Surface Kinetics and Simulation of Feature Profile Evolution in Chlorine Etching of Patterned Polysilicon

by

**Jane Pei-chen Chang**

B. S. Chemical Engineering  
National Taiwan University, Taiwan, 1993

M. S. Chemical Engineering Practice  
Massachusetts Institute of Technology, 1995

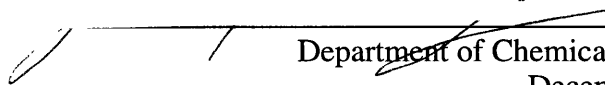
Submitted to the Department of Chemical Engineering  
in partial fulfillment of the requirements for the degree of


**Doctor of Philosophy**  
in  
**Chemical Engineering**

at the  
**Massachusetts Institute of Technology**

~~December 1997~~  
February 1998

© 1997 Massachusetts Institute of Technology  
All rights reserved

Signature of Author \_\_\_\_\_  
  
Department of Chemical Engineering  
December 10, 1997

Certified by  \_\_\_\_\_  
Herbert H. Sawin  
Professor of Chemical Engineering and  
Electrical Engineering and Computer Science  
Thesis Advisor

Accepted by \_\_\_\_\_  
Professor Robert E. Cohen  
St. Laurent Professor of Chemical Engineering  
Chairman, Committee for Graduate Students

APR 13 1998

LIBRARIES





# Study of Plasma-Surface Kinetics and Simulation of Feature Profile Evolution in Chlorine Etching of Patterned Polysilicon

by Jane Pei-chen Chang

Submitted to the Department of Chemical Engineering on December 10, 1997 in partial fulfillment of the requirements for the degree of Doctor of Philosophy in Chemical Engineering

## Abstract

This work characterized the chlorine ion-enhanced plasma-surface interactions with polysilicon, silicon dioxide, and photoresist as a function of the plasma compositions ( $\text{Cl}^+$ ,  $\text{Cl}$ ,  $\text{Cl}_2$ ,  $\text{SiCl}_2$ ), ion energy ( $E_{\text{ion}}$ ), ion incident angle ( $\phi_{\text{ion}}$ ) and other important process parameters. A direct beam scattering apparatus capable of generating low energy ions (20-100eV) and reactive neutral species and controlling their flux levels independently was utilized to simulate accurately a high-density plasma environment. Etching of polysilicon, silicon dioxide, and photoresist was quantified to better describe etching of patterned polysilicon in fabricating the gate electrode of a transistor in the IC manufacturing process. These kinetic measurements facilitate the formulation of surface kinetic models usable in a Monte Carlo based profile simulator, and enable predictive simulations of feature profiles evolutions.

The ion-enhanced etching yields of polysilicon, silicon dioxide and photoresist were characterized as a function of ion energy, ion flux, neutral/ion flux ratio, the flux of etching by-products, and angle of ion impingement. The etching yields of all three materials by  $\text{Ar}^+$  and  $\text{Cl}$  increased with the increase of flux ratios and gradually saturated at high flux ratios as the depletion of ion-flux limits the etching yield. Etching selectivity of 30 and 2.5 are achieved for polysilicon/silicon dioxide and polysilicon/photoresist with  $\text{Ar}^+$  and  $\text{Cl}$  bombardments. The ion energy dependence in etching polysilicon and silicon dioxide was found to scale linearly with  $(E_{\text{ion}}^{1/2} - E_{\text{th}}^{1/2})$ , where the threshold energies,  $E_{\text{th}}$ , are 16 and 40 eV for etching polysilicon and silicon dioxide, respectively. With  $\text{Ar}^+$  ion bombardment,  $\text{Cl}$  was found to dominate the etching reaction over  $\text{Cl}_2$ , as the dissociative adsorption rate of  $\text{Cl}_2$  was limited on chlorinated polysilicon and silicon dioxide surfaces. Etching of photoresist was strongly dependent upon the heat treatment to the photoresist prior to etching. The angular dependence in etching polysilicon and silicon dioxide was also examined. Maximum etching yield of polysilicon was observed at normal ion incident angle, indicating that the etching reaction is chemically driven and ion-induced surface chlorination compensated for the less efficient momentum transfer to the surface atoms at near normal incident angles. Maximum etching yield of silicon dioxide was observed at  $60^\circ$  off-normal ion incident angle where the momentum transfer to the silicon dioxide surface was most sufficient; suggesting that the etching of silicon dioxide was

physically driven. Possible reaction pathways were proposed and reduced into kinetic models that are usable in a profile simulator.

$\text{Cl}^+$  was utilized to assess the chemical effect of a reactive ion, and simulate accurately a high-density chlorine plasma.  $\text{Cl}^+$  further enhanced etching of polysilicon, comparing to  $\text{Ar}^+$ , especially at low ion energies or low flux ratios where  $\text{Cl}^+$  sufficiently chlorinates the silicon surface and produces volatile etching products. The threshold energy was reduced to 10 eV with  $\text{Cl}^+$  bombardment. The effect of deposition of etching products was determined utilizing a  $\text{SiCl}_2$  beam. The presence of  $\text{SiCl}_2$  significantly suppressed the etching of the polysilicon by both  $\text{Cl}^+$  and  $\text{Cl}/\text{Cl}^+$ , by almost an order of magnitude.

Notching formation at the polysilicon/silicon dioxide interface during overetching is demonstrated to be caused in part by stress enhanced spontaneous etching and is not solely a result of feature charging. Mechanically bending of a patterned polysilicon sample was employed to change the stress of the polysilicon film without any other modification of the film. The degree of notching was enhanced by the imposed mechanical stress, indicating that the notching formation was greatly affected by the stress, as charging and ion trajectory distortion were not significant in the beam system.

A Monte Carlo based profile simulator was constructed to simulate feature profile evolution during plasma etching processes. The etching yield models implemented were formulated from our beam scattering studies in which the functional role of  $\text{Cl}^+$ ,  $\text{Cl}$ ,  $\text{Cl}_2$  and  $\text{SiCl}_2$  were characterized, and dominant reaction mechanisms such as surface chlorination under ion bombardment, surface re-emission, and ion reflection were accounted. The profile evolution of patterned samples etched with the combined  $\text{Cl}^+$  and  $\text{Cl}$  beams were simulated to validate the simulation results. Quantitatively good agreement was found between the simulated profiles and the measured profiles with one adjustable parameter, the chlorine recombination probability on photoresist surfaces.

Thesis Advisor:  
Herbert H. Sawin  
Professor of Chemical Engineering and Electrical Engineering and Computer Science



## **Dedication**

To my parents,  
for loving me and supporting me everyday.



## Acknowledgement

I would like to thank my thesis advisor Professor Herb Sawin for his guidance and support in the course of this thesis work. I am grateful for Herb's commitment and enthusiasm towards this project, and I have benefited greatly from his visionary thinking and insightful suggestions. I thank Professor Klavs Jensen for providing a Monte Carlo code upon which the simulator used in this work was constructed, and his useful discussions. I extend my thanks to my other committee members, Professor Karen Gleason and Professor Jackie Ying for their help and suggestions. I would like to acknowledge Sematech and Semiconductor Research Corporation for their funding support to this project.

I am indebted to everyone in the METL group for sharing with me the good and bad times in the lab, for insightful discussions, for lending a hand in lifting heavy objects, and for raising the standards of jokes told in the office. I have the luxury to interact with three distinct "generations" of fun people on board this plasma-processing enterprise, and I thank every one of you for making the life at MIT and the long hours in the lab enjoyable and endurable. I have no list of names here since I have memorized it all after updating the address and name list for this group for three years!

I offer my sincere thanks to the staffs at the Microsystem Technology Center, machine shops at the Laboratory of Nuclear Science and the Chemistry department, and the Center of Material Science and Engineering for their technical support of the facilities that enable the continual progress of this project. I thank many of the support staff members in the Department of Chemical Engineering for making this place full of laughter and fun.

I would thank my friends at MIT, in Taiwan, and in the States for the conversations, letters, emails, and phone calls at the time when I needed them. Thank you for reminding me the good old times and for being with me heading towards the future.

Special thanks go to Mingchih for his encouragement, love and support.

Finally, I am thankful to my family for their love and encouragement from thousands of miles away. Mom, Dad, Peggy, Karen, Amy and Peter, thank you for always being there for me. None of this work could have been accomplished without your continual support.



## Table of Contents

<b>Abstract</b> .....	3
<b>Dedication</b> .....	5
<b>Acknowledgement</b> .....	7
<b>Table of Contents</b> .....	9
<b>List of Figures</b> .....	12
<b>List of Tables</b> .....	18
<b>1. Introduction</b> .....	19
1.1 Fundamentals of Plasma Etching .....	21
1.2 Studies of Ion Enhanced Chlorine Etching of Silicon.....	24
1.2.1 Etching studies with beam scattering techniques .....	27
1.2.2 Etching studies in high density plasma reactors.....	30
1.2.3 Studies and simulations of notching formation .....	31
1.2.4 Molecular dynamic (MD) simulations .....	32
1.3 Studies of Ion Enhanced Chlorine Etching of SiO <sub>2</sub> and Photoresist.....	33
1.3.1 Studies of ion-enhanced etching of SiO <sub>2</sub> .....	33
1.3.2 Studies of ion-enhanced etching of photoresist.....	34
1.4 Predictive Modeling of the Profile Evolution .....	35
<b>2. Experimental Setup</b> .....	37
2.1 Multiple Beam Chamber .....	37
2.2 Clustered Processing System (First Setup) .....	41
2.3 Integrated Processing System (Second Setup) .....	42
2.4 Beam Sources .....	44
2.4.1 Compact electron cyclotron resonance (CECR) ion source.....	44
2.4.2 Coaxial microwave atom source .....	49
2.4.3 Thermal beam source .....	54
2.5 Diagnostics .....	55
2.5.1 Laser interferometry .....	55
2.5.2 Gridded ion energy analyzer .....	56
2.5.3 Neutral flux probe .....	59
2.5.4 X-ray photoelectron spectroscopy (XPS).....	59
2.5.5 Ellipsometry .....	60
<b>3. Argon Ion Enhanced Chlorine Etching of Polysilicon</b> .....	63
3.1 Low Energy Ar <sup>+</sup> Sputtering of Polysilicon .....	63
3.2 Spontaneous Etching of Polysilicon by Cl and Cl <sub>2</sub> .....	67
3.3 Ar <sup>+</sup> Ion Enhanced Etching of Polysilicon with Chlorine .....	69
3.4 Angular Dependence of Polysilicon Etching with Ar <sup>+</sup> .....	73
3.5 XPS Analysis of Polysilicon Surface after Ar <sup>+</sup> and Cl Bombardment.....	76

3.6 Phenomenological Model for Etching of Polysilicon with Ar <sup>+</sup> .....	80
<b>4. Argon Ion Enhanced Chlorine Etching of SiO<sub>2</sub> and Photoresist .....</b>	<b>85</b>
4.1 Low Energy Ar <sup>+</sup> Sputtering of SiO <sub>2</sub> .....	86
4.2 Spontaneous Etching of SiO <sub>2</sub> by Cl and Cl <sub>2</sub> .....	87
4.3 Ar <sup>+</sup> Ion Enhanced Etching of SiO <sub>2</sub> with Chlorine.....	88
4.4 Angular Dependence of SiO <sub>2</sub> Etching with Ar <sup>+</sup> and Cl.....	92
4.5 Angular Resolved XPS (AR-XPS) Analysis of SiO <sub>2</sub> Etching .....	94
4.6 Etching Selectivity between Si and SiO <sub>2</sub> with Ar <sup>+</sup> and Cl .....	98
4.7 Phenomenological Model for Etching of SiO <sub>2</sub> with Ar <sup>+</sup> .....	99
4.8 Ar <sup>+</sup> Ion-enhanced Etching of Photoresist with Cl .....	101
<b>5. Chlorine Ion Enhanced Etching of Polysilicon.....</b>	<b>105</b>
5.1 Low Energy Cl <sup>+</sup> Sputtering of Polysilicon.....	105
5.2 Cl <sup>+</sup> Ion Enhanced Etching of Polysilicon.....	107
5.3 Angular Dependence of Polysilicon Etching with Cl <sup>+</sup> .....	114
5.4 Effect of Etching By-product Deposition: SiCl <sub>2</sub> .....	116
5.5 XPS Analysis of Polysilicon Surface after Cl <sup>+</sup> Bombardment.....	118
5.6 Phenomenological Model for Polysilicon Etching with Cl <sup>+</sup> .....	120
<b>6. Etching of Patterned Polysilicon Samples.....</b>	<b>125</b>
6.1 Argon Ion-enhanced Etching of Photoresist Masked Polysilicon.....	127
6.1.1 Ar <sup>+</sup> and Cl etching of photoresist masked polysilicon .....	127
6.1.2 Ar <sup>+</sup> and Cl etching of mechanically stressed, patterned polysilicon .....	128
6.2 Chlorine Ion-enhanced Etching of Photoresist Masked Polysilicon .....	134
6.2.1 Cl <sup>+</sup> etching of photoresist masked polysilicon .....	134
6.2.2 Cl <sup>+</sup> and Cl etching of photoresist masked polysilicon .....	135
<b>7. Quantitative Modeling of the Feature Profile Evolution.....</b>	<b>139</b>
7.1 Factors Affecting Feature Profile Evolution .....	140
7.2 Direct Simulation Monte Carlo Method.....	141
7.3 DSMC Model Description .....	142
7.3.1 Simulation domain .....	142
7.3.2 Surface interactions .....	144
7.3.3 Surface advancement.....	146
7.4 Comparison of Experimental and Modeling Results .....	146
7.4.1 Ar <sup>+</sup> and Cl etching of photoresist masked polysilicon .....	146
7.4.2 Cl <sup>+</sup> and Cl etching of photoresist masked polysilicon .....	147
7.5 Generalized Chemistry Model.....	152
7.6 Summary .....	156
<b>8. Conclusions .....</b>	<b>159</b>

8.1 Conclusions .....	159
8.2 Suggestions for Future Work .....	161
<b>Bibliography</b> .....	<b>163</b>
<b>Appendices</b> .....	<b>171</b>
A. Mechanical Drawings.....	171
B. Electrical Systems.....	213
C. Operating Procedures.....	217

## List of Figures

	Page
Figure 1.1	20
Figure 1.2	21
Figure 1.3	23
Figure 1.4	25
Figure 1.5	31
Figure 2.1	38
Figure 2.2	39
Figure 2.3	41
Figure 2.4	42
Figure 2.5	43
Figure 2.6	45
Figure 2.7	46
Figure 2.8	46
Figure 2.9	47
Figure 2.10	48



Figure 2.11	Schematic diagram of the coaxial microwave cavity atom beam source. ....	50
Figure 2.12	Schematic diagram of the hot thermal beam source. ....	54
Figure 2.13	Schematic diagram of the gridded ion energy analyzer. ....	56
Figure 2.14	Schematic diagram of the data acquisition system. ....	58
Figure 2.15	Schematic diagram of the setup of the XPS system. ....	60
Figure 3.1	Physical sputtering yield of polysilicon by $\text{Ar}^+$ . ....	64
Figure 3.2	Schematic diagram illustrating a collision cascade in the near surface region. ....	65
Figure 3.3	Verification of the neutral to ion flux ratio as a proper scaling factor for ion-enhanced etching of polysilicon. ....	69
Figure 3.4	Ion enhanced etching yields of polysilicon by Cl atom with $\text{Ar}^+$ ion at three energy levels. ....	70
Figure 3.5	Ion enhanced etching yields of polysilicon by Cl and $\text{Cl}_2$ beams with 100 eV $\text{Ar}^+$ . ....	71
Figure 3.6	Etching yield of polysilicon as a function of ion energy with $\text{Ar}^+$ alone, $\text{Ar}^+$ with molecular chlorine, and $\text{Ar}^+$ with atomic chlorine. ..	73
Figure 3.7	Angular dependence of ion enhanced etching of polysilicon with 100 eV $\text{Ar}^+$ and atomic chlorine as a function of flux ratios. ....	74
Figure 3.8	Angular dependence of ion enhanced etching of polysilicon with 100 eV $\text{Ar}^+$ and Cl at a flux ratio of 600. ....	75
Figure 3.9	A survey spectrum of the polysilicon surface prior to etching. ....	77
Figure 3.10	A survey spectrum of the polysilicon surface after etching by 100 eV $\text{Ar}^+$ and Cl. ....	77
Figure 3.11	Silicon and chlorine photoelectron emission spectrum from a polysilicon surface after etching by 100 eV $\text{Ar}^+$ and Cl. ....	78
Figure 3.12	Silicon and chlorine photoelectron emission spectra from a polysilicon surface after etching by 100 eV $\text{Ar}^+$ and Cl at two take-off angles. ....	79

Figure 3.13	Fitted parameters $\beta$ and $s$ versus $\sqrt{E_{ion}}$ for Ar <sup>+</sup> /Cl etching of polysilicon. ....	82
Figure 3.14	Graphical illustration of the ion enhanced polysilicon etching with Cl and Ar <sup>+</sup> . ....	83
Figure 4.1	Physical sputtering yield of silicon dioxide by Ar <sup>+</sup> . ....	86
Figure 4.2	Cl(2p) photoelectron emission spectra taken after silicon dioxide surfaces exposed to atomic and molecular chlorine, respectively. ...	87
Figure 4.3	Etching yield of silicon dioxide by Ar <sup>+</sup> , Ar <sup>+</sup> and Cl <sub>2</sub> , and Ar <sup>+</sup> and Cl, as a function of the square root of ion energy. ....	88
Figure 4.4	Ion enhanced etching of silicon dioxide by Cl atom with Ar <sup>+</sup> ion as a function of flux ratios, at two energy levels. ....	90
Figure 4.5	Cl(2p) photoelectron emission spectra illustrating the effect of ion energy on etching of silicon dioxide. ....	91
Figure 4.6	Angular dependence of ion enhanced etching of silicon dioxide with 100 eV Ar <sup>+</sup> and atomic chlorine as a function of flux ratio. ....	92
Figure 4.7	Etching yield of silicon dioxide at a function of ion incident angles. Different dependencies in etching yield are observed between 100 eV Ar <sup>+</sup> /Cl and 200 eV CF <sub>x</sub> <sup>+</sup> bombardment. ....	93
Figure 4.8	Survey spectra of the oxide surfaces before and after etching by 100 eV Ar <sup>+</sup> and Cl. ....	94
Figure 4.9	Angular resolved Cl(2p) and Si(2p) photoelectron emission spectra taken after a silicon dioxide surface is etched by 100 eV Ar <sup>+</sup> and Cl. ....	95
Figure 4.10	Angular resolved XPS analysis of the etched silicon dioxide surface, shown as a function of take-off angles. ....	96
Figure 4.11	Schematic diagram illustrating the incorporation of chlorine in silicon dioxide surface film. ....	97
Figure 4.12	Angular resolved XPS analysis of the etched silicon dioxide surface: the composition of Cl calculated as a function of ion bombardment energy. ....	97
Figure 4.13	Comparison of the etching yields of polysilicon and silicon dioxide by 100 eV Ar <sup>+</sup> and Cl. ....	98

Figure 4.14	Comparison of the angular dependencies of etching polysilicon and silicon dioxide by 100 eV Ar <sup>+</sup> and Cl. ....	99
Figure 4.15	Normalized etching yields of photoresist by 65 eV Ar <sup>+</sup> and Cl as a function of Cl to Ar <sup>+</sup> flux ratio. ....	102
Figure 4.16	Normalized etching rate of polymer films by various gases as a function of ion incident angles. ....	104
Figure 5.1	Sputtering yield of polysilicon by Cl <sup>+</sup> in the low energy regime. ....	106
Figure 5.2	Ion enhanced etching of polysilicon by Cl atoms with 35 eV Cl <sup>+</sup> ions and Ar <sup>+</sup> ions, respectively. ....	108
Figure 5.3	Surface morphology after Cl <sup>+</sup> ion bombardment and Cl <sup>+</sup> ion-enhanced etching with Cl. ....	109
Figure 5.4	Ion enhanced etching of polysilicon by a Cl <sub>2</sub> beam with 55 eV Cl <sup>+</sup> and 100 eV Ar <sup>+</sup> , respectively. ....	110
Figure 5.5	Ion enhanced etching of polysilicon by Cl atoms with Cl <sup>+</sup> ions at three ion energy levels. ....	111
Figure 5.6	Ion enhanced etching of polysilicon by Cl and Cl <sub>2</sub> beams with 55 eV Cl <sup>+</sup> . ....	112
Figure 5.7	Etching yield of polysilicon by Cl <sup>+</sup> -Cl, Cl <sub>2</sub> <sup>+</sup> and Cl <sup>+</sup> as a function of the square root of ion energy. ....	113
Figure 5.8	Angular dependence of ion enhanced etching of polysilicon with Cl and 35 eV Cl <sup>+</sup> . ....	114
Figure 5.9	Angular dependence of ion enhanced etching of polysilicon with Cl and 35 eV Cl <sup>+</sup> at a flux ratio of 200. ....	115
Figure 5.10	The effect of SiCl <sub>2</sub> on chlorine ion-enhanced etching of polysilicon in the presence of Cl <sup>+</sup> and in the presence Cl <sup>+</sup> and Cl. ....	118
Figure 5.11	Survey spectra of the polysilicon surface before and after etching by 35 eV Cl <sup>+</sup> . ....	119
Figure 5.12	Silicon photoelectron emission spectrum from a polysilicon surface after etching by 35 eV Cl <sup>+</sup> and Cl. ....	120
Figure 5.13	Fitted parameters $\beta$ and $s$ versus $\sqrt{E_{ion}}$ for Cl <sup>+</sup> /Cl etching of polysilicon. ....	123

Figure 5.14	Model prediction of the suppression of polysilicon etching yield with simultaneous deposition of $\text{SiCl}_2$ . .....	124
Figure 6.1	Layout of the patterned samples. ....	125
Figure 6.2	The orientation of the patterned samples with respect to the beam plane. (a) Un-shadowed orientation (b) shadowed orientation. ....	126
Figure 6.3	Initial profiles of the photoresist patterned polysilicon. ....	126
Figure 6.4	Profile etched by 95 eV $\text{Ar}^+$ and Cl at a neutral-to-ion flux ratio of 200, prior to the end point, in the unshadowed orientation. ....	127
Figure 6.5	Profile etched by 95 eV $\text{Ar}^+$ and Cl at a neutral-to-ion flux ratio of 200, with ~ 15% overetch, in the unshadowed orientation. ....	128
Figure 6.6	Setup for three-point bending of the patterned polysilicon samples.	130
Figure 6.7	Profile etched by 95 eV $\text{Ar}^+$ and Cl, without and with the applied mechanical stress. ....	131
Figure 6.8	Illustration of the notching formation as a combination of ion deflection by feature charging, removal of sidewall passivation, and spontaneous etching of the stressed polysilicon by chlorine atoms.	133
Figure 6.9	Profile etched by 35 eV $\text{Cl}^+$ , in the unshadowed orientation. ....	134
Figure 6.10	Profile etched by 85 eV $\text{Cl}^+$ , in the unshadowed orientation. ....	135
Figure 6.11	Profile etched by 35 eV $\text{Cl}^+$ and Cl at a neutral-to-ion flux ratio of 200, prior to the end point, in the unshadowed orientation. ....	136
Figure 6.12	Profile etched by 35 eV $\text{Cl}^+$ and Cl at a neutral-to-ion flux ratio of 200, with ~20% overetch, in the unshadowed orientation. ....	137
Figure 6.13	Profile etched by 35 eV $\text{Cl}^+$ and Cl at a neutral-to-ion flux ratio of 200, in the shadowed orientation. ....	137
Figure 7.1	Schematic diagram illustrating the factors affecting the feature profile evolution. ....	140
Figure 7.2	Schematic diagram of the simulation domain. ....	143
Figure 7.3	Simulation of the profile etched by 90 eV $\text{Ar}^+$ and Cl, in the unshadowed orientation. ....	147

Figure 7.4	Simulation of the profiles observed in the shadowed orientation. Recombination probability of 0.0 for Cl on photoresist was used. ...	149
Figure 7.5	Simulation of the profiles observed in the shadowed orientation. Recombination probability of 1.0 for Cl on photoresist was used. ...	149
Figure 7.6	Simulation of the profiles observed in the shadowed orientation. Recombination probability of 0.5 for Cl on photoresist was used. ...	151
Figure 7.7	Simulation of the profile observed in the unshadowed orientation. A recombination probability of 0.5 for Cl on the photoresist was used. ....	151
Figure 7.8	Validation of the generalized chemistry model by reproducing the yield-to-flux ratio dependence. ....	153
Figure 7.9	Schematic diagram illustrating the generalized surface chemistry model, when only Si, Cl and O are considered. ....	154
Figure 7.10	Schematic diagram illustrating the generalized surface chemistry model, when Si, C, Cl and O are considered. ....	155

## List of Tables

Table 1.1	Experimental parameter ranges and products reported in literature for Ar <sup>+</sup> ion-enhanced etching of Si with chlorine. ....	27
Table 3.1	The parameter values used to describe Ar <sup>+</sup> sputtering of silicon, with the universal energy dependence model. ....	66
Table 3.2	Arrhenius rate parameters for Cl and F atoms etching of Si. ....	67
Table 3.3	A simplified phenomenological surface kinetic model for Ar <sup>+</sup> ion-enhanced etching of polysilicon with Cl. ....	80
Table 3.4	Model parameters for Ar <sup>+</sup> ion-enhanced etching of polysilicon with Cl and Cl <sub>2</sub> , as a function of ion energy. ....	81
Table 4.1	A simplified phenomenological surface kinetic model for Ar <sup>+</sup> ion-enhanced etching of silicon dioxide with Cl. ....	100
Table 4.2	Model parameters for Ar <sup>+</sup> ion-enhanced etching of silicon dioxide with Cl, as a function of ion energy. ....	101
Table 5.1	The simplified phenomenological surface kinetic model for Cl <sup>+</sup> ion-enhanced etching of polysilicon with Cl. ....	121
Table 5.2	Model parameters for Cl <sup>+</sup> ion-enhanced etching of polysilicon with Cl, as a function of ion energy. ....	122

# Chapter 1

## Introduction

The objective of this work is to determine the plasma surface interactions and develop flexible and predictive simulation tools for design, optimization and control of plasma etching processes. Specifically, the chlorine ion-enhanced plasma-surface interactions are characterized, as a function of the plasma compositions ( $\text{Cl}^+$ ,  $\text{Cl}$ ,  $\text{Cl}_2$ ,  $\text{SiCl}_2$ ), ion energy ( $E_{\text{ion}}$ ), ion incident angle ( $\phi_{\text{ion}}$ ) and other important process parameters. The chlorine interaction with polysilicon, silicon dioxide, and photoresist are investigated, and the kinetic measurements are used to formulate surface kinetic models usable in a profile simulator. The incorporation of the kinetic rate coefficients in simulators allows predictive modeling of the feature profile evolution in the beam system and can also be used to simulate profiles observed in high-density plasma reactors.

We are interested in investigating the chlorine ion-enhanced plasma etching of patterned polysilicon as polysilicon is widely used to fabricate gate electrodes in metal-oxide-silicon (MOS) electronic devices. The National Technology Road Map by Semiconductor Industry Association (SIA) recognizes the next generation gate thickness to be less than 100 Å with less than 20 Å underlying gate silicon dioxide in year 2002, which imposes greater challenges to the development and control of the plasma processing. Successful patterning of the polysilicon requires a thorough understanding of the reaction mechanisms to reduce the time and cost associated with process development and equipment design.

A multiple beam scattering apparatus is used to generate  $\text{Cl}^+$  ( $\text{Ar}^+$ ),  $\text{Cl}$ ,  $\text{Cl}_2$  and  $\text{SiCl}_2$  beams to simulate a chlorine plasma and study the interaction of each reactive species with various materials, including polysilicon, silicon dioxide, and photoresist that form patterned polysilicon. A database comprising the critical rate coefficients of surface reactions is established to allow development of profile simulators based rigorously upon

the kinetic measurements. A Monte Carlo based profile simulator is constructed to model the feature profile evolution of patterned polysilicon samples etched in the beam system and in high-density plasma reactors.

The objective of this thesis is to combine the experimental efforts with simulation work to understand the ion-enhanced plasma etching process and predict feature profile evolution. The approach is illustrated below, and in Figure 1.1.

- (1) Determine rate coefficients for ion-enhanced plasma etching by direct beam scattering technique.
- (2) Develop kinetic models based on experimental measurements.
- (3) Construct a Monte Carlo based profile simulator.
- (4) Validate the profile simulator by comparing the simulation results with profiles measured in the beam system.
- (5) Predict etched feature profiles observed in high-density plasma reactors.

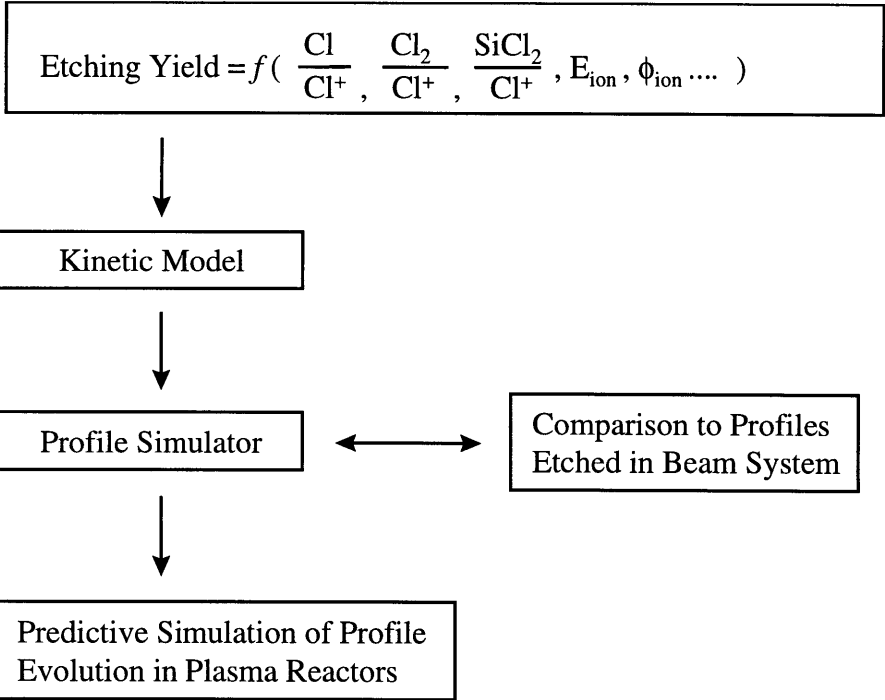


Figure 1.1: Thesis objective: combining experimental efforts with simulation work to characterize the ion-enhanced plasma etching process and predict feature profile evolution.



## 1.1 Fundamentals of Plasma Etching

Plasma etching has been widely used in semiconductor industry to selectively remove thin film material, achieve high fidelity pattern transfer, thereby facilitating the fabrication of electronic devices. Plasma is a low pressure, partially ionized gas through which an electric current is passed to accelerate free electrons that in turn excite and dissociate molecules to form energetic ions and reactive neutrals. The plasma-surface interactions are depicted in Figure 1.2 using chlorine etching of photoresist patterned polysilicon over a silicon dioxide film as an example.

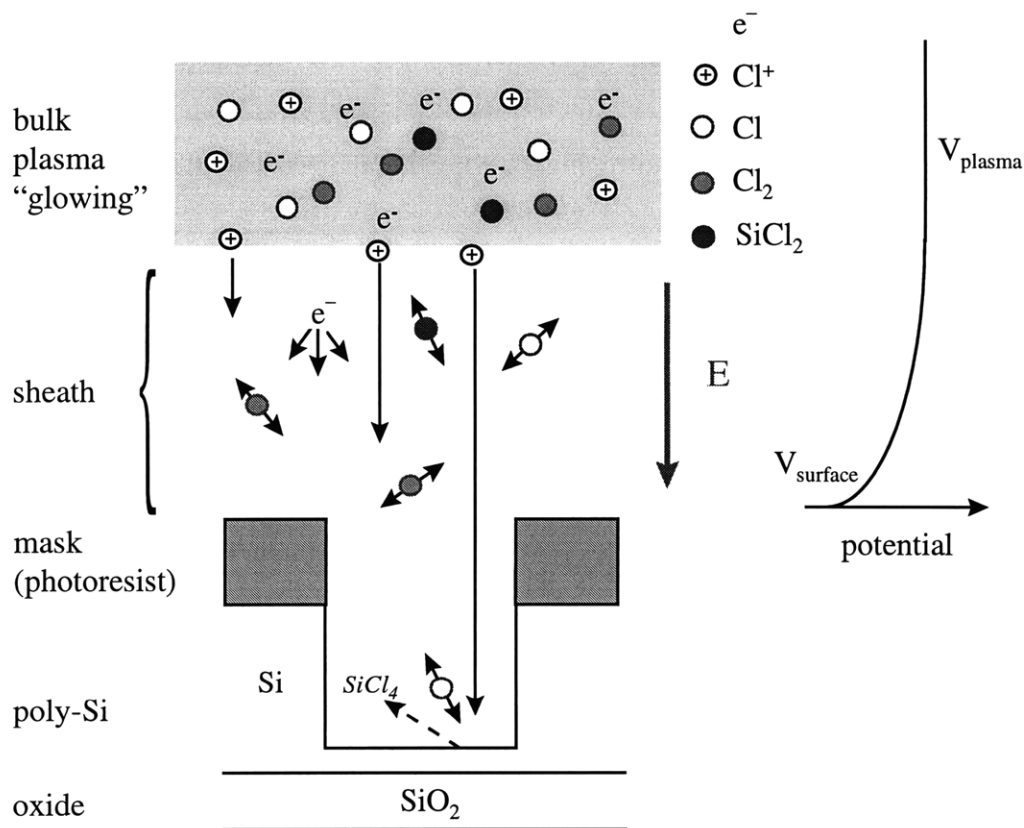


Figure 1.2: Schematic diagram illustrating the chlorine ion-enhanced etching of photoresist patterned polysilicon. The major reactive species in plasma include energetic chlorine ions ( $\text{Cl}^+$ ) and reactive neutrals ( $\text{Cl}$ ,  $\text{Cl}_2$ ,  $\text{SiCl}_2$ ).

The relaxation of the excited atoms in the plasma emits photons and makes the plasma glow. Since electrons move much faster than ions, the surface in contact with the

plasma very rapidly build up a negative charge, and thus a negative potential with respect to the plasma. This electrical field then repels electrons and accelerates ions and leads to the formation of a sheath, a dark space region around the surface. As the electron density is low in the sheath region, the sheath does not glow as much. Ions ( $\text{Cl}^+$ ) are accelerated across the plasma sheath with high energy, impinge the surface with high directionality, enhance the surface reactions by forming volatile etching products ( $\text{SiCl}_4$ ), and achieve etching anisotropy. Therefore, plasma etching process is also referred as an “ion-enhanced” etching process.

An ideal plasma etching process requires perfect pattern transfer by anisotropic (directional) etching of polysilicon (the portion not protected by the photoresist), and no etching of either photoresist or silicon dioxide upon ion bombardment (infinite selectivity). This typically requires highly directional ions and minimal spontaneous etching of polysilicon by reactive neutrals.

In reality, many non-ideal factors including transport of reactive species into the feature and interactions of reactive species with the surface affect etched profiles. For example, ions undergo collisions across the sheath, bear a finite angular distribution, and affect the etching anisotropy. As the aspect ratio (depth/width) of the feature increases, shadowing effect of the neutral species due to their non-zero reaction probabilities on the sidewall of the feature can cause concentration gradients within the feature and significantly alter the etching profiles and the etching uniformity. The etching products or by-products with high sticking probabilities can deposit on the surfaces within the feature and alter the profile evolution. Specifically, etching of photoresists or electron impact dissociation of the etching products ( $\text{SiCl}_4$ ) lead to the formation of carbonaceous contamination and  $\text{SiCl}_2$  that form passivation layers in the feature and prevent the sidewall from being etched. The balance between etching and deposition processes achieves the profile topography change during plasma etching processes. Moreover, shadowing of the isotropic electrons and positive charging on the silicon dioxide surface in etching high aspect ratio (width/depth) features can build up an electrical field on the oxide surface to distort the ion trajectory. These etching phenomena are highly

convoluted and a thorough understanding of the fundamental mechanisms by which the etching anisotropy is achieved is required to develop rapid, directional, high resolution and damage-free etching processes.

High density plasma reactors have been developed to address the challenges in patterning features less than  $0.25\ \mu\text{m}$  with high aspect ratios. The challenges include maintaining etching uniformity, etching selectivity, high etching rate, and reducing the substrate damage. Various high density plasma sources such as transformer coupled plasma (TCP) and electron cyclotron resonance (ECR) reactors have been developed to achieve high fidelity pattern transfer for manufacturing of very large scale integrated (VLSI) electronic devices. Figure 1.3 is a schematic diagram of a high density transformer coupled plasma (TCP) reactor.

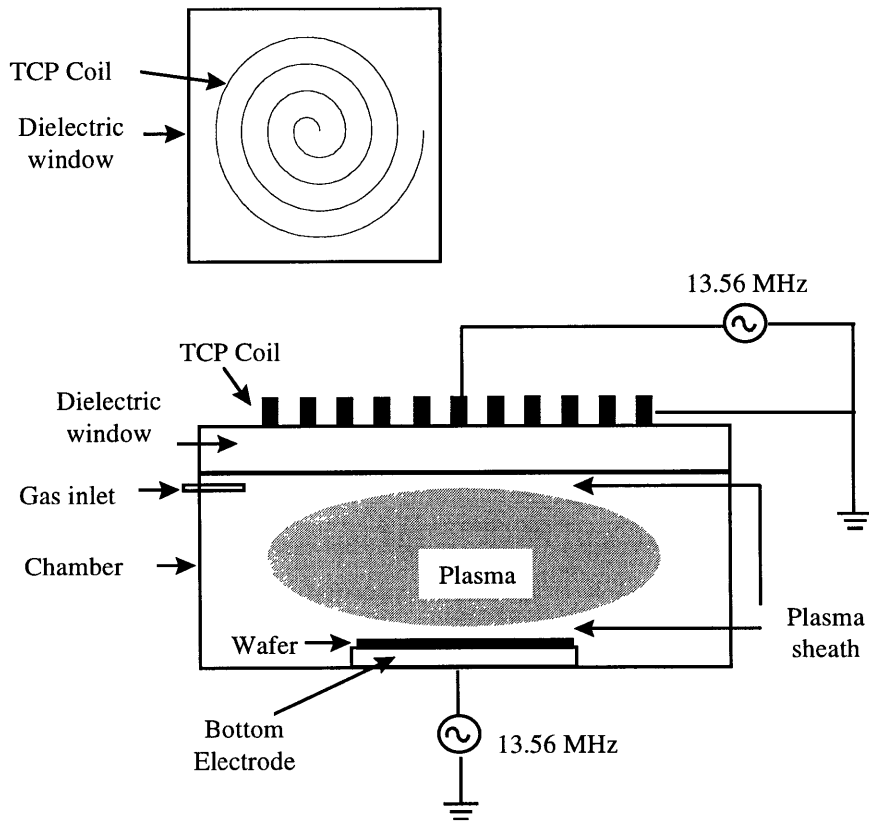


Figure 1.3: Schematic diagram of a transformer coupled plasma (TCP) reactor. The TCP coil is powered by a 13.56 MHz rf power supply to generate the plasma, the bottom electrode is powered by another rf power supply to control the ion bombardment energy. Plasma sheath is the dark space between the bulk plasma and the electrodes.

A spiral planar inductive coil is mounted on a dielectric window on the reactor. Plasma is generated by coupling the oscillating rf magnetic field (13.56 MHz) inductively. Plasma sheath, a dark space between plasma and the electrodes, is developed due to the different mobility of electrons and ions. The bottom electrode can be powered by a separate rf source to control the ion bombardment energy. The energetic ions and reactive neutrals produced are highly reactive, thereby facilitating surface (and/or gas phase) reactions with lower activation energies, and enhance greatly the reaction kinetics.

High density plasma is favored as its high ion flux and low ion energy maintain high etching rates, improve etching selectivity, and reduce substrate damage. The plasma sheath becomes less collisional which reduces aspect ratio dependent etching phenomena. Even though high density plasma sources have been successful in patterning features of 0.25  $\mu\text{m}$  on 8 inch wafers, the fundamental mechanisms by which better etching anisotropy occurs are not well understood.

## **1.2 Studies of Ion Enhanced Chlorine Etching of Silicon**

In order to accurately simulate a high density chlorine plasma and understand the synergism of energetic ions and reactive neutrals, the functional roles of the major reactants in a chlorine discharge such as  $\text{Cl}^+$ ,  $\text{Cl}$ ,  $\text{Cl}_2$  and  $\text{SiCl}_x$  must be characterized.  $\text{Ar}^+$  has been widely used instead of  $\text{Cl}^+$  in the literature to circumvent the difficulties associated with generating a  $\text{Cl}^+$  beam. The synergistic effect of  $\text{Ar}^+$  and  $\text{Cl}$  in etching polysilicon is illustrated in Figure 1.4.  $\text{Ar}^+$  ions physically sputter the polysilicon and remove silicon atom by energy and momentum transfer. The etching yield scales with the energy and momentum transfer to the silicon sample, and is relatively small at low ion energies. The etching yield of undoped polysilicon by  $\text{Cl}$  atoms is essentially zero at room temperature. Even though  $\text{Si-Cl}$  bonds are stronger than  $\text{Si-Si}$  bonds, the incorporation of chlorine into the silicon lattice is sterically hindered, leaving the surface saturated with chlorine with minimal etching of silicon. However, upon simultaneous ion

bombardment, chlorine atoms react with the silicon dangling bonds created by ion impact, incorporate into the silicon lattice by knock-on, form volatile etching products,  $\text{SiCl}_4$ , and greatly enhance the etching rates [Coburn, 1979] [Barker, 1983]. This phenomenon has also been observed in the  $\text{Ar}^+$  and fluorine system. However, fluorine spontaneously etches polysilicon due to its greater reactivity and less steric hindrance effect.

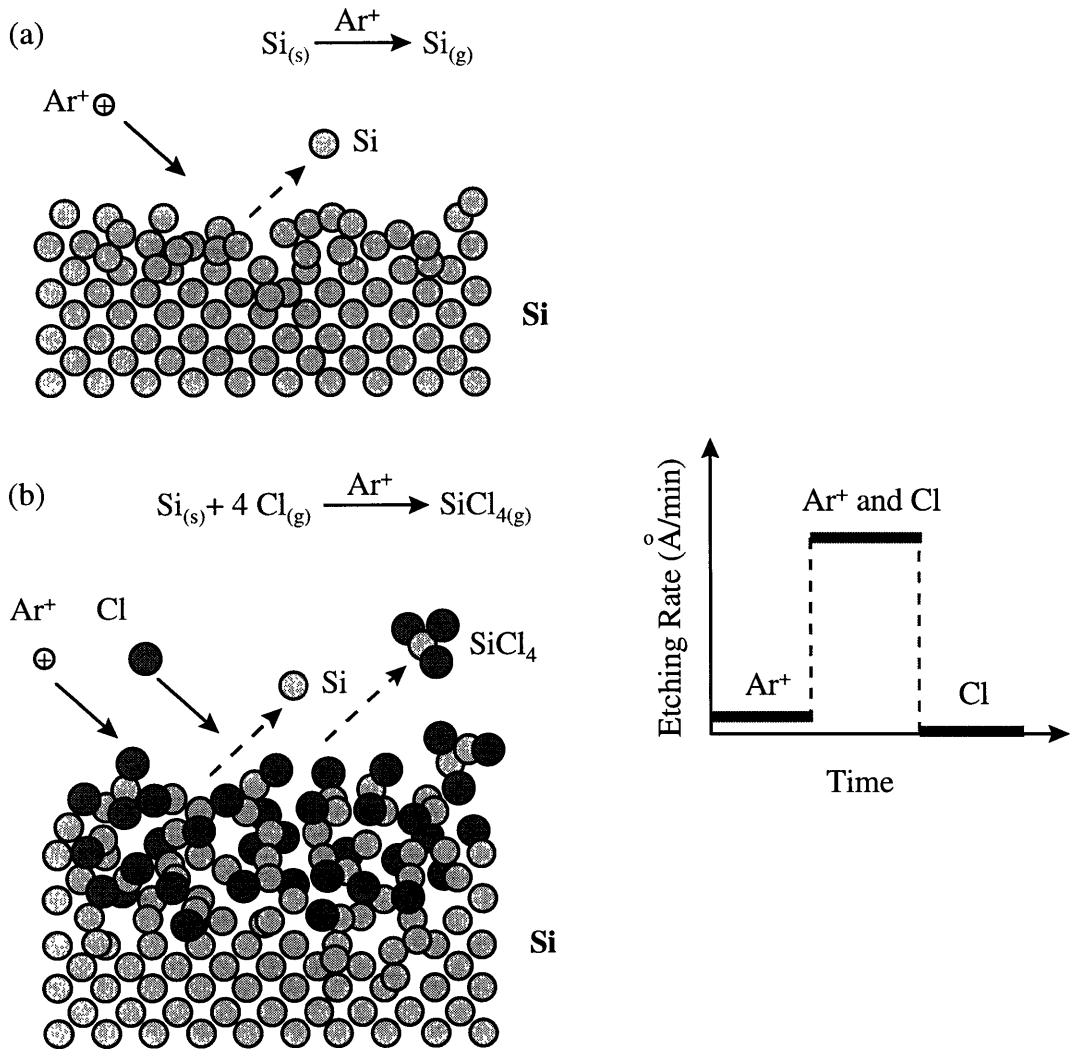


Figure 1.4: The synergistic effect of  $\text{Ar}^+$  and Cl in etching of polysilicon. The etching rate of polysilicon increases by an order of magnitude upon simultaneous  $\text{Ar}^+$  and Cl impingement. The enhancement is due to the formation of volatile etching products (e.g.  $\text{SiCl}_4$ ) during ion bombardment.

It is pertinent to identify the reaction probability of both Cl and Cl<sub>2</sub> to understand better their functional roles in ion-enhanced plasma etching processes. The chlorine atom is believed to be the primary reactant in plasma etching, however, molecular chlorine also reacts with silicon upon ion bombardment so that a significant concentration of the Cl<sub>2</sub> molecule in the Cl atom beam could affect the surface chemistry. Since it is hard to generate a beam of Cl due to its high surface recombination loss rate, great effort has been made to generate chlorine atoms in order to simulate a real chlorine discharge and assess the difference between Cl and Cl<sub>2</sub>. Matsuo et. al. [Matsuo, 1992] observed distinct differences in reaction probability between atomic and molecular chlorine. Chlorine molecules dissociatively adsorb on the silicon surface and form SiCl on the topmost silicon layer without breaking the Si-Si bonds. The adsorption rate of molecular chlorine approaches zero at near monolayer coverage [Szabo, 1994]. Chlorine atoms, however, can penetrate the lattice, break Si-Si bonds and form chlorinated species as SiCl<sub>x</sub> (x=1-4). Exposure to atomic chlorine therefore results in higher surface chlorination, which favors the formation of highly chlorinated products. Very recently, Szabo et. al. [Szabo, 1994] also showed insignificant etching rate of silicon by either a thermal Cl beam or a hyperthermal Cl<sub>2</sub> beam at temperatures of 130-200 K, where a non-thermally activated, collision-induced desorption mechanism is operative. The thermal Cl beam creates a high Cl coverage, but the collision induced desorption rate is too low to desorb the etching product. The hyperthermal Cl<sub>2</sub> beam transfers sufficient energy to desorb the weakly bounded species, but the rate of dissociative adsorption is too low to produce SiCl<sub>4</sub> on the surface.

The inhibitors generated in a plasma reactor can build up to a high concentration that is inversely proportional to the gas flow rate [Lee, 1996]. With a high sticking probability, the inhibitors can deposit on the sample and significantly alter the profile evolution. In the case of chlorine etching of polysilicon, SiCl<sub>2</sub> is considered as one of the major inhibitors. SiCl<sub>2</sub> is one of the major etching products (especially with high ion bombardment energy) and a product of electron impact dissociation of SiCl<sub>4</sub>. Therefore, the reaction probability of SiCl<sub>2</sub> has to be determined in order to model its contribution to the feature profile evolution.

### 1.2.1 Etching studies with beam scattering techniques

To explore the etching of silicon in high density plasma sources, the first step is to identify the effect of major ionic and radical species. Direct beam scattering technique [Gerlach-Meyer, 1981] [Coburn, 1994] [Gray, 1993] is therefore developed to generate reactive plasma species in the form of a beam to allow determination of the functional roles of each reactive species. This technique has been widely used in the literature to characterize the ion-enhanced plasma etching reactions; however, most of the work has been done in the high ion energy regime with noble ions (*e.g.*, Ar<sup>+</sup>) [McNevin, 1985] [Rossen, 1988] [Levinson, 1997].

Studies have focused on the Si/Cl<sub>2</sub>/Ar<sup>+</sup> system to identify the reactive species and volatile products, and quantitatively model the ion-enhancement effects, as summarized in Table 1.1. The combination of Ar<sup>+</sup> and Cl<sub>2</sub> represents an ideal model for the study of ion enhancement since chlorine does not spontaneously etch undoped silicon at room temperature and the incident Ar<sup>+</sup> ions are chemically inert.

Table 1.1: Reported experimental parameter ranges for Cl<sub>2</sub>/Si/Ar<sup>+</sup> system

Study	E <sub>ion</sub> (eV)	Ion flux (#/cm <sup>2</sup> /s)	Neutral flux (#/cm <sup>2</sup> /s)	Flux ratio	Sample	Etching Products
Gerlach-Meyer	1,000	3-6×10 <sup>13</sup>	>>	0-1820	sp-Si	SiCl <sub>4</sub>
Barker	400-900	6×10 <sup>13</sup> -3×10 <sup>15</sup>	0-6×10 <sup>16</sup>	2.5-250	Si(100)	SiCl <sub>4</sub>
McNevin	3000	4.5×10 <sup>14</sup>	2×10 <sup>12</sup> -4×10 <sup>14</sup>	0.004-1	Si(100)	SiCl <sub>4</sub>
Rossen	125-800	3×10 <sup>12</sup>	7×10 <sup>13</sup> -7×10 <sup>14</sup>	20-200	Si(100)	SiCl <sub>2</sub> /SiCl <sub>4</sub>
Sanders	250-3000	5×10 <sup>14</sup>	5×10 <sup>16</sup>	10-200	Si(111)	SiCl <sub>2</sub> /SiCl
Coburn	450	6×10 <sup>13</sup>	7×10 <sup>15</sup>	100		SiCl <sub>4</sub>
Okano	350	2-7×10 <sup>15</sup>	5×10 <sup>16</sup>	7-20		
Balooch	40-900	30 μA/cm <sup>2</sup>	>>		poly-Si	

Despite of great efforts devoted to identify the rate limiting step and the major volatile products in the etching processes, the current understanding of the Si/Cl<sub>2</sub>/Ar<sup>+</sup> system remains incomplete and inconclusive in a way that the rate limiting steps and the major reaction products remain controversial. Several reaction pathways have been

proposed to explain the formation of volatile silicon-chlorides ( $\text{Si-Cl}_x$ ) [Winters, 1983] [Sanders, 1984] [Rossen, 1987]. The surface chemistry has been noticed as a function of chlorine coverage, ion bombardment energy, the chemical nature of the impinging ion and temperature. Coburn and Winters [Winters, 1978] [Coburn, 1987] [Coburn, 1989] [Coburn, 1994] demonstrated the importance of ion-enhancement in gas surface chemistries. The synergistic effect greatly enhanced the overall silicon etching rates over those seen in the presence of the individual beams ( $\text{Cl}_2$  or  $\text{Ar}^+$ ). They proposed a series of five sequential steps involved in plasma-surface interaction:

- (1) nondissociative adsorption of gas phase species at the substrate surface being etched;
- (2) dissociation of the adsorbed gas (i.e. dissociative chemisorption);
- (3) reaction between adsorbed atoms and the solid surface to form an adsorbed product molecule (i.e.  $\text{SiCl}_4$ );
- (4) desorption of the product molecules into the gas phase;
- (5) removal of non-reactive residues from the surface.

This sequence is similar to the analysis of the heterogeneously catalyzed reaction proposed by Langmuir-Hinshelwood. Ion bombardment may enhance each step, for instance, it can facilitate sputtering of physisorbed species, dissociation of physisorbed surface species, or chemisorption of reactive neutrals on surface reactive sites created during ion impact. Ion impact can cause local heating of the silicon substrate, implantation of adsorbed Cl into silicon sub-layers, and generation of reactive surface sites via silicon bond breakage, and production of excited surface species via ion-induced chemical reaction pathway (chemical sputtering). Moreover, ion bombardment can accelerate the desorption of the weakly bounded surface species,  $\text{SiCl}_x$ , which have been referred to as “chemical enhanced physical sputtering” by Winters et. al. [Winters, 1992]. The energetic ion bombardment may enhance several of the above steps where the influence on the rate-limiting step is profound to increase the etching rate by orders of magnitude.

Sanders et. al. [Sanders, 1984] suggested the modification of the top atomic layers of silicon and sputtering of the products are rate limiting.  $\text{SiCl}_2$  and  $\text{SiCl}$  were observed



to be the major products while little or no  $\text{SiCl}_4$  was detected. However, they neglected the possibility that  $\text{SiCl}_4$  is emitted in excited states that may lead to fragmentation and convolution of the mass spectra.

Rossen [Rossen, 1988] views the major enhancement as surface reaction. Her modulated reactive molecular beam scattering studies indicated both  $\text{SiCl}_2$  and  $\text{SiCl}_4$  as primary reaction products. Product energy distribution analysis suggested that  $\text{SiCl}_2$  is emitted at 2900K after a first order surface process with a 0.15 ms relaxation time. Cracking patterns for the  $\text{SiCl}_2$  signal indicate that a measurable fraction of this species may also be emitted in a vibrational or excited state. The  $\text{SiCl}_4$  was emitted at 315 K after a pseudo-first order surface process with a relaxation time on the order of 0.25 ms. Sputtering was observed for ion energy greater than 400 eV. Although no qualitative modeling was attempted, the linear dependence of the etch rate on ion flux was observed.

Barker et. al. [Barker, 1983] proposed a simple mass balance model for steady-state chlorine coverage where the operative mechanism is ion-induced desorption of chlorine containing species due to a localized collision cascade and concluded that the rate limiting step is the desorption of strongly bound product species,  $\text{SiCl}_4$ . However, Gerlach-Meyer [Gerlach-Meyer, 1981] suggested the energy deposition at the halogenated surface enhanced the chemical reactions in the film, and the weakly bound  $\text{SiCl}_4$  products were thermally accommodated by the surface and spontaneously desorbed.

Recently, Balooch et. al. [Balooch, 1996] reported the ion-enhanced etching yield measurement with  $\text{Cl}_2^+$  and  $\text{Ar}^+$  beams of energy between 40 to 900 eV. The yield measured with  $\text{Cl}_2^+$  (with sufficient background chlorine flux to saturate the etching rate) exhibits a linear relationship with the square root of ion energy, and compares favorably with the etching yield measured with the same energy  $\text{Ar}^+$  in a chlorine background. However, the reported etching yield was 4-5 times lower than what we measured with argon ion and atomic chlorine. Cheng et. al. [Cheng, 1994] have observed enhanced chlorination by Cl atoms and interpreted the enhancement as evidence for a thicker silicon-chloride layer. All these evidences again justify the importance of distinguish the

difference between Cl and Cl<sub>2</sub> under ion bombardment to accurately simulate a chlorine plasma.

### ***1.2.2 Etching studies in high density plasma reactors***

In addition to beam experiments, researchers have performed numerous studies in various high density plasma reactors where the ion and neutral fluxes are less well defined. These studies are more relevant to industrial applications, and facilitate immediate advancement in the plasma etching processes. Dane et. al. [Dane, 1994] evaluated and modeled the parametric dependence of silicon etching in an ECR chlorine plasma. They have observed SiCl as the initial surface reaction product and SiCl<sub>2</sub> as the final volatile product.

Cheng et. al. [Cheng, 1994] used laser-induced desorption, combined with laser-induced fluorescence of SiCl<sub>(g)</sub>, to quantify the Si-chloride layer formed during etching of silicon by a high density, low pressure Cl<sub>2</sub> plasma in a helical resonator where the neutral-to-ion flux ratio is around 2. N-type Si(100) substrates were used in the laser-induced desorption experiments and undoped polysilicon were used in etch rate measurements. They measured a more highly chlorinated SiCl<sub>x(ads)</sub> layer ( x closer to 2 ) during plasma etching than a predominant SiCl<sub>(ads)</sub> layer when clean Si(100) was dosed with Cl<sub>2</sub>. Surface chlorination during plasma etching is attributed to Cl<sub>2</sub> impingement up to a coverage of  $5 \times 10^{14}$  Cl/cm<sup>2</sup>, and to Cl atom impingement and Cl<sub>2</sub><sup>+</sup> dissociative adsorption up to a saturated coverage of  $1 \times 10^{15}$  Cl/cm<sup>2</sup>. The reported etching yields are lower than what we measured at high chlorine-to-Ar<sup>+</sup> flux ratios. At a neutral-to-ion flux ratio of ~2, a substantial amount of the chlorine required to form volatile SiCl<sub>x(g)</sub> products is thought to be supplied by the impinging ions.

Layadi et. al. [Layadi, 1997] performed angular resolved x-ray photoelectron spectroscopy analysis to quantify the chlorinated surface layer formed during Cl<sub>2</sub> plasma etching of Si(100). It was found that the amount of chlorine incorporated into the silicon

surface layer increases with ion energy, and the chlorination depth is on the order of 13-25 Å for ion energies of 40 – 280 eV. Most importantly, SiCl<sub>2</sub> and SiCl<sub>3</sub> are found to be confined at the near surface region (~5 Å), while SiCl and disordered Si are present below the surface.

### 1.2.3 Studies and simulations of notching formation

Notching, the lateral etching at the foot of the polysilicon line, is commonly observed during overetching of a patterned polysilicon (aluminum as well) over an insulating material (e.g. silicon dioxide) [Nozawa, 1995] [Fujiwara, 1995] [Maruyama, 1997] [Tabara, 1996], as shown in Figure 1.5. Notching is formed along the interface of the conductive material and the insulating material. Notching can significantly change the critical dimension control in defining the polysilicon gate and should be eliminated.

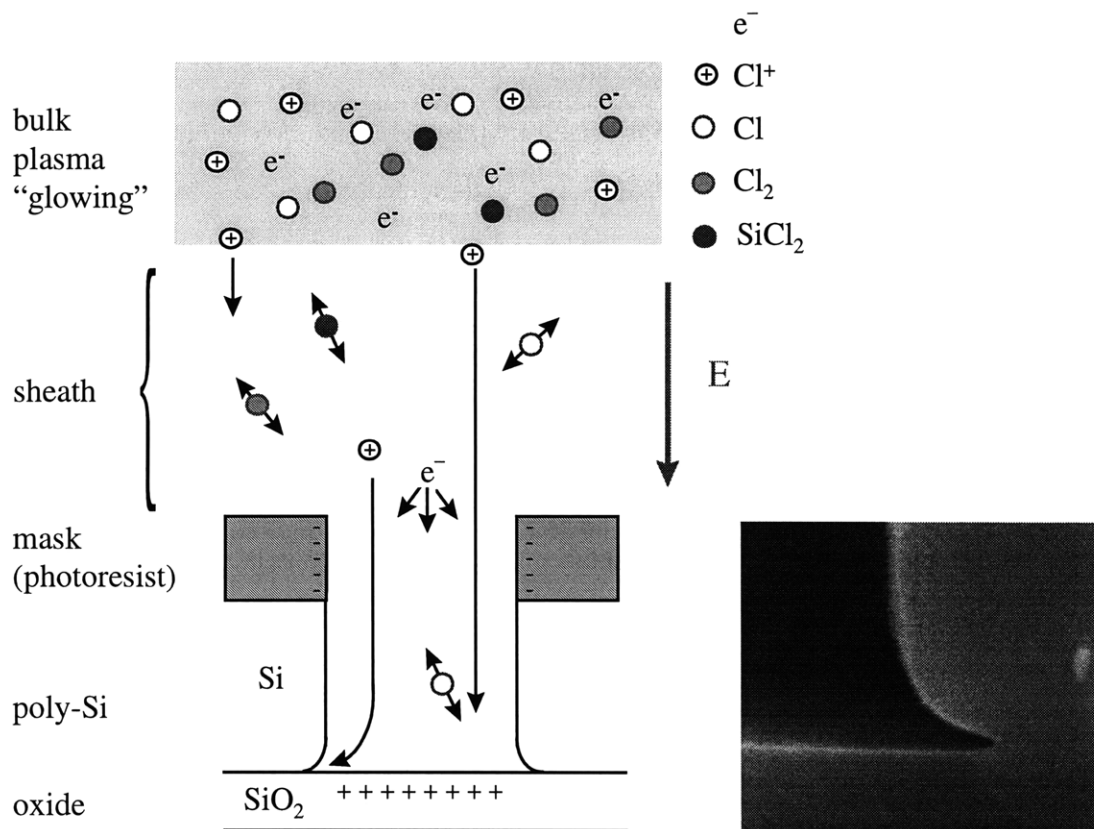


Figure 1.5: The illustration of notching formation during overetching of the polysilicon. The image shown on the right is a notch formed during etching of polysilicon in the beam

system after ~15% overetch, taken by Scanning Electron Microscopy (SEM). The setup of the experiments will be detailed in chapter 6.

Notching has long been attributed to the electric-field-induced ion trajectory distortion and the subsequent etching of polysilicon by these ions [Arnold, 1991] [Hwang, 1997] [Kinoshita, 1996]. The local electric field is built up due to the difference in the directionality and temperature (energy) of ions and electrons. Isotropic electrons charge the photoresist negatively and the directional ions charge the underlying oxide positively during overetch. The built-up field on the oxide surface deflects the incoming ions to the foot of the polysilicon lines and results in notching formation. The degree of notching is found to be a function of the ion to electron energy ratio [Arnold, 1991], and the electron temperature has also been shown to be critical in pattern-dependent charging [Hwang, 1997]. Notching occurs at the inner sidewall of the feature neighboring an open area, correlates well with the line and space layout, and the electrical connection of the patterned lines [Nozawa, 1995].

However, we proposed that stress at the polysilicon/oxide interface enhances spontaneous etching of polysilicon by reactive neutrals (Cl) and leads to the notch formation, as charging and ion trajectory distortion are not significant in the beam system. This assumption is investigated in this work and will be detailed in chapter 6.

#### ***1.2.4 Molecular dynamic (MD) simulations***

Molecular dynamic (MD) simulation has been used to enhance the understanding of the fundamental surface reaction mechanism during plasma etching processes. MD simulation of reactive ion etching of silicon by energetic chlorine ions have been reported by Athavale et. al. [Athavale, 1995], Barone et. al. [Barone, 1995] and Hanson et. al. [Hanson, 1997]. The etching yield is found to be a linear function of the square root of ion energy, agreeing well with the experimental results. MD simulation also revealed that the dominant silicon etching mechanism and the silicon etching product stoichiometry changed with ion energy. Surface roughening was observed by MD

simulation, and agrees qualitatively well with the experimental measurements. In addition to physical and chemical sputtering, Barone et. al. [Barone, 1995] reported an additional etching mechanism, direct abstractive etching (DAE), in which an incoming energetic ion reacts with a surface species, forms a volatile species, and leaves the surface with nonthermal energy. However, this mechanism is found to be operative and significant at very low ion energies (10-50 eV). The use of MD simulation combined with transition state computations are of great assistance in interpreting the beam kinetics and generalizing the results to conditions where similar measurements can not be made.

### **1.3 Studies of Ion Enhanced Chlorine Etching of SiO<sub>2</sub> and Photoresist**

#### ***1.3.1 Studies of ion-enhanced etching of SiO<sub>2</sub>***

Etching of silicon dioxide typically occurs during the overetch step in patterning the polysilicon gate. Overetch is performed to overcome the aspect ratio dependent etching and to ensure complete removal of polysilicon within all features. Since the etching characteristics of polysilicon and silicon dioxide are very different, interactions between the energetic and reactive species in the plasma and silicon dioxide can potentially change the concentration of reactive species within the feature (concentration of etchants or inhibitors). Moreover, the positive charging of the silicon dioxide surface could possibly affect the ion trajectories and result in notching at the foot of the polysilicon lines. A thorough understanding of etching of silicon dioxide is thus needed for better process modeling and for prediction of feature profile evolutions.

Etching of silicon dioxide was not well understood in the chlorine chemistry even though the chlorine-silicon system has been extensively studied. Since high selectivity between silicon and silicon dioxide can be achieved in a chlorine plasma etching process (compared to a fluorine plasma), etching of silicon dioxide was less a concern in the semiconductor industry and was not well characterized. However, as the feature dimension shrinks down to less than 0.25  $\mu\text{m}$  with the corresponding gate oxide thickness

less than 50 Å, etching of the underlying silicon dioxide during the overetch step can be problematic. Overetching is performed to overcome the commonly observed reactive ion etching lag (RIE lag), in that smaller feature etches slower than larger features due to the synergism of transport and surface reaction of reactive species within a feature. Therefore, silicon dioxide in larger features is subjected to prolonged etching, which in turn affects the integrity of the gate oxide and the performance of the device. For example, microtrenches are observed when the thin gate oxide was etched through, exposing the underlying silicon substrate to be etched at a rapid rate. It is thus important to characterize the etching of silicon dioxide in a chlorine based plasma process in order to properly simulate and predict the feature profile evolution.

Oostra et. al. [Oostra, 1986] has characterized the sputtering of SiO<sub>2</sub> with 3keV Ar<sup>+</sup> ions in a chlorine atmosphere and observed hardly any chemical enhancement when Cl<sub>2</sub> is added. Bello et. al. [Bello, 1994] characterized the etching of silicon surfaces with low energy chlorine ions and concluded the main oxide removal mechanism was physical sputtering. Thomas III et. al. [Thomas III, 1990] reported the etching of native oxide in an rf diode reactor and determined the threshold energy for native oxide removal is 72 eV. However, the product distribution and reaction pathways in chlorine etching of silicon dioxide have not been well characterized.

### ***1.3.2 Studies of ion-enhanced etching of photoresist***

Etching of photoresist in a chlorine plasma has not been well characterized, though great efforts have been directed to the development and characterization of the photoresist materials. Novolac-based photoresist has been widely used in industry to pattern various thin films in the plasma etching processes. In order for the patterning process to be successful, photoresist is designed and engineered to withstand ion bombardment and chemical erosion during the etching process. However, some degree of etching or erosion of the photoresist is commonly observed in the etching processes. Etched photoresist materials can deposit/redeposit on the sample surface and affect the

feature profile evolution; therefore, the etching mechanism and the product sticking probability have to be explored to quantify the effect of photoresist etching.

Photoresist is typically removed in an oxygen containing plasma with freons (e.g.  $\text{CF}_4$ ), after successful pattern transfer to the underlying thin film. This process is favorably referred as a plasma ashing process. Hsiao et. al. [Hsiao, 1997], Baggerman et. al. [Baggerman, 1994], and Varhue et. al. [Varhue, 1992] have characterized the etching of novolac-based photoresist in oxygen plasmas at various pressure and power conditions. Ion power density impinging upon the substrate is found to dominate the etching rate. Cook et. al. [Cook, 1983] suggested that oxygen induces chain scission in etching photoresist, and fluorine enhances the etching reaction by insertion into the carbon chain. Egitto et. al. [Egitto, 1985] pointed out that fluorine at high concentrations can inhibit the etching reaction by competing with oxygen for surface reactive sites.

Barklund et. al. [Barklund, 1992] measured the angular dependence of polymer etching and found the angular dependence varies as the etching chemistry changes. Carl et. al. [Carl, 1990] observed maximum etching yield of KTI-820 photoresist in an oxygen plasma at normal incidence angle. It is crucial to systematically characterize the etching of photoresist in a chlorine based plasma process to properly model the etching and deposition of the photoresist materials within the feature.

#### **1.4 Predictive Modeling of the Profile Evolution**

The ever-shrinking device dimensions with corresponding higher aspect ratios have made profile control in plasma etching processes a much more difficult task. These phenomena include variation of the etching rates (RIE), variation of etching profile shapes (bowing, faceting, trenching), variation in selectivity to the underlying film, and variation in film morphology. At the same time, etch rates need to be maximized while minimizing the device damage to make the etching processes economically viable. Therefore, the simulation and prediction of etching profile evolution becomes increasingly important to ensure the success of a deep-submicron etching process.

Predictive profile simulation has been long sought as a means to reduce the time and cost associated with trial-and-error process development and/or equipment design. Profile control is one of the most important aspects in pattern transfer as it determines the success of subsequent deposition processes and ultimately the device performance. To date, simulation work has given invaluable insight into the surface profile evolution during ion-enhanced plasma etching, using various techniques such as string algorithm [Ulacia F, 1988], characteristics method [Shagfeh, 1989], shock-tracing method [Hamaguchi, 1994] and direct simulation Monte Carlo (DSMC) method [Tait, 1994]. Dominant reaction mechanisms incorporated in these simulators include ion induced etching and ion reflection. More recently, localized surface charging effects [Arnold, 1991] [Murakawa, 1994] [Hwang, 1997] and redeposition [Tuda, 1996] on the sidewalls have also been taken into account.

Commonly observed high-density plasma etching peculiarities such as bowing, tapering, undercutting, trenching and micro-trenching have been predicted as different physical or chemical mechanisms are incorporated. However, comparing simulation results to etching profiles can not unambiguously determine the dominant surface phenomena as the profile evolution is often a function of the difference between several mechanisms, e.g. competition between etching and deposition processes. The profiles can often be fitted using more than one set of surface kinetics. Therefore, a comprehensive understanding of the dominant plasma-surface reaction pathways is needed to develop a general, predictive profile simulator. The use of beam studies in which the fluxes are well characterized to measure unambiguously the etching kinetics is valuable in determining the functionality of reactive species at specific, well-defined etching conditions, which can be generalized to the much more complex plasma environment.



## Chapter 2

### Experimental Setup

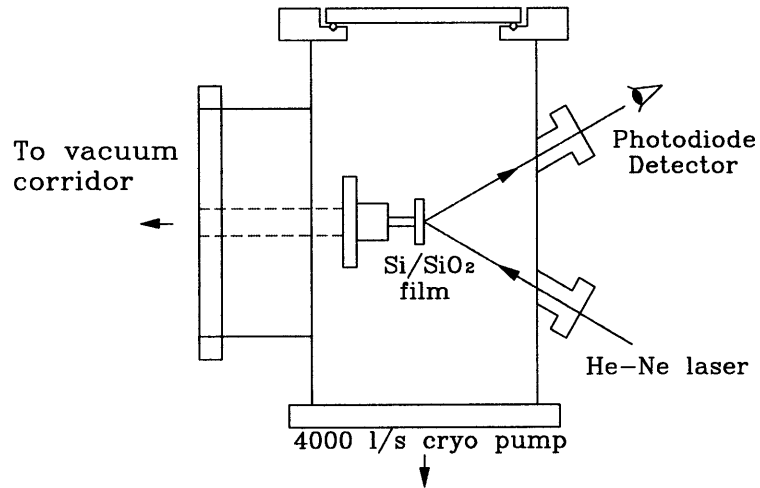
The experimental apparatus was designed and fabricated to accommodate the three beam sources utilized to simulate a plasma environment. In order to accurately simulate a high-density chlorine plasma, low energy ions ( $\text{Ar}^+$  or  $\text{Cl}^+$ ), reactants ( $\text{Cl}$  and  $\text{Cl}_2$ ), and inhibitors ( $\text{SiCl}_2$ ) are generated at flux levels comparable to those in a high density plasma reactor. Moreover, independent variation of the beam fluxes enables the determination of the functional role of each reactive species. The experimental setup undergoes a major modification during the course of this work, and is detailed in this chapter.

#### 2.1 Multiple Beam Chamber

The multiple beam apparatus used in this study consists of an 8" diameter stainless steel reaction vessel evacuated by a 4000 l/s cryogenic pump (CTI Cryogenics Cryo-torr 8). The cross-sectional view and beam-plane cross-sectional view of this apparatus are shown in Figure 2.1(a) and (b), respectively. Chamber base pressure is monitored with a Bayard-Alpert type ionization gauge (Perkin Elmer DGC III) and is typically  $2 \times 10^{-8}$  torr after over-night bake. Two  $40^\circ$  optical ports which allow *in situ* interferometric measurement of the thin film etch rates are also shown in Figure 2.1 (a). In addition, one 2.75" conflat port allows main chamber roughing via a roughing pump and the introduction of dry  $\text{N}_2$  to vent the system.

A 4 mW He-Ne (633 nm, Uniphase 1507P) polarized laser beam is introduced through the lower port, striking the sample at the chamber center, and reflecting through the upper port where the interferometric signal is measured with a photometer (Metrologic). The top flange is a quartz window that allows the visual inspection of the chamber interior during process.

(a)



(b)

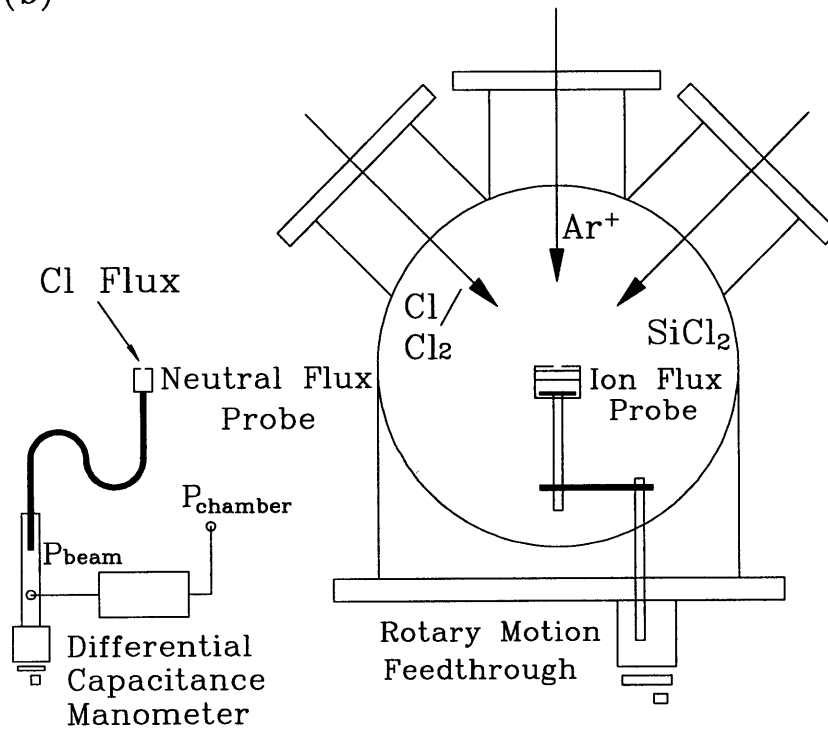


Figure 2.1: Cross-sectional view (a) and beam-plane cross-sectional view (b) of the multiple beam apparatus. Setup for laser interferometry and beam flux measurements is shown in (a) and (b) respectively.

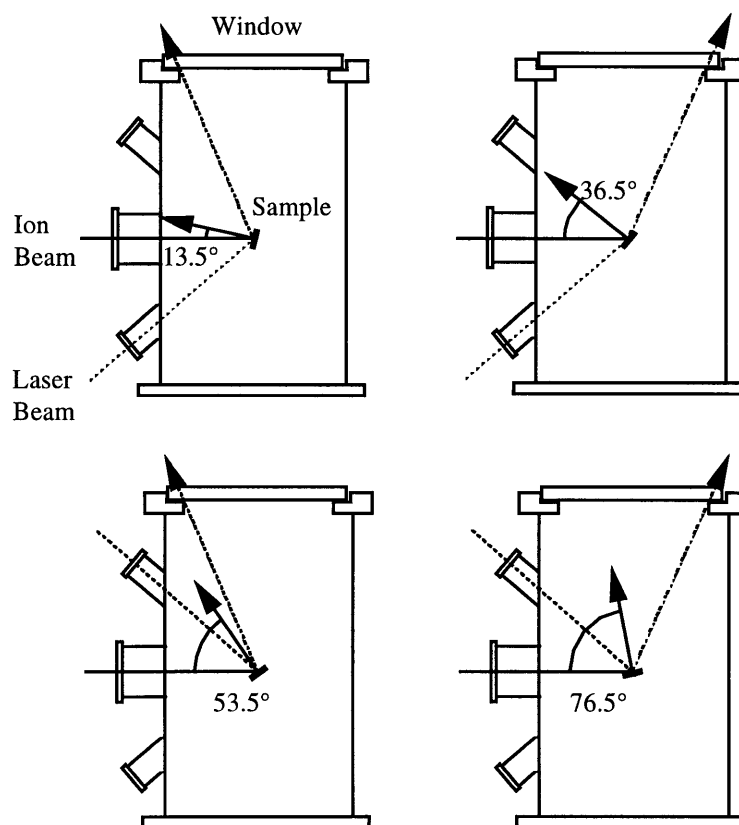


Figure 2.2: Measurement of etching rate at ion incidence angles other than normal. Ion incident angle is varied utilizing tilted sample holders. Etching rate is measured by allowing laser beam exit through the quartz window on top of the chamber.

When samples are set at off-normal positions, the incident laser is sometimes introduced from the top view port and exit from the top quartz window as shown in Figure 2.2. In this case, the measured ionic and neutral flux has to be corrected taking into account the angle between the source and the sample surface normal to yield the correct incident fluxes.

Three 4.62" conflat ports, oriented 45 degree apart, defined the molecular beam plane are equipped on the vertical mid-plane of the chamber. Ionic, atomic and molecular beam sources have been constructed directly on 4.62" conflat flanges to facilitate easy mounting and removal the various sources onto the beam chamber. Typically, the ion beam is directed normal to the sample surface, and the neutral beam(s)

are directed to the sample surface at a  $45^\circ$  angle. The operating ranges of flux levels are  $6 \times 10^{13} - 1 \times 10^{16}$  #/cm<sup>2</sup>/s for ion beam,  $6 \times 10^{15} - 1 \times 10^{17}$  #/cm<sup>2</sup>/s for the atom beam, and  $1 \times 10^{15} - 6 \times 10^{16}$  #/cm<sup>2</sup>/s for the thermal beam. The substrate temperature is controlled at  $40 \pm 5^\circ\text{C}$ .

The sample was introduced into the chamber after retrieving the ion energy analyzer, heated to the desired temperature, and then etched by ion and atom beams simultaneously. The etching rate of polysilicon and the deposition rate of SiCl<sub>2</sub> were measured *in situ* by recording the periodic variation of the sample reflectivity. Samples used in this work included:

(1) Undoped polysilicon: Planar undoped polysilicon ( $\sim 5000 \text{ \AA}$ ) deposited over a  $1000 \text{ \AA}$  thick thermal oxide film is used as sample substrates. The observed etching rate was determined after etching through  $\sim 2000 \text{ \AA}$  of the polysilicon corresponding to about 2 cycles of the interferometric fringes.

(2) Thermal oxide: Approximately  $1000 \text{ \AA}$  SiO<sub>2</sub> thermally grown over a p-type silicon substrate is used as sample substrates. The thickness change of the SiO<sub>2</sub> film was determined by *in situ* ellipsometry and *ex situ* Nanospec measurements.

(3) Photoresist: Approximately  $9500 \text{ \AA}$  OCG-825 positive photoresist (OCG Microelectronic Materials, Inc.) was spin-coated over a  $1000 \text{ \AA}$  thick thermal oxide film and was used as sample substrates. The etch rate was measured by laser interferometry and can also be determined by *in situ* ellipsometry.

(4) Photoresist patterned polysilicon (supplied by Sematech): n-type doped polysilicon ( $\sim 5000 \text{ \AA}$ ) patterned by  $\sim 5000 \text{ \AA}$  Apex-E deep UV photoresist was etched to generate profiles for simulation confirmation. The patterns consisted of  $0.35 \text{ \mu m}$  lines with spacings of  $0.35$ ,  $0.7$ , and  $1.4 \text{ \mu m}$ , and  $0.5 \text{ \mu m}$  lines with spacings of  $0.5$ ,  $1.0$ , and  $2.0 \text{ \mu m}$ .

The gases used in this work included: 99.997% argon (BOC research grade), 99.98% chlorine (Matheson research grade), and 99.99% dichlorosilane (Matheson research grade).

## 2.2 Clustered Processing System (First Setup)

The first experimental setup is detailed in Gray's thesis [Gray, 1993] and is summarized in Figure 2.3.

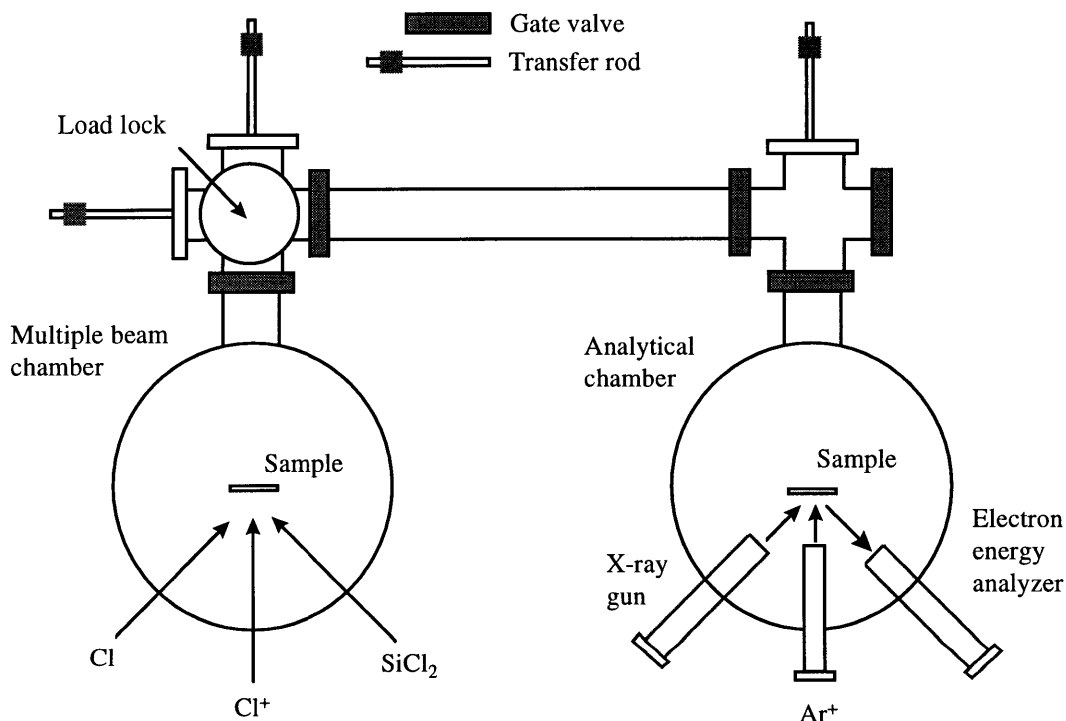


Figure 2.3: Schematic diagram of the clustered vacuum transfer system. This system allows *in situ* vacuum transfer of a sample from the multiple beam chamber to an analysis chamber where X-ray photoelectron spectroscopy analysis can be performed.

A 10" conflat flange adapter to which a load-lock and an internal sample/probe mounting platen are attached is installed opposite to the beam mounting ports. The sample mounting assembly is introduced into the main chamber on a differentially pumped transfer rod, and mates to a pair of alignment pins, placing the substrate face at

the reactor center and ensuring reliable electrical contact. Beam diagnostic probes are also mounted on this side flange adapter as shown in Figure 2.1(b). The diagnostic probes can be rotated to the sample position before and after the experiments for quantitative flux measurements.

The chamber is connected to a load-lock which is evacuated by a 110 l/s turbo pump (Balzers TPU 110) for rapid introduction of the sample into the vacuum system. An analytical chamber equipped with an X-ray Photoelectron Spectrometer is also connected to the load-lock, available for post-etching surface analysis. It is worth noting that the take-off angle for XPS analysis is fixed at normal ( $90^\circ$ ) in this setup. Detailed description of the XPS system can be found in section 2.5.4.

### 2.3 Integrated Processing System (Second Setup)

An integrated processing system was fabricated to increase the material processing capability, and the multiple beam apparatus is connected to a 34 feet long, vacuum transfers tube as shown in Figure 2.4.

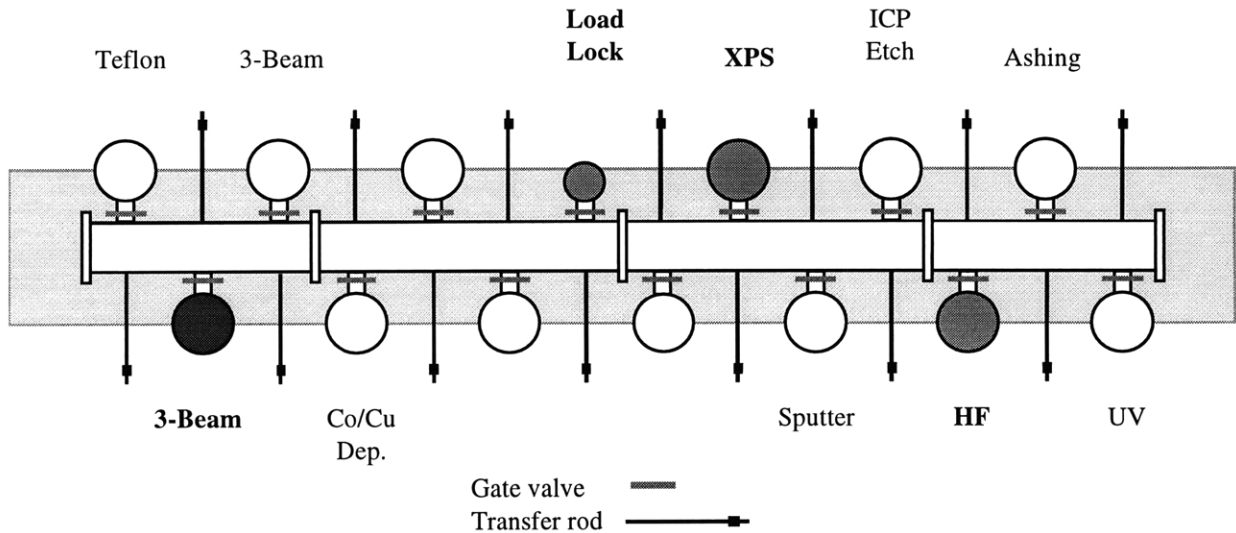


Figure 2.4: Schematic diagram of the integrated vacuum transfer system. This system allows *in situ* vacuum transfer of a sample between various process chambers to achieve integrated material processing, which is required as the process criteria becomes more

stringent. An analysis chamber equipped with X-ray photoelectron spectroscopy allows *in situ* surface analysis after processes.

The vacuum transfer tube facilitates *in situ* sample transfer, and is evacuated by two 4000 l/s cryogenic pumps (CTI Cryogenics Cryo-torr 8), with a base pressure of  $4 \times 10^{-9}$  torr. A load-lock chamber is available on the transfer system for introduction of thin film samples into the vacuum transfer tube and thereby the 3-beam chamber. An analytical chamber equipped with an X-ray Photoelectron Spectrometer is also available on the transfer system for post-etching surface analysis. In this setup, samples can be rotated in the analytical chamber to allow angular resolved XPS (AR-XPS) analysis, as detailed in section 2.5.4. An ellipsometer is equipped on the HF/H<sub>2</sub>O processing chamber to facilitate *in situ* oxide thickness measurement.

Sample mounting assembly and beam diagnostic probes are equipped on the multiple beam apparatus via two 2.75" conflat ports lying on the mid-plane of the chamber, as shown in Figure 2.5.

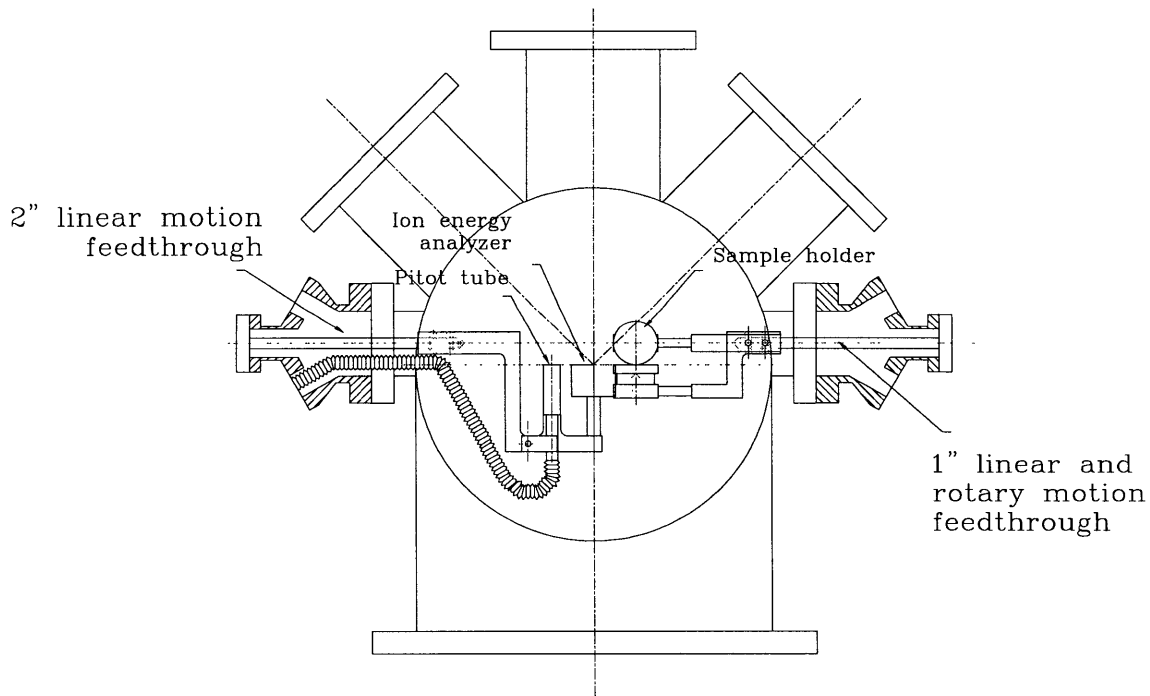


Figure 2.5: Beam plane cross sectional view of the modified multiple beam chamber. The beam flux diagnostic probes are shown.

The sample mounting assembly is coupled with a 1" linear and rotary motion feedthrough to facilitate transfer and manipulation of the samples. A sample is clamped on a one-inch stainless steel holder (#SAM-1, MDC), and is transferred into the chamber via a magnetic transfer fork, as shown in Figure 2.4. The pin on the sample mounting assembly mates with the sample holder and allows transfer of the sample into the chamber. The sample can be rotated 90 degree and becomes perpendicular to the beam plane and faces the beam sources during experimental runs. A resistive sample heater and a K-type thermocouple are used to control and measure the temperature of the sample. The ion energy analyzer and a pitot tube are coupled with a 2" linear motion feedthrough to allow measuring ion energy and ion and neutral fluxes at the sample position when sample is rotated away from its vertical position during etching runs. The beam diagnostic probes are retrieved during experimental runs.

## **2.4 Beam Sources**

Great effort has been devoted to the development of the beam sources in the first phase of this project. It is necessary to simulate accurately a high-density plasma environment by generating beams representative of low energy ions and reactive neutral radicals. The chamber pressure is maintained  $< 10^{-5}$  torr when all three beams are operational to ensure that gas phase collisions are not important.

### ***2.4.1 Compact electron cyclotron resonance (CECR) ion source***

An ASTeX (Applied Science and Technology, Inc., Woburn, MA) Compact Electron Cyclotron Resonance (CECR EX 4300) plasma source was utilized to produce nearly mono-energetic, low energy (30-100 eV) and high flux ( $0.01-2 \text{ mA/cm}^2$ ) argon or chlorine ions, as shown in Figure 2.6. A high density plasma,  $>10^{12} \text{ cm}^{-3}$  ionization, is generated in CECR between the applied microwave (2.45 GHz, 250 W) and magnetic field.



The source was modified as following to generate a beam of low energy ions. The ions are extracted from the CECR plasma through a 0.5-inch diameter extraction grid at the exit of the plasma chamber. The holes of the extraction grid (#228 Buckbee-Mears) are on the order of the debye length of the plasma, about 10  $\mu\text{m}$ , to prevent plasma flow through the grid. A 1" long nickel or stainless steel biasing liner is added inside the quartz plasma chamber to bias the plasma to the desired potential. The ion energy is adjusted by varying the plasma potential. Ions are accelerated across the sheath with respect to the extraction grid, and then transported into the main chamber in which an electron filament is used to maintain the beam quasi-neutrality and avoid coulombic expansion of the beam. The design of the CECR makes it simple to select ion type by changing the feed gas. A detailed description of the modification and characterization of this source can be found elsewhere [Zau, to be published].

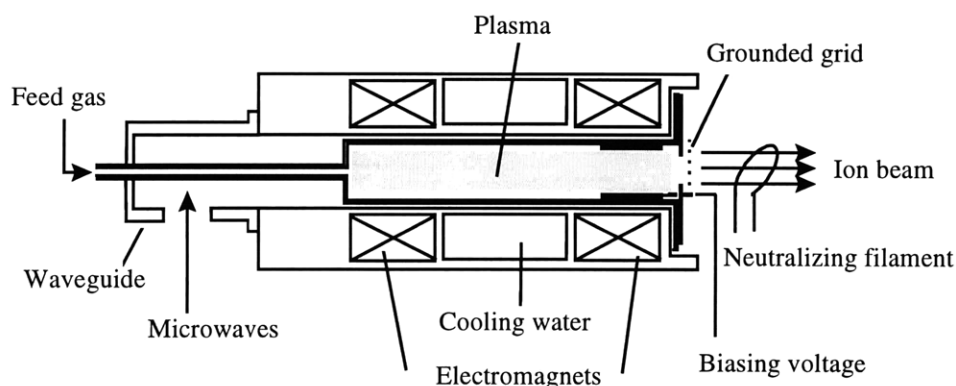


Figure 2.6: Schematic diagram of a modified ASTeX Compact ECR source for generating high density, low energy ions. Plasma is generated by the applied microwave and magnetic field and its potential is determined by the applied biasing voltage to a nickel or stainless-steel liner. Ions are extracted and accelerated through a ground stainless-steel mesh, space charge compensated by electrons from a neutralizing filament and transported to the sample.

Monoatomic  $\text{Cl}^+$  is found to be the primary ion by mass spectrometry measurement, as shown in Figure 2.7. The major ionic species is  $\text{Cl}^+$  and the  $\text{Cl}_2^+$  signal is relatively small. Trace amount of oxygen (16), silicon (28), chromium (52) and iron (56) are also observed due to the sputtering of the quartz chamber and the stainless steel liner. The ion beam at the sample position is fairly uniform, with less than 10% variation

across a  $1\text{cm} \times 1\text{cm}$  silicon die, as shown in Figure 2.8. The ion flux increases as the bias voltage increases, and depends strongly on the tuning of the magnetic field and the current to the electron filament.

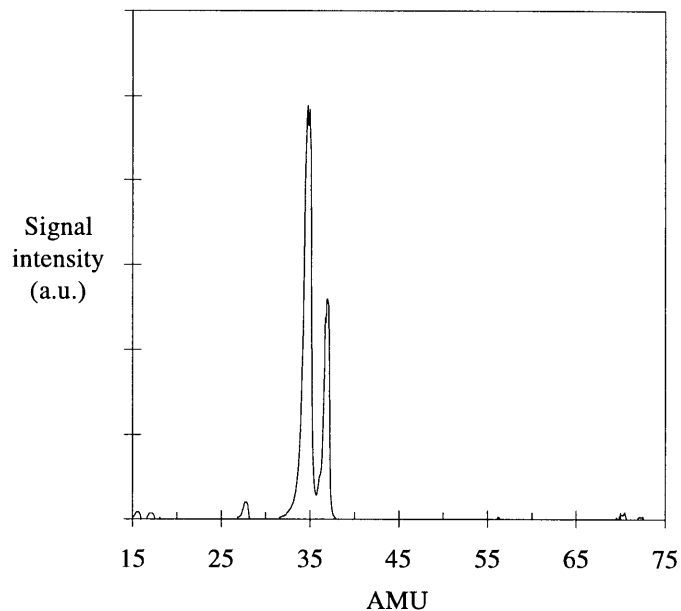


Figure 2.7: Chlorine ion beam characterization measured by a mass spectrometer. Mono-atomic  $\text{Cl}^+$  is found to be the primary ion generated by the modified ASTeX CECR source.

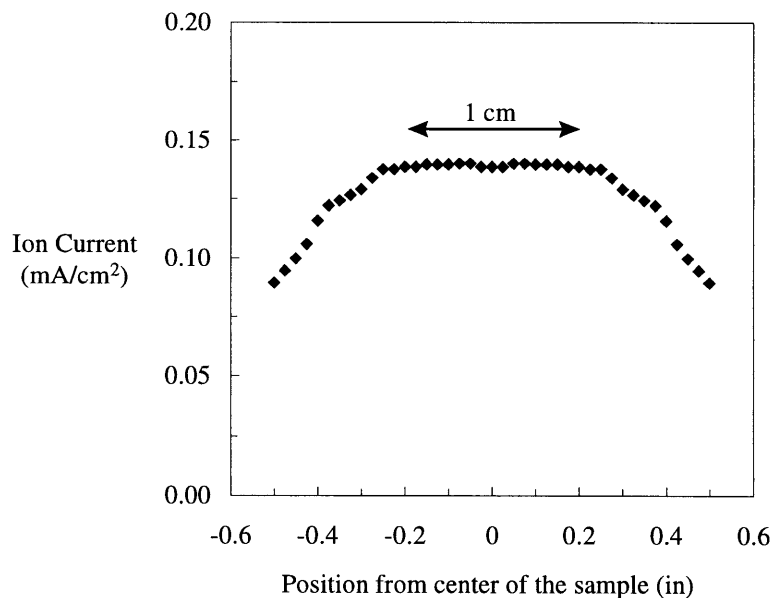


Figure 2.8: Measured ion flux profile with respect to the center of the sample. The ion flux was fairly uniform over the entire sample ( $\sim 1\text{cm} \times 1\text{cm}$ ). Reduction of the ion flux in the periphery is a consequence of the diverging magnetic field.

A typical ion-energy-distribution-function measured *in situ* by the gridded ion energy analyzer is shown in Figure 2.9. The left axis represents the ion current and the right axis is the derivative of the ion current to ion energy and represents the energy distribution. Typically, ion energy equals the bias voltage plus 15-20 eV plasma self-bias. The ions have an energy distribution with approximately 10 eV spread at full width at half maximum. This is due to the variation of potential at which ionization occurs along the length of the ECR source as suggested by Kaufman et. al. [Kaufman, 1982].

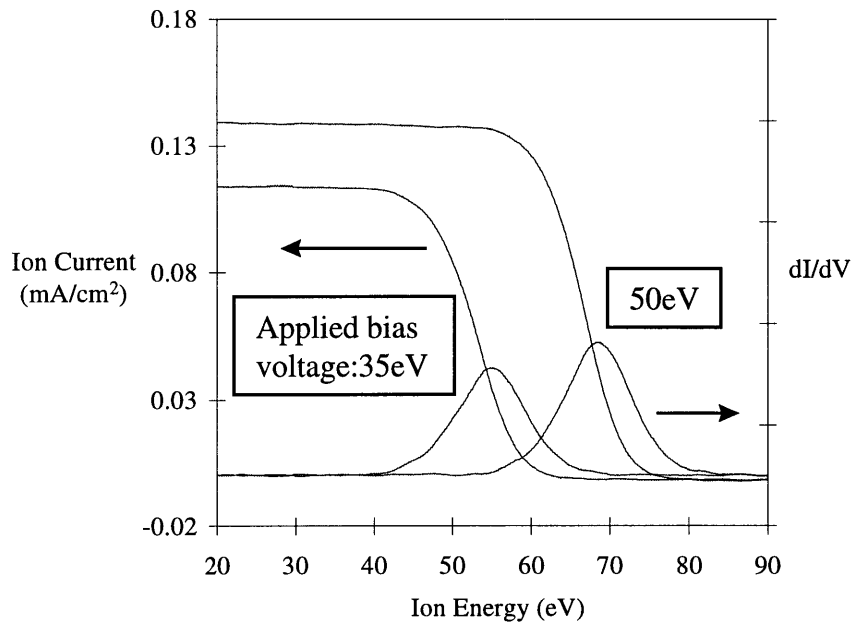


Figure 2.9: Characteristic ion energy distribution function measured by the gridded ion energy analyzer. The left axis represents the ion current and the right axis is the derivative of the ion current to ion energy and represents the energy distribution. The ion beam energy is the sum of the applied bias voltage and plasma self-bias which is typically 15 - 20 eV. The full width at half maximum of the energy distribution is approximately 10 eV that is due to the ionization position and potential variation within the plasma.

The ion current and energy as a function of the accelerating voltage is shown in Figure 2.10. The ion current density is in a space charge limited regime where Coulombic repulsion force between the ions is the limiting factor. The voltage dependence of the measured ion fluxes is governed by the Child-Langmuir Law:

$$I \propto \frac{V_t^{3/2}}{d^2} \text{ [Chapman, 1980], where } V_t \text{ is the ion energy and } d \text{ is the distance between the}$$

two grids in the ion energy analyzer, which will be described later. As shown in Figure 2.10, the plasma self-bias remained on the order of 15-20 eV over the ion energy range of 30-100 eV.

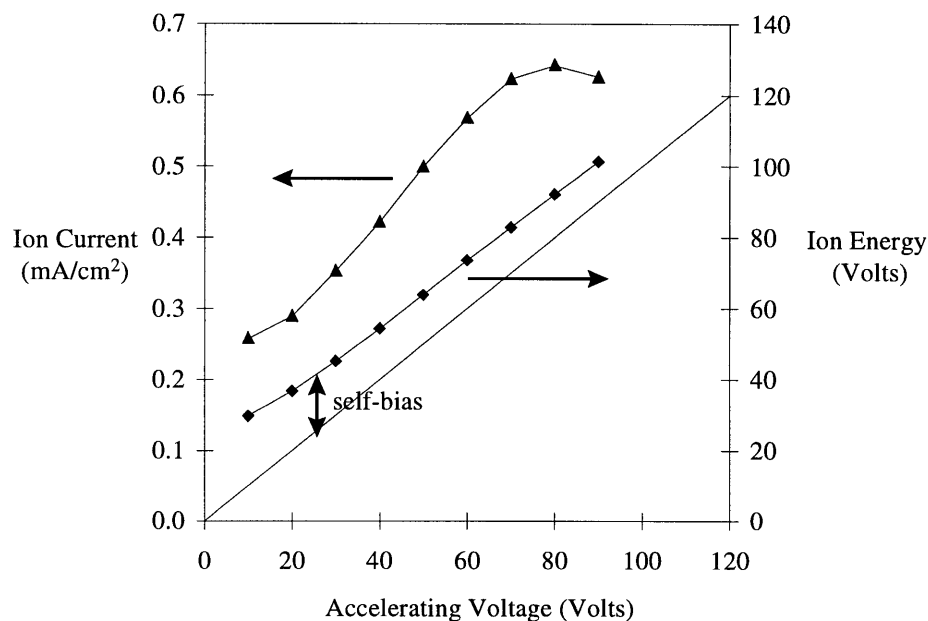


Figure 2.10: Ion current and energy as a function of accelerating voltage. Data are taken with chlorine at a flowrate of 0.5 sccm with 200 Watts forward power (2 Watts reflected power).

There is a concern that the charge exchange collision,  $A^+ + A \rightarrow A + A^+$ , produces fast neutrals that attribute to etching but are not measured as ion current. The charge exchange cross section for argon is approximately  $(30-60) \times 10^{-16} \text{ cm}^2$  [Robinson, 1982] [Chapman, 1980]. The charge exchange cross section for chlorine is assumed to be about the same. At the operating pressure of 0.1-0.3 mtorr, the mean free path for charge exchange is approximately 35 cm. Therefore, the charge exchange collisions are neglected.

The major difficulties associated with the development and modification of the ECR source are: 1) poor thermal contact of the extraction grid to the extraction plate results in over-heating of the grid and ultimately the deformation of the grid. 2) back streaming of the plasma to the gas feed line results in over-heating of the ECR source. Consequently, conductive composite (Dupont) was applied to the extraction grid to

ensure good thermal contact, and a ceramic tube was inserted into the gas feed line to eliminate plasma back-streaming.

#### ***2.4.2 Coaxial microwave atom source***

One major challenge in this work is to create a high density, directed flux of atomic chlorine to simulate accurately a high density chlorine plasma. The atom source is a vacuum compatible coaxial cavity microwave source which yields high flux of atomic chlorine ( $6 \times 10^{15} - 1 \times 10^{17} \text{ cm}^{-2} \text{ s}^{-1}$ ). Microwave cavities have long been used to generate atom beams. Approximately 90% dissociation is measured by utilizing a UTI mass spectrometer in line-of-sight on another vacuum system [Zau, to be published]. In a traditional microwave cavity atom beam source, the feed gas flows from a discharge on the air side, through a vacuum feedthrough, and into the vacuum. The generated atoms are then transported over significant distance into the vacuum chamber and are emitted as a beam through a channel. This method works well for atoms with low surface recombination rates, e.g. fluorine in an alumina tube. For atoms with high surface recombination rates, such as chlorine, hydrogen and oxygen, most of the generated atoms are lost by surface recombination during transportation from the plasma to the channel. The resultant atom beam flux is therefore very low, and in some cases, not measurable.

In order to reduce surface recombination, increase the feed gas dissociation, and thus increase the atom beam flux, various surface passivation techniques such as adding catalyst gases [Kikuchi, 1993] [Spence, 1988] and surface treatment for the discharge tube [Yu-Jahnes, 1992] [Deshmukh, 1993] have been used. These rely on changing the surface of the discharge tube or laying down a passivation film to lower the surface recombination rate of the atoms, thus increasing the feed gas dissociation. Adding catalyst gases introduces unwanted impurities into the atom beam. The surface treatments are complex, their effectiveness can change over time as the passivation layer is worn out and can be sensitive to the history of the beam source. Therefore, minimizing the transport of the

atoms between the plasma where it is generated and the channel where it is emitted as a beam can reduce the surface recombination loss.

In this work, a novel coaxial microwave cavity atom beam source that can generate high atomic beam flux was developed, eliminating the need to transport atoms over significant distances, as shown in Figure 2.11.

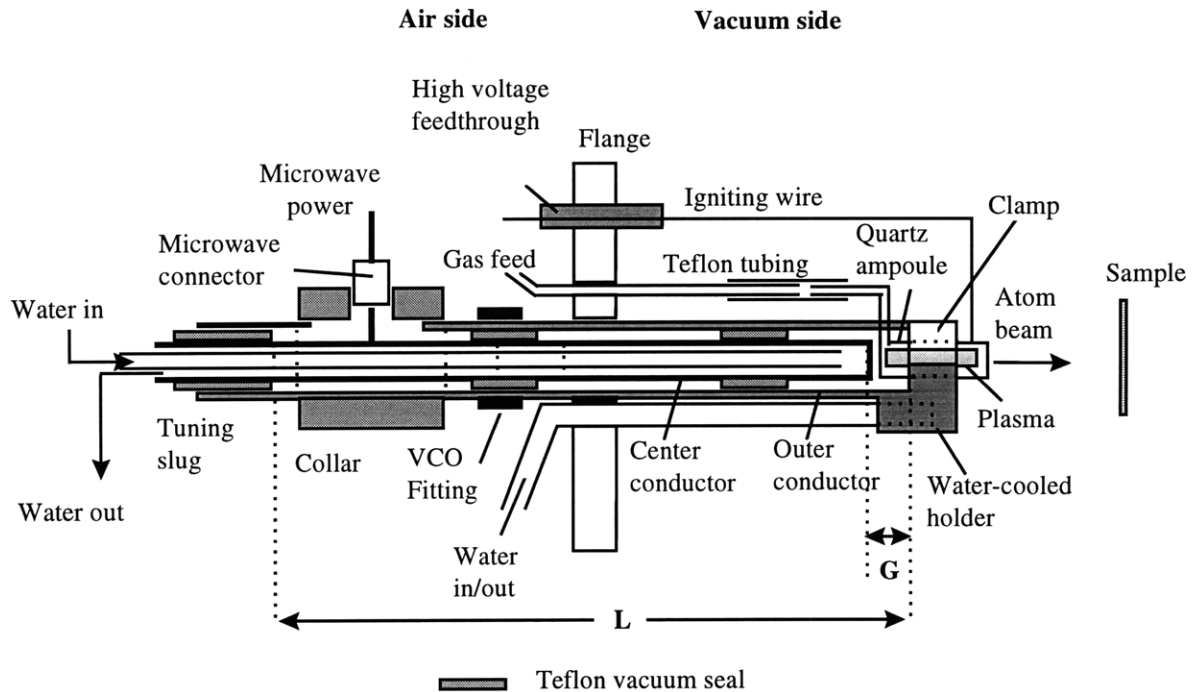


Figure 2.11: Schematic diagram of a coaxial microwave cavity atom beam source. Microwave power is fed into the cavity through a slot in the outer conductor and generates a plasma inside the quartz ampoule at the vacuum end of the source. The cavity length  $L$  is determined by the sliding short ( tuning slug ) at the left end and the plasma ampoule that acts as a short at the right end. The plasma dissociates the feed gas into atoms, which are then emitted directly through a channel built into the quartz ampoule to form the atom beam. Silicon sample is approximately 1.5 cm away from the channel surface.

The coaxial microwave cavity beam source works by moving the plasma from the traditional remote location on the air side of the system to the vacuum side near the location where the atom flux is required. The use of a coaxial cavity rather than a waveguide allows the cavity to be compact, i.e. much smaller in diameter than the wavelength,  $\sim 10$  cm. The applied microwave power generates plasma inside the quartz ampoule that acts as

an electrical short between the inner and outer conductors at the vacuum end of the source. The plasma dissociates the feed gas into atoms that in turn emitted directly through a channel built into the quartz ampoule to form the atom beam. As a result, the loss from transporting the atoms from the plasma to the channel is eliminated.

The atom source acts like a foreshortened coaxial line cavity [Ramo, 1953] similar to an “Evenson” cavity [Fehsenfeld, 1964]. The resonance condition is given by:

$$\frac{2\pi L}{\lambda} = \tan^{-1}\left(\frac{1}{Z_o \omega C_o}\right) \quad (2.1)$$

where  $Z_o$  is the impedance of the coaxial line,  $\omega$  is the microwave frequency (2.45 GHz),  $C_o$  is the capacitance of the foreshortened end of the cavity and  $\lambda$  is the wavelength of the microwave frequency used. The atom source is designed such that  $G \ll \lambda$ , where  $G$  is the gap between the center conductor and the end of the cavity, and  $Z_o \omega C_o \ll 1$  so that the resonance cavity length is given by:

$$L_{resonance} = \left(\frac{n}{2} + \frac{1}{4}\right)\lambda \quad \text{where } n = 0,1,2,3,\dots \quad (2.2)$$

The cavity length can therefore be incremented by half wavelength increments making the atom beam adaptable to any physical length requirement.

The effective cavity length,  $L$ , of the atom source is defined by the distance between the tuning slug and the clamp that holds the quartz ampoule. The cavity length can be changed by moving the tuning slug located at the air side. Microwave power is fed into the cavity through a slot in the outer conductor through an N-type microwave connector (Huber-Suhner) which is mounted on a movable collar. The collar is moved along the outer conductor tube to match the cavity to the  $50 \Omega$  impedance of the microwave cable. Both tuning elements for the atom source are external to the vacuum environment, and thus allow easy tuning and eliminate the need for a complex vacuum motion feed through.

One of the most important design and operation issues with the atom source is cooling of the source. The microwave plasma generates a significant amount of heat and conductive heat transfer inside a vacuum environment is limited. Therefore, both the center conductor (gold plated) and the ampoule holder are water cooled. The center conductor is a 0.25" tube with a coaxial inner tube of 0.125". Cooling water flows in through the inner tube and out through the annular space. The holder is a solid block of metal through its lower part the cooling water circulates to facilitate heat removal. The quartz ampoule is held in place by the clamp with a layer of indium foil between the quartz ampoule and the holder to improve thermal contact. This is very important since poor thermal contact will cause the ampoule to rise to high temperatures and cause the Teflon sleeve to flow.

The main vacuum seal of the atom source is a compression Teflon seal that is formed at both the outer surface of the center conductor and the inner surface of the outer conductor. The tapered Teflon seal piece is held by a modified VCO<sup>®</sup> fitting (Cajon Company) welded onto the outer conductor on the air side. This seal alone is adequate to maintain  $< 10^{-8}$  torr vacuum in our system. A secondary Teflon seal is located on the vacuum side and the space between the two Teflon seals can be differentially pumped if lower leak rates are required.

The atom source is also equipped with an ignition wire that runs from the channels on the quartz ampoule to a high voltage feed through on the mounting flange. Touching a Tesla coil to the high voltage feedthrough ignites the plasma.

Quartz ampoules are used to contain the plasma, and a schematic diagram of the quartz ampoule is included in Appendix A. The feed gas to the quartz ampoule passes through a 6 cm long capillary feed gas line (0.15 mm inside diameter) to prevent the plasma back-streaming into the feed gas line. The atoms generated by the plasma inside the ampoule ( $\sim 350 \text{ mm}^3$ ) are emitted as a beam through laser drilled channels at the front plate of the ampoule. Multiple channels were used in order to maintain a low enough



pressure inside the quartz ampoule to sustain a plasma, and achieve higher flux at the sample surface.

The channel dimension and number of channels were designed to obtain high atom flux at the sample surface. Moreover, channel design and layout have to be optimized to prevent plasma extrusion, maintain the adequate ampoule pressure maximize chlorine dissociation rate, and eliminate the probability of chlorine atoms collide the wall, which lead to the recombination of the chlorine atoms. Zau [Zau, to be published] has characterized the dissociation efficiency of the atom source as a function of feed gas flowrate and applied power, and concluded 85-95% dissociation efficiency can be achieved with his original design (channel dimension: 0.5mm×3.0mm) with 1 sccm gas flowrate. To prevent plasma extrusion, the channel dimension was reduced to 0.25 mm but the number of holes was increased to 16 to maintain similar pressure inside the ampoule that favors the high dissociation rate of chlorine. The length of the channels is 1.5 mm, to maintain the aspect ratio of six.

The directionality of the beam is approximated by calculating the channel diameter to tip mean free path ratio,  $\eta$ , that is proposed by Gray [Gray, 1992] for characterizing the angular dispersion in opaque regime tube flow:

$$\eta = \frac{d}{\lambda_{tip}} = \frac{d\sqrt{2\pi}\sigma^2 P_{tip}}{k_b T} \quad (2.3)$$

$$P_{tip} = \frac{N_{tot} 4k_b T}{\pi d^2 v} \quad (2.4)$$

$d$  is the channel diameter,  $\lambda_{tip}$  is the mean free path at the channel exit,  $\sigma$  is mean molecular collision diameter,  $P_{tip}$  is the pressure at the exit of the channels,  $k_b$  is the Boltzman constant,  $T$  is the gas temperature (assumed to be 500K),  $N_{tot}$  is the total molecular flow, and  $v$  is the mean molecular speed. At a typical gas flowrate of 0.2 sccm, calculated  $\eta$  is 0.5. For  $\eta < 1$ , the beam is indeed operated at the opaque molecular flow regime where the beam flux is somehow directional. As the beam directionality decreases with increasing  $\eta$ , the beam directionality is compromised for higher beam flux at the sample surface.

The atom beam is uniform across a  $0.5 \text{ cm} \times 0.5 \text{ cm}$  area. When 0.2-1 sccm gas flow rate was used, 0.02-0.3 mtorr flux level was achieved at the sample surface. The atom source was operated at 60W forward power, 9W reflected power (250W, 2.45GHz ASTeX microwave power supply). Detailed characterization of this source can be found elsewhere [Zau, to be published].

### 2.4.3 Thermal beam source

A hot beam source is constructed to generate neutral radicals pyrolytically. It consists of an alumina tube about which a coiled heating filament is wrapped with a water cooled radiation shield that is used to prevent heating of the sample and chamber, as shown in Figure 2.12.

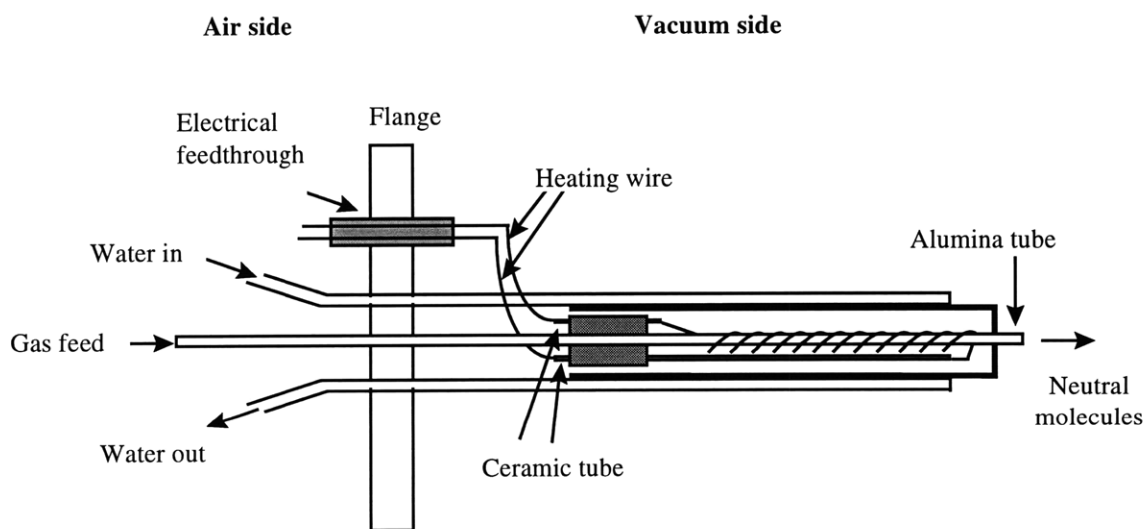


Figure 2.12: Schematic diagram of a thermal beam source. It consists of an alumina tube about which a coiled heating filament is wrapped with a water cooled radiation shield that is used to prevent heating of the sample and chamber. A thermocouple in contact with the alumina tube is used to monitor the pyrolysis temperature (not shown here).

A thermocouple in contact with the alumina tube is used to monitor the pyrolysis temperature. The gas flow through the alumina beam tube is rarefied during operation making the pyrolysis a surface mediated process. Beam tube temperatures up to  $1200^{\circ}\text{C}$

can be achieved to dissociate or excite gas molecules such as dichlorosilane. Dichlorosilane has been used in semiconductor industry as a source for silicon epitaxy due to its ability to form high quality films at low temperatures [Bloem, 1980] [Coon, 1991]. The major pyrolysis products measured are  $\text{SiCl}_2$  and  $\text{H}_2$  [Hierlemann, 1995] [Sasaoka, 1994].  $\text{SiCl}_2$  is the most stable and greatest in concentration of the decomposition products at low temperatures according to an *ab initio* molecular orbital calculation [Ishitani, 1987]. The surface fluxes produced by the beams was approximately  $1 \times 10^{15} - 6 \times 10^{16} \text{ cm}^{-2} \text{ s}^{-1}$ .

## 2.5 Diagnostics

### 2.5.1 Laser interferometry

The etching or deposition rate of polysilicon can be accurately measured *in situ* using laser interferometry. Application of this technique requires an abrupt change in refractive index at the thin film/substrate interface. A sufficiently thin and transparent film is required to ensure some laser reflection at the interface. The interference created between the light reflected from the film being etched and the underlying thin film (“gate oxide” in this case) produces a sinusoidal intensity that can be used to monitor the etching rate of the thin film. For a laser beam striking the film at an angle  $\theta$  to the normal, the reflected beam amplitude oscillates due to interference, and the change of film thickness  $d$  is given by:

$$\Delta d = \frac{\lambda / 2}{\sqrt{(n^2 + \sin^2 \theta)}} \quad (2.5)$$

where  $\lambda$  is wavelength of the light source,  $\theta$  is the incident angle of laser,  $n$  is the refractive index of the thin film. A 4 mW polarized He-Ne 633 nm laser (Uniphase 1507P) is used as the light source, a Metrologic photometer is used to detect the reflected light signal which is in turn sent to a data acquisition board for further data analysis. A strip chart record is also available for data recording.

### 2.5.2 Gridded ion energy analyzer

The gridded ion analyzer used in this work was constructed by collaborating with Gibson [Gibson, 1995]. A schematic diagram of the ion energy analyzer is shown in Figure 2.13. Gibson's original design was an extremely small ion energy analyzer, which is capable of measuring ion energy distribution functions (IEDF) with sub-eV full width at half maximum (FWHM). However, due to the difficulties associated with reproducibility, several modifications have been made to maximize the electrical isolation between grids to gain reproducibility and reliability of the ion energy analysis.

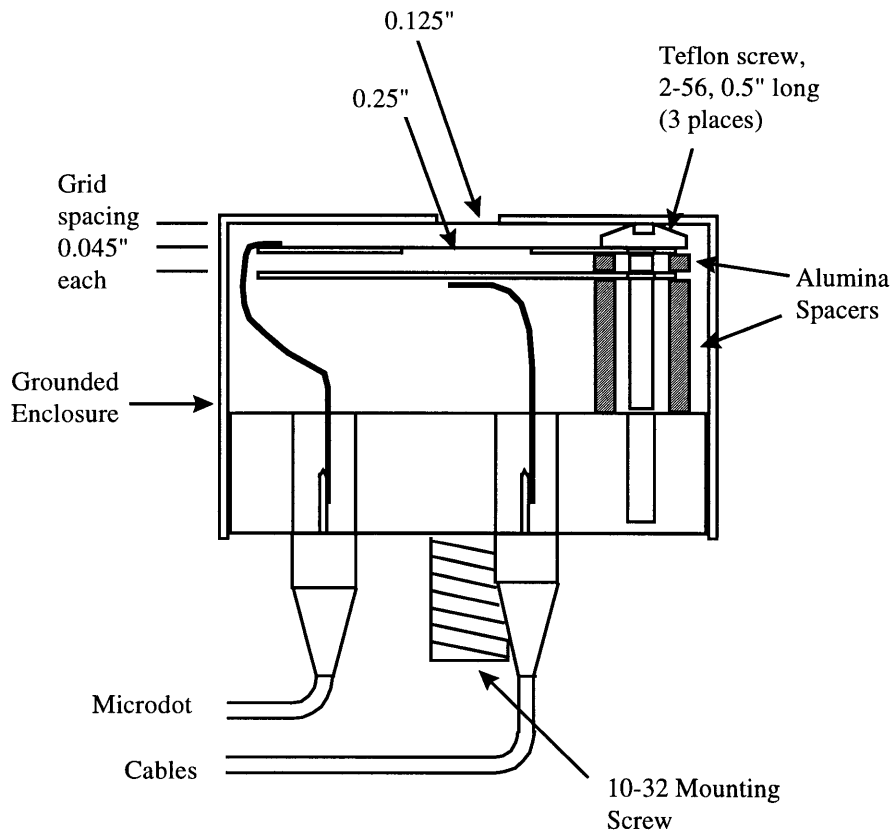


Figure 2.13: Schematic diagram of the gridded ion energy analyzer. The analyzer consists of a stainless steel can with a 0.125" orifice at the center of the front plate, one stainless steel disk with an orifice at the center (repeller), a stainless steel disk (collector), and a 0.2" thick stainless steel plate with two built-in microdot connectors and one mounting screw. The two orifices were covered with stainless meshes, alumina spacers were used to separate the stainless disks and the can, and Teflon screws were used to assemble the analyzer in place.

A stainless steel can with a 0.125” orifice at the center of the front plate is used as a ground shield. A stainless steel disk with a 0.25” orifice at the center is used as electron repeller, and a stainless steel disk as ion collector. A 0.2” thick stainless steel plate with two built-in microdot connectors and one mounting screw serves as the enclosure of the analyzer and provides electrical connections to the analyzer. The two orifices were covered with stainless meshes (0.003” holes, 0.002” thick, #228 Buckbee-Mears), alumina spacers were used to separate the stainless disks and the can, and Teflon screws were used to assemble the analyzer in place. It is worth noting that the inter-grid spacing was chosen to be on the order of 0.045”, which is smaller than the mean free path of the ions, to avoid the broadening of the IEDF due to collisions and minimize the effect of space charge corruption.

Ions enter the grounded orifice and stainless-steel grid that was used to minimize charging of insulating surfaces in the ion beam path. The electron repeller disk covered with fine stainless steel mesh was electrically connected to the a power supply and was biased to -100 eV to repel electrons as well as return secondary electrons created at the collector. The collector disk is electrically connected to a computer controlled power supply through a floating picoammeter (Keithley 485) and is biased positively to obtain proper IEDFs. As the biasing voltage increases, only ions with sufficient energy to overcome the potential hill will impinge upon the collector. Therefore, the collected current is the integral of the distribution function for the ions,  $I(V_c) = \int_0^{eV_c} f(E)dE$ .

Therefore, the ion energy distribution function is proportional to the derivative of the I-V curve measured from the ion energy analyzer  $f(E) = \frac{1}{\int_0^\infty f(E)dE} \cdot \frac{dI}{dV_c}$ .

Schematic of the data acquisition system is shown in Figure 2.14. An operational amplifier (PA08, Apex) is utilized to amplify a signal from a D/A board (Lab PC+, National Instrument). The floating picoammeter is used as a transimpedance amplifier and the measured current was sent through a isolated amplifier (AS-289J, Analog

Device) before being digitized by the A/D board. Lab CVI software was used for data recording and analysis.

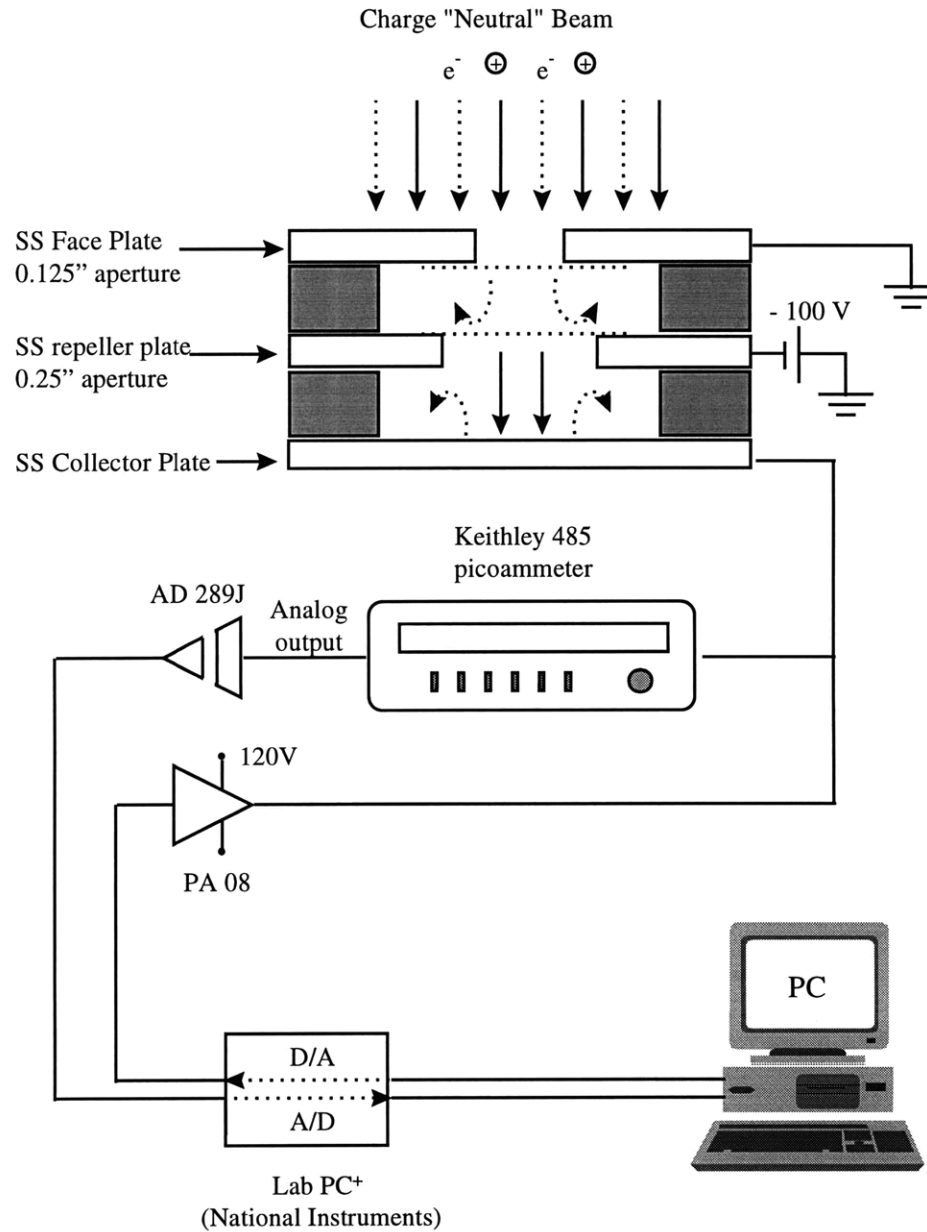


Figure 2.14: Schematic diagram of the data acquisition system. A operational amplifier is utilized to amplify a signal from a D/A and A/D board. The floating picoammeter is used as a transimpedance amplifier and the measured current was sent through a isolated amplifier before being digitized by the A/D board.

A typical current vs. voltage measurement and its ion energy distribution function are shown in Figure 2.9. The ion current measured is on the order of microamps, and can be characterized by  $j = \frac{I}{\pi r^2 t^n}$ , where  $I$  is the collected ion current,  $r$  is the radius of the orifice,  $t$  is the transmission of the mesh, and  $n$  is the number of the mesh. The result resolution is on the order of  $\pm 1\text{eV}$ , and the ion energy distribution is sharp and free of noise.

### ***2.5.3 Neutral flux probe***

The neutral flux probe consists of a pitot tube and a differential capacitance manometer that measures the pressure difference between the neutral flux impinging upon the probe surface and the background pressure in the chamber. The tube consists of a 1.125" long, 0.5" in diameter cap with a 1/16" orifice on the front plate, pressed fit over a 12" long, 1/4" flexible, stainless steel tube (#321-4-X-6, Cambridge Valve and Fittings). The tube is welded to the center of a 1-1/3" conflat rotatable flange on the vacuum side, with a male VCR fitting welded on the air side, as shown in Appendix A. Beam pressure was acquired manually from a digital panel display. A detailed description and working theory can be found elsewhere [Gray, 1993].

### ***2.5.4 X-ray photoelectron spectroscopy (XPS)***

A surface analysis chamber is available for XPS analysis of the sample surface after etching in the 3-beam chamber. A schematic diagram of the analytical chamber in the second setup is shown in Figure 2.15. It illustrates the setup of the X-ray gun, electron energy analyzer, and the sample rotation mechanism which facilitates the angular-resolved XPS (AR-XPS) analysis. A non-monochromatic X-ray source (1254 eV Mg  $K\alpha$ ) and a VG 100AX electron energy analyzer were used to measure the photoelectrons emitted from the sample surface. The pass energy was typically set at 50 eV; however, 20 eV was used when better resolution (1.2 eV FWHM) is required.

The angle between the X-ray gun and the electron energy analyzer is fixed at  $\sim 67^\circ$ , while the angle between the sample and the analyzer can be adjusted by tilting the sample around its supporting arm. The take-off angle is defined as the angle between the electron analyzer and the sample surface, and the maximum and minimum take-off angle in this system is  $85^\circ$  and  $30^\circ$ , respectively. Since the escape depth of photoelectrons is constant, the effective sampling depth,  $z$ , is a function of the take-off angle; i.e.  $z = \lambda \cdot \sin\theta$ . If we assume the average attenuation length is  $25 \text{ \AA}$ , the effective sampling depth is then 11, 19, and  $22 \text{ \AA}$  at  $35^\circ$ ,  $60^\circ$ , and  $85^\circ$  take-off angles. In other words, the electron energy analyzer probes deeper into the surface as the take-off angle increases and the sensitivity of surface species is enhanced relative to the bulk materials as the take-off angle decreases.

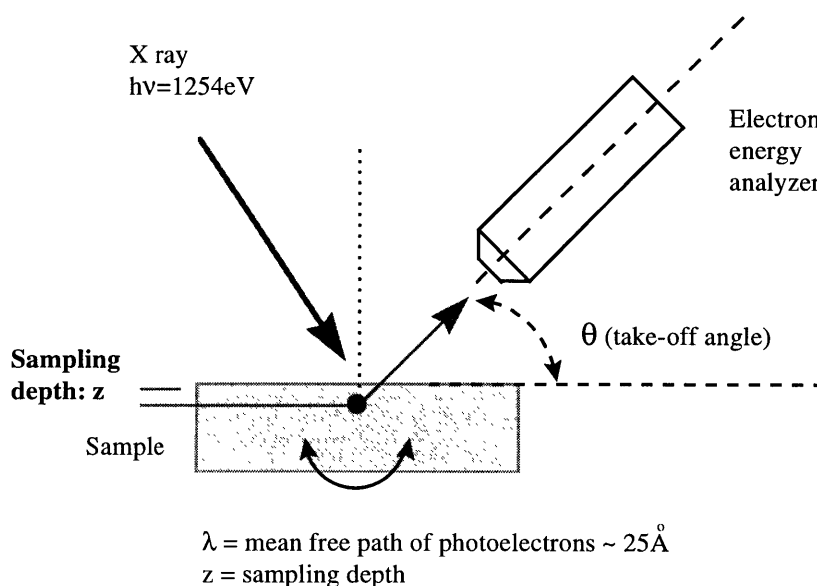


Figure 2.15: Schematic diagram of the setup of the XPS system. An non-monochromatic X-ray source and a VG 100AX electron energy analyzer were used to measure the photoelectrons emitted from the sample surface. The angle between the X-ray gun and the electron energy analyzer is fixed at  $\sim 67^\circ$ , while the take-off angle, angle between the sample and the analyzer, can be adjusted by rotating the sample around its supporting arm. The sensitivity of surface species is enhanced relative to the bulk materials as the take-off angle decreases.

### 2.5.5 Ellipsometry



A spectroscopic ellipsometry (M44, J. J. Woollam Co., Inc.) was utilized to measure the oxide thickness before and after the etching process *in situ*. The film thickness was determined by measuring the light intensity reflected from the sample at 40 discrete wavelengths in less than 1 s covering the spectral range from 400 to 800 nm. The ellipsometric signals are used to determine the thickness and the refractive index of transparent surface films. The number of wavelengths improves the accuracy of the thickness and refractive index measurements by providing a redundant system of equations that can be averaged to get a final result. This instrument has the capability to monitor the growth or removal of surface films in real time, and it is presently being used to determine the etching kinetics of silicon oxide in a HF/H<sub>2</sub>O gas mixture.



## Chapter 3

### Argon Ion Enhanced Chlorine Etching of Polysilicon

In this chapter, argon ions, atomic and molecular chlorine are used to characterize the ion-enhanced chlorine plasma etching of polysilicon. The etching yield of polysilicon is characterized as a function of ion energy, neutral-to-ion flux ratio and ion incidence angle. The reactivity of Cl and Cl<sub>2</sub> under argon ion bombardment is determined. Since very little kinetic data are available for low energy ion-enhanced plasma-surface interactions, this work focuses on the low ion energy regime to simulate accurately a high-density plasma process. The combination of inert ions and reactive neutrals allow us to investigate the importance of ion energy and momentum transfer (eliminating the chemical reactivity of the ions) and the subsequent surface chlorination in the presence of reactive neutrals. As a result, the ion-enhanced chlorine etching yield can be characterized by the classic model Gerlach-Meyer [Gerlach-Meyer, 1981] proposed. The overall etching rate is the sum of the physical sputtering rate, thermal (spontaneous) etching rate and ion-enhanced etching rate:  $ER_{total} = ER_o + ER_s + ER_i$ . A simple kinetic model is proposed to incorporate the major etching dependencies. The parameters needed to describe the model are either measured experimentally or determined by fitting the model to the available kinetic data. The physical sputtering (Ar<sup>+</sup>), spontaneous etching (Cl), and ion-enhanced etching (Ar<sup>+</sup> and Cl) components are measured separately, and discussed in the following.

#### 3.1 Low Energy Ar<sup>+</sup> Sputtering of Polysilicon

Low ion energy is favored in plasma etching processes due to less substrate damage induced by ion bombardment, and better etching selectivity achieved. Ion bombardment by definition physically sputters the substrate, induces collision cascade in the surface region by energy and momentum transfer, and ejects particles into the gas

phase. The measured physical sputtering yield of polysilicon by  $\text{Ar}^+$  is shown in Figure 3.1. The reported sputtering yield of polysilicon by  $\text{Ar}^+$  with energies higher than 100 eV are shown for comparison in Figure 3.1 [Tachi, 1986] [Steinbruchel, 1989] [Balooch, 1996]. The etching yield measurements reported at higher ion bombardment energies showed good agreement in trend with our experimental results.

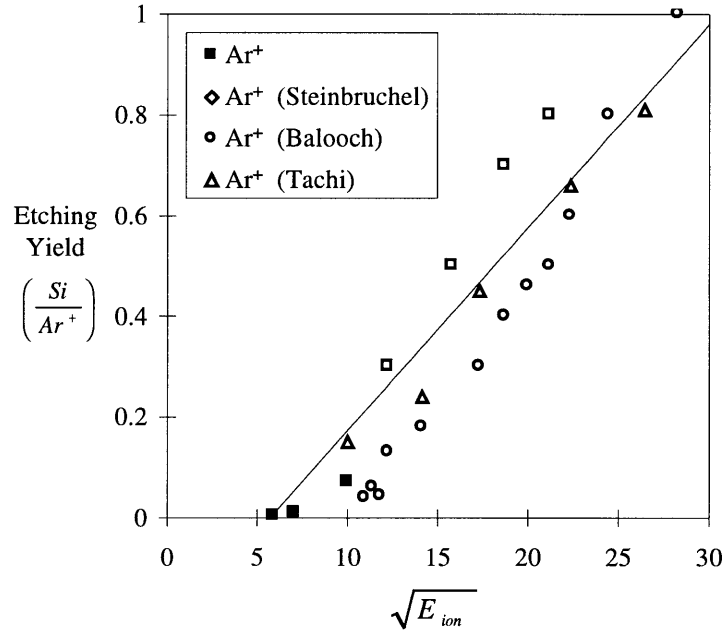


Figure 3.1: Physical sputtering yield of polysilicon by  $\text{Ar}^+$ . Sputtering yield reported by other researchers at higher  $\text{Ar}^+$  ion energy is shown for comparison. The line of a slope of 0.04 shown here is a least square fit to both our, Tachi's, and Steinbruchel's experimental data. The sputtering yield scales with the square root of ion energy; the extrapolated threshold energy is approximately 35 eV.

The characterization of the physical sputtering yield at the low energy regime was attempted by employing the collision cascade model first proposed by Sigmund [Sigmund, 1969] to characterize the sputtering yield of amorphous and polycrystalline targets. The sputtering yield can be approximated by assuming that ions slow down randomly in an infinite medium, considering elastic scattering (nuclear stopping), inelastic scattering (electron scattering), and surface binding energy. A schematic diagram of a collision cascade is shown in Figure 3.2.

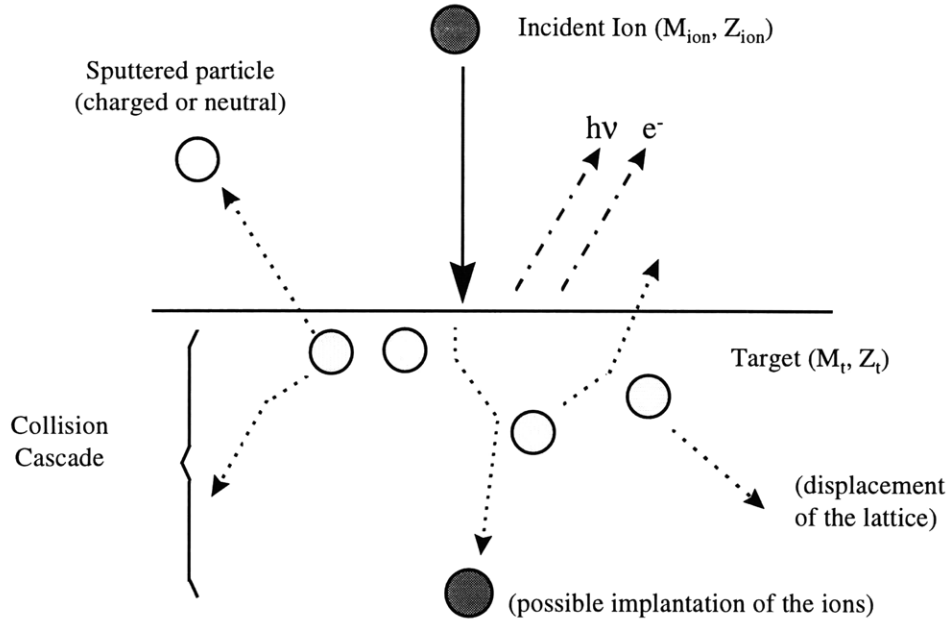


Figure 3.2: Schematic diagram of a collision cascade in the near surface region. The incident ion undergoes elastic (nuclear stopping) or inelastic (electronic stopping) collisions until it loses its energy and rests. Target atoms can be rejected and/or disordered as a result of the induced collision cascade. Photon or electron can also be emitted as a consequence of the collision cascade.

In the low ion energy regime ( $< 1$  kV), the binary particle interactions can be characterized by a Born-Mayer-type cross section, and the sputtering yield is linear to the square root of ion incident energy and can be described as following [Zalm, 1983]:

$$Y(E_{ion}) = C_{it} \cdot S_n \left( \frac{E_{ion}}{E_{it}} \right) \quad (3.1)$$

$C_{it}$  and  $E_{it}$  are constants dependent on the particular ion – target combination ( $Z_i$  and  $Z_t$  are atomic numbers, and  $M_i$  and  $M_t$  are masses of the ion and target atoms, respectively), and  $S_n \left( \frac{E_{ion}}{E_{it}} \right)$  represents the nuclear stopping power. However, this model overestimates the etching yield by at least a factor of 5 at energies lower than 75 eV, where the ion incident energy is on the same order of magnitude of the surface binding energy. Therefore, the threshold energy has to be taken into account to properly model the sputtering yield at low ion energies.

The universal energy dependence of ion bombardment induced etching processes proposed by Steinbrüchel [Steinbrüchel, 1989] is therefore used to model the experimental measurements. An empirical form was proposed by Steinbrüchel as following:

$$Y(E_{ion}) = C_{it} \cdot S_n \left( \frac{E_{ion}}{E_{it}} \right) \cdot f \left( \frac{E_{th}}{E_{ion}} \right) \quad (3.2)$$

where the modified nuclear stopping function was proposed by Wilson [Wilson, 1977] and  $f(E_{th}/E_{ion})$  was a functions proposed by Matsunami [Matsunami, 1980], and the etching yield can be expressed as:

$$S_n \left( \frac{E_{ion}}{E_{it}} \right) \propto E_{ion}^{1/2}, \text{ and } f \left( \frac{E_{ion}}{E_{it}} \right) = 1 - \left( \frac{E_{th}}{E_{ion}} \right)^{1/2} \quad (3.3)$$

$$Y(E_{ion}) = A \cdot (E_{ion}^{1/2} - E_{th}^{1/2}) \quad (3.4)$$

where  $E_{th}$  is the threshold energy and  $A$  is a constant depending on the particular ion-target combination. Good agreement is observed by employing this universal energy dependence of ion bombardment induced etching processes to both our, Tachi's and Steinbrüchel's data sets, as shown in Figure 3.1. The parameter values reported by Steinbrüchel for  $Ar^+$  and Si combination are shown for comparison in Table 3.1:

Table 3.1: The parameters describing the universal energy dependence

$A(\sqrt{eV})^{-1}$	$E_{th}$ (eV)	Reference
0.04	35	Chang
0.04	27	Harper [Harper, 1981]
0.04	31	Tachi [Tachi, 1986]
0.03	64	Oostra [Oostra, 1988]

The extrapolated threshold energy from this work is approximately 35V, which is higher than the 20 eV threshold energy reported for physical sputtering silicon with  $Ar^+$  by Gray [Gray, 1993]. However, it agrees reasonably well with other researcher's work listed in Table 3.1.

### 3.2 Spontaneous Etching of Polysilicon by Cl and Cl<sub>2</sub>

Spontaneous etching is a process in which neutral species interacts with a solid surface to form volatile products in the absence of energetic radiation (*e.g.*, ion bombardment or UV radiation). Spontaneous etching of undoped polysilicon at room temperature with chlorine atoms is not measurable by laser interferometry and thus negligible. An Arrhenius form is used to describe the thermal etching rate of silicon:

$$ER_s = k_o e^{\left(\frac{-E_a}{kT}\right)} Q_{Cl} \quad (3.5)$$

where  $Q_{Cl}$  is the atomic chlorine flux,  $T$  is the substrate temperature,  $k_o$  is the preexponential factor and  $E_a$  is the activation energy. We can normalize equation (3.5) by ion flux to show the etching yield as a function of neutral-to-ion flux ratio:

$$Y_s = k_o e^{\left(\frac{-E_a}{kT}\right)} R \quad (3.6)$$

where  $Y_s$  represents the spontaneous etching yield of polysilicon and  $R$  is the neutral-to-ion flux ratio. The preexponential factors and activation energies for both Cl and F atoms etching of silicon are shown in Table 3.2 for comparison. The substrates for both cases are undoped.

Table 3.2: Arrhenius rate parameters for Cl and F atoms etching of silicon.

Neutral	Substrate	Reference	Q {#/cm <sup>2</sup> /s}	k <sub>o</sub> {Åcm <sup>2</sup> s/#min}	E <sub>a</sub> {eV}
Cl	Poly-Si	Walker	6×10 <sup>19</sup>	2.57×10 <sup>-14</sup>	0.29
F	Si<100>	Flamm	2.3×10 <sup>19</sup> -1.1×10 <sup>22</sup>	3.59×10 <sup>-15</sup>	0.108

The activation energy of atomic chlorine etching polysilicon is approximately three times larger than that of atomic fluorine. Therefore, the etching yield by atomic chlorine is two orders of magnitude lower than that of atomic fluorine even with a larger preexponential factor. This is consistent with the high energy barriers for penetration of chlorine (13 eV) into the silicon backbones than that of fluorine (1 eV), as reported by Seel et. al. [Seel, 1983]. Equation (3.6) predicts an etching yield of 0.006 at a flux ratio of 1000 which is 2-3 orders of magnitude less than the overall ion-enhanced etching yield and thus can be ignored.

It is worth noting here that the doping level of the silicon substrate can greatly change the spontaneous etching rate of polysilicon by Cl atoms. Atomic chlorine does not appreciably etch p-type and undoped polysilicon at room temperature, however, it etches n<sup>+</sup>-type polysilicon spontaneously with one to two order magnitude increase in etching rate. Ogryzlo et. al. [Ogryzlo, 1990] termed this effect “field enhanced etching”, in that the large electron density in the valence band causes the Fermi level to bend upwards [Winters, 1987]. This band bending facilitates “charge transfer” from silicon lattice to the electronegative chemisorbed Cl atoms, make the Si-Cl bonding more ionic, allows for more flexibility in the bonding geometry, and creates more chemisorption sites. The incorporation of chlorine atoms is thus enhanced, as well as the etching rate. Houle [Houle, 1981] also contributed her observation of visible laser enhanced spontaneous etching of silicon to the band bending in the silicon substrate.

Thermal etching of undoped polysilicon at room temperature with molecular chlorine was not measurable, and therefore is ignored. This is expected because the sticking and reaction probability of molecular chlorine is much smaller than that of atomic chlorine. The recombination of atomic chlorine to form molecular chlorine on silicon surfaces is not measured in this study. Kota et al. [Kota, 1997] has measured the recombination probability of atomic chlorine on polysilicon surface to be 20%. The recombination probability is measured on a chlorine-saturated silicon surface where no ion bombardment occurs.

Thermal beam etching has been investigated by many researchers recently as a mean to replace ion-enhanced plasma etching processes due to less substrate damage incurred during thermal etching processes. As the gate oxide thickness of a MOS device shrinks to less than 20 Å thick, substrate damage induced by energetic ion bombardment can be problematic. However, in order for the thermal beam processing to be viable, elevated energy (1-10 eV) is required to sufficiently break the Si-Si bonds, enhance the formation of volatile products, remove the substrate materials in a defined, selective manner, and maintain a reasonable high etching rate. A pulsed beam of hyperthermal fluorine atoms (4.8eV) [Giapis, 1995] and a translationally excited chlorine beam (1eV)



[Teraoka, 1996] have been demonstrated to etch silicon more anisotropically. However, certain degree of undercutting due to the isotropic nature of the neutral species remained severe and needed to be overcome.

### 3.3 Ar<sup>+</sup> Ion Enhanced Etching of Polysilicon with Chlorine

The synergistic effect of Ar<sup>+</sup> and atomic and/or molecular chlorine in etching polysilicon is studied at 40°C. The etching yield is found to be independent of the individual beam flux as shown in Figure 3.3, but a strong function of the atom to ion flux ratio. There is no significant changes in etching yield over an order of magnitude change of ion flux (100 eV Ar<sup>+</sup>) at a constant Cl/Ar<sup>+</sup> ratio, suggesting that flux ratio is an appropriate dimensionless group for scaling. It is worth noting that ion-induced lattice damage is considered not important in accelerating the etching reactions because enhanced etching rate was not observed when the surface is either previously bombarded with Ar<sup>+</sup> and then exposed to Cl, or pre-saturated with Cl and then subject to Ar<sup>+</sup> ion bombardment.

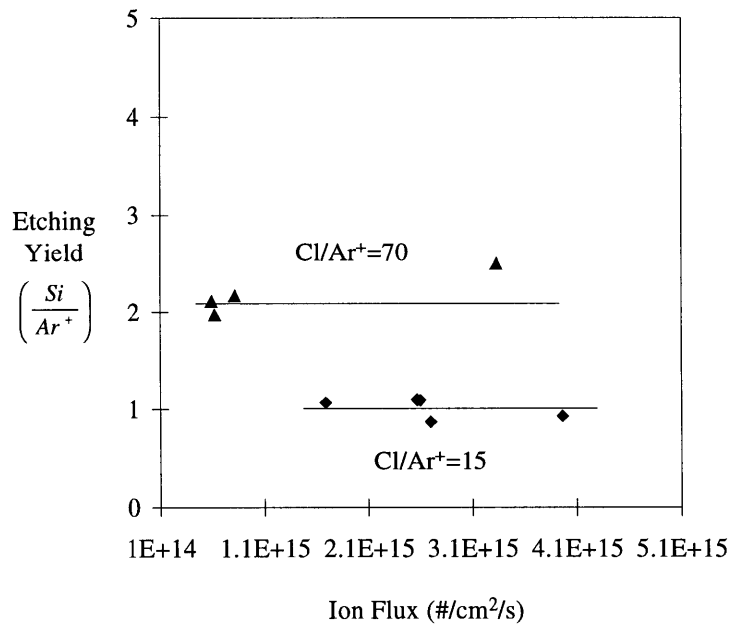


Figure 3.3: The neutral to ion flux ratio is a proper scaling factor for ion-enhanced etching of polysilicon as the etching yield remained invariant over an order of magnitude change in ion flux.

The etching yield of polysilicon versus chlorine atom to argon ion flux ratio at three ion energy levels is shown in Figure 3.4. The etching yield increases significantly with increasing flux ratio at low flux ratios, indicating the etching reaction is limited by the availability of atomic chlorine on the etching surface. At higher flux ratios where the surface is highly chlorinated, the etching yield increases moderately with increasing flux ratio as the etching reaction is ion flux limited.

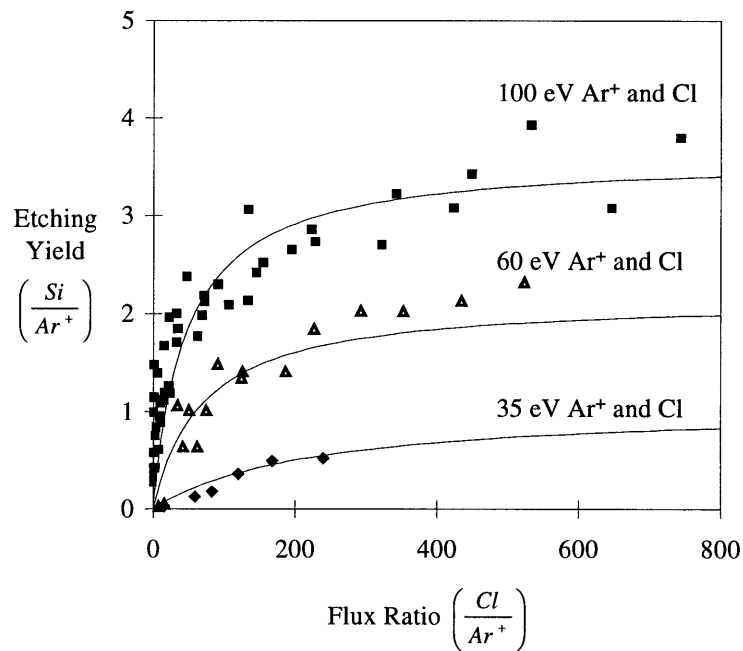


Figure 3.4: Ion enhanced etching of polysilicon by Cl atom and  $Ar^+$  ion. An initial sharp rise in the etching yield is observed at low flux ratios where reaction is limited by the availability of reactive neutrals. The etching yield then gradually saturates, as the reaction becomes ion-flux limited at higher flux ratios. The etching yield is a function of the square root of ion energy. Lines shown here are fits from the surface kinetic model detailed in section 3.6.

This can also be explained by the reduced sticking probability of Cl on a highly chlorinated surface, as suggested by Szabo et. al. [Szabo, 1994] and Coburn [Coburn, 1994]. As Winters et. al. [Winters, 1992] pointed out, the reaction probability of Cl decreases at high chlorine fluences due to the formation of a highly chlorinated layer and the reduced field-assisted motion through the chlorinated layer. Gray [Gray, 1993] has shown that the transition between the neutral-flux-limited and ion-flux-limited regimes in fluorine etching of silicon is a strong function of ion energy as higher energy ions

promote the surface reaction more efficiently. The spacing between these three energy dependent yield curves indicates the etching yield is linearly proportional to  $(\sqrt{E_{ion}} - \sqrt{E_{th}})$ . Again, this is consistent with the universal linear energy dependence observed in ion-induced etching systems. The lines are fits from a kinetic model that will be detailed in section 3.6.

The enhancement of silicon etching yield under simultaneous  $Ar^+$  and Cl exposure is due to the formation of Si-Cl bonds which in turn form the volatile etching products. Formation of Si-Cl is thermodynamically favored since its bond strength is stronger than Si-Si bonds.

The difference between atomic and molecular chlorine in etching polysilicon is shown in Figure 3.5 at an ion energy of 100 eV.

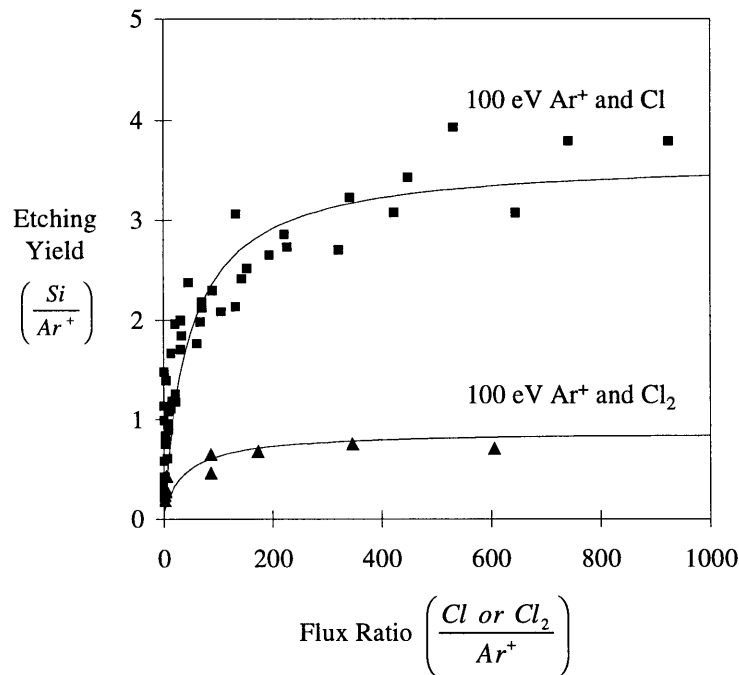


Figure 3.5: Ion enhanced etching of polysilicon by Cl and Cl<sub>2</sub> beams with 100 eV Ar<sup>+</sup>. The etching yields are similar at low flux ratios where high ion flux facilitates the dissociatively adsorption mechanism of Cl<sub>2</sub> on the silicon surface. The adsorption of Cl<sub>2</sub> on the silicon surface is limited at the low ion flux regime (high flux ratios) where the silicon surface is highly chlorinated and distinct difference in etching yield between Cl

and  $\text{Cl}_2$  is observed. Lines shown here are fits from the surface kinetic model detailed in section 3.6.

At very low flux ratios, the Ar ion-enhanced etching yield of polysilicon with Cl or  $\text{Cl}_2$  is similar. However, approximately four times difference in etching yield is observed at higher flux ratios. A factor of 5-10 difference in the etch rate with Cl and  $\text{Cl}_2$  in the temperature range 200-800 K is observed by Szabo [Szabo, 1994]. They observed higher etch rate with atomic chlorine than with molecular chlorine when the etching rate is reaction limited. The sticking coefficient of  $\text{Cl}_2$  is similar to that of Cl for at low neutral-to-ion flux ratios where the surface chlorine coverage is low and the ion bombardment produces more reactive surface silicon sites. At higher flux ratios at which most of the high density plasmas are operated, however, the etching yield of polysilicon by  $\text{Cl-Ar}^+$  is one order of magnitude higher than that by  $\text{Cl}_2\text{-Ar}^+$  because the dissociative adsorption of  $\text{Cl}_2$  is limited on a highly chlorinated surface. This indicates that Cl dominates the etching process over its parent gas chemistry ( $\text{Cl}_2$ ) at high chlorine coverages, which are encountered in most of the plasma etching processes.

Coburn [Coburn, 1994] studied the effect of flux ratios on ion-assisted etching of Si with  $\text{Cl}_2$  with 1 keV  $\text{Ar}^+$  ions for a wide range of neutral-to-ion flux ratios, i.e. up to 10,000. The etching yield increased as the flux ratio increased and the reaction probability was determined as a function of the neutral-to-ion flux ratio by using the reflected chlorine signal and combining the etching yield with the measurement of etching products. The reaction probability dropped from near unity at flux ratio of one to approximately 0.01 at flux ratio of 1,000, as the surface is chlorinated.

Balooch et. al. [Balooch, 1996] reported the  $\text{Ar}^+$  ion-enhanced etching yield of polysilicon with  $\text{Cl}_2$  as a function of Ar ion energy (40 eV-900 eV). The  $\text{Cl}_2$  flux used in their work was at least a factor of 100 larger than the ion flux at the silicon surface and the  $\text{Cl}_2$  flux was increased until no increase in the etching rate was observed. An etching yield of 0.7 was reported with 100 eV  $\text{Ar}^+$  ions and  $\text{Cl}_2$  at saturation coverages. This agrees well with our flux ratio dependence study with 100 eV  $\text{Ar}^+$  and  $\text{Cl}_2$ : an etching yield of 0.7 is observed at flux ratios above 100, as shown in Figure 3.5.

Shown in Figure 3.6 is the comparison of etching yields of polysilicon measured by  $\text{Ar}^+$  alone, with molecular, and with atomic chlorine. The etching yields shown with atomic and molecular chlorine are taken at high flux ratios ( $\sim 300$ ), where the etching yield is not a strong function of flux ratios. Data reported by several researchers are shown for comparison. Equation (3.4) is used to fit our experimental results and other available data shown in Figure 3.6, and the fitted parameters are shown below. With addition of Cl or  $\text{Cl}_2$ , the slope of the energy dependence lines increases, suggesting that the chlorination of the silicon surface enhances the etching rate, and reduces the threshold energy.

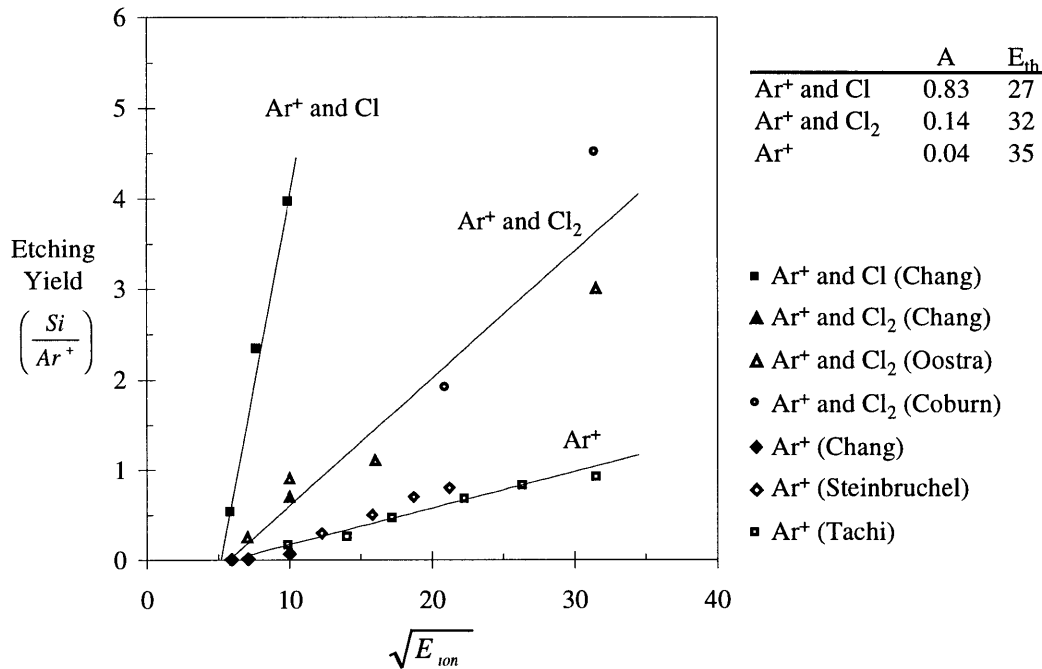


Figure 3.6: Etching yield of polysilicon by  $\text{Ar}^+$  alone, with molecular chlorine, and with atomic chlorine in the low ion energy regime. The increase in slope of the energy dependence lines suggests that the chlorination of the silicon surface enhances the etching rate, and reduces the threshold energy.

### 3.4 Angular Dependence of Polysilicon Etching with $\text{Ar}^+$

The effect of ion incident angle is characterized to reveal the etching of polysilicon on the sidewalls where ion impingement is at grazing angle. Ion incident

angles were changed from normal incidence to 60° off-normal. The etching yields measured at 60° off-normal ion incident angle exhibit a similar dependence on flux ratios, but are reduced by 35% comparing to the etching yield measurement at normal ion incident angle. The reduction in the etching yield remains fairly constant over a wide range of flux ratios, as shown in Figure 3.7.

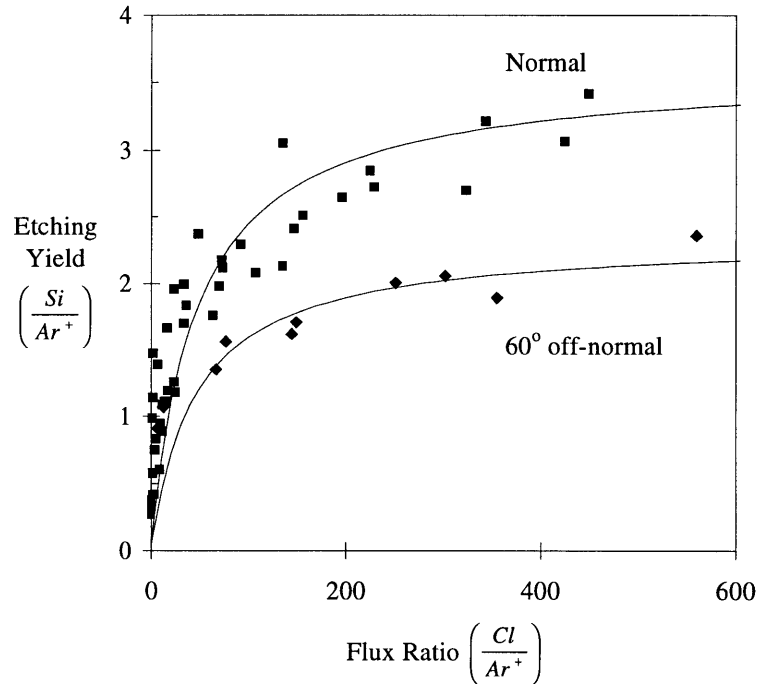


Figure 3.7: Angular dependence of ion enhanced etching of polysilicon with 100 eV  $Ar^+$  and atomic chlorine. Etching yield at normal and 60° off-normal incident angles are shown for comparison. Lines shown here are fits from the surface kinetic model detailed in section 3.6.

The measured etching yields of polysilicon at various ion incident angles at a neutral-to-ion flux ratio of 600 are shown in Figure 3.8. The etching yield showed no significant change as the incidence angle increased from normal to 40° off normal, but decreased by 35% at 60° off-normal angle. The zero etching yield at glancing angle (90° off-normal) is assumed. This result does not agree with the angular dependence for a physical sputtering system for most materials where maximum yields are observed at approximately 50°-60° off-normal ion incident angles due to the most efficient energy deposition to the surface layer at these angles of incidence. However, similar angular

dependence results are observed by Mayer et. al. [Mayer, 1981] for chlorine etching of polysilicon at elevated ion energies (400-1200 eV) and in other reactive ion etching systems [Okano, 1981]. Maximum etching yield is observed at normal ion incident angle and decrease in etching yield starts at 30-40° off-normal angles.

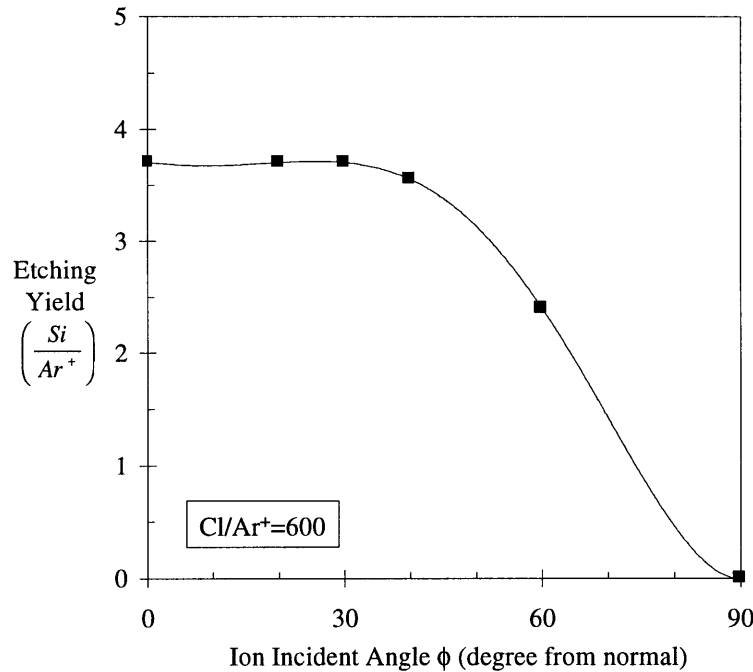


Figure 3.8: Angular dependence of ion enhanced etching of polysilicon with 100 eV  $Ar^+$  and Cl at flux ratio of 600. The zero etching yield at glancing angle ( $90^\circ$  off-normal) was assumed. Maximum etching yield is observed at normal incident angle and the line represents a polynomial fit to the experimental data.

A possible reaction mechanism attributing to the observed angular dependence is that reactive atoms are implanted into the substrate more readily with normally incident ions. The normally incident ions consequently create mixing of the absorbed surface atoms into the lattice whereby enhancing the etching yield. Therefore, the chemical reactivity of chlorine atoms, together with the ion-induced chlorination, may compensate for the less efficient momentum transfer to the surface atoms at near normal incident angles. In addition, the processes leading to the product formation by chemical sputtering are associated with the number of bonds breaking within the surface layers, rather momentum transfer to the surface atoms which is needed for physical sputtering. The number of bonds broken by the ion impingement within the surface layers is not

expected to vary significantly except at large off-normal angles where ion scattering occurs without losing much energy to the surface. It is necessary to incorporate this angular dependence into a profile simulator to properly predict the feature evolution, as ions with certain angular dispersion would strike the sidewall of the feature at high off-normal angles. It would become even more crucial as the feature size decreases and the aspect ratio increases.

Since the percentage of etching yield reduction is approximately the same over a fairly broad range of flux ratios as shown in Figure 3.7, the etching yield at off-normal incident angles is expressed in the following form:

$$Y(\phi) = c(\phi) \cdot Y(\phi = 0^\circ) \quad (3.7)$$

$Y(\phi = 0^\circ)$  is the etching yield measured at normal ion incident angle and  $c(\phi)$  is a constant extracted from a polynomial fit to the experimental data, as indicated by the line in Figure 3.8. This angular dependence of etching yield can be incorporated into a profile simulator to characterize better the etching rate at the sidewall of a feature.

### **3.5 XPS Analysis of Polysilicon Surface after Ar<sup>+</sup> and Cl Bombardment**

A survey spectrum of the photoemission of the polysilicon surface prior to etching is shown in Figure 3.9. A native oxide surface film (silicon dioxide formed due to exposure to air) is present and both carbon and oxygen are detected at significant levels. The silicon emission intensity was attenuated due to the presence of the native oxide film. The removal of the native oxide is performed in the beam system by Ar<sup>+</sup> sputtering or Ar<sup>+</sup> and Cl etching.

A survey spectrum of the photoemission of the polysilicon surface after etching by 100 eV A<sup>+</sup> and Cl is shown in Figure 3.10. The surface is terminated with Cl without any other measurable contamination (C or O). The spectra consist of core-level photoelectron emission peaks of Si(2p), Si(2s), Cl(2p) and Cl(2s) at 99, 150, 198.5, and 269.5 eV respectively.



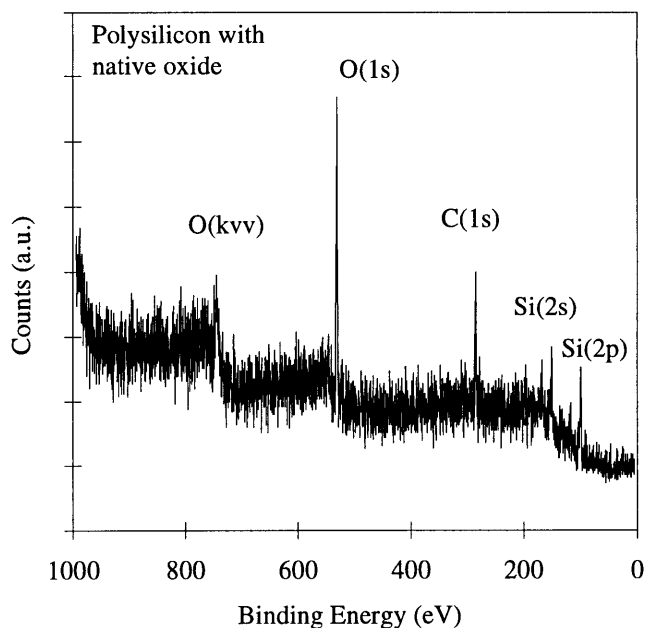


Figure 3.9: A survey spectrum of photoemission of the polysilicon surface before etching. Native oxide and an appreciable amount of carbonaceous contamination are observed. The take-off angle is at  $35^\circ$ .

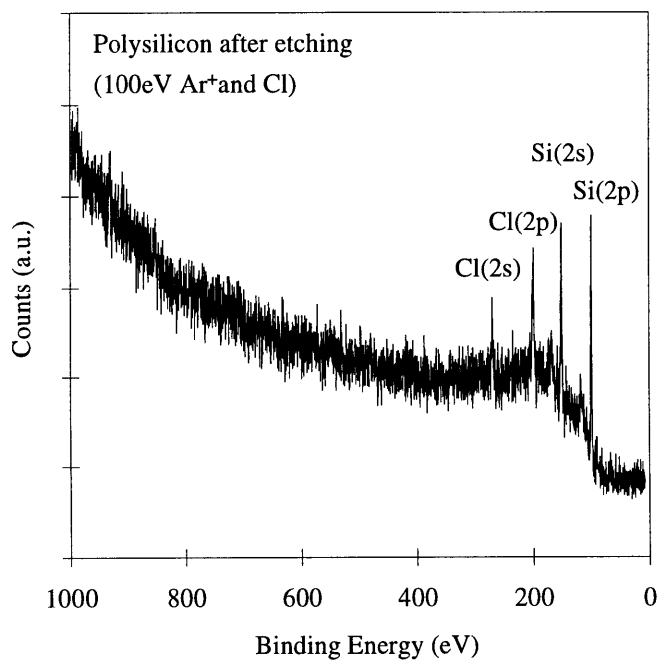


Figure 3.10: A survey spectrum of photoemission of the polysilicon surface after etching by 100 Ar<sup>+</sup> and Cl. The surface is highly terminated with Cl without other measurable surface contamination (C or O). The take-off angle is at  $35^\circ$ .

A typical low resolution spectrum recorded between binding energy 300 and 50 eV illustrates the resonant loss features of both Si(2p) and Si(2s), as indicated by arrows in Figure 3.11. These peaks measured at approximately 17 eV above the core-level Si(2p) and Si(2s) emissions are referred as bulk silicon plasmon loss peaks which is associated with the resonant inelastic scattering of photoelectrons in bulk silicon. Plasmon loss peaks are a series of smaller, broader, and equally spaced peaks with successively decreasing intensity away from the core-level peak. Only the fundamental or “first” plasmon loss peak is observed in Figure 3.11. The surface plasmon loss peak or other plasmon peaks are not resolved here. Plasmon peak can be greatly reduced by surface contamination and have been used for diagnosing surface cleanliness [Briggs, 1983].

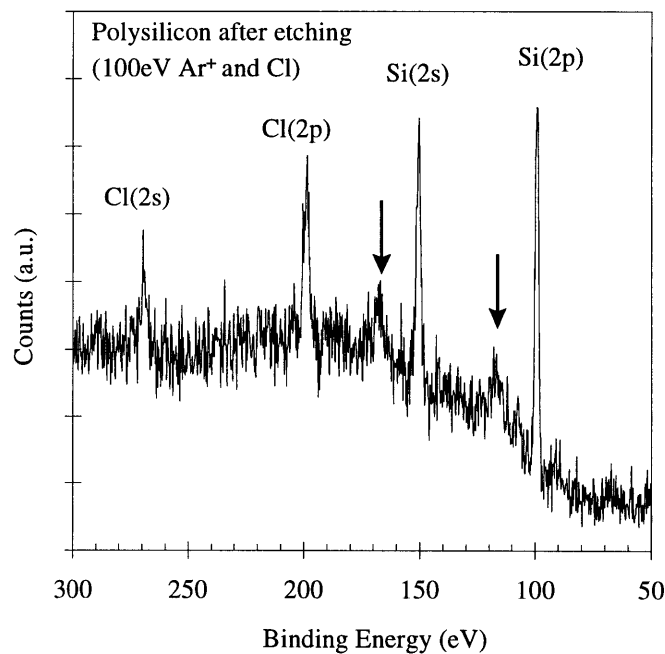


Figure 3.11: Photoemission of silicon and chlorine from a polysilicon surface after etching by 100 Ar<sup>+</sup> and Cl. Plasmon loss peaks of Si(2p) and Si(2s) are observed, as indicated by the arrows. The take-off angle is at 35°.

A higher resolution of silicon and chlorine photoemission spectra taken after etching at 35° and 85° take-off angles are shown in Figure 3.12. The Cl(2p) photoemission line at 198.5 eV is attributed to Cl-Si, and its spin-orbit split is resolved

with a spin-orbit split constant of 1.6 eV [Bello, 1994]. The relative chlorine to silicon signal was determined by the following equation:

$$C_i = \frac{n_i}{\sum_i n_i} = \frac{I_i / s_i}{\sum_i (I_i / s_i)} \quad (3.8)$$

The integrated intensity of the Cl(2p) and Si(2p) peaks are normalized with their atomic sensitivity factors,  $S_{Cl(2p)}=0.48$ ,  $S_{Si(2p)}=0.17$ , respectively. The relative chlorine intensity is therefore 0.2 and 0.13, at take-off angles of 35° and 85° respectively. The relative intensity of chlorine decreases with increasing take-off angle, suggesting that the chlorination layer is comparable to the mean free path of the photoelectron and is confined on the top surface layers. The bulk plasmon loss peak of Si(2p) is better resolved here, as indicated by the arrows. A few smaller peaks observed between Si(2p) and Si(2s) are believed to be surface plasmon loss peak, successive bulk plasmons and coupling between surface and bulk plasmons.

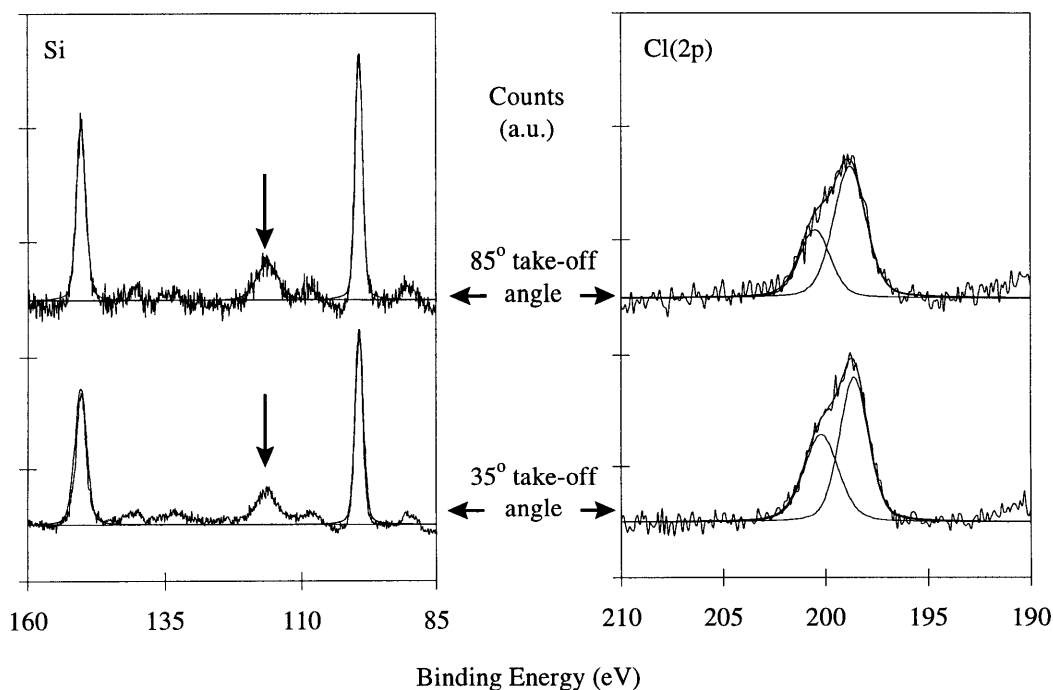


Figure 3.12: Photoemission spectra of silicon and chlorine from a polysilicon surface after etching by 100 Ar<sup>+</sup> and Cl, at two take-off angles. Bulk plasmon loss peak of Si(2p) is better resolved, as indicated by the arrows.

### 3.6 Phenomenological Model for Etching of Polysilicon with Ar<sup>+</sup>

A phenomenological model is constructed to characterize the ion-enhanced etching yield of polysilicon as a function of Ar<sup>+</sup> ion energy, ion flux, neutral/ion flux ratio, and angle of ion impingement. Since many reaction mechanisms are convoluted, a simplified model is proposed and presented in Table 3.3.

Physisorption, chemisorption, desorption and ion-induced desorption of chlorine atoms are reduced into an overall adsorption reaction, with an assigned surface chlorination coefficient,  $s$ . The major product is assumed to be SiCl<sub>4</sub> as reported in the literature, as shown in Table 1.1. Rossen [Rossen, 1988] has identified both SiCl<sub>2</sub> and SiCl<sub>4</sub> as the primary etching products, however, she also observed the emission of SiCl<sub>4</sub> is enhanced relative to SiCl<sub>2</sub> as the bombardment energy is reduced. The energy regime in her work is between 125 and 800 eV, higher than 35-100 eV used in this work. Therefore, the emission of unsaturated SiCl<sub>x</sub> is not considered in this model.  $\beta$  is the ion-enhanced etching reaction probability and  $I^+$  is the ion flux. Physical sputtering yield,  $Y_o$ , is also considered.

Table 3.3: The simplified phenomenological surface kinetics model for Ar<sup>+</sup> ion-enhanced polysilicon etching of polysilicon with Cl.

Simplified kinetics model	Mechanism
$Cl_{(g)} + * \xrightarrow{s, Q_{cl}} Cl_{(s)}$	Overall adsorption
$Si_{(s)} + 4Cl_{(s)} \xrightarrow{\beta, I^+} SiCl_{4(g)} + 4*$	Ion-enhanced etching
$Si_{(s)} \xrightarrow{Y_o, I^+} Si_{(g)}$	Physical sputtering

The etching yield is then derived from equation:  $Y_{total} = Y_o + Y_s + Y_i$ , where  $Y_o$ ,  $Y_s$ , and  $Y_i$  represent the physical sputtering yield, spontaneous etching yield and ion-enhanced etching yield, respectively.  $Y_s$  is ignored as discussed previously, and  $c(\phi)$ , the constant extracted from the angular dependence study, is incorporated into the kinetic model as a multiplier; therefore:

$$\begin{aligned}
Y &\approx c(\phi) \cdot (Y_o + Y_i) \\
&= c(\phi) \cdot [Y_o \cdot (1 - \theta) + \beta \cdot \theta]
\end{aligned}
\tag{3.9}$$

where  $\theta$  represents the extent of surface chlorination which can be expressed by the following form by performing a site balance:

$$\theta = \frac{s \cdot R}{s \cdot R + 4 \cdot \beta}
\tag{3.10}$$

Substituting  $\theta$  in equation (3.9) and rearranging the equation yields the following equations:

$$Y_{total} = c(\phi) \cdot \left[ Y_o + (\beta - Y_o) \frac{s \cdot R}{s \cdot R + 4 \cdot \beta} \right]
\tag{3.11}$$

$$\frac{1}{Y} \equiv \frac{1}{Y_{total} - c(\phi) \cdot Y_o} = \frac{1}{c(\phi)} \left[ \frac{1}{\beta - Y_o} + \frac{4 \cdot \beta}{s \cdot (\beta - Y_o)} \cdot \frac{1}{R} \right]
\tag{3.12}$$

$\beta$  and  $s$  can be derived respectively from the intercept and slope of a linear regression of  $\frac{1}{Y}$  versus  $\frac{1}{R}$ . The physical sputtering yield in this model is inversely proportional to the extent of surface chlorination. Winters et. al. [Winters, 1992] pointed out that physical sputtering rate always drops in the presence of a chemically active gas, and Barone et. al. [Barone, 1995] validated this point with their molecular dynamic simulation results. The available etching yield data for  $\text{Cl}_2\text{-Ar}^+$  are also regressed with the same method and all the parameters are summarized in Table 3.4.

Table 3.4: Model parameters for  $\text{Ar}^+$  ion-enhanced etching of polysilicon with  $\text{Cl}$  and  $\text{Cl}_2$ , as a function of ion energy.

	$E_{\text{ion}}$	$Y_o$	$s$	$\beta$
$\text{Ar}^+, \text{Cl}$	35	--	0.02	1.06
	60	0.007	0.12	2.15
	100	0.07	0.30	3.59
$\text{Ar}^+, \text{Cl}_2$	100	0.07	0.07	0.83

Interestingly, both  $\beta$  and  $s$  parameters scale linearly with the square root of ion energy, similar to the energy dependence of physical sputtering yield,  $Y_o$ . Figure 3.13 illustrates the energy dependence of these two parameters. The effective etching yield,  $\beta$ , increases with incident ion energy because the ion enhanced surface kinetics are initiated

by a collision cascade which scales with the ion momentum. The products are emitted after this collision cascade by a number of mechanisms. This ion energy dependence was found to scale linearly with  $(E_{ion}^{1/2} - E_{th}^{1/2})$ , where  $E_{th}$ , the threshold energy, is found to be 16 eV. This value is lower compared to that observed in a physical sputtering system (~20 eV). The reduction in the threshold energy has also been observed for other chemical sputtering system, such as bombardment of silicon with fluorine ion or with  $Ar^+$  in the presence of fluorine atoms. Approximately 4 eV is reported by Gray [Gray, 1993] as the threshold energy for  $Ar^+$  ion-enhanced fluorine etching, due to the formation of a fluorosilyl surface layer. Since reactive ions or inert ions in the presence of reactive neutrals lead to the formation of volatile products, the average surface binding energy is reduced and so is the threshold energy. The fluorine atom reduces the threshold energy more than the chlorine atom due to its higher chemical reactivity and smaller atomic size which allows it to penetrate more effectively into the silicon lattice and induce "mixing" of the silicon surface. The energy barriers for penetration of fluorine and chlorine into the silicon backbones were reported to be 1 eV and 13 eV, respectively [Seel, 1983].

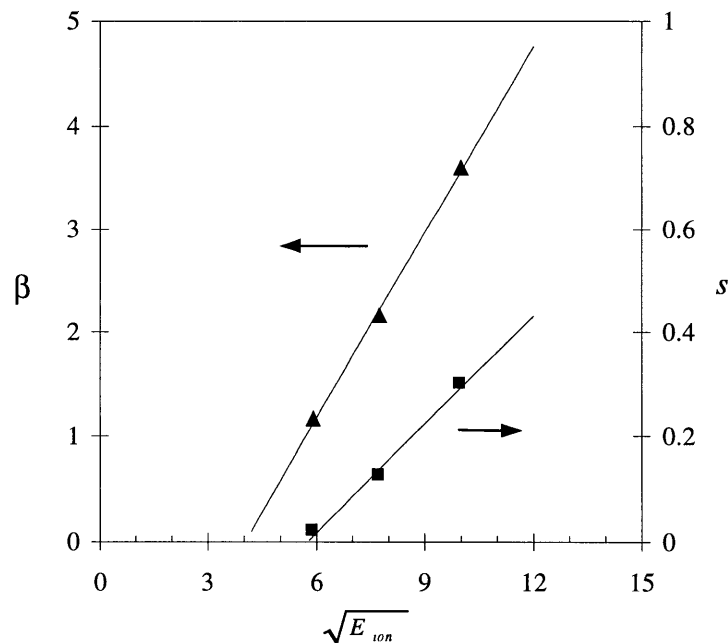


Figure 3.13: Fitted parameters  $\beta$  and  $s$  versus  $E_{ion}^{1/2}$  for  $Ar^+/Cl$  etching of polysilicon. The extrapolated threshold energy is 16 eV, which is lower than that of the physical sputtering of polysilicon with  $Ar^+$ .

The derived surface chlorination coefficient also scales linearly with the square root of ion energy. Since the sticking probability of Cl is near unity on a clean silicon surface and dropped to essentially zero above 1.5 monolayer coverage, it suggests that high energy ions create more dangling bonds or adsorption sites for the subsequent etching reactions.

A graphical illustration of the model is shown in Figure 3.14 where the contributions of physical sputtering, thermal etching and ion-enhanced etching are shown. The model represents the data well, as shown in Figure 3.4, 3.5 and 3.7.

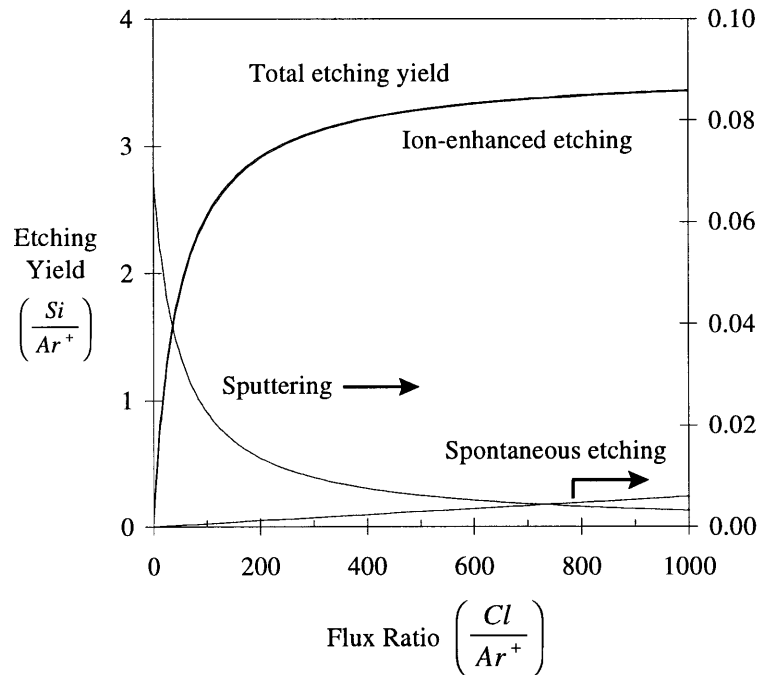


Figure 3.14: Graphical illustration of the ion enhanced etching of polysilicon with Cl and 100 eV  $Ar^+$ . The etching yields for both physical sputtering and thermal etching of polysilicon are shown in the right y-axis.

Equation (3.8) is a complete form of the kinetics model that accounts for the energy, flux and angular dependencies of  $Ar^+$  ion-enhanced etching of polysilicon with chlorine. All three parameters,  $Y_0$ ,  $\beta$ , and  $s$ , of the model scale linearly with the square root of ion energy and can be incorporated readily into a profile simulator to predict

feature evolution in argon ion-enhanced chlorine etching of polysilicon. The predicted feature profile evolution of patterned polysilicon sample etched by  $\text{Ar}^+$  and  $\text{Cl}$ , utilizing this model, is shown in chapter 7.



## Chapter 4

### Argon Ion Enhanced Chlorine Etching of SiO<sub>2</sub> and Photoresist

Argon ions, atomic and molecular chlorine are used in this chapter to characterize the ion-enhanced chlorine plasma etching of silicon dioxide. The etching yield of silicon dioxide is characterized as a function of ion energy, neutral-to-ion flux ratio and ion incidence angle. This work focuses on the determination of chlorine-silicon dioxide interactions in the low ion energy regime, since little was known about the etching mechanism of silicon dioxide in a chlorine plasma. Etching of silicon dioxide is much slower than that of silicon in a chlorine plasma, therefore the concentration of various reactive species within the feature can be significantly changed upon etching through the polysilicon film and exposing the underlying silicon dioxide surface to the plasma. Moreover, the shadowing of electrons to a high aspect ratio feature and positive charging of the silicon dioxide surface can result in an electrical field within the feature and distort the ion trajectory. These deflected ions have been thought to locally etch the polysilicon lines at the polysilicon/oxide interface and result in notch formation. Investigation and/or simulation of the charging effect is beyond the scope of this work, however, stress is found to cause notching formation during the overetching step, as will be detailed later in chapter 6.

The etching of photoresist in a chlorine chemistry is also characterized to complete the database needed to accurately simulate etching of photoresist patterned polysilicon film over a thin oxide film. Photoresist is known to be etched in a chlorine or an oxygen plasma, and the carbonaceous etching product can deposit on the surfaces within the feature, passivate the sidewalls, thereby altering the subsequent etched profiles. Therefore, it is crucial to quantify etching of both silicon dioxide and photoresist to quantitatively simulate the profile evolution during chlorine etching of patterned polysilicon.

## 4.1 Low Energy Ar<sup>+</sup> Sputtering of SiO<sub>2</sub>

Sputtering of SiO<sub>2</sub> utilizing low energy Ar<sup>+</sup> is found to scale linearly with the square root of the ion incident energy, as shown in Figure 4.1. Our experiments focus on the low ion energy regime, and the results agree favorably with other researchers' work [Oostra, 1986] [Harper, 1981] [Jorgenson, 1965].

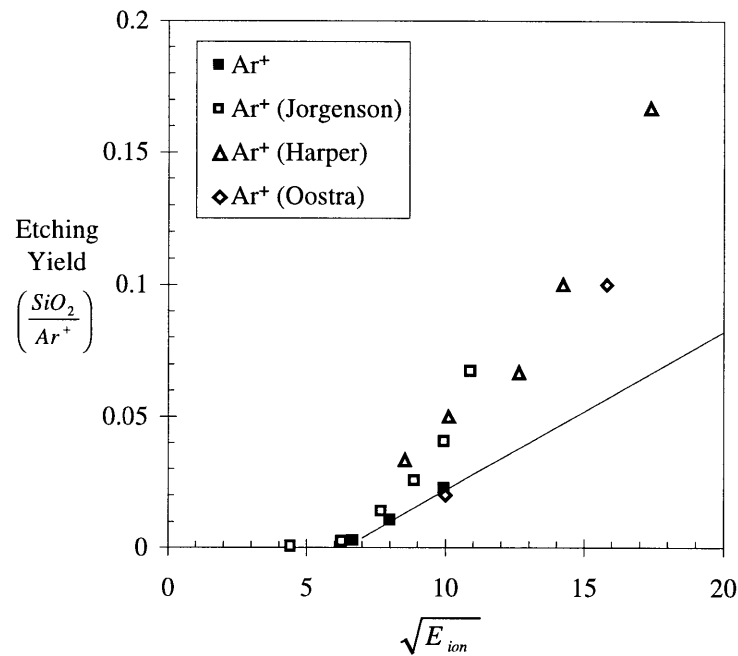


Figure 4.1: Physical sputtering yield of silicon dioxide by Ar<sup>+</sup>. Sputtering yield reported by other researchers at high ion energies is shown for comparison. The sputtering yield scales linearly with the square root of ion energy, and the extrapolated threshold energy is approximately 40 eV.

The universal energy dependence of ion bombardment induced etching processes proposed by Steinbrüchel, is again used to fit our data in Figure 4.1. The extrapolated threshold energy is approximately 40 eV, which is slightly higher than a 35 eV threshold energy reported for etching of silicon dioxide in a CHF<sub>3</sub> plasma [Joubert, 1994]. Thomas III [Thomas III, 1990] reported the threshold energy for sputtering the native oxide to be 72±5 eV. They observed no etching of the native oxide film on silicon in a chlorine plasma with less than 90V dc bias voltage at the powered electrode in an rf diode reactor. The reported threshold energy for oxide etching varies, but the values are always

higher than the threshold energy reported for polysilicon etching. This is a result of Si-O bonds being stronger than Si-Si bonds.

## 4.2 Spontaneous Etching of SiO<sub>2</sub> by Cl and Cl<sub>2</sub>

Neither atomic nor molecular chlorine spontaneously etches silicon dioxide at near room temperature. However, atomic chlorine physisorbed and/or chemisorbed on clean oxide surfaces while molecular chlorine did not. The chlorine photoelectron emission spectra from a clean silicon dioxide surface exposed to either atomic or molecular chlorine clearly show the different reactivity of Cl and Cl<sub>2</sub> on an oxide surface, as depicted in Figure 4.2.

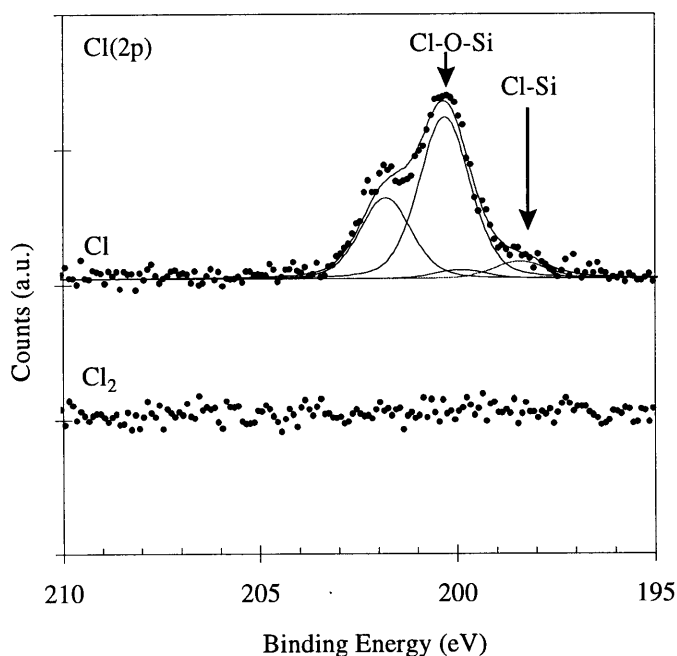


Figure 4.2: Cl(2p) photoelectron emission spectra illustrating the difference between atomic and molecular chlorine adsorption to a clean silicon dioxide surface. Atomic chlorine physisorbed and/or chemisorbed on clean oxide surfaces while molecular chlorine did not.

It is worth noting that in fitting the Cl(2p) spectra shown in Figure 4.2, two chemical components, whose binding energies are at 198.5 and 200.3 eV respectively, are used. The two different binding states are contributed to Cl-Si and Cl-O-Si, respectively.

For each chemical bonding state of chlorine, the spin-orbit split is resolved and a spin-orbit split constant is assigned at 1.6 eV [Bello, 1994]. More discussion and justifications about the peak assignments can be found in the next section.

### 4.3 Ar<sup>+</sup> Ion Enhanced Etching of SiO<sub>2</sub> with Chlorine

The SiO<sub>2</sub> sputtering yield is measured with simultaneous Ar<sup>+</sup> and chlorine exposure as a function of ion energy, shown in Figure 4.3. The etching yields of SiO<sub>2</sub> shown with Cl or Cl<sub>2</sub> are “saturated” etching yields, which remained invariant with increasing chlorine flux. The SiO<sub>2</sub> sputtering yield is hardly affected by the presence of Cl<sub>2</sub>; however, a factor of three to four enhancement is observed with Cl. This is consistent with the distinct chemical reactivity of Cl<sub>2</sub> and Cl on silicon dioxide surface without ion bombardment.

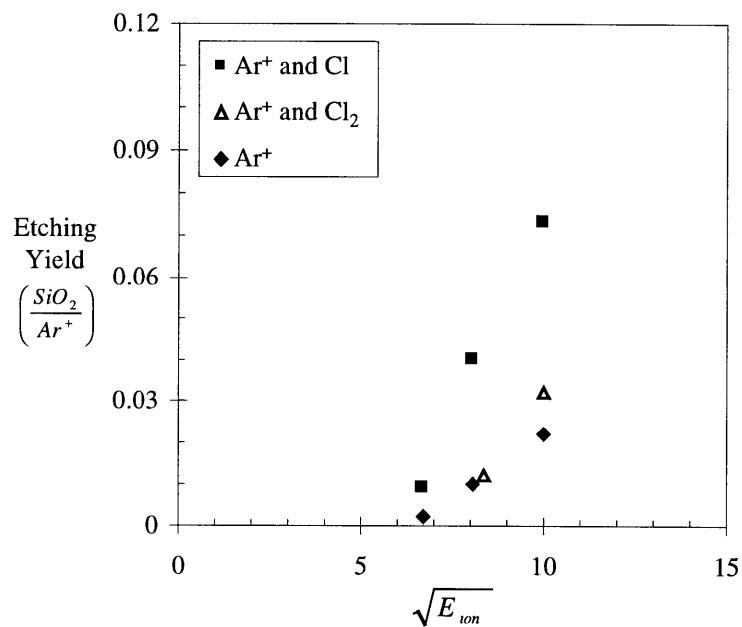
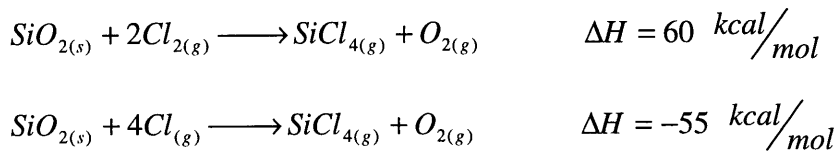


Figure 4.3: Etching yield of silicon dioxide by Ar<sup>+</sup>, Ar<sup>+</sup> and Cl<sub>2</sub>, and Ar<sup>+</sup> and Cl. Cl<sub>2</sub> does not appreciably enhance the etching of silicon dioxide; however, Cl enhanced the etching yield by a factor of three to four.

Though Cl<sub>2</sub> addition did not significantly enhance the etching of silicon dioxide, the sample surface was terminated with Cl after this etching process. This indicates that some molecular chlorine dissociatively physisorbed and/or chemisorbed on the oxide surface upon simultaneous Ar<sup>+</sup> ion bombardment. The lack of chemical enhancement in the etching yield of SiO<sub>2</sub> by Ar<sup>+</sup> and Cl<sub>2</sub> is attributed to the stronger Si-O bonds, and exchanging Si-O bonds with Si-Cl bonds are not thermodynamically favored [Oostra, 1987]. With 3 keV Ar<sup>+</sup> and Cl<sub>2</sub>, Oostra et. al. [Oostra, 1987] measured the sputtered species to be SiCl<sub>x</sub><sup>+</sup> and SiOCl<sub>y</sub><sup>+</sup> (x,y=0-2). They measured the kinetic energy distribution of the sputtered Cl, and concluded some Cl was mixed into the subsurface due to ion bombardment, but the Cl present in the lattice was chemically unbound. However, mixing of chlorine into the silicon dioxide lattice with 100 eV Ar<sup>+</sup> ions is less likely.

If we compare the two very simple reactions below, SiO<sub>2</sub> will react with atomic chlorine to form SiCl<sub>4</sub> as the reaction is exothermal; however, it will not react with molecular chlorine spontaneously. This explains in part the greater reactivity of atomic chlorine on a silicon dioxide surface.



The extrapolated threshold energy measured with Ar<sup>+</sup> and chlorine is approximately 40 eV that is not lower than that measured with Ar<sup>+</sup> alone, indicating that chlorination of the silicon dioxide surface does not substantially lower the surface bonding energy. This threshold energy remains higher than the 16 eV threshold energy measured for sputtering of polysilicon by Ar<sup>+</sup> and Cl. This is consistent with the stronger bonding energy of Si-O than that of Si-Cl, making surface chlorination less likely.

The enhancement in etching yield by Ar<sup>+</sup> and Cl can be better illustrated by presenting the etching yield as a function of atomic chlorine to argon ion flux ratio, as shown in Figure 4.4. The etching yield increases as the flux ratio and energy increases, and a factor of three to four enhancements is observed at flux ratios above 60.

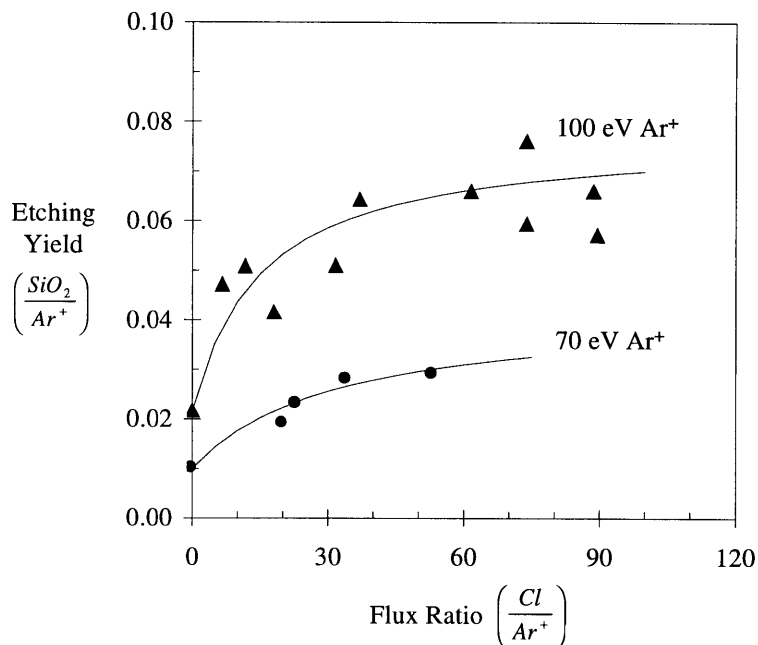


Figure 4.4: Etching yield of silicon dioxide by  $Ar^+$  and Cl as a function of Cl to  $Ar^+$  flux ratio. The etching yield "saturated" at relatively low flux ratios, and a factor of four enhancements was observed at flux ratios above 60. The etching yield increases as the ion energy increases.

The enhancement in etching yield is consistent with the greater reactivity of atomic chlorine to an oxide surface compared to that of molecular chlorine. The etching yield "saturated" at a relatively low flux ratio,  $\sim 30$ , compared to that measured in etching of polysilicon. This suggests that the reactive sites on the oxide surface are less readily available than on a polysilicon surface. The relatively small chemical enhancement factor indicates that the etching of oxide is more "physical" or "ion-driven".

The incorporation of chlorine into the  $SiO_2$  is best illustrated by the Cl(2p) photoemission spectra taken after the etching process, as shown in Figure 4.5. The overall integrated intensity area increases as ion energy increases, indicating more chlorine is incorporated into the silicon dioxide surface. The change in the shape of the spectra indicates that more chlorine bonds to silicon as ion energy increases, as ions sputter silicon and oxygen and allow atomic chlorine bonds to silicon dangling bond created by ion impact. At an ion energy of 45 eV, slightly above the threshold energy, the Cl(2p) photoemission spectrum is similar to that measured after exposing a clean

silicon dioxide surface to Cl without ion bombardment (Figure 4.2). This suggests that chlorine incorporation into the surface is minimal as ion induced lattice mixing is limited. As ion energy increases, ions more effectively sputter silicon and oxygen and facilitate the formation of Si-Cl bonds.

Bello et. al. [Bello, 1994] demonstrated in their work of etching silicon surfaces with low energy  $\text{Cl}^+$  ions that the removal of the surface oxygen depends critically on the ion bombardment energy and physical sputtering is the main oxide removal mechanism. They have shown that chlorine ions initially drove surface oxygen to surface oxide, removed oxide by physical sputtering, and then enhanced silicon etching after oxide removal. Our results also suggest that physical sputtering of silicon and oxygen took place as the major etching mechanism, and the subsequent chlorine reacting with the silicon would lead to the formation of volatile  $\text{SiCl}_x$  and enhance the etching yield.

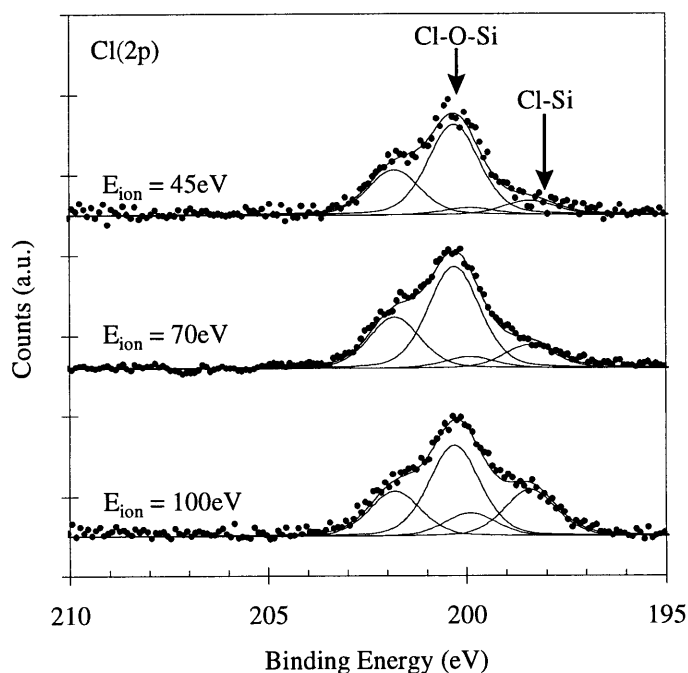


Figure 4.5: Cl(2p) photoelectron emission spectra illustrating the effect of ion energy on etching of silicon dioxide. As the ion energy increases, the amount of chlorine bonded to silicon increases and the etching yield is enhanced.

#### 4.4 Angular Dependence of SiO<sub>2</sub> Etching with Ar<sup>+</sup> and Cl

The etching yield of silicon dioxide by 100 eV Ar<sup>+</sup> and Cl is characterized as a function of flux ratios at normal and 60° off-normal ion incidence angles, as shown in Figure 4.6. The etching yield measured at 60° off-normal ion incident angle is two times of that measured at normal ion incident angle at flux ratios up to 100. The angular dependence of oxide etching is shown as a function of ion incidence angle (at a flux ratio of 90) in Figure 4.7. The maximum etching yield is observed at 60° off-normal ion incident angle, where the momentum transfer to the silicon dioxide surface is the most sufficient. This angular dependence indicates the ion enhanced etching of silicon dioxide is more of a physical sputtering process than a chemically driven process. This is consistent with our previous argument that physical sputtering is the dominant mechanism of etching silicon dioxide. Mayer et. al. [Mayer, 1981] reported a similar angular dependence when bombarding the SiO<sub>2</sub> surface with 600eV Ar<sup>+</sup>.

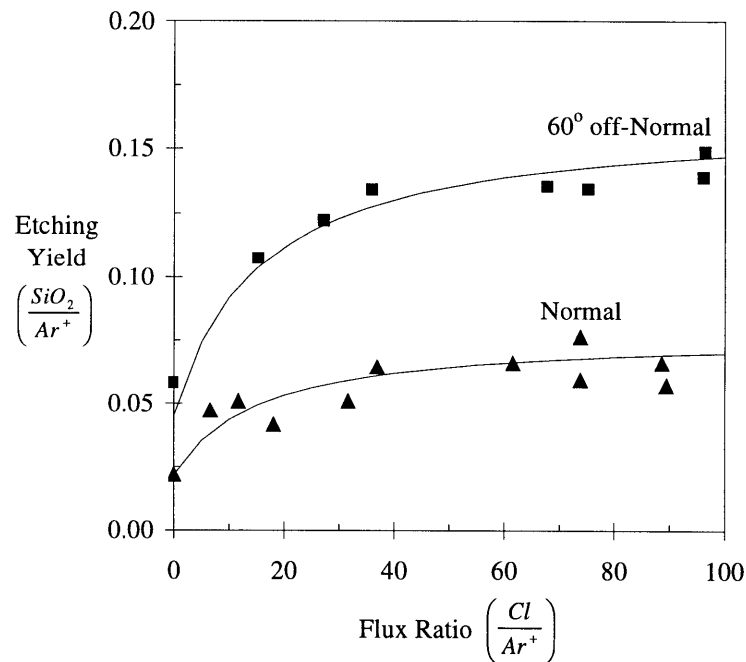


Figure 4.6: Etching yield of silicon dioxide by 100 eV Ar<sup>+</sup> and Cl as a function of Cl to Ar<sup>+</sup> flux ratio. The etching yield is increased by a factor of two at 60° off normal ion incident angle.



However, when SiO<sub>2</sub> is etched by fluorocarbon gases [Mayer, 1981], the angular dependence changed drastically: the maximum etching yield is observed at normal ion incidence angle, as shown in Figure 4.7. This result indicates that SiO<sub>2</sub> etching in the fluorocarbon chemistry was chemically driven, as CO, CO<sub>2</sub>, COF<sub>2</sub>, CF<sub>4</sub> and SiF<sub>4</sub> was liberated as etching products. The comparison shown in Figure 4.7 suggests that the chemistries used can significantly change the angular dependence in etching a certain material, depending on whether their chemical reactivity exceeds the effect of energy and momentum transfer induced by sputtering.

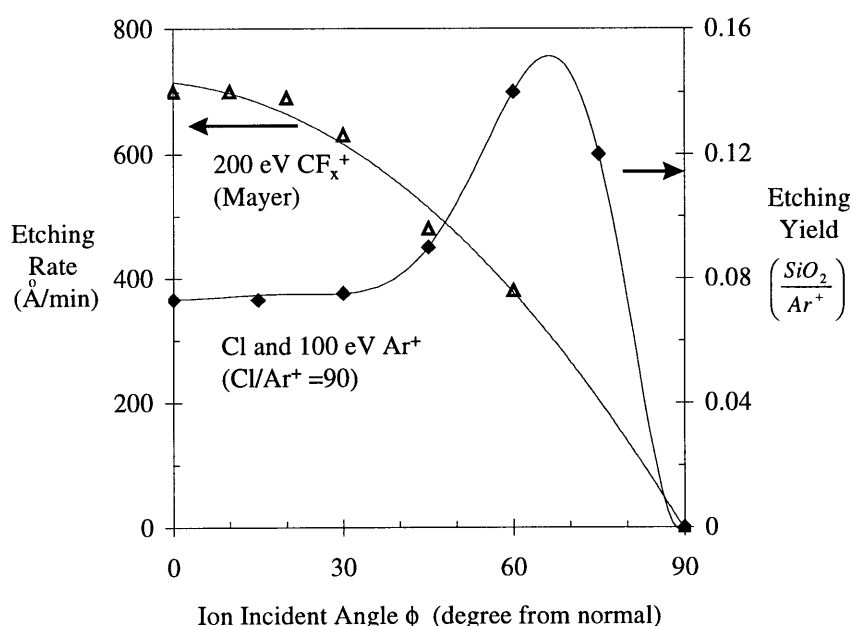


Figure 4.7: Etching yield of silicon dioxide as a function of ion incident angle. Solid diamonds represent the etching yields measured with Cl and 100 eV Ar<sup>+</sup> at a flux ratio of ~90. Maximum etching yield is observed at 60° off normal ion incident angle. The hollow triangles represent the etching yields of silicon dioxide measured with 200 eV CF<sub>x</sub><sup>+</sup> and maximum etching yield is observed at normal incident angle.

The etching yields of silicon dioxide by Ar<sup>+</sup> and Cl shown in Figure 4.7 is fitted by the following equation:

$$Y(\phi) = \sum_{i=1}^6 a_i \cos^i(\phi) = c(\phi) \cdot Y(\phi = 0^\circ) \quad (4.1)$$

$Y(\phi = 0^\circ)$  is the etching yield at normal ion incident angle and  $c(\phi)$  is a constant that can be incorporated in a profile simulator to characterize the etching of silicon dioxide

#### 4.5 Angular Resolved XPS (AR-XPS) Analysis of SiO<sub>2</sub> Etching

Survey spectra of photoemission of silicon dioxide surfaces before and after etching by 100 eV Ar<sup>+</sup> and Cl are shown in Figure 4.8. No measurable amount of contamination (C) is found on a clean silicon dioxide surface. Oxygen remains as the most abundant species before and after etching by 100 eV Ar<sup>+</sup> and Cl, but the emission of chlorine is clearly resolved after the etching process.

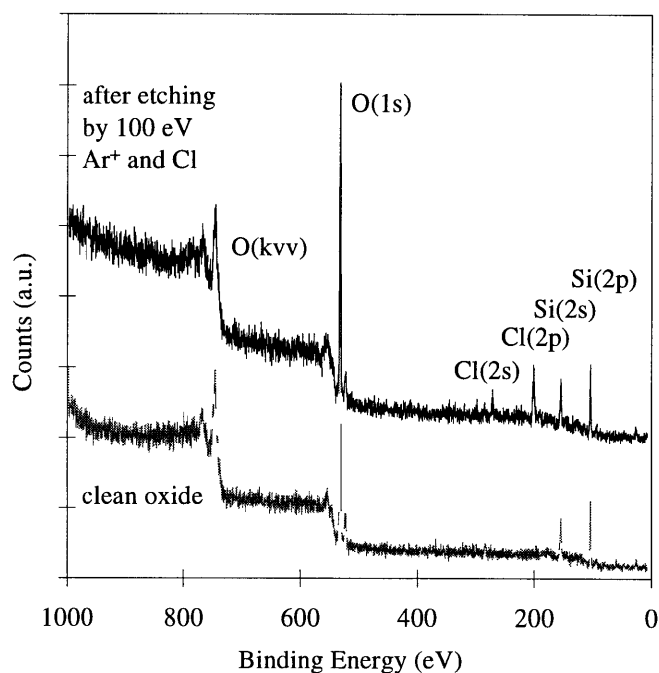


Figure 4.8: Survey spectra of photoemission of silicon dioxide surfaces before and after etching by 100 eV Ar<sup>+</sup> and Cl. No measurable amount of contamination (C) is observed. Oxygen is the most abundant species.

Angular resolved XPS analysis was performed to quantify the extent of surface chlorination in a SiO<sub>2</sub> film as a function of ion energy. Figure 4.9 illustrates the signal intensity change as the take-off angle is varied. The Cl(2p) photoemission intensity did not change significantly with the take-off angle, suggesting that chlorine is confined on the top surface with layer thickness comparable to the mean-free path of the photoelectron. Si(2p) increases significantly as the take-off angle increases, as the XPS is probing deeper into the substrate.

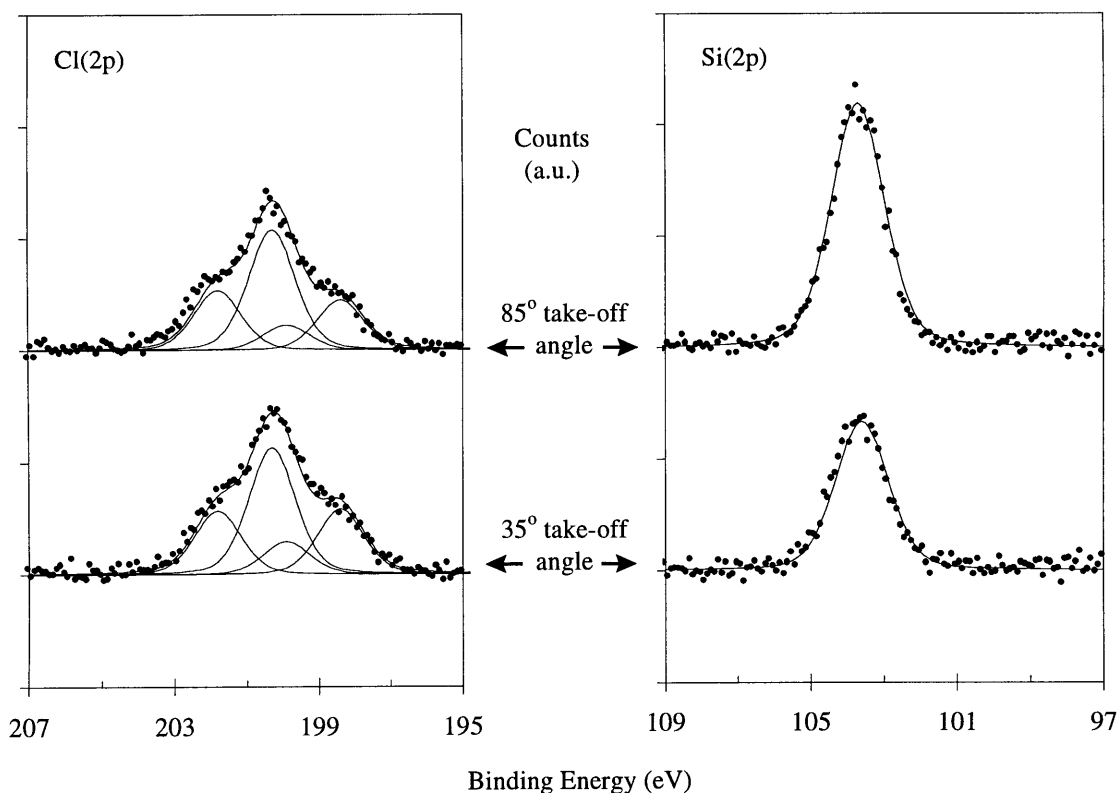


Figure 4.9: Cl(2p) and Si(2p) photoelectron emission spectra, after the silicon dioxide surface is etched by 100 eV Ar<sup>+</sup> and Cl, taken at different take-off angles. As the take-off angle decreases, the ratio of chlorine-to-silicon emission increases, indicating that chlorine remained mostly on the top silicon dioxide surface.

The relative chlorine to silicon signal was determined by the following equation:

$$C_i = \frac{n_i}{\sum_i n_i} = \frac{I_i / s_i}{\sum_i (I_i / s_i)} \quad (4.2)$$

The integrated intensity of the Cl(2p), Si(2p) and O(1s) peaks are normalized with their atomic sensitivity factors,  $S_{Cl(2p)}=0.48$ ,  $S_{Si(2p)}=0.17$ ,  $S_{O(1s)}=0.63$ , respectively. For chlorine, both 2p spin-orbit components are included in the integration, and the calculated composition as a function of take-off angles is shown in Figure 4.10. The relative chlorine signal increases as the take-off angle decreases; indicating the chlorinated layer is comparable to or thinner than the mean free path of the photoelectrons. The chlorine composition is enhanced relative to the oxygen concentration at low take-off angle, indicating that chlorine is mainly confined on the top silicon surface and oxygen is depleted near the top surface due to ion sputtering.

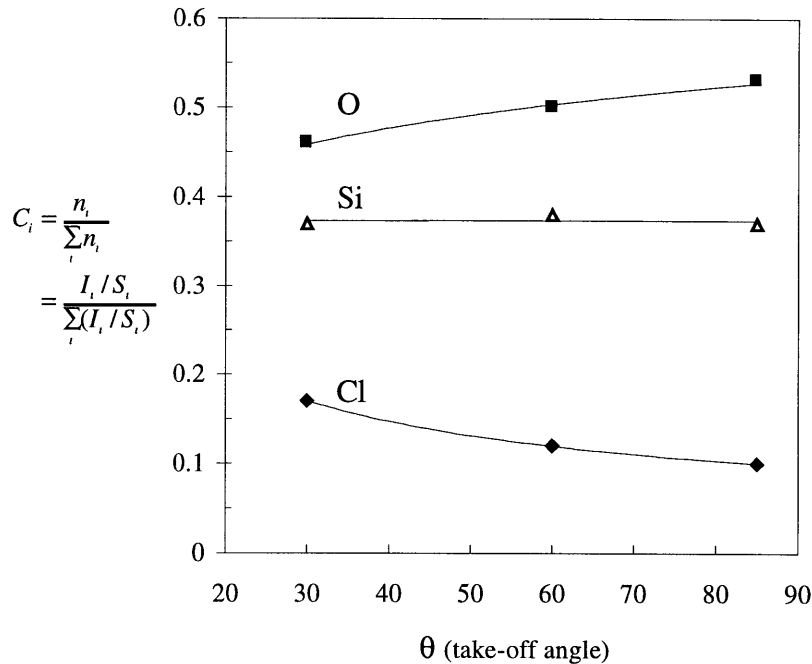


Figure 4.10: The compositions of Cl, Si, and O are calculated as a function of the take-off angles. The Cl(2p), Si(2p) and O(1s) peaks are normalized with their atomic sensitivity factors,  $S_{Cl(2p)}=0.48$ ,  $S_{Si(2p)}=0.17$ ,  $S_{O(1s)}=0.63$ , respectively. The relative chlorine signal increases as the take-off angle decreases; indicating the chlorinated layer is comparable to or thinner than the mean free path of the photoelectrons.

A schematic diagram illustrating the incorporation of chlorine in silicon dioxide surface film is shown in Figure 4.11. Note that a  $SiO_2$  film consists of  $SiO_4$  tetrahedral units (encircled by dotted line in Figure 4.10), and Cl bonds to silicon on the top surface. The physisorption of Cl on oxygen is not shown here. As the take-off angle changes from  $85^\circ$  to  $30^\circ$ , the effective sampling depth decreases from  $25 \text{ \AA}$  to  $12 \text{ \AA}$ . Therefore better surface sensitivity is achieved at a shallower take-off angle, where the relative Cl intensity appears higher.

The relative chlorine composition also increases with the ion energy, suggesting the extent of chlorination increases with increasing ion energy, as shown in Figure 4.12. This is consistent with the observation that the amount of chlorine bonded to silicon increases as the ion energy increases. Also, atomic chlorine achieves a higher extent of surface chlorine incorporation than molecular chlorine, as the reactivity of atomic chlorine is higher than that of molecular chlorine on an oxide surface.

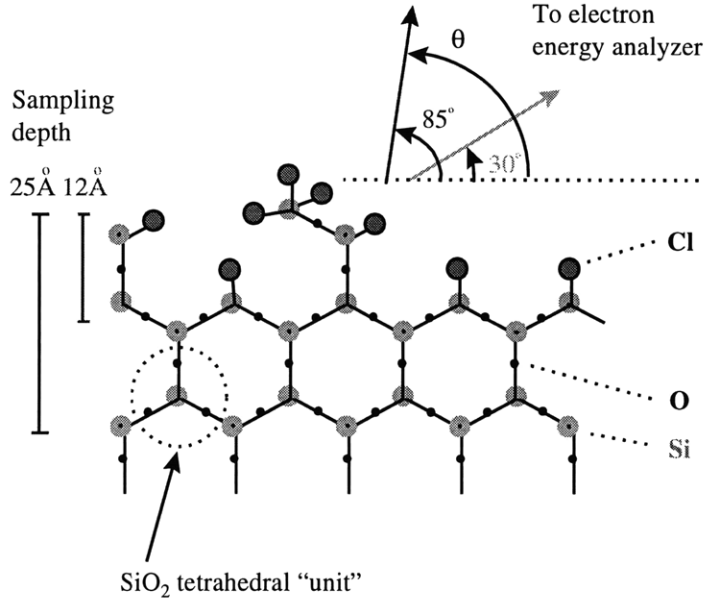


Figure 4.11: A schematic diagram illustrates the incorporation of chlorine in silicon dioxide surface film. Silicon dioxide formed a 3-D network structure with SiO<sub>4</sub> tetrahedral units, encircled by the dashed line. The chlorine is mainly confined on the top silicon dioxide surface and oxygen is depleted near the top surface due to ion sputtering.

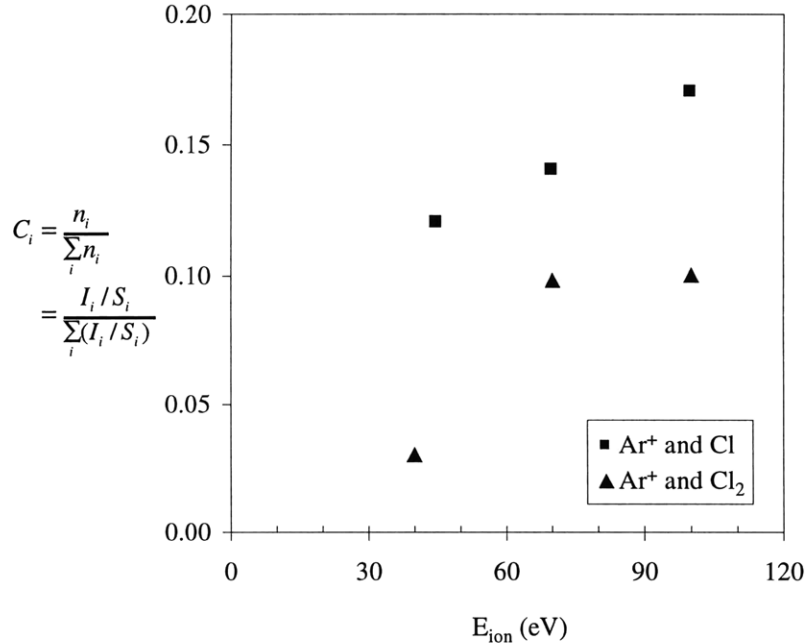


Figure 4.12: Angular resolved XPS analysis of the etched silicon dioxide surface: the composition of Cl calculated as a function of ion bombardment energy. The relative chlorine signal increases as the ion energy increases. Atomic chlorine achieves a higher extent of surface chlorination than molecular chlorine.

## 4.6 Etching Selectivity between Si and SiO<sub>2</sub> with Ar<sup>+</sup> and Cl

The etching selectivity between Si and SiO<sub>2</sub> measured by 100 eV Ar<sup>+</sup> and Cl is approximately 30, as shown in Figure 4.13. The etching selectivity between Si and SiO<sub>2</sub> has been reported to be from 20 to 50 in plasma reactors [Cook, 1990]. Our measurements with energetic Ar<sup>+</sup> ion and atomic chlorine agreed well with what has been reported. Higher selectivities for polysilicon with respect to silicon dioxide or photoresist are desired for patterning finer features. Addition of 1% oxygen to a chlorine plasma is found to reduce the etching rate of silicon dioxide significantly, and increase the selectivity of polysilicon over silicon dioxide to 70 [Cook, 1990].

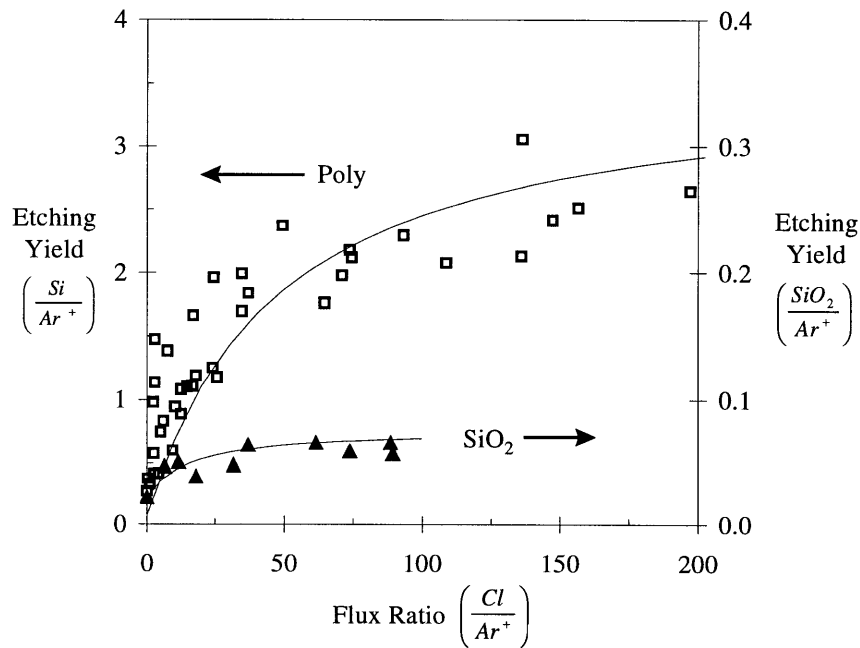


Figure 4.13: Etching yield of polysilicon and silicon dioxide by Ar<sup>+</sup> and Cl as a function of Cl to Ar<sup>+</sup> flux ratio. The selectivity is on the order of 30 between etching of polysilicon and silicon dioxide.

The angular dependence of etching polysilicon differs from that of SiO<sub>2</sub> with 100 eV Ar<sup>+</sup> and Cl, as shown in Figure 4.14. The etching yield measurements are taken at a constant flux ratio where the etching yield of either Si or SiO<sub>2</sub> is considered “saturated”. The etching yield of polysilicon at a flux ratio of 600 exhibits no significant dependence on the angle of incidence from normal to 40° off-normal, but decreases by 35% at the angle

of 60° off-normal. Maximum etching yield at near normal ion incident angles is attributed to the rapid implantation of reactive atoms into the substrate with normally incident ions. The normally incident ions consequently create mixing of the absorbed surface atoms into the lattice, induce surface chlorination, and achieve maximum etching yield at near normal ion incident angles. However, etching of silicon dioxide is mainly ion-driven, as chlorine incorporation into the SiO<sub>2</sub> film is limited. Ions physically sputter oxygen and silicon, allow chlorine to react to silicon, and achieve subsequent slight enhancement in the etching yield. It is necessary to incorporate proper angular dependence for each material into a profile simulator to model the surface topography evolution during the plasma etching processes.

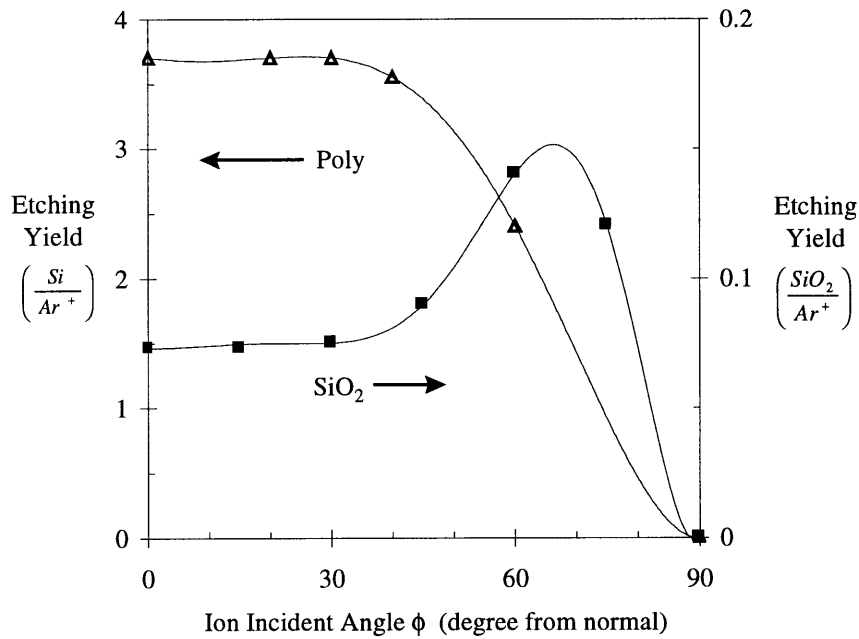


Figure 4.14: Etching yield of polysilicon and silicon dioxide by 100 eV Ar<sup>+</sup> and Cl as a function of ion incident angles. The etching yields of polysilicon and silicon dioxide are measured at flux ratios of 600 and 90, respectively.

#### 4.7 Phenomenological Model for Etching of SiO<sub>2</sub> with Ar<sup>+</sup>

A phenomenological model similar to the one we developed for etching of polysilicon is utilized to characterize the ion-enhanced etching yield of silicon dioxide as a function of Ar<sup>+</sup> ion energy, ion flux, neutral-to-ion flux ratio, and angle of ion

impingement. A simplified model is proposed to represent the chlorine-silicon dioxide surface reactions, as shown in Table 4.1.

Physisorption, chemisorption, desorption, and ion-induced desorption of chlorine atoms are reduced into an overall adsorption reaction, with an assigned surface chlorination coefficient,  $s$ . The recombination of chlorine atoms on the silicon dioxide (quartz) surface in the absence of ion bombardment was measured to be less than 0.02 at above room temperature [Kota, 1997], and is ignored in the model. The major products are assumed to be Si, O<sub>2</sub> and SiCl<sub>2</sub>. The model should be updated as detailed product distributions and surface compositions as a function of ion energy and neutral-to-ion flux ratio become available.  $\beta$  is the ion-enhanced reaction probability and  $\Gamma^+$  is the ion flux. Physical sputtering is the dominant reaction mechanism and  $Y_o$  represents the physical sputtering yield.

Table 4.1: A simplified phenomenological surface kinetic model for Ar<sup>+</sup> ion-enhanced etching of silicon dioxide with Cl.

Surface Reactions	Reaction Mechanism
$Cl_{(g)} + *Si - O_{2(s)} \xrightarrow{s \cdot \theta_{Cl}} Cl - Si - O_{2(s)}$	Surface chlorination
$2Cl - Si - O_{2(s)} \xrightarrow{\beta \cdot \Gamma^+} SiCl_{2(g)} + O_{2(g)} + *Si - O_{2(s)}$	Ion-enhanced etching
$2 * Si - O_{2(s)} \xrightarrow{Y_o \cdot \Gamma^+} Si_{(g)} + O_{2(g)} + *Si - O_{2(s)}$	Physical sputtering

The etching yield is then derived from:  $Y_{total} = Y_o + Y_i$ , where  $Y_o$  and  $Y_i$  represent the physical sputtering yield and ion-enhanced etching yield, respectively. The spontaneous etching of silicon dioxide by atomic and molecular chlorine is ignored. The constant  $c(\phi)$  extracted from the angular dependence study is incorporated into the kinetic model as a constant multiplier; therefore:

$$\begin{aligned}
 Y_{total} &= c(\phi) \cdot (Y_o + Y_i) \\
 &= c(\phi) \cdot [Y_o \cdot (1 - \theta_{Cl}) + \beta \cdot \theta_{Cl}]
 \end{aligned}
 \tag{4.3}$$

where  $\theta_{Cl}$  is the surface coverage of chlorine which can be expressed in the following form by performing a site balance:



$$\theta_{Cl} = \frac{s \cdot R}{s \cdot R + \beta} \quad (4.4)$$

Substituting  $\theta$  in equation (4.2) and rearranging the equation yields the following equations:

$$Y_{total} = c(\phi) \cdot \left[ Y_o + (\beta - Y_o) \frac{s \cdot R}{s \cdot R + \beta} \right] \quad (4.5)$$

$$\frac{1}{Y} \equiv \frac{1}{c(\phi)} \cdot \frac{1}{Y_{total} - Y_o} = \frac{1}{c(\phi)} \cdot \left[ \frac{1}{\beta - Y_o} + \left( \frac{\beta}{s \cdot (\beta - Y_o)} \right) \frac{1}{R} \right] \quad (4.6)$$

where  $\beta$  and  $s$  can be derived respectively from the intercept and slope of a linear regression of  $1/Y$  versus  $1/R$ . The derived parameters are shown in Table 4.2, and the model fits to the experimental data are lines shown in Figure 4.4 and 4.6.

Table 4.2: Model parameters for  $Ar^+$  ion-enhanced etching of silicon dioxide with Cl, as a function of ion energy.

$E_{ion}$	$Y_o$	$\beta$	$s$
70	0.01	0.04	0.001
100	0.02	0.08	0.005

Equation (4.3) is a complete form of the kinetic model that accounts for the energy, flux and angular dependencies of  $Ar^+$  ion-enhanced etching of silicon dioxide with chlorine, and can be incorporated readily into a profile simulator.

#### 4.8 $Ar^+$ Ion-enhanced Etching of Photoresist with Cl

The etching of photoresist is characterized to complete the database required to accurately simulate etching of photoresist patterned polysilicon film over a thin oxide film. Approximately 9500Å photoresist was spin-coated on a 1000Å silicon dioxide film on a silicon substrate. The photoresist was then subject to 60 seconds baking at 150°C on a hot plate (one baking cycle). Some samples were subject to two baking cycles to allow evaluation of the effect of heat treatment. The photoresist films are then etched by 65 eV  $Ar^+$  and Cl. To quantify the etching of photoresist, the etching rate of photoresist (Å/min)

is normalized with respect to the ion flux, assuming that photoresist is comprised of only carbon, and has a density of  $1.1 \text{ g/cm}^3$ . Typically the density of the novolac based photoresist is on the order of  $1 \text{ g/cm}^3$ , and varies slightly with the spin-coating speed and the baking temperature and duration.

The “normalized” etching yield of photoresist is found to be a strong function of the heat treatment to the photoresist (e.g. baking cycle), as shown in Figure 4.15. The etching yield of photoresist is clearly enhanced as the atomic chlorine fluxes increases. However, lower etching rate is observed at samples subject to two baking cycles. Based on the etching rates of both polysilicon and photoresist measured under the same ion and neutral fluxes, the etching selectivity between polysilicon and photoresist is approximately 1.2 for samples subject to one baking cycle, and 2.5 for samples subject to two baking cycles. This suggests that prolonged baking of photoresist (2 cycles) results in more efficient removal of residual solvents and hardening of the photoresist and leads to a better etching selectivity.

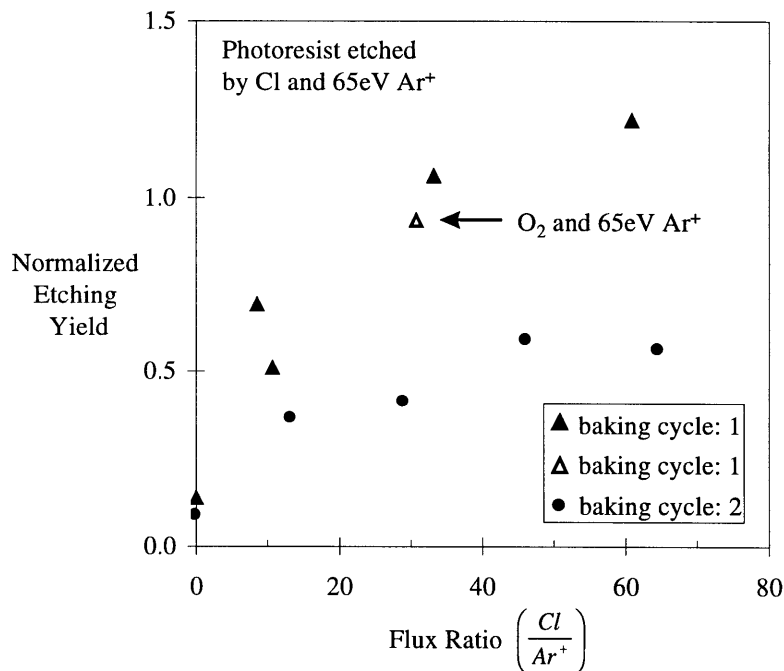


Figure 4.15: Normalized etching yield of photoresist by 65 eV Ar<sup>+</sup> and Cl as a function of Cl to Ar<sup>+</sup> flux ratio. The etching yield increases with increasing flux ratios, but decreases by a factor of two as the photoresist is subject to two baking cycles on a hot plate. (The photoresist is baked at 150°C for 60 seconds for each cycle).

Molecular oxygen was also used to etch photoresist under  $\text{Ar}^+$  bombardment. The preliminary results indicates that high etching rate, comparable to that measured with atomic chlorine, is achieved. Oxygen plasma has long been used to “ash” photoresist, and atomic oxygen has been thought to induce chain scission in photoresist upon simultaneous ion bombardment, and etch the photoresist at a significant rate.

Barklund et. al. [Barklund, 1992] investigated the angular dependence of polymer etching with a reactive ion beam etching (RIBE) system in that a sample holder can be tilted with respect to the ion beam gun. The silicon samples are coated with approximately 5000Å thick polymer film formed from a  $\text{CHF}_3$  plasma. Argon,  $\text{CF}_4$ , and  $\text{CHF}_3$  with 6%  $\text{O}_2$  are used in the RIBE system to etch the polymer film at various ion incident angles; the results are shown in Figure 4.16. The angular dependence measured with argon is typical for a physical sputtering system with a maximum at 60° off-normal angle of incidence. The etching yield measured with  $\text{CF}_4$  exhibits monotonic decrease with increasing angle of incidence, as atomic fluorine is generated as the major reactant in etching the polymer –  $\text{CF}_4$  is known to yield the highest  $\text{F}/\text{CF}_x$  ratio among most other freons [d'Agostino, 1990]. This angular dependence resembles what we observed for chlorine etching of polysilicon, and we believe this type of angular dependence is common for other chemical etching processes as well.

The angular dependence of etching photoresist in an oxygen chemistry is investigated by Carl et. al. [Carl, 1990], as oxygen is widely used to “ash” the photoresist after successful pattern transfer;  $\text{CO}$ ,  $\text{CO}_2$  are typically formed as etching products. Their results are also shown in Figure 4.16 for comparison. The photoresist (KTI-820) samples were etched in an electron cyclotron resonance reactor, and the sample holder can be rotated with respect to the plasma. The angular dependence of etching photoresist in an oxygen plasma is shown to be similar to that observed with atomic fluorine etching ( $\text{CF}_4$ ) etching of photoresist. This resemblance indicates that maximum etching yield at normal ion incident angle is indeed observed for a chemical etching system. They also reported an apparent threshold energy of ~ 25 eV for photoresist etching.

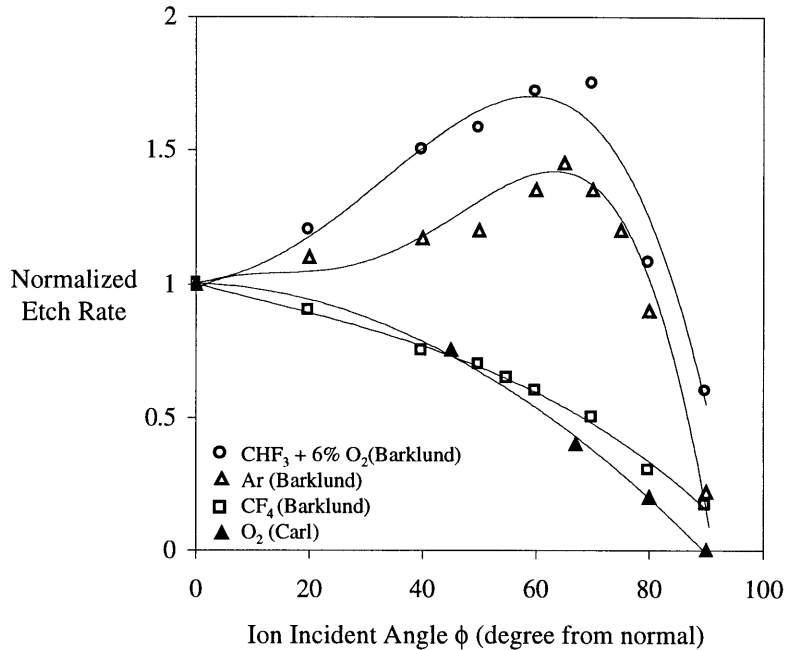


Figure 4.16: Etching rate of a polymer film by various gases as a function of ion incident angles [Barklund, 1992]. The angular dependence of etching photoresist in an oxygen chemistry is also shown for comparison [Carl, 1990].

The angular dependence for etching of polymer with CHF<sub>3</sub> and 6% O<sub>2</sub>, however, requires more discussion. Maximum etching yield is observed at 60° to 70° off-normal ion incident angle, a dependence similar to that measured with Ar<sup>+</sup> sputtering. This is due to the increased deposition from CHF<sub>3</sub>, making the measured etching yield a combination of etching and deposition. The hydrogen in CHF<sub>3</sub> is known to reduce the fluorine concentration, and increase the polymer precursor concentration, CF<sub>2</sub>. Therefore, the observed angular dependence can not be interpreted simply as a result of a sputtering or a chemical etching reaction, as the deposition complicates the surface chemistry and the subsequent etching reactions.

## Chapter 5

### Chlorine Ion Enhanced Etching of Polysilicon

The importance of low energy chlorine ions in etching of polysilicon is elucidated in this chapter. The effect of reactive ions in etching of polysilicon has not been addressed systematically by beam experiments despite of the extensive studies of chlorine ion-enhanced etching of silicon and polysilicon in the past decade.  $\text{Ar}^+$  ions with similar mass to reactive  $\text{Cl}^+$  ions have been used to circumvent the difficulties associated with generating a  $\text{Cl}^+$  beam. However, several studies showed drastic differences in sputtering yields between  $\text{Ar}^+$  and  $\text{Cl}^+$ , at high ion energies.

In this work, a  $\text{Cl}^+$  ion beam at low energies is generated to characterize the functional role of a reactive ion in etching of polysilicon, especially its chemical reactivity. In addition, utilizing a low energy  $\text{Cl}^+$  ion beam in conjunction with  $\text{Cl}$  and  $\text{Cl}_2$  allows us to accurately simulate a high-density chlorine plasma source, and determine the synergism between reactive ions and neutrals. We also attempt to increase the ion flux to a level at which most of the high-density plasma reactors are operated. Moreover, the effect of etching by-products ( $\text{SiCl}_2$ ) is also characterized in conjunction with  $\text{Cl}^+$  and  $\text{Cl}$  exposure to accurately simulate a high-density chlorine plasma.

$\text{Cl}^+$  has been identified as the major ionic species in a high density, inductively coupled plasma reactor [Johannes, 1997].  $\text{Cl}_2^+$  and  $\text{Cl}^-$  have also been reported as other important ionic species in a high density chlorine plasma reactor [Font, 1997]. Characterization of the effects of  $\text{Cl}_2^+$  and  $\text{Cl}^-$  is beyond the scope of this work.

#### 5.1 Low Energy $\text{Cl}^+$ Sputtering of Polysilicon

Reactive ions are known to yield higher etching rate than that of inert ions [Tachi, 1986]. The sputtering yield of polysilicon by  $\text{Cl}^+$  is a linear function of the square root of

the ion energy, as shown in Figure 5.1. The sputtering yield of low energy  $\text{Ar}^+$  ion is shown for comparison. The physical sputtering yield at this low energy regime is again characterized by the universal energy dependence of ion bombardment induced etching processes,  $Y(E_{ion}) = A \cdot (E_{ion}^{1/2} - E_{th}^{1/2})$ , where  $Y(E_{ion})$  is the etching yield as a function of ion energy and  $E_{th}$  is the threshold energy. The extrapolated threshold energy is approximately 10 eV, which is lower than that measured by  $\text{Ar}^+$  sputtering of polysilicon ( $\sim 35$  eV). The reduction in threshold energy is caused by the formation of a heavily chlorinated layer that reduces the surface bonding energy and allows for subsequent incorporation of chlorine into the silicon lattice. Good agreement is observed by comparing our experimentally measured sputtering yield to molecular dynamic simulation results reported by Barone et. al. [Barone, 1995]. They confirmed the square root ion energy dependence of reactive chlorine ion etching of silicon over the energy range of 10 to 50 eV, and observed that the etching product stoichiometry depends strongly on the ion energy.

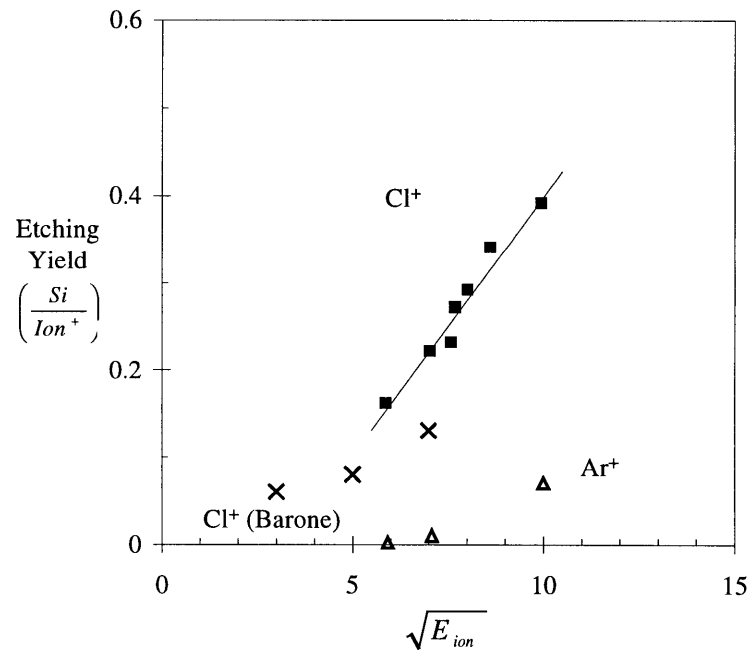


Figure 5.1: Sputtering yield of polysilicon by  $\text{Cl}^+$  in the low energy regime. The line shown is a least square fit to our experimental data (slope  $\sim 0.06$ ). The sputtering yield scales with the square root of ion energy and the threshold energy is approximately 10 eV. Qualitatively good agreement is observed with the molecular dynamic simulation results [Barone, 1995]. Low energy sputtering yield by  $\text{Ar}^+$  is shown for comparison.

Chlorine ions achieved a higher sputtering yield than argon ions due to the surface chlorination induced by  $\text{Cl}^+$  and the subsequent formation of volatile products.  $\text{Ar}^+$  physically bombards the silicon surface, transfers energy and momentum, ejects silicon atoms as sputtering products, but does not bond/react with the silicon.  $\text{Cl}^+$ , on the other hand, induces surface chlorination, creates a mixed layer of chloro-silyl and produces  $\text{SiCl}_x$  as sputtering products. Barone et. al. [Barone, 1995] reported  $\text{SiCl}$  and  $\text{SiCl}_2$  as the major sputtering products by reactive  $\text{Cl}^+$  ion etching of polysilicon. Therefore, sputtering of the silicon surface by  $\text{Cl}^+$  can not be viewed as a pure physical sputtering process. We termed this process chemical sputtering [Winter, 1992] in that ion bombardment causes chemical reactions to occur and produces species weakly bounded to the surface. These species then desorb spontaneously with thermal energy or gain energy from a collision cascade and desorb with excess energy into gas phase.

## 5.2 $\text{Cl}^+$ Ion Enhanced Etching of Polysilicon

The effect of  $\text{Cl}^+$  vs.  $\text{Ar}^+$  in the presence of an atomic or a molecular chlorine beam is characterized by measuring the etching yield of polysilicon as a function of neutral to ion flux ratios. The chlorine ion-enhanced etching yield is also found to be independent on the individual beam flux, and is a strong function of the neutral to ion flux ratio. The measured etching yields of polysilicon by  $\text{Cl}^+$  or  $\text{Ar}^+$  at an energy of 35 eV with an atomic chlorine beam are shown in Figure 5.2. Even though the etching rate is greatly enhanced upon simultaneous impingement of  $\text{Ar}^+$  and  $\text{Cl}$  while neither of the individual species etches the silicon substrate rapidly,  $\text{Cl}^+$  and  $\text{Cl}$  achieved higher etching yields than  $\text{Ar}^+$  and  $\text{Cl}$ . Drastic difference in etching yield is observed at very low flux ratios. The difference in etching yield between  $\text{Cl}/\text{Cl}^+$  and  $\text{Cl}/\text{Ar}^+$  was diminished at high flux ratios where the surface is highly chlorinated, and reaction becomes ion flux limited. This result suggests the chemical reactivity of  $\text{Cl}^+$  contributes to the surface chlorination, and further enhances the etching rate at low flux ratios. The difference in etching yield between  $\text{Cl}/\text{Cl}^+$  and  $\text{Cl}/\text{Ar}^+$  is also less pronounced at higher ion energies ( $\sim 100$  eV), as more sufficient energy and momentum transfer dominates the etching reactions. This

suggests that the effect of  $\text{Cl}^+$  is the greatest at energies comparable to the threshold energy, as  $\text{Cl}^+$  is capable of chlorinating the silicon surface and lowering the surface bonding energy, while low energy  $\text{Ar}^+$  fails to effectively promote surface reactions. It is worth noting that the etching yield curve measured with  $\text{Cl}^+/\text{Cl}$  reaches the “plateau” at a lower flux ratio than that with  $\text{Ar}^+/\text{Cl}$ , suggesting the silicon surface reaches the saturation coverage faster when bombarded with  $\text{Cl}^+$ .

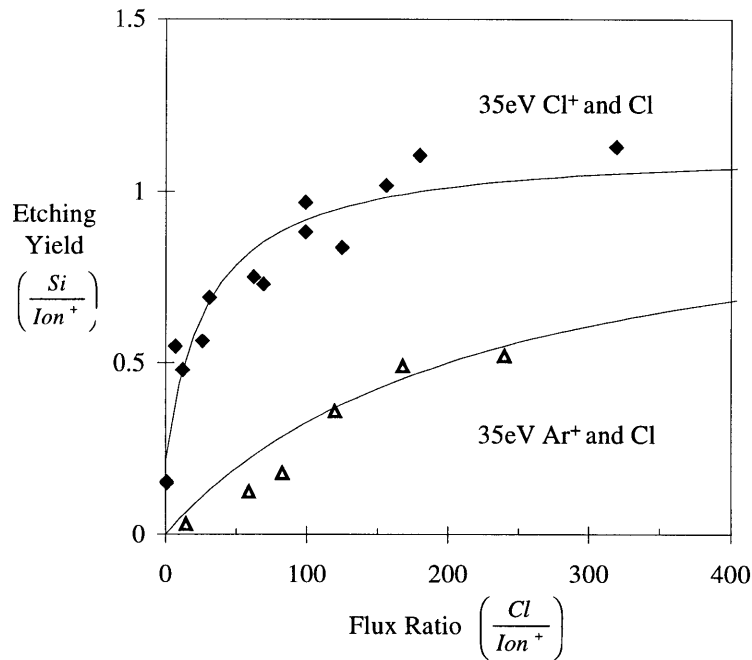


Figure 5.2: Ion enhanced etching of polysilicon by Cl atoms with 35 eV  $\text{Cl}^+$  ions and  $\text{Ar}^+$  ions, respectively. A factor of 2 (more at lower flux ratios) difference in etching yield is observed due to the greater chemical reactivity of  $\text{Cl}^+$  than that of  $\text{Ar}^+$ . Lines shown there are fits from the surface kinetic model detailed in section 5.6.

The polysilicon surface roughness after  $\text{Cl}^+$  and  $\text{Cl}^+/\text{Cl}$  bombardment is shown for comparison in Figure 5.3. Both silicon surfaces shown were cleaned by Piranha and HF solutions to remove surface carbonaceous contamination and native oxide prior to insertion into the vacuum system. However, formation of pillars is observed on the surface bombarded by  $\text{Cl}^+$  alone. This surface morphology was attributed to the residual surface contamination micro-masked the etching of polysilicon.



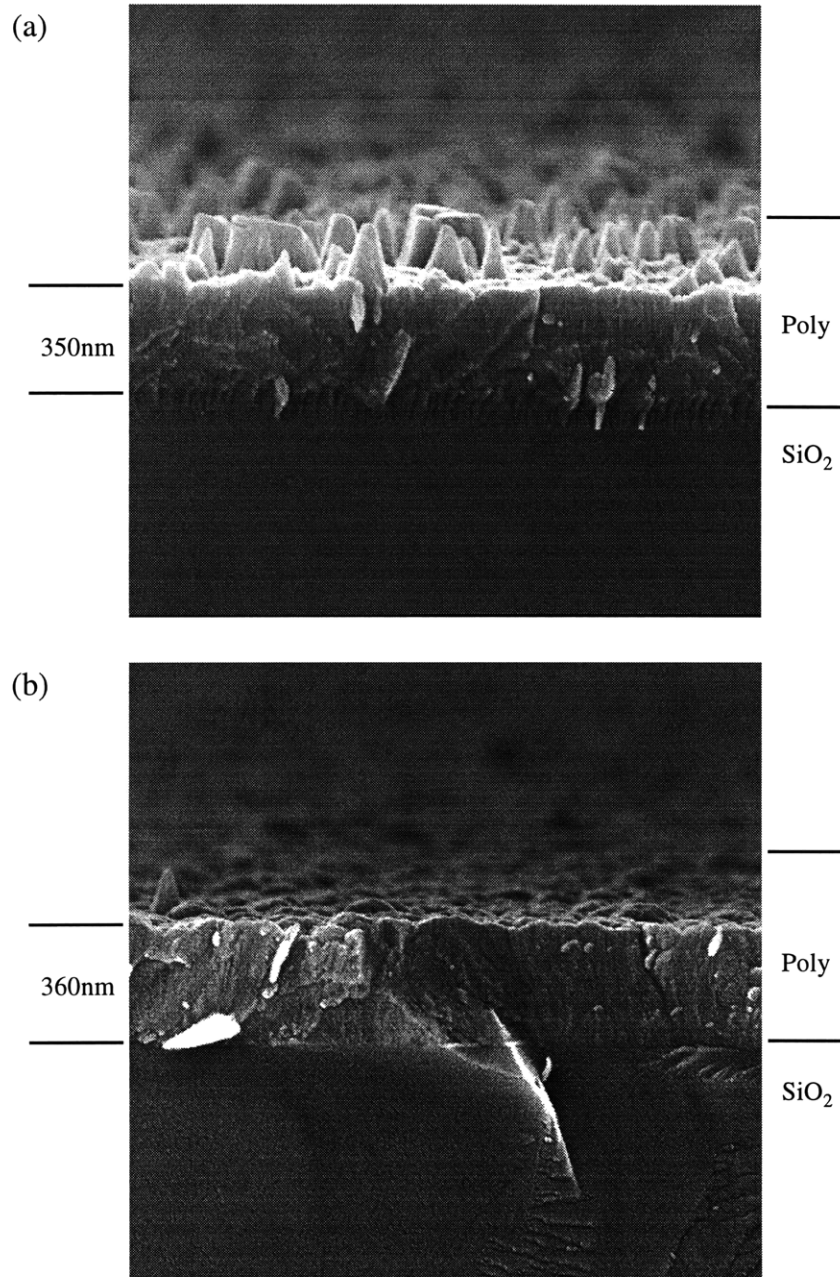


Figure 5.3: (a) Polysilicon surface morphology after Cl<sup>+</sup> ion bombardment, and (b) polysilicon surface morphology after simultaneous Cl<sup>+</sup> and Cl bombardment. Both silicon surfaces are cleaned with Piranha and HF to remove carbonaceous contamination and native oxide prior to the etching process. Micromasking effect is greatly reduced with simultaneous Cl impingement.

Micro-masking effect is caused by residual surface contamination whose sputtering yield is lower compared to the surrounding substrate. Preferential sputtering

of polysilicon about the masking materials leads to the formation of pillars, as shown in Figure 5.3 (a). The development of these pillars also depends strongly on the angular dependent sputtering yield of polysilicon. As an initial pillar develops due to the difference in sputtering yields between the contamination and the thin film to be etched, ion scattering from the sloped sides of the pillars enhances the etching of the thin film material around the pillar and increase the size of the pillars. This surface phenomenon has been observed for various combination of substrates and surface contamination [Robinson, 1982] [Auciello, 1981]. In the presence of atomic chlorine, the pillar structure is greatly reduced as the isotropic atomic chlorine may enhance the etching of the contamination material, or induce undercutting of the pillar in the presence of ion bombardment.

The difference in measured etching yields of polysilicon by  $\text{Cl}^+/\text{Cl}_2$  and  $\text{Ar}^+/\text{Cl}_2$  is shown in Figure 5.4. Note the  $\text{Cl}^+$  and  $\text{Ar}^+$  energies are different.

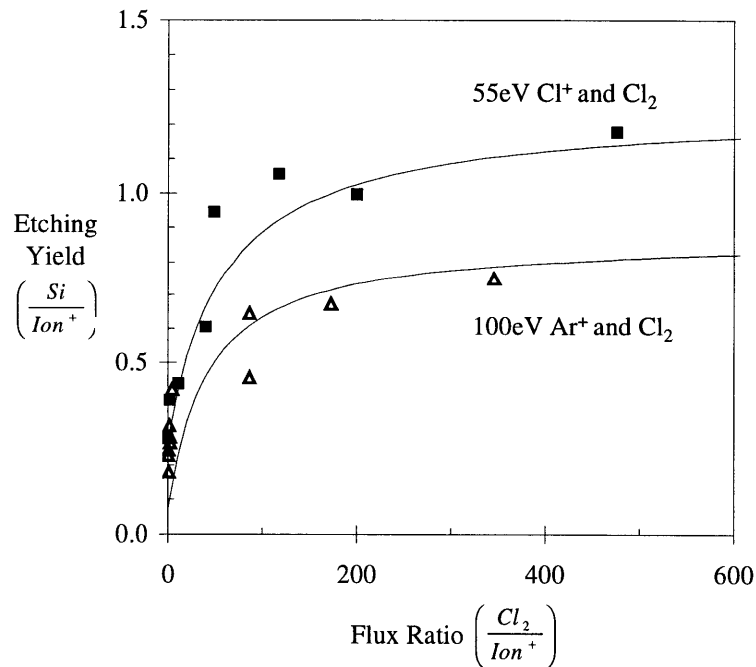


Figure 5.4: Ion enhanced etching of polysilicon by a  $\text{Cl}_2$  beam with 55 eV  $\text{Cl}^+$  and 100 eV  $\text{Ar}^+$ , respectively. Higher etching yield is achieved with 55 eV  $\text{Cl}^+$  due to the greater chemical reactivity of  $\text{Cl}^+$  than that of  $\text{Ar}^+$ . Lines shown here are fits from surface kinetic models detailed in section 5.6 and section 3.6.

55 eV  $\text{Cl}^+$  achieves greater etching yield than 100 eV  $\text{Ar}^+$  at higher  $\text{Cl}_2$ -to-ion flux ratios, indicating the chemical contribution of  $\text{Cl}^+$  impingement exceeds the momentum transfer of a higher energy  $\text{Ar}^+$  in chlorinating the silicon surface.

The chlorine ion-enhanced etching yield versus atomic to ionic chlorine flux ratio at three ion energy levels is shown in Figure 5.5. The etching yield increases significantly with increasing flux ratio at low flux ratios, indicating the etching reaction is limited by the availability of reactive atoms on the etching surface. At higher flux ratios, while the surface is highly chlorinated, the etching yield increases moderately with the flux ratio, where the reaction is ion flux limited. The spacing between the “saturated” etching yields suggested that the etching yield scales with  $(E_{\text{ion}}^{1/2} - E_{\text{th}}^{1/2})$ , consistent with the momentum transfer limited etching mechanism induced by ion bombardment.

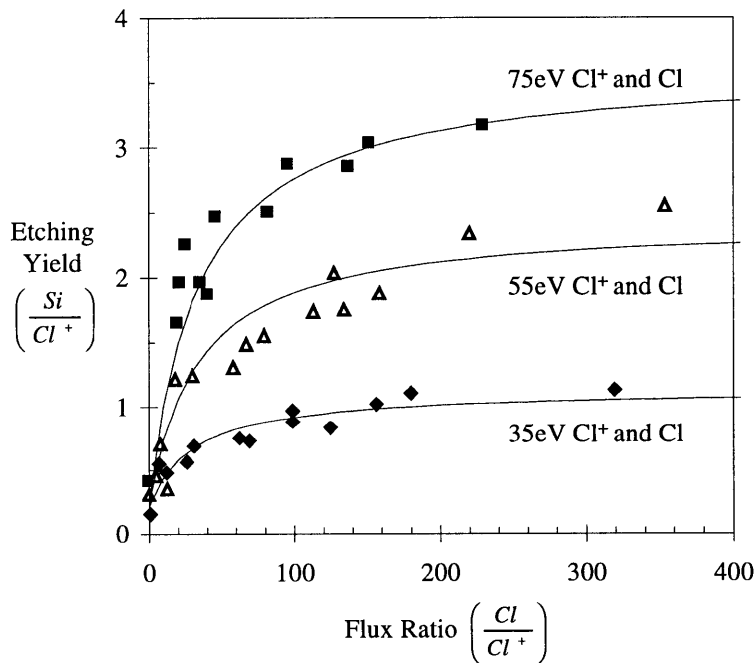


Figure 5.5: Ion enhanced etching of polysilicon by Cl atoms and  $\text{Cl}^+$  ions at three ion energy levels. An initial rise in the etching yield is observed at low flux ratios where reaction is limited by the supply of reactive neutrals. The etching yield then gradually saturates as the reaction becomes ion-flux limited at high flux ratios. The etching yield scales linearly with the square root of ion energy. Lines shown here are fits from the surface kinetic model detailed in section 5.6.

The effect between Cl and Cl<sub>2</sub> in the presence of Cl<sup>+</sup> is shown in Figure 5.6. A factor of two to three enhancement in etching yield is observed at higher flux ratios. Lower etching yield is achieved with Cl<sub>2</sub> at higher flux ratios because the dissociative adsorption of molecular chlorine is limited on a highly chlorinated surface. The more rapid adsorption of Cl indicates that the Cl flux rather than Cl<sub>2</sub> flux limits the etching at high chlorine coverages, which are encountered in most of the plasma etching processes.

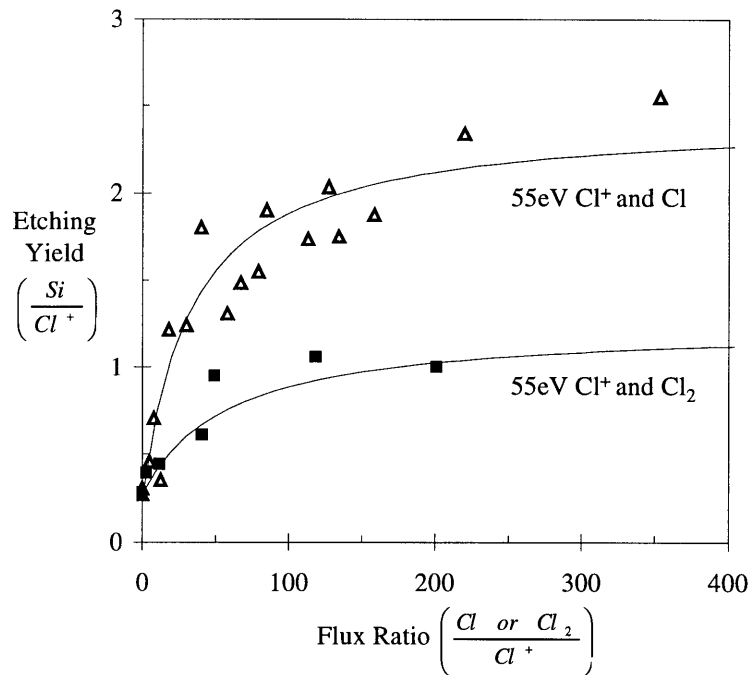


Figure 5.6: Ion enhanced etching of polysilicon by Cl and Cl<sub>2</sub> beams with 55 eV Cl<sup>+</sup>. Distinct difference in etching yield measured by Cl and Cl<sub>2</sub> in the presence of ion bombardment is observed. Lines shown here are fits from the surface kinetic model detailed in section 5.6.

The energy dependence of Cl<sup>+</sup> ion enhanced etching of polysilicon is shown in Figure 5.7. The etching yield of polysilicon by Cl<sup>+</sup> and Cl and the sputtering yield of polysilicon by Cl<sup>+</sup> and Cl<sub>2</sub><sup>+</sup> are shown for comparison as a function of the square root of ion energy. For Cl<sup>+</sup> induced sputtering, our measurement in the low energy regime agrees well with Tachi's work [Tachi, 1986] in the high-energy regime (100eV-1keV). Balooch et. al. [Balooch, 1996] reported a higher sputtering yield by Cl<sub>2</sub><sup>+</sup> than that of Cl<sup>+</sup> due to the higher momentum and energy transfer by diatomic chlorine ions. The

expected etching yield measured with  $\text{Cl}_2^+$  should be square root of two times of that measured with  $\text{Cl}^+$ . However, the reported etching yield measured with  $\text{Cl}_2^+$  is greater than two times of that measured with  $\text{Cl}^+$  in our work, especially in the high ion energy regime. Since the background chlorine pressure in Balooch's work ( $\sim 10^{-4}$  Torr) was two orders of magnitude higher than that in our system ( $\sim 10^{-6}$  Torr), the sufficiently high chlorine pressure could create saturated chlorine coverage on the surface and increased the etching yield. This is consistent with the prediction from the collision cascade model where the etching yield is enhanced as surface chlorination reduces the binding energy of the silicon atoms. With addition of Cl or  $\text{Cl}_2$ , the slope of the energy dependence lines increases, suggesting that the chlorination of the silicon surface enhance the etching rates.

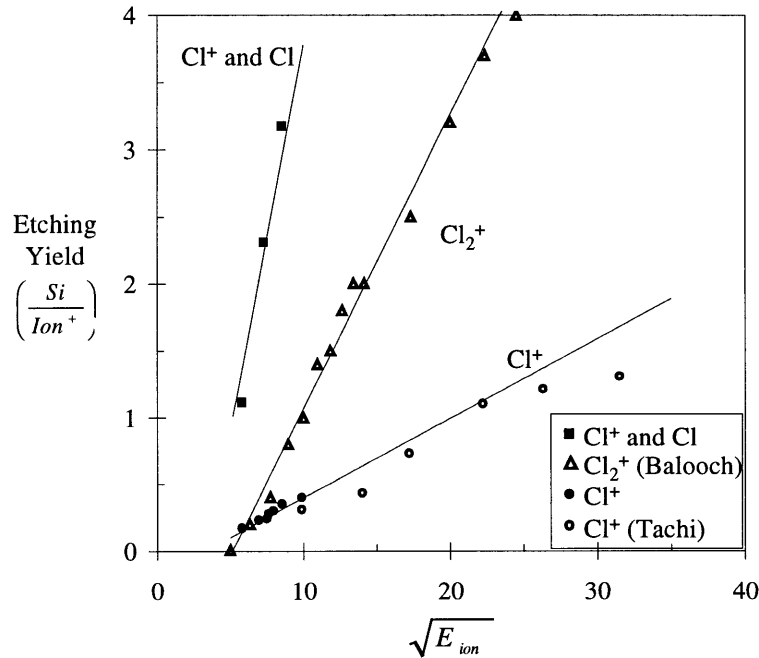


Figure 5.7: Etching yield of polysilicon by  $\text{Cl}^+$  and Cl,  $\text{Cl}_2^+$  and  $\text{Cl}^+$  as a function of the square root of ion energy. The etching yields of polysilicon by utilizing  $\text{Cl}^+$  and Cl beams are taken in the saturation regime (flux ratio of 200 or above, depending upon the data available). The universal energy dependence of ion induced etching process favorably explains the measured etching yield of polysilicon by  $\text{Cl}^+$  and Cl,  $\text{Cl}_2^+$  and  $\text{Cl}^+$  respectively.

We observed further enhancement in the etching yield by utilizing  $\text{Cl}^+$  and Cl beams simultaneously. The slopes of the line fits to the energy dependent yields are 0.06,

0.22, and 0.57 for  $\text{Cl}^+$ ,  $\text{Cl}_2^+$ , and  $\text{Cl}^+$  and  $\text{Cl}$ , respectively. The increased slope indicates that  $Y_{(\text{Cl}^+ \text{ and } \text{Cl})} > Y_{(\text{Cl}_2^+)} > Y_{(\text{Cl}^+)}$  at a constant energy level and that the increased etching yield is caused by a higher extent surface chlorination.

### 5.3 Angular Dependence of Polysilicon Etching with $\text{Cl}^+$

The effect of ion incident angle is shown in Figure 5.8. Ion incident angles were selected to be from normal to  $70^\circ$  off normal. With ion bombardment at  $70^\circ$  off normal, the etching yield still increases as the flux ratio increases; however, approximately 50% constant reduction in the etching yield was observed comparing to that measured at normal ion incident angle, up to flux ratios of 400.

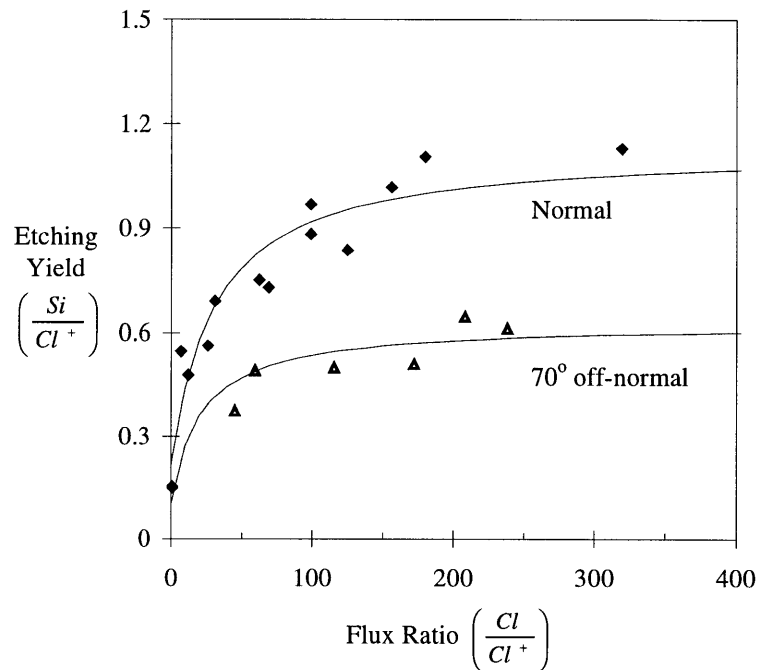


Figure 5.8: Angular dependence of ion enhanced polysilicon etching with  $\text{Cl}$  and 35 eV  $\text{Cl}^+$ . Etching yields measured at normal and at  $70^\circ$  off-normal incident angles are shown for comparison. Approximately 50% reduction in etching yield is observed over a wide range of flux ratios as the ion incident angle changes from normal to  $70^\circ$  off-normal ion incident angles. Lines shown here are fits from the surface kinetics model described in section 5.6.

The measured etching yields at various ion incident angles at a flux ratio of 200 are shown in Figure 5.9. The etching yield showed no significant change as the ion incident angle increased from normal to 40° off normal, but decreased by 30 % and 50 % at 60° and 70° off-normal angles. The zero etching yield at glancing angle (90° off-normal) is assumed. Maximum etching yield is observed at normal ion incident angle and the etching yield starts decreasing at 30-40° off-normal angles, similar to the angular dependence we measured for Cl/Ar<sup>+</sup> etching of polysilicon. A highly chlorinated layer is produced by chlorine ion bombardment and the maximum etching yield is achieved at normal incident angle. The etching yield at off-normal incident angles is expressed in the following form:  $Y(\phi) = c(\phi) \cdot Y(\phi = 0^\circ)$  where  $Y(\phi = 0^\circ)$  is the etching yield measured at normal ion incident angle and  $c(\phi)$  is a constant extracted from a polynomial fit to the experimental data, as indicated by the line in Figure 5.9. This angular dependence of ion-enhanced polysilicon etching can be incorporated into a profile simulator to better characterize the etching rate at the sidewall of the feature, especially as the feature size decreases and the aspect ratio increases.

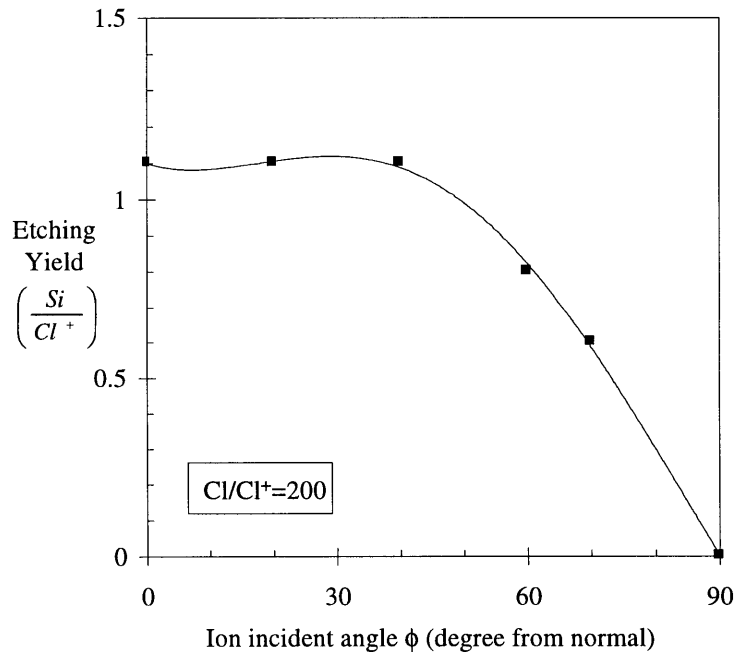


Figure 5.9: Angular dependence of ion enhanced polysilicon etching with Cl and 35 eV Cl<sup>+</sup> at a flux ratio of 200. Maximum etching yield is observed at normal ion incident angle and the line represents a polynomial fit to the experimental data.

#### 5.4 Effect of Etching By-product Deposition: $\text{SiCl}_2$

In high-density plasma etching processes, deposition from the plasma and redeposition of less volatile etching products within the trench are known to compete with the etching reactions and can significantly modify the etching profiles. Factors affecting the etching rate in a plasma etching process include: (1) partial depletion of the feed gas in a low pressure operating condition, the subsequent reduction of etchant production (e.g. Cl), and the reduction of etching rate at a given feed gas flow rate. (2) deposition of the etching product and by-product on the silicon surfaces during the etching process.

Volatile etching products such as  $\text{SiCl}_4$  do not appreciably react with surfaces, but they can build up an appreciable concentration (~10%) which is inversely proportional to the gas flow rate in a plasma reactor [Lee, 1996]. Electron impact dissociation of  $\text{SiCl}_4$  produces  $\text{SiCl}_2$ , which has a higher sticking probability than that of  $\text{SiCl}_4$ , and can deposit readily on silicon surfaces. Less volatile etching products such as  $\text{SiCl}_2$  would leave the surface upon ion bombardment and redeposit on the sidewall of the feature where less ion bombardment occurs. Therefore, deposition from the plasma or redeposition of less volatile etching products within the trench have to be characterized in order to understand the competing deposition mechanisms and predict the etching profile evolution.

Lee et. al. [Lee, 1996] modeled the role of etching products in polysilicon etching in a high-density chlorine plasma, and observed that etching products significantly reduced the etching rate of polysilicon. Lii et. al. [Lii, 1990] and Lehmann et. al. [Lehmann, 1977] proposed similar simple models which take into account ion-enhanced etching and redeposition to simulate the effect of redeposition on the deep trench etching profiles. Dalton [Dalton, 1993] observed inverse reactive ion etching lag which can be explained by the redeposition of the etching products at low temperatures.



It is crucial to understand the functional role of the depositing species as they can significantly alter the etching profiles and determine the success of subsequent deposition processes. It has been observed that deposition/redeposition during deep trench etching can passivate the sidewall to prevent bowing, cause tapering of the sidewall, and ultimately result in etch-stop as the concentration of depositing species increases. The modification of the sidewall is critical to the definition of the etched profile, as it may change the ion scattering path, which is the major cause for trenching and bowing. Addition of passivating species to the etching gas has been utilized to control the etching profiles [Sato, 1987].

$\text{SiCl}_2$  and  $\text{SiCl}_4$  have been reported as the primary etching products in chlorine ion-enhanced etching of polysilicon as shown in Table 1.1. Rossen [Rossen, 1988] has shown that the emission of  $\text{SiCl}_4$  is enhanced relative to  $\text{SiCl}_2$  as the ion bombardment energy is reduced. Therefore,  $\text{SiCl}_4$  is believed to be the dominant etching product in the low ion energy regime (35 eV-75 eV) we studied.  $\text{SiCl}_4$  is volatile and relatively non-reactive, and is assumed to have no effect on the profile evolution in etching patterned polysilicon wafers  $\text{Cl}^+$  and Cl beams. To study the effect of reactive etching products and etching by-products, we used a hot thermal beam to generate  $\text{SiCl}_2$  by pyrolyzing dichlorosilane ( $\text{SiCl}_2\text{H}_2$ , DCS).

The sticking coefficient of  $\text{SiCl}_2$  to form a stable  $\text{SiCl}_x$  film was calculated to be approximately 0.3 based on our measurement of the incident DCS beam flux and the  $\text{SiCl}_2$  deposition rate observed by laser interferometry using the index of refraction of polysilicon. As the flux of  $\text{SiCl}_2$  has been estimated to be on the order of 10% of the Cl flux in high-density low-pressure polysilicon etching processes, use of this sticking coefficient would suggest deposition rather than etching of polysilicon. Therefore, the effect of  $\text{SiCl}_2$  on chlorine ion-enhanced etching yield was measured with simultaneous  $\text{Cl}^+$  or Cl/ $\text{Cl}^+$  bombardment at an energy of 35 eV, as shown in Figure 5.10. The x-axis in Figure 5.10 represents the  $\text{SiCl}_2$  to  $\text{Cl}^+$  flux ratios. At  $\text{SiCl}_2/\text{Cl}^+$  flux ratio of zero, the etching yields are those measured with  $\text{Cl}^+$  alone or with Cl and  $\text{Cl}^+$  at a flux ratio of 200. The etching yield of polysilicon (y-axis) by  $\text{Cl}^+$  or Cl and  $\text{Cl}^+$  was suppressed significantly by  $\text{SiCl}_2$ ; however, the apparent deposition probability of  $\text{SiCl}_2$  with  $\text{Cl}^+$  was on the order of 0.01, and with  $\text{Cl}^+$  and

Cl was 0.05. This indicates that the apparent sticking probability of SiCl<sub>2</sub> was greatly reduced by the chlorination and/or other modification of the surface caused by the Cl<sup>+</sup> and Cl fluxes.

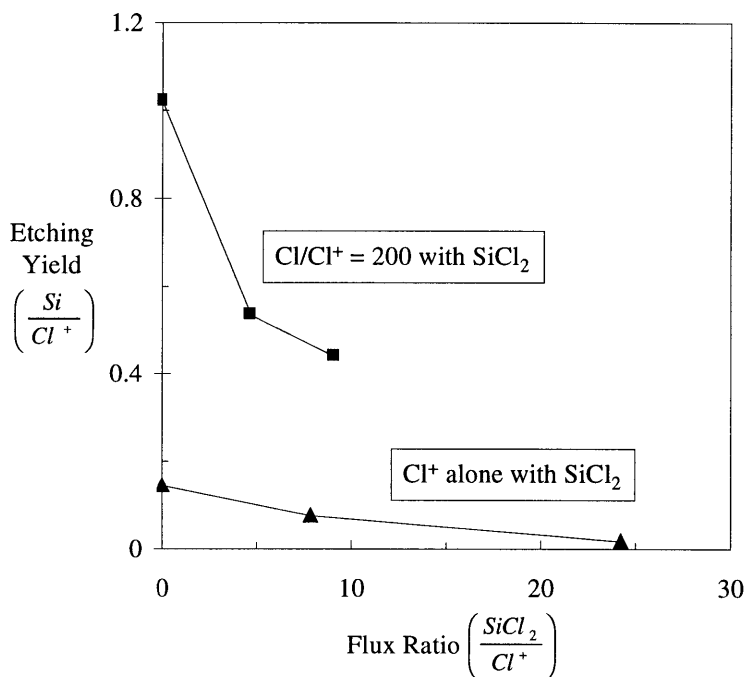


Figure 5.10: The effect of SiCl<sub>2</sub> on chlorine ion-enhanced etching yield measured with 35 eV Cl<sup>+</sup> or 35 eV Cl<sup>+</sup> and Cl. The y-axis represents the etching rate measured with increasing SiCl<sub>2</sub> fluxes. Etching of the polysilicon by Cl<sup>+</sup> or Cl<sup>+</sup> and Cl was suppressed significantly by SiCl<sub>2</sub>, and the apparent sticking probability of SiCl<sub>2</sub> was greatly reduced by the chlorination and/or other modification of the surface caused by the Cl<sup>+</sup> and Cl fluxes.

### 5.5 XPS Analysis of Polysilicon Surface after Cl<sup>+</sup> Bombardment

Survey spectra of photoemission of the polysilicon surface before and after etching by 35 eV Cl<sup>+</sup> is shown in Figure 5.11. The surface is terminated with Cl without any other measurable contamination (C or O). The spectra are taken at a 90° take-off angle. The integrated intensity of the Cl(2p) and Si(2p) peaks are normalized with their atomic sensitivity factors to quantify extent of surface chlorination. The relative chlorine to silicon signal was calculated to be 0.24 and 0.3 at chlorine ion energies of 35 and 55 eV, respectively. This is consistent with the molecular dynamic simulation predicting a

higher chlorine coverage at higher  $\text{Cl}^+$  energy. It is worth noting that the extent of surface chlorination (relative chlorine intensity measured by XPS) achieved by low energy  $\text{Cl}^+$  bombardment is higher than that achieved by 100 eV  $\text{Ar}^+$  and Cl etching, indicating that the direct chlorination of the silicon surface by  $\text{Cl}^+$  is more effective.

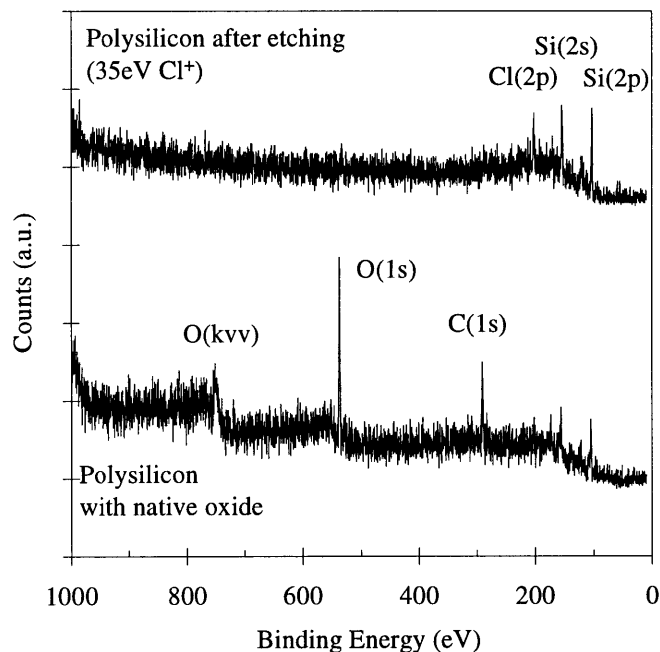


Figure 5.11: Survey spectra of photoemission of polysilicon surfaces before and after etching by 35 eV  $\text{Cl}^+$ . The surface is highly terminated with Cl after etching without other measurable surface contamination (C or O). The take-off angle is at  $90^\circ$ .

The silicon photoemission spectra taken after etching by 35 eV  $\text{Cl}^+$  and Cl is shown in Figure 5.12. The take-off angle is at  $90^\circ$ . The plasmon loss feature for Si(2p) is clearly resolved. Very limited XPS analysis was performed at samples etched by both  $\text{Cl}^+$  and Cl. The relative chlorine intensity obtained after  $\text{Cl}^+$  and Cl exposure is slightly lower than that observed after  $\text{Cl}^+$  bombardment only. These etching experiments were performed in the first experimental setup in which the atomic chlorine flux is turned off after the experiments while the ionic chlorine flux is left on for one to two minutes before retrieving the sample to avoid excess chlorine contamination of the load-lock chamber. It is likely that the “post-etching”  $\text{Cl}^+$  bombardment reduces the highly chlorinated surface

layer formed during  $\text{Cl}^+$  and Cl enhanced etching. More experiments need to be done to corroborate this argument.

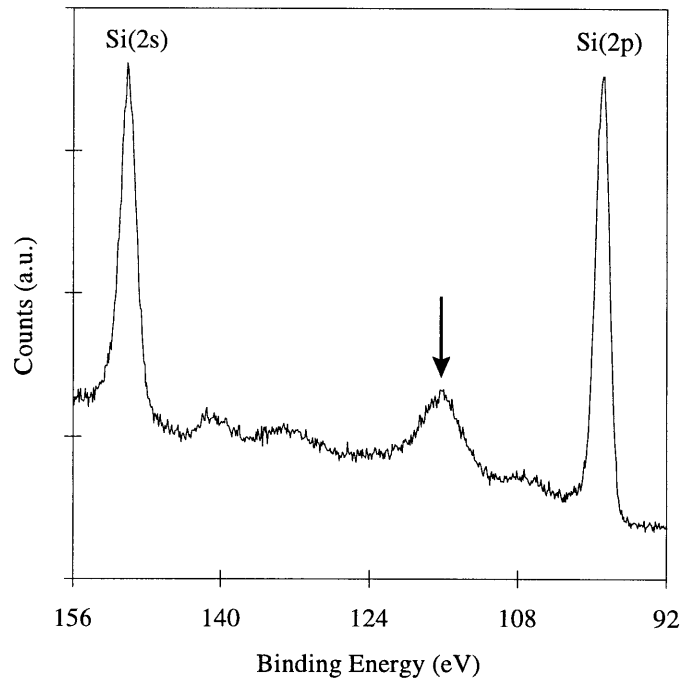


Figure 5.12: The silicon photoemission spectra taken after etching by 35 eV  $\text{Cl}^+$  and Cl. The plasmon loss feature is indicated by the arrow. The surface is highly terminated with Cl after etching without other measurable surface contamination (C or O). The take-off angle is at  $90^\circ$ .

### 5.6 Phenomenological Model for Polysilicon Etching with $\text{Cl}^+$

Because  $\text{Cl}^+$  is capable of chlorinating the silicon surface and producing volatile etching products, the simple model proposed for Ar ion-enhanced etching process is modified to take into account the surface chlorination, and the enhanced etching yield induced by  $\text{Cl}^+$ . A phenomenological model that accounts for the energy, flux and angular dependencies of  $\text{Cl}^+$  ion-enhanced polysilicon etching with Cl was proposed as following for use in profile simulators, as shown in Table 5.1.

The chlorination of the silicon due to Cl was taken as the product of the Cl flux, the unchlorinated fraction of the surface film, and the surface chlorination coefficient,  $s$ .

The recombination of chlorine atoms on a chlorine-saturated polysilicon surface, without ion bombardment, was measured to be 20% by Kota *et al*; however, a rigorous incorporation of the recombination coefficients awaits more experimental evidence on chlorine atom recombination during simultaneous ion bombardment. The chlorination of the silicon surface due to  $\text{Cl}^+$  was also considered. The reaction coefficient of  $\text{Cl}^+$  to silicon is assumed to be a function of the ion incidence angle; and  $c(\phi)$  represents the angular dependency of  $\text{Cl}^+$  ion-enhanced etching of polysilicon. The reaction product is assumed to be  $\text{SiCl}_4$  in this low energy regime (35-75 eV), as reported in the literature; and the formation of unsaturated  $\text{SiCl}_x$  is not considered. The ion-enhanced reaction probability is denoted as  $\beta$ , and the ion flux is  $\text{Cl}^+$ . However,  $\text{SiCl}$  is modeled as the primary etching product when the polysilicon surface is bombarded with only  $\text{Cl}^+$ , as Barone *et. al.* [Barone, 1995] and Hanson *et. al.* [Hanson, 1997] reported in their molecular dynamic (MD) simulation studies. This is a consequence of a lower extent of surface chlorination in the absence of atomic chlorine.

Table 5.1: The simplified phenomenological surface kinetics model for  $\text{Cl}^+$  ion-enhanced etching of polysilicon with Cl.

Simplified kinetics model	Mechanism
$\text{Cl}_{(g)} + * \xrightarrow{\delta} \text{Cl}_{(s)}$	sorption of atomic chlorine
$\text{Cl}_{(g)}^+ + * \xrightarrow{c(\phi)} \text{Cl}_{(s)}$	sorption of ionic chlorine
$\text{Si}_{(s)} + 4\text{Cl}_{(s)} \xrightarrow{\beta \cdot c(\phi) \text{Cl}^+} \text{SiCl}_{4(g)} + 4*$	ion-enhanced etching

The  $\text{Cl}^+$  ion-enhanced etching rate is assumed to be proportional to the product of the angular dependency, the surface chlorination and the ion flux:

$$ER = c(\phi) \cdot \beta \cdot \theta \cdot I^+ \quad (5.1)$$

Therefore, the ion-enhanced etching yield, Y, can be expressed in the following form:

$$Y = c(\phi) \cdot \beta \cdot \theta \quad (5.2)$$

The parameter  $c(\phi)$  denotes the angular dependence and was obtained by fitting the experimental data, and  $\theta$  represents the extent of surface chlorination, which can be expressed in the following form by performing a site balance:

$$\theta = \frac{s \cdot R + c(\phi)}{s \cdot R + c(\phi) + 4 \cdot c(\phi) \cdot \beta} \quad (5.3)$$

The parameter R is the atomic to ionic chlorine flux ratio. Substituting  $\theta$  in equation (5.2) and rearranging the equation yields the following equations:

$$\frac{1}{Y} = \frac{1}{c(\phi) \cdot \beta} + \frac{4}{s \cdot R + c(\phi)} \quad (5.4)$$

At higher flux ratios where  $s \cdot R \gg c(\phi)$ , equation (5.4) can be approximated as:

$$\frac{1}{Y} = \frac{1}{c(\phi) \cdot \beta} + \frac{4}{s} \cdot \frac{1}{R} \quad (5.5)$$

Therefore, we can calculate  $\beta$  and  $s$  from the intercept and slope by a linear regression of  $\frac{1}{Y}$  versus  $\frac{1}{R}$ . The model predictions to the experimental data are shown as lines in Figure 5.5 and Figure 5.8. The values of the parameters at various ion energies are shown in Table 5.2.

Table 5.2: Model parameters for  $\text{Cl}^+$  ion-enhanced etching of polysilicon with Cl, as a function of ion energy.

	$E_{\text{ion}}$	$s$	$\beta$
$\text{Cl}^+, \text{Cl}$	35	0.18	1.14
	60	0.32	2.42
	100	0.45	3.61

Both  $\beta$  and  $s$  scale with the square root of incident ion energy, as shown in Figure 5.13. The effective etching yield,  $\beta$ , increases with incident ion energy as the ion enhanced surface reactions scale with the transfer of momentum to the surface. The ion energy dependence was found to scale linearly with  $(E_{\text{ion}}^{1/2} - E_{\text{th}}^{1/2})$ , where  $E_{\text{th}}$  is the threshold energy. The derived surface chlorination coefficient,  $s$ , also scales with the square root of ion energy. As we discussed in chapter 3, this suggests that high energy ions create more dangling bonds or adsorption sites for the subsequent surface chlorination. This model represents the data shown in Figure 5.5 and Figure 5.8 quantitatively well at flux ratios above 5. Slight deviation from the experimental results is observed at flux ratios

less than 5 because of the simplification of the model and the negligence of the formation of unsaturated silicon chlorides ( $\text{SiCl}_x$ ) at low flux ratios. The MD simulation results of  $\text{Cl}^+$  etching silicon reported by Barone et. al. [Barone, 1995] and Hanson et. al. [Hanson, 1997] suggest that the formation of  $\text{SiCl}_x$  ( $x < 4$ ) is enhanced as the ion energy increases. This is consistent with the lower degree of surface chlorination, as  $\text{Cl}^+$  is the only source contributed to the surface chlorination. Revision of the model is needed as the products distribution of low energy  $\text{Cl}^+$  ion-enhanced etching with Cl is better characterized, at all flux ratios.

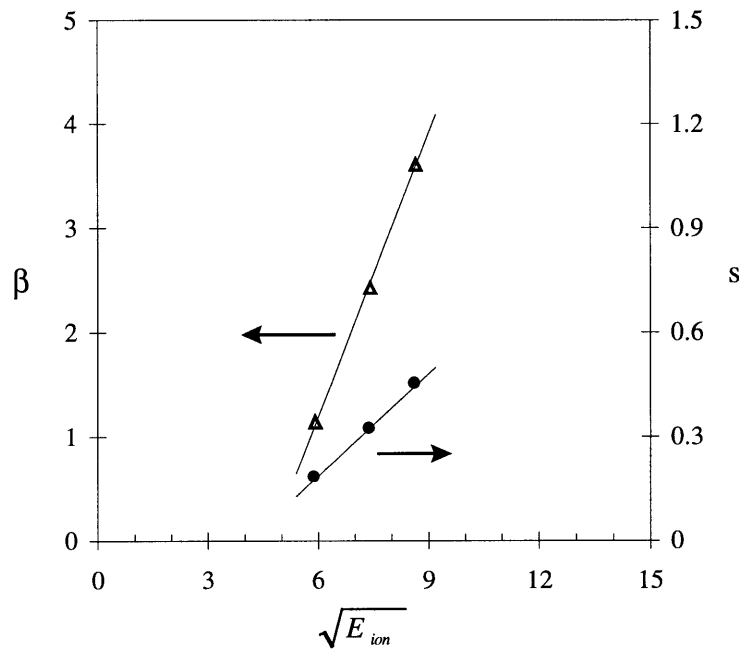
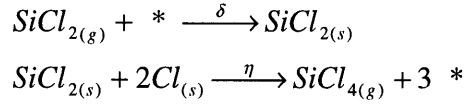


Figure 5.13: Fitted parameters  $\beta$  and  $s$  versus  $E_{ion}^{1/2}$  for  $\text{Cl}^+/\text{Cl}$  etching of polysilicon.

Equation (5.2) is a complete form of a kinetic model that accounts for the energy, flux and angular dependencies of  $\text{Cl}^+$  ion-enhanced polysilicon etching with chlorine. The two parameters,  $\beta$  and  $s$ , of the model scale linearly with the square root of ion energy and are incorporated into a profile simulator to predict feature evolution in high-density plasma etching processes.

To model the suppression in polysilicon etching yield by  $\text{SiCl}_2$  deposition, the following two reactions are taken into account:



SiCl<sub>2</sub> is assumed to compete with Cl for the reactive sites on the surface and consume surface chlorine to form volatile etching products, SiCl<sub>4</sub>. Due to the limited experimental data, we assume the sticking coefficient of SiCl<sub>2</sub> is a constant,  $\delta = 0.3$ , and all the parameters previously derived for Cl<sup>+</sup>/Cl/Si etching system is still valid. Therefore, the extent of surface chlorination can be rewrite as the following equation, and with R' represents the SiCl<sub>2</sub> to Cl<sup>+</sup> flux ratio.

$$\theta = \frac{s \cdot R + c(\phi) + \delta \cdot R'}{s \cdot R + c(\phi) + 4 \cdot c(\phi) \cdot \beta + \delta \cdot R' + 3 \cdot \eta \cdot \delta \cdot R'} \quad (5.6)$$

At a Cl-to-Cl<sup>+</sup> flux ratio of 200, the suppression of the polysilicon etching yield can be fitted by setting  $\eta = 10$ , as shown in Figure 5.14. This value is much greater than the value of  $\beta$  that describes the etching of silicon, suggesting that etching of partially chlorinated silicon (SiCl<sub>2</sub>) to form SiCl<sub>4</sub> has a higher reaction probability.

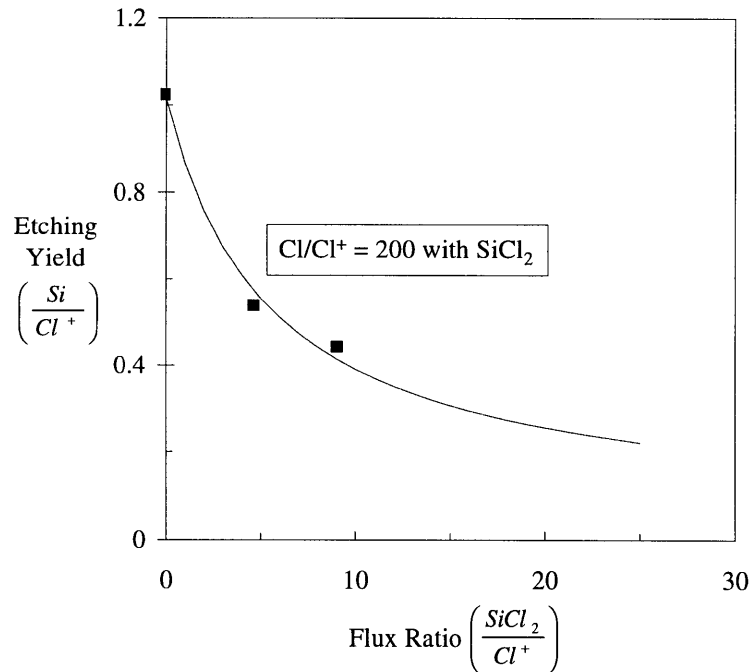


Figure 5.14: Model prediction of the suppression of polysilicon etching yield with simultaneous deposition of SiCl<sub>2</sub>.



## Chapter 6

### Etching of Patterned Polysilicon Samples

Patterned polysilicon samples were etched in the beam apparatus to generate test structures for testing the kinetic model and the profile simulator. The patterned samples consist of alternating lines and spaces, i.e. rectangular trenches with various line widths ( $0.35, 0.5 \mu\text{m}$ ) and spacings, as shown in Figure 6.1. An ionic beam ( $\text{Cl}^+$  or  $\text{Ar}^+$ ) and a neutral beam ( $\text{Cl}$ ) were operated at various flux ratios to etch these samples. Changing the ion energy and the neutral-to-ion flux ratio allowed us to assess the effects of ion bombardment and chlorination by neutral species, and verify the kinetic model we formulated.

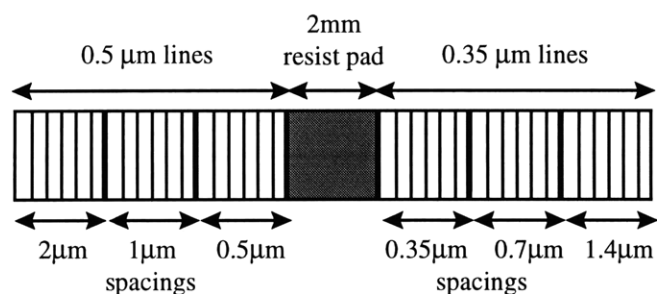


Figure 6.1: Layout of the patterned samples.

The alignment of patterned samples in the beam apparatus was varied so that the ionic and atomic fluxes to the trench features are varied to investigate the importance of transport of reactive species within the feature. The patterned lines were either parallel or perpendicular to the beam plane, as shown in Figure 6.2. The ionic beam ( $\text{Cl}^+$  or  $\text{Ar}^+$ ) impinged normally on the patterned sample, while the atomic chlorine beam impinged upon the pattern sample at an angle of  $45^\circ$ . When the patterned lines were parallel to the beam plane, uniform incident ionic and atomic fluxes were obtained at the bottom of the feature since the photoresist did not shadow the atomic beam flux. We termed this alignment “un-shadowed” orientation. However, when the patterned lines were perpendicular to the beam plane, the photoresist “blocked” the  $\text{Cl}$  beam flux from

reaching part or all of the feature bottom, and we termed this alignment “shadowed” orientation.

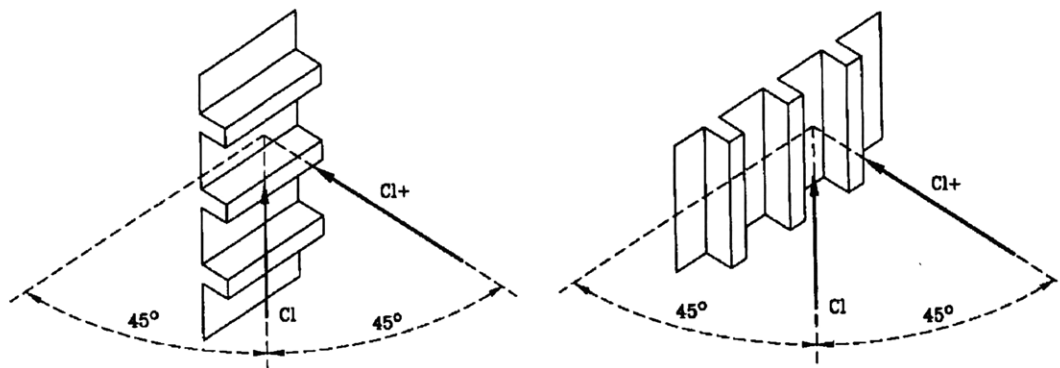


Figure 6.2: Orientation of the patterned samples with respect to the beam plane. (a) The photoresist lines were parallel to the beam plane: un-shadowed orientation (b) The photoresist lines were perpendicular to the beam plane: shadowed orientation.

The initial profiles of the photoresist-patterned polysilicon with two different initial aspect ratios, the ratios of the feature width to depth, are shown in Figure 6.3. Slight faceting is observed at the top of the photoresist.

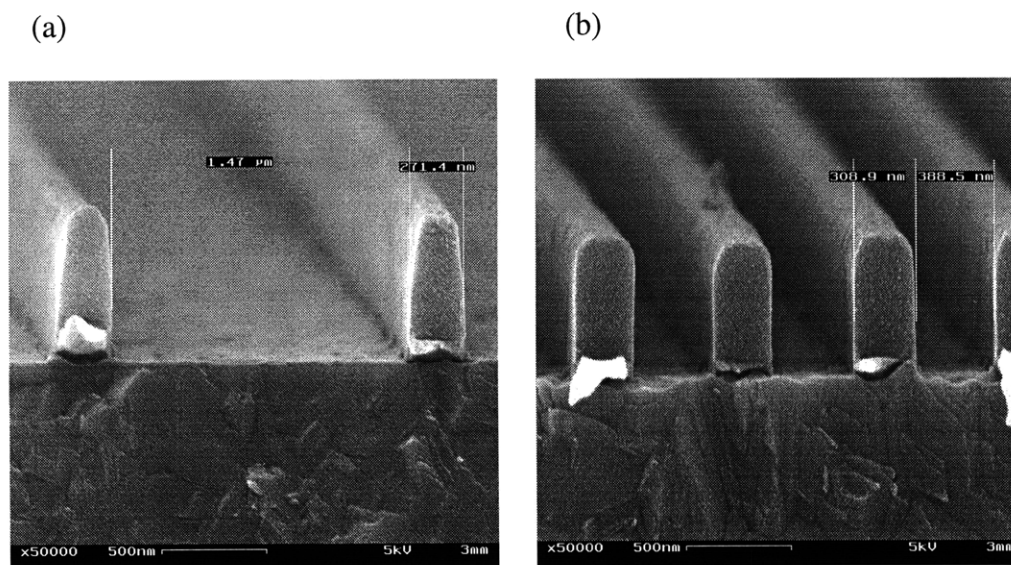


Figure 6.3: Initial profile of the photoresist patterned polysilicon: (a) 0.35 μm lines and 1.4 μm spacings. (b) 0.35 μm lines and 0.35 μm spacings. Approximately 5000Å thick photoresist was used to pattern ~5000 Å thick polysilicon over 1000 Å thermal oxide.

## 6.1 Argon Ion-enhanced Etching of Photoresist Masked Polysilicon

### 6.1.1 $Ar^+$ and $Cl$ etching of photoresist masked polysilicon

In order to maintain high etching rates, 95 eV  $Ar^+$  ions were used to etch photoresist masked polysilicon samples. The flux ratio was controlled at around 100. Poor selectivity was observed between etching of polysilicon and photoresist. Faceting of the photoresist is observed as a consequence of ion sputtering and/or ion-enhanced etching. Cross sectional view of the etched profile obtained in the unshadowed orientation, prior to the end-point, is shown Figure 6.4. Due to the slight dispersion of ions, off-normal ions scattered from the sidewall bombarded the bottom of the feature to cause trenching in polysilicon and the sidewall was slightly tapered. The polysilicon surface at the bottom of the feature was roughened, due to micromasking of the polysilicon by deposition of the sputtered and/or etched photoresist. “Grass” was only observed in the beam studies when photoresist was present on the sample.

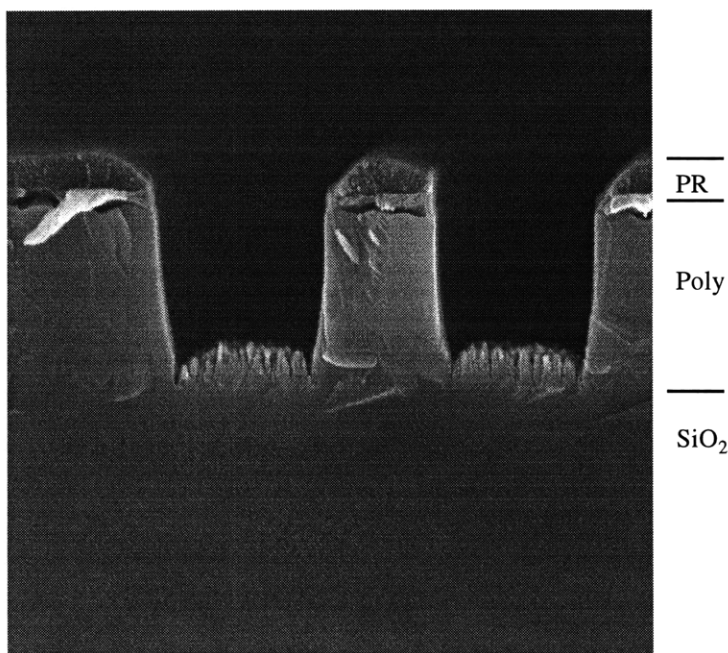


Figure 6.4: Cross section of photoresist patterned polysilicon etched by 95 eV  $Ar^+$  and  $Cl$  in the unshadowed orientation. Poor selectivity is observed for etching polysilicon over photoresist at this energy level. Trenching in polysilicon is observed.

As the etching proceeded, directional/anisotropic etching of the sidewall was achieved after ~15% overetch as shown in Figure 6.5. The etching selectivity between polysilicon and photoresist at this energy level is approximately 1.5. Some degree of notching at the polysilicon/oxide interface is thought to be an artifact of stress-induced spontaneous etching at the polysilicon-oxide interface. This phenomenon was explored later in this chapter by etching some patterned samples under various applied mechanical stresses.

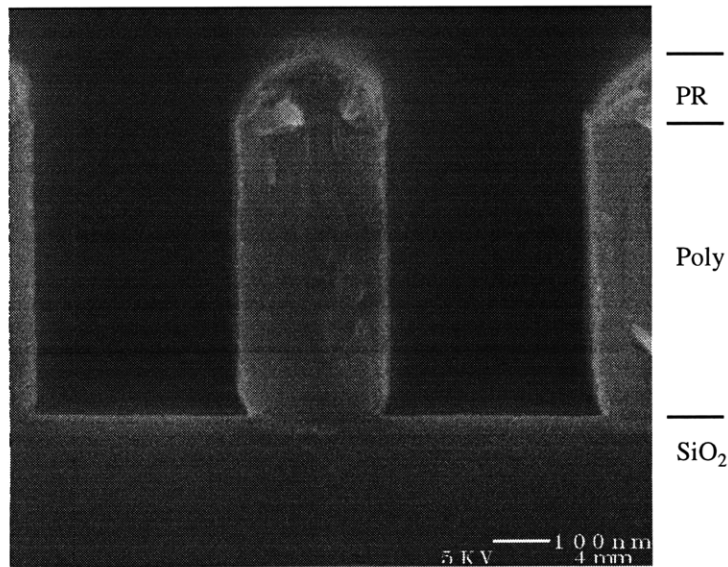


Figure 6.5: Cross section of photoresist patterned polysilicon etched by 95 eV  $\text{Ar}^+$  and Cl in the unshadowed orientation. Selectivity of approximately 1.5 between etching of polysilicon and photoresist is achieved at this energy level. Approximately 15% overetch was performed. Some degree of notching is observed at the poly/oxide interface.

### ***6.1.2 $\text{Ar}^+$ and Cl etching of mechanically stressed, patterned polysilicon***

Notching has long been attributed to the electric-field-induced ion trajectory distortion and the subsequent etching of polysilicon by these ions [Arnold, 1991] [Hwang, 1997] [Kinoshita, 1996]. The large local charging potential at the silicon dioxide surface is caused by the difference in the directionality of ions and electrons; i.e. isotropic electrons charge the photoresist negatively and the directional ions charge the underlying oxide positively during overetch. The potential necessary to deflect low

energy ions (<45eV) to form notches is ~500V/μm (5V/100Å) on an oxide surface [Hwang, 1997]. However, the magnitude of this field is within a factor of two to the breakdown voltage for bulk oxide [Sze, 1981], ~1000V/μm. Such a large field is likely to cause leakage along the surface, reducing the field and thereby preventing the deflection of ions to the extent needed to form notches. Even through bulk oxide, Baglee [Baglee, 1984] reported that bulk leakage became significant for 100Å oxide above applied voltage of 5V. Moreover, ion, electron, and UV photon bombardments from the plasma will excite electronic states, thereby enhancing the oxide leakage and further reducing the fields within the feature and the associated ion deflection.

We proposed that stress at the polysilicon/oxide interface enhances spontaneous etching of polysilicon by reactive neutrals and leads to the notch formation. Non-uniform stress fields are observed within the patterned lines and large localized stresses are induced at the interface, especially the corner adjacent to the substrate [Shen, 1996].

The total stress,  $\sigma_{total}$ , in a film consists of intrinsic, thermal and external stresses, as shown in the following equations:

$$\sigma_{total} = \sigma_{intrinsic} + \sigma_{thermal} + \sigma_{external} \quad (6.1)$$

$$\sigma_{intrinsic} = f(t, R_{dep}, T_{dep}, \dots)$$

$$\sigma_{thermal} = (\alpha_{film} - \alpha_{substrate})(\Delta T)E_{film}$$

$$\sigma_{external} = \text{another film, mechanical stress } \dots$$

where:  $t$  represents the film thickness;  $R_{dep}$  and  $T_{dep}$  are deposition rate and temperature;  $\alpha_{film}$  and  $\alpha_{substrate}$  are thermal expansion coefficients of the film and the substrate respectively;  $\Delta T$  represents the temperature difference between the deposition temperature and the temperature of measurement; and  $E_{film}$  is the Young's modulus of the film. The intrinsic stress results from the structure of the film, and is a function of film thickness, deposition rate, and deposition temperature. The thermal stress is due to the thermal mismatch (different thermal expansion coefficient) between the deposit film and the substrate. The external stress results from the presence of another film or bending of a sample.

To unambiguously change the stress in a film without any other modification of the thin, we employed a three-point bending of the film to introduce mechanical stress to the film. This technique allows us to change the film stress while maintain the intrinsic and thermal stresses within the film constant. The setup of the sample bending is shown in Figure 6.6.

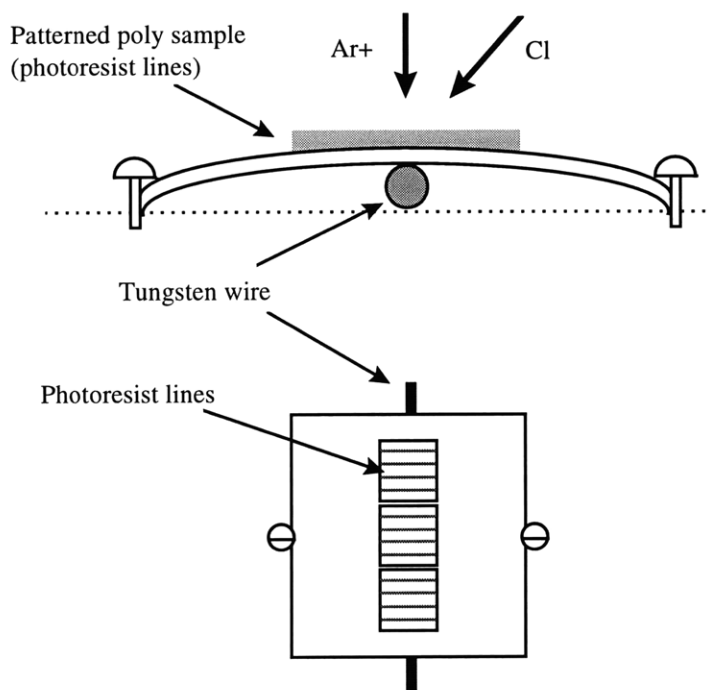


Figure 6.6: Setup of three-point bending of a patterned polysilicon sample. A 0.008” thick tungsten wire was placed underneath the 0.030” thick patterned polysilicon sample, perpendicular to the patterned lines. Two stainless steel screws were used to fasten the sample edges against the sample holder to introduce mechanical stress to the surface thin films. Samples from the same wafer were also etched without the wire being present

Patterned samples were cut from the same 6” wafer, and metal wires with thickness ranges from 0.001” to 0.008” were placed underneath the 0.030” thick patterned polysilicon samples, perpendicular to the patterned lines. Two stainless steel screws were used to tighten the sample edges against the sample holder. The curvature of the samples is determined by measuring the intensity variation of a laser beam originating from a fixed source and deflecting from the surface of the sample (Tencor FLX-2320 thin film stress measurement tool). The curvature of a film allows us to determine the stress caused by deposition or mechanical bending. Chen et. al. [Chen, 1994] suggested that the

bending stress of a wafer can be described by the linear deflection theory for deflections less than one-fifth of the wafer thickness in that the stress is increased linearly with increasing deflection. The imposed mechanical stress determined from the curvature of the sample is 35 MPa, which is one order of magnitude higher than that of a typical polysilicon film without mechanical bending. Note the ultimate yield stress of silicon is 45 MPa.

The samples were then etched in the beam system by 90eV Ar<sup>+</sup> and Cl with approximately 15% overetch, and the etched profiles of patterned polysilicon samples with and without the imposed mechanical stress are shown for comparison in Figure 6.7. The degree of notching is enhanced by the imposed mechanical stress, indicating that stress can enhance spontaneous etching of polysilicon by atomic chlorine. The overetch time used in these experiments was much smaller (15%) than that reported for notch formation (200%) in a commercial ECR plasma reactor [Nozawa, 1995] where notching of comparable extents were observed. The greater notching rate of our experiments demonstrates that notching is accelerated by greater stress. However, slight notching is observed without the applied mechanical stress indicating that these patterned polysilicon samples prepared by Sematech have sufficient stress that notching would occur with extensive overetching.

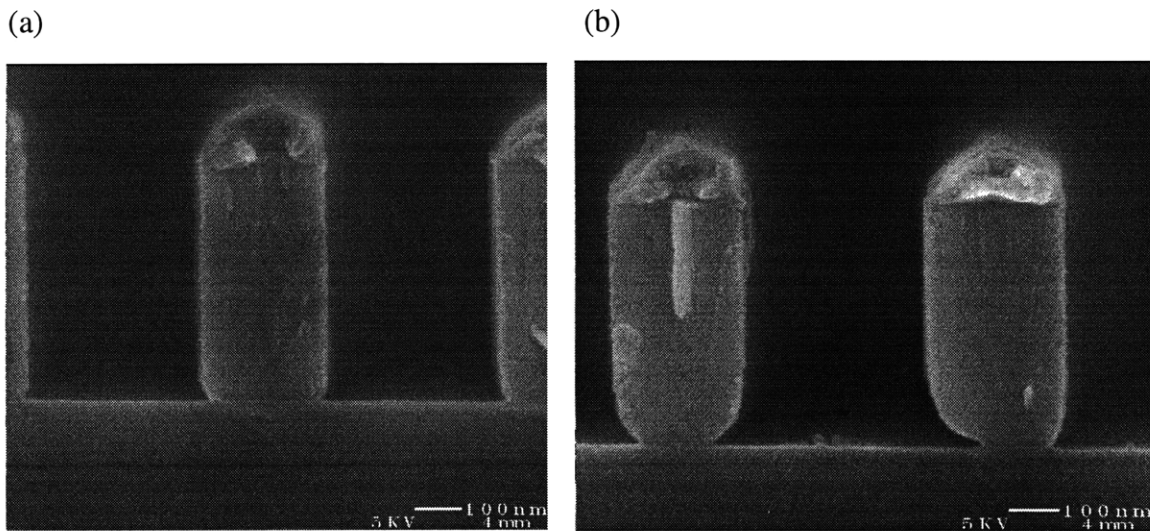


Figure 6.7: Cross sections of photoresist patterned polysilicon etched by 90 eV Ar<sup>+</sup> and Cl. (a) The sample is etched without mechanical bending/stress. (b) The sample is

etched with mechanical bending/stress. Both samples were taken from the same 6" wafer.

The pronounced notching formation in etching polysilicon under mechanical stress strongly suggests that the notching formation is greatly affected by the stress, as charging and ion trajectory distortion are not significant in the beam system. The beam experiments reported in this work use a highly collimated ( $<2^\circ$ ) ion beam with an energy distribution of  $<15$  eV FWHM with electron temperatures expected to be less than 1 eV. The fields necessary to deflect the ions under these conditions are  $\sim 1000\text{V}/\mu\text{m}$ , i.e. equal to that necessary for bulk oxide breakdown. Notching is observed with 15% overetching even without additional applied mechanical stress of the sample. Moreover, notching has been shown to be affected by the mechanical mounting stress under the same etching conditions.

Stress may enhance the spontaneous etching by reducing the energy barrier for Cl to penetrate into the silicon lattice and attack the underlying Si-Si bonds. Spontaneous etching of polysilicon by reactive neutrals have been observed under conditions where: (1) polysilicon is  $n^+$  doped [Ogryzlo, 1990], (2) polysilicon is locally radiated by visible laser light [Houle, 1983]. In these cases spontaneous etching has been attributed to the increased penetration of halogen atoms into the polysilicon substrate. The elongation of Si-Si chemical bonds by stress should reduce the energy barrier for Cl penetration into the silicon lattice and allow spontaneous etching to occur at room temperature. Greater notching with increased polysilicon conductivity ( $n^+$  doping) has been reported [Chi, 1996], in agreement with the proposed mechanism.

The correlation between charging and notching may be caused by modest feature charging in which ions are deflected, and remove the sidewall passivation at the polysilicon/oxide interface, thereby allowing the atomic chlorine to spontaneously etch the polysilicon, as shown in Figure 6.8. Sidewall passivation is originated from sputtering deposition of the photoresist, redeposition of the etching product and/or by-products, and is commonly observed in high-density plasma etching systems. Highly



directional etched profiles can thus be achieved by balancing the etching with deposition, as shown in Figure 6.8(a). During the overetch step, the potential buildup at the oxide surface deflects low energy ions towards the foot of polysilicon lines to remove the sidewall passivation, as shown in Figure 6.8(b). The un-protected, stressed polysilicon is spontaneously etched by atomic chlorine, as shown in Figure 6.8(c).

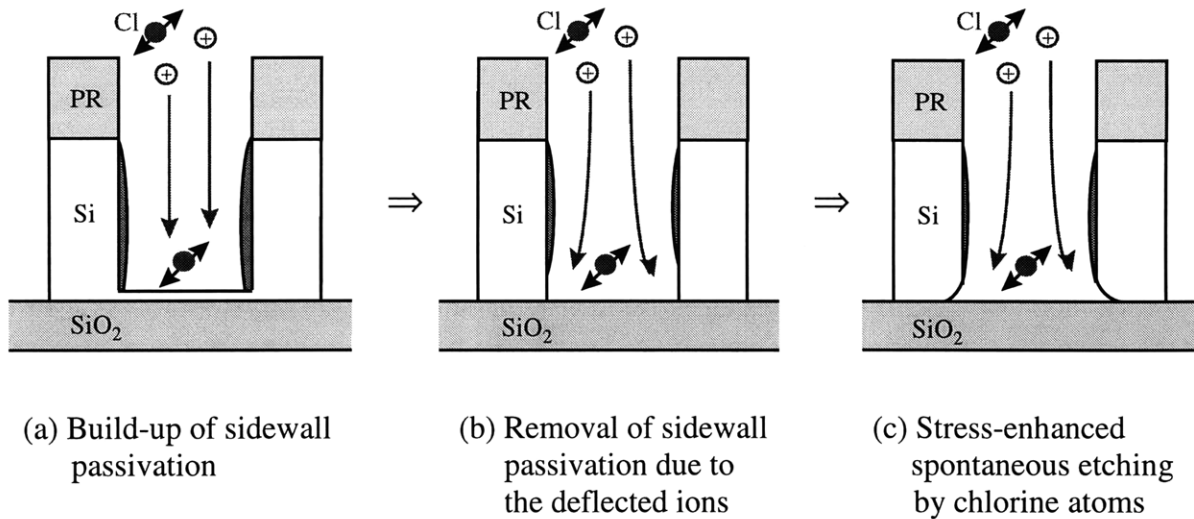


Figure 6.8: Illustration of the notching formation as a combination of ion deflection by feature charging, removal of sidewall passivation, and spontaneous etching of the stressed polysilicon by chlorine atoms. (a) Sidewall passivation originates from deposition and/or redeposition of the etching products, during chlorine etching of polysilicon. (b) Sidewall passivation at the foot of the polysilicon lines are removed during the overetch step due to ions deflected by charging. (c) After the sidewall passivation is removed, atomic chlorine spontaneously etches the stressed polysilicon and results in notching formation.

Therefore, stress induced etching is important in notch formation, but is aided by charge induced ion deflection. Since charging is not solely responsible for the notch formation, notching can be eliminated or reduced by conditions that favor greater sidewall passivation. Increased sidewall passivation has been demonstrated to prevent the notching formation [Maruyama, 1997] [Tabara, 1996]. Another approach is to reduce the stress of the polysilicon film by annealing or varying the polysilicon deposition conditions.

## 6.2 Chlorine Ion-enhanced Etching of Photoresist Masked Polysilicon

### 6.2.1 $\text{Cl}^+$ etching of photoresist masked polysilicon

$\text{Cl}^+$  ions are used to etch patterned polysilicon samples and the ion energy is varied to study its effect on the etching selectivity. At 35 eV,  $\text{Cl}^+$  achieves relatively anisotropic etching of polysilicon with great etching selectivity, as shown in Figure 6.9. No trenching in the polysilicon is observed. Trenching has been attributed to higher ion concentration at the corners of the feature, resulting from off-normal ion scattering from the sidewalls. The absence of trenching suggests that the off-normal, low energy ions (35eV) lost a portion of their energies upon striking the sidewall, and failed to etch polysilicon sufficiently after scattering as their remaining energies fell below or closer to the threshold energy. Molecular dynamic simulation [Hanson, 1997] of  $\text{Cl}^+$  etching of polysilicon has indicated that low energy ions scattered from the polysilicon surface non-specularly; i.e., some ions lost a portion of their energy and the deflected angle is not identical to the incident angle.

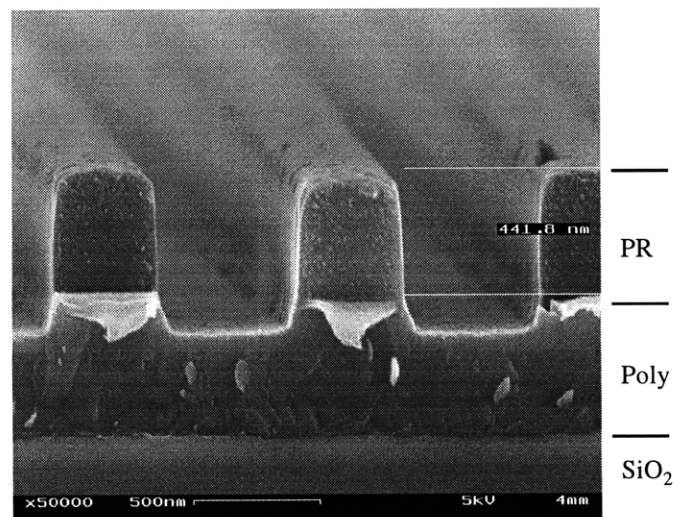


Figure 6.9: Cross section of photoresist patterned polysilicon etched by 35 eV  $\text{Cl}^+$  in the unshadowed orientation. The line width and the spacing between lines are 0.5  $\mu\text{m}$ . Good selectivity is observed between etching of polysilicon and photoresist at this energy level, and no trenching in the polysilicon is observed.

At a high ion energy level, 85 eV, poor selectivity was observed and the photoresist lines were faceted at a 30° angle, as shown Figure 6.10. The sidewall of the feature is tapered, and no trenching is observed. These observations can possibly be explained by the deposition of sputtered photoresist (mainly carbonaceous species) which prohibits the etching of polysilicon, and causes the sidewall to taper.

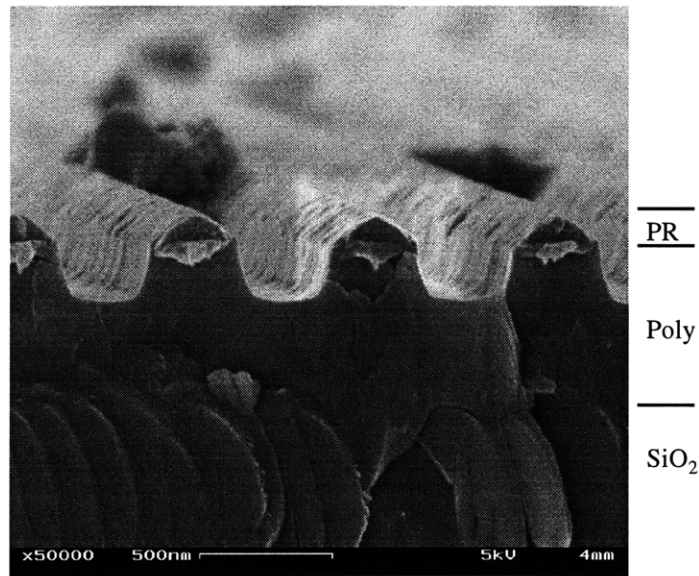


Figure 6.10: Cross section of photoresist patterned polysilicon etched by 85 eV  $\text{Cl}^+$  in the unshadowed orientation. The line width and spacing between lines are 0.35  $\mu\text{m}$ . Poor selectivity is observed between etching of polysilicon and photoresist at this energy level.

### 6.2.2 $\text{Cl}^+$ and Cl etching of photoresist masked polysilicon

Anisotropic etching profiles were observed when samples were etched by a 35 eV  $\text{Cl}^+$  beam and a Cl beam in the unshadowed orientation. Figure 6.11 shows an etched profile prior to the end point. Slight trenching was observed with relatively straight sidewalls. The degree of trenching is reduced comparing to the trenches observed in Figure 6.4 (by 90 eV  $\text{Ar}^+$  and Cl) is again attributed to non-specular scattering of the low energy ions from the sidewall into the bottom of the feature. Good selectivity for etching of polysilicon over photoresist, approximately 6, was achieved.

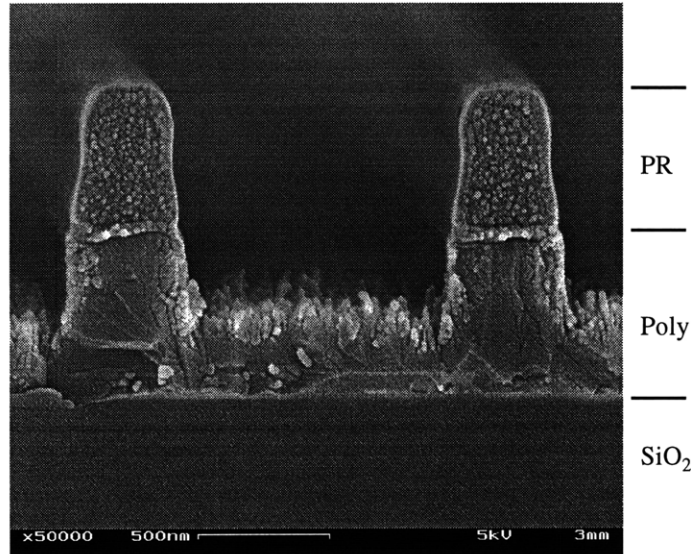


Figure 6.11: Cross section of photoresist patterned polysilicon etched by 35 eV  $\text{Cl}^+$  and Cl in the unshadowed orientation. The line width and spacing between lines are 0.5 and 1.0  $\mu\text{m}$ , respectively. Good selectivity is observed between etching of polysilicon and photoresist at this energy level. Slight trenching is observed.

As etching proceeded, an anisotropic etching profile was observed with ~20 % overetch after etching through the polysilicon film to the underlying oxide film, as shown in Figure 6.12. Slight undercutting of the sidewall indicated no sidewall passivation. This is consistent with good etching selectivity of polysilicon over photoresist at this low energy level. Sidewall passivation is typically observed when carbonaceous products from etching of the photoresist or silicon bearing by-products deposit on the sidewalls. Our observation of a slight undercutting and no apparent sidewall passivation is consistent with the good photoresist integrity and lack of by-product deposition in the beam apparatus.

In the shadowed orientation, ions were directed normal to the sample while the neutrals were directed to the sample at an angle of  $45^\circ$ , as depicted in Figure 6.13. Approximately 15 % overetch was performed. Since atomic chlorine flux is blocked to some extent due to the presence of the photoresist lines, the etched profiles in this configuration would allow us to determine the importance of atomic chlorine species in defining the profile evolution.

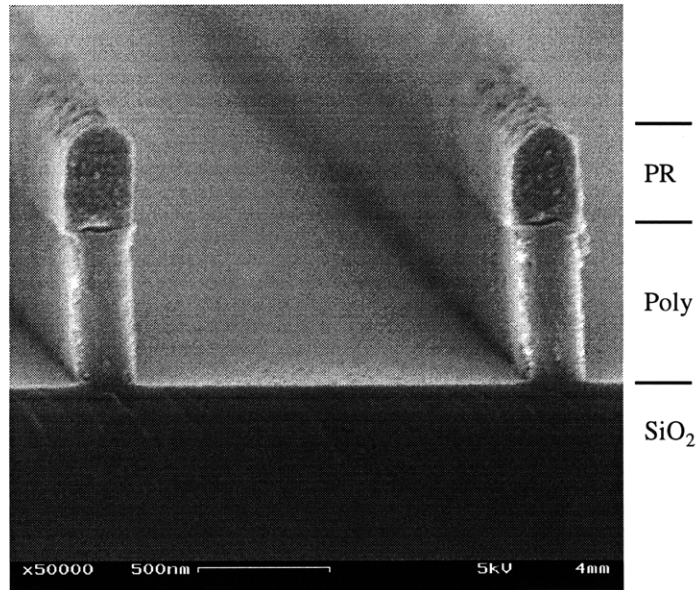


Figure 6.12: Cross section of photoresist patterned polysilicon etched by 35 eV  $\text{Cl}^+$  and  $\text{Cl}$  in the unshadowed orientation. The line width and spacing between lines are 0.35 and 1.4  $\mu\text{m}$ , respectively.

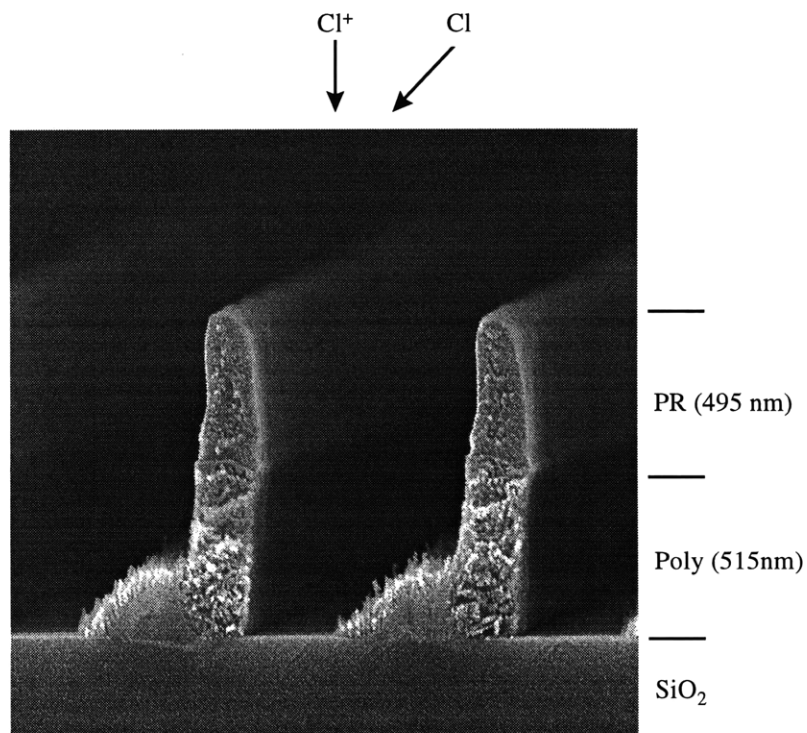


Figure 6.13: Cross section of photoresist patterned polysilicon etched by 35 eV  $\text{Cl}^+$  and  $\text{Cl}$  in the shadowed orientation. The line width and spacing between lines are 0.35 and 0.70  $\mu\text{m}$ , respectively.

A directional etched sidewall was observed at the left side of the trench where sufficient  $\text{Cl}^+$  and  $\text{Cl}$  fluxes induced anisotropic etching of the polysilicon. The reduced  $\text{Cl}$  flux on the right side of the trench due to the presence of photoresist caused a slower etching rate resulting in unetched polysilicon. The etching rate on the right was too large to be caused by  $\text{Cl}^+$  flux alone (the sputtering yield of polysilicon by  $\text{Cl}^+$  at 35 eV was one order of magnitude less than the ion-enhanced etching yield). We believe that the observed etching rate at the right side of the feature is a combination of  $\text{Cl}^+$  sputtering and  $\text{Cl}^+$  ion-enhanced etching with  $\text{Cl}$  atoms scattered from the left sidewall. In our simulation, the recombination/scattering probability of  $\text{Cl}$  atoms on the photoresist was explored to fit the profiles. There were some “grassy” structures on the remained polysilicon, which were attributed to the micromasking of the polysilicon by deposition of sputtered and/or etched photoresist materials. Since the sputtering or etching rate of the carbonaceous species is slower than that of polysilicon, preferential etching of polysilicon occurred about the deposited material, and the grassy structures are formed. This effect is similar to the micromasking effect we observed on a planar polysilicon sample after ion bombardment (Figure 5.3).

## Chapter 7

### Quantitative Modeling of the Feature Profile Evolution

As feature dimensions shrink to below 0.25  $\mu\text{m}$ , the substrate size increases to 300 mm, and development cycles shorten, the development in plasma etching processes becomes time and capital intensive and more difficult. Profile control and critical dimension control become increasingly important as they determine the success of subsequent deposition process and ultimately the device performance. Prediction of the feature profile evolution is therefore of great value, as it reduces the time and cost associated with trial-and-error process development and/or equipment design. A systematic approach to link the tool scale simulation to the feature scale simulation is also economically viable and technologically challenging.

In this work, we initiate the development of a general and predictive model based on the critical reaction coefficients measured by beam scattering experiments. Definitive characterization of the effects affecting etching rates of polysilicon, silicon dioxide and photoresist sheds lights on accurate modeling of the feature profile evolution. The ultimate goal of this simulation effort is threefold: (1) elucidate the origins of etching peculiarities such as bowing, tapering, undercutting, trenching, micro-trenching and notching, (2) suggest process recipes leading to perfect etching anisotropy based on our fundamental understanding of the causalities of etching peculiarities, and (3) facilitate predictive process modeling, and aid the next generation equipment design and process development.

A Direct Simulation Monte Carlo (DSMC) simulator was developed to simulate the profile evolution observed in the beam apparatus and also the profiles measured in high-density plasma reactors. This simulator is constructed based upon the kinetic models we developed utilizing beam experiments. All the dominant physical and chemical mechanisms of the etching process such as sputtering, angular dependent ion-enhanced etching, spontaneous etching, ion scattering, surface recombination and deposition and

redeposition of etching by-products were incorporated. A generalized chemistry model is proposed and is incorporated in the simulator to account for etching of mixed compositions.

## 7.1 Factors Affecting Feature Profile Evolution

The feature profile evolution of patterned polysilicon is affected by all the species in a chlorine plasma, to various extents. Figure 7.1 illustrates the factors affecting feature profile evolution of patterned polysilicon in a chlorine plasma.

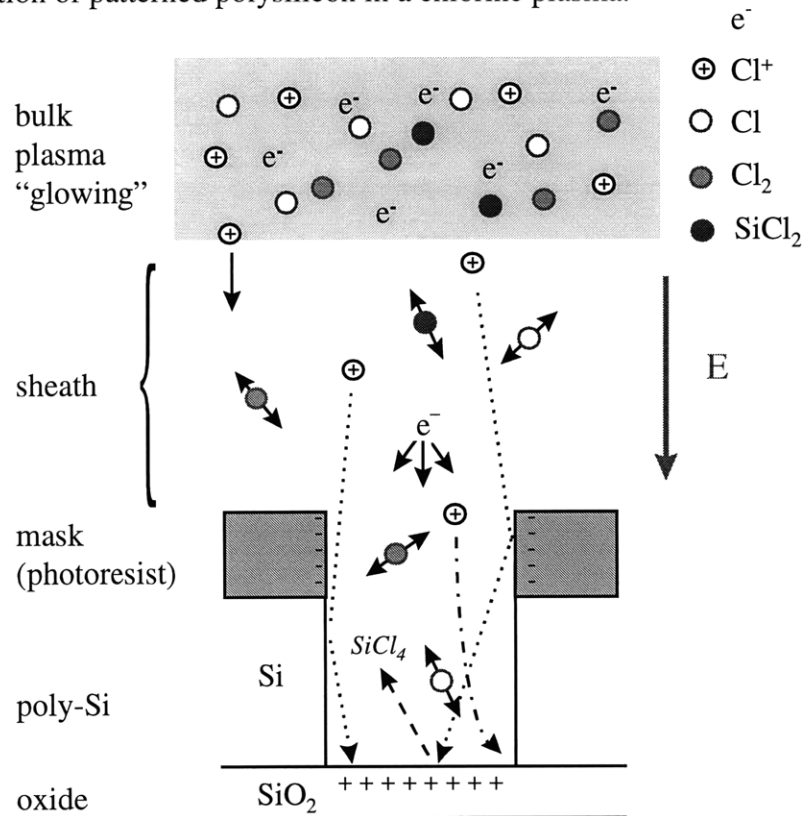


Figure 7.1: Schematic diagram illustrating the factors affecting the feature profile evolution of patterned polysilicon in a chlorine plasma:

- (a) Transport of reactive species into the feature:
- Ion scattering from the photoresist
  - Ion scattering from the sidewall
  - Ion trajectory deflection due to surface charging
  - Neutrals diffusion into the feature, neutral shadowing
- (b) Surface kinetics:
- Angular dependence of ion-enhanced etching
  - Product (re-)deposition



The transport of reactive species, including ions, electrons and neutrals, into the feature enables the etching and/or deposition reactions within the feature. Ion trajectory can be altered upon scattering from the sidewall of the feature, or by the electrical field within the feature (typically during the overetch step). Neutrals diffuse into the feature and undergo collisions with surfaces depending upon their sticking probabilities. As the aspect ratio of the feature increases, shadowing of neutral etchants and inhibitors can significantly change the etching and/or deposition rate within the feature and result in aspect ratio dependent etching (ARDE). The shadowing of electrons and charging of the silicon dioxide surface can form an electrical field that deflects ions towards the sidewall of a feature. All these phenomena are highly coupled and have to be modeled properly to predict the feature profile evolution.

Etching of photoresist and silicon dioxide has to be taken into account as only finite etching selectivity of photoresist and silicon dioxide can be achieved. Surface reactions occurred during plasma etching include: sputtering, ion-enhanced angular dependent etching, spontaneous etching, (re-)deposition, and recombination. These kinetic reactions govern the surface composition and the profile evolution. Understanding the competition between these reactions and/or balance among these reactions would aid in control of the etched profiles and reduction of the aspect ratio dependent etching (ARDE).

## **7.2 Direct Simulation Monte Carlo Method**

Direct Simulation Monte Carlo (DSMC) methodology was implemented to simulate the profile evolution in plasma etching. DSMC methodology allows simulation of gas phase transport and gas-surface interaction by modeling a gas flow with a finite number of particles. Each particle represents a large number of the real molecules and is sampled from representative distributions. The velocity and position components of the particles in a Cartesian coordinate (in this work) are tracked, and updated as the particles undergo collisions or boundary interactions. For simplification, a two-dimensional

simulation is developed; however, the third velocity component is always stored, as the collision has to be calculated as a three-dimensional phenomenon to properly determine the incident and reflected angles in a scattering event. The flow field (simulation domain), consisting of gas phase and various materials to be etched, is divided into a network of cells [Bird, 1976]. Each solid cell contains a finite number of particles that represent the materials to be etched. The dimension of the cell has to be small, typically some fraction of the mean free path, such that the change in flow properties across each cell is small.

To properly simulate the physics of the gas flow and surface kinetics, the number of simulated particles, the size of the cell, the number of particles in each cell, and the step size of the particle movement must be properly determined. With DSMC method, the particles are typically moved in step sizes smaller than the mean free path  $\lambda$ , the average distance a molecule travels between collisions, to uncouple the molecular motion and gas-phase or gas-surface collisions. The simulated domain is discretized into a network of cells with dimensions smaller than the mean free path. In this work, we chose the cell dimension (as unit length) to be 25-50 Å, as this corresponds to the chlorination depth induced by ion bombardment and homogeneous composition can be assumed in surface cells within this length scale.

The DSMC technique is robust, accurate, and free of convergence problems; however, long simulation time is expected. For the purpose of validation of the kinetic models and accurate prediction of the feature profile evolution, DSMC technique offers advantages over other simulation techniques.

## **7.3 DSMC Model Description**

### ***7.3.1 Simulation domain***

The simulation domain spanned between the centerlines of two adjacent photoresist lines that define the trench to be etched, as shown in Figure 7.2. A two-

dimensional simulation code was developed, and the structure illustrated in Figure 7.2 represents a rectangular trench with infinite length in the z direction (perpendicular to the simulation domain). Periodic boundary conditions were employed at the centerlines of the photoresist to simulate a structure with alternating lines and spaces. The domain was discretized into square cells with 25 to 50 Å sides, a dimension comparable to the surface chlorination layer depth induced by ion bombardment during etching processes. Therefore, the cells were regarded as continuous stirred tank reactors (CSTRs) in which homogeneous chemical contents were assumed. This assumption enables the calculation of surface compositions that determine the subsequent surface reactions. Each cell had a memory structure in which cell-specific information (e.g. the concentration of various species) is stored. The resulting array of such structures was the primary consumption of computer memory resources. A typical simulation required approximately 12 Mbytes of memory.

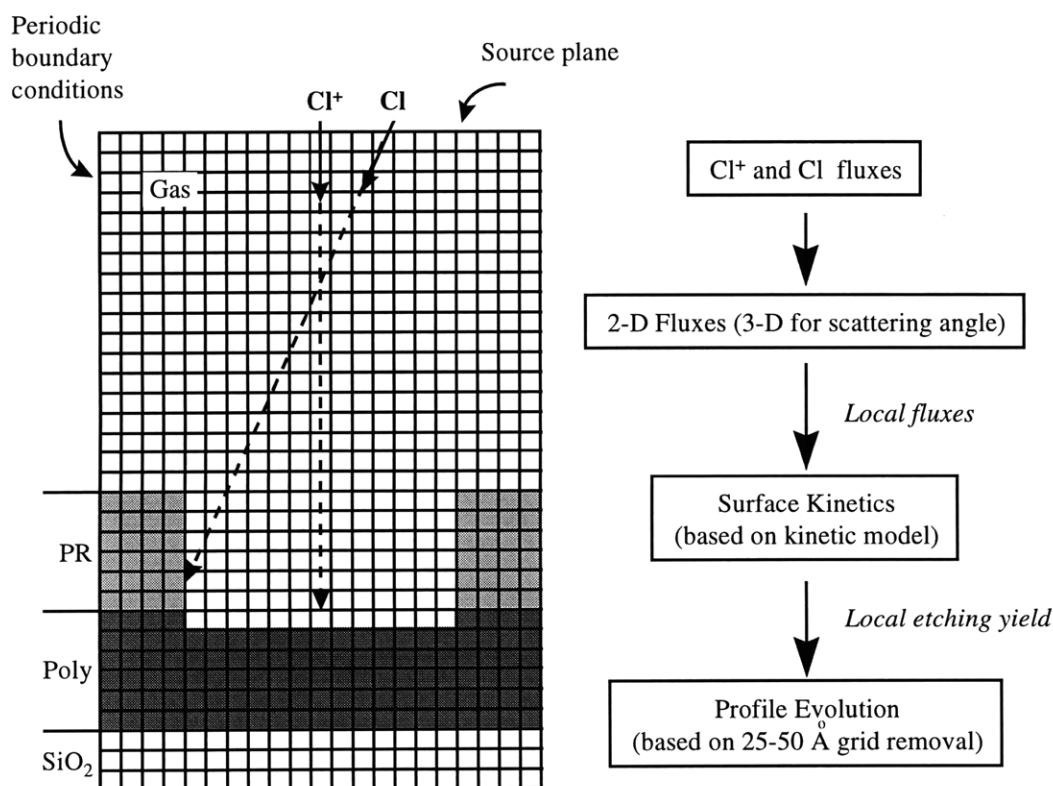


Figure 7.2: Schematic diagram of the simulation domain. The 2-D simulation domain spanned between the centerlines of two adjacent photoresist lines, and was discretized into square cells with 25-50 Å sides. A source plane was assigned at distance of much

less than a mean-free path above the feature from which the ionic and atomic chlorine fluxes emanated and passed into the feature without gas-phase collisions. Lateral periodic boundary conditions were employed.

A source plane was assigned at a distance much less than a mean-free path above the feature from which the ionic and atomic chlorine fluxes originated and passed into the feature. The chlorine ions and particles were sampled from proper angular and energy distributions. Acceptance-rejection criteria were used to sample representative particles from prescribed distributions. The initial x position of each particles was determined based on a random number generation. Each particle was followed from its origin with unit length steps till it encountered a surface cell. The particle moved in a straight line as gas phase collision and surface charging effects were ignored. A particle crossing the boundary was introduced into the simulation domain from the other boundary (periodical boundary condition), and crossing the source plane from below was eliminated from the simulation.

### ***7.3.2 Surface interactions***

The DSMC algorithm allows us to incorporate the dominant physics and chemistry of the plasma etching process easily by using kinetically based probabilities for each surface process and performing an elemental balance in a surface cell each time it interacted with a reactant particle. A few important aspects incorporated in the profile simulator are detailed here.

#### **(1) Scattering Mechanism:**

A particle that did not react with the surface was scattered. To properly determine the scattering angle, the surface normal was determined by least square fitting of five adjacent surface cells on either side about and including the cell of impact. In a scattering event, a neutral particle scattered non-specularly, *i.e.* it re-emitted from the surface after thermally equilibrated with the surface, and bears a cosine distribution. An ion underwent specular scattering in which the ion scatter angle was identical to the ion

incident angle. The third velocity component of the ions was also used in calculating the ion incident and scattering angles. After scattering, an ion was assumed to retain all its initial energy. As we have pointed out in chapter 6, recent molecular dynamic simulation indicates that low energy ion scattering bears both a specular and a non-specular component. This is attributed to some degree of energy loss of the ions upon bombarding the surface. This phenomenon becomes critical for low energy ions as their energy might drop below the threshold energy upon scattering and fail to enhance the etching reaction afterwards.

## **(2) Surface Reaction:**

The surface reaction probabilities were determined by the kinetic models proposed in chapter 4-6, depending upon the type of ions and materials included. The inclusion of carbon etching and deposition will be described in the generalized chemistry model. The reaction probability of ions was calculated based on the measured ion angular dependence, and the sticking probability of chlorine and oxygen neutrals was determined based on the extent of surface chlorination/oxygenation.

Recombination of Cl on the surface to form  $\text{Cl}_2$  was assumed to have a constant probability upon collision and the determination of this constant is discussed in the next section. Recombination reactions provided a route for loss of reactive neutrals within the feature.  $\text{Cl}_2$ , once formed, leaves the surface with assigned zero reaction probability on all surfaces. This is justified by our experimental observation that the reactivity of  $\text{Cl}_2$  is limited at a highly chlorinated surface. The reaction probability of  $\text{SiCl}_4$  was assumed to be zero at all surfaces as it is volatile.

Plasma etching processes are frequently accompanied by deposition processes, e.g. the deposition of sticky entities such as C or  $\text{SiCl}_2$ , generated from sputtering of photoresist or etching of polysilicon. The depositing particles (carbon,  $\text{SiCl}_2$ ) could be introduced at the source plane and their trajectories are tracked till they react with a surface cell or escape from the simulation domain.

### ***7.3.3 Surface advancement***

Elemental balances were performed in surface cells every time a reactant particle reacted with a surface cell. The individual counters for the various types of particles present in the cell were updated. Each cell initially contained  $N$  particles; and the cell could either add more particles (deposition) till it reached a total of  $2N$  or lose particles (etching) till it contained only  $N/6$  particles. When a limit was reached, the cell of interest either deposited another cell or was etched; the surface was then redefined. The deposited cell was filled with half the contents of the parent cell while the etched cell passed its residual contents to a neighboring cell based on pre-determined rules.

## **7.4 Comparison of Experimental and Modeling Results**

To simulate the beam experiments, the incoming ion and atom fluxes were nearly mono-directional to reproduce the experimental beam studies. Note that  $\text{Cl}^+$  attributes to the surface chlorination, while  $\text{Ar}^+$  does not – as described in the kinetic models.

Since the photoresist integrity was preserved after etching in the beam system at low ion energies, photoresist is considered not etched. To account for the photoresist erosion in the high ion energy levels, carbon was etched in a manner similar to polysilicon, but the etched carbon did not deposit in the feature. The selectivity of polysilicon-to-photoresist is assumed to be 1.5 with 95 eV  $\text{Ar}^+$  and  $\text{Cl}$ ; and infinity with 35 eV  $\text{Cl}^+$  and  $\text{Cl}$ . The inclusions of carbon deposition and the subsequent etching of carbon chlorides and oxides are discussed in the generalized chemistry model.

### ***7.4.1 $\text{Ar}^+$ and $\text{Cl}$ etching of photoresist masked polysilicon***

Simulation of the profile etched by 95 eV  $\text{Ar}^+$  and  $\text{Cl}$  in the unshadowed orientation (Figure 6.3 and 6.4) is shown in Figure 7.3. Trenching is observed in etching of polysilicon prior to the end point. Slight tapering of the sidewall is also observed. The formation of trenches in polysilicon is indeed due to ion scattering within the feature. In

our simulations, ion directionality had an important effect on the degree of sidewall bowing as well as feature bottom trenching. As the ions entering the simulation domain became more directional, the trenching became narrower and located closer to the edge of the polysilicon lines while the bowing was reduced. The observed etching and faceting of the photoresist agreed well with the incorporated kinetics. As the etching of polysilicon proceeded to the end point, anisotropic etching of the polysilicon sidewalls was observed. The notching at the foot of the polysilicon were not simulated as the proper kinetic coefficients have not yet been implemented.

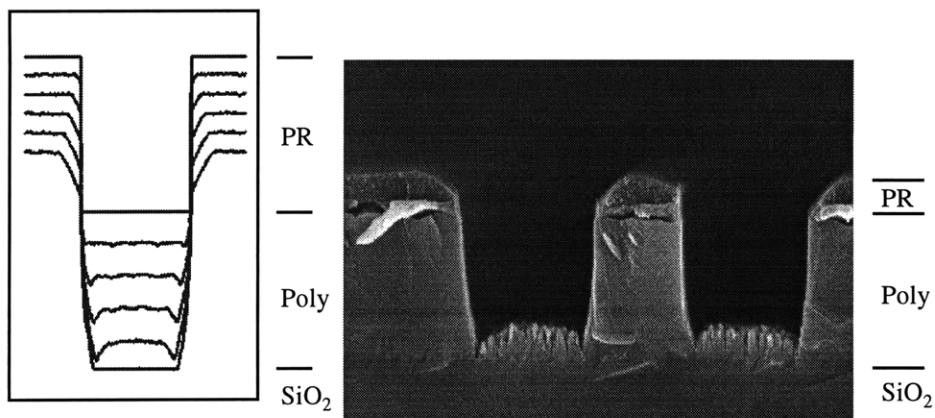


Figure 7.3: Simulation of the profile etched by 90 eV Ar<sup>+</sup> and Cl, in the unshadowed orientation. The photoresist is etched in the simulation, but the etching product C did not redeposit within the feature. Anisotropic etching of the polysilicon sidewall is achieved.

#### 7.4.2 Cl<sup>+</sup> and Cl etching of photoresist masked polysilicon

Simulation of the profiles observed in the shadowed orientation was then attempted to demonstrate the importance of atomic chlorine in defining the feature profile evolution. With no adjustable parameter to the simulator (no recombination of Cl on the photoresist is considered), the simulated profile is shown in Figure 7.5. Qualitatively good agreement is observed comparing the simulation results with the experimental measurement. However, the simulated etching rate of polysilicon on the right side was much faster than that observed experimentally, leaving less polysilicon remained at the

right side at the time when etching was stopped. Note in this simulation, all Cl atoms colliding the photoresist were scattered and a major portion of the scattered chlorine atoms contributed to the etching of polysilicon on the right side of the feature. Since etching of polysilicon is enhanced by the simultaneous exposure of  $\text{Cl}^+$  and Cl, it is reasonable to expect that a reduction of the atomic chlorine flux to the right side of the feature would result in better agreement with our experimental result.

One possible mechanism that would lead to the reduction of atomic chlorine flux within the feature is the recombination of chlorine atoms. Since interactions between chlorine and polysilicon or silicon dioxide are described rigorously by the kinetic models that we proposed, the only possible cause for a mismatch between our simulation result and experimental measurement is the assumption that we made on chlorine interacting with photoresist.

We then considered unity recombination probability of Cl on photoresist, and further assumed that the reactivity of molecular chlorine, once it is formed, to be zero. This is justified from our kinetic measurements, which suggested the reactivity of  $\text{Cl}_2$  is much smaller than that of Cl especially at a highly chlorinated surface. The corresponding simulated profile is shown in Figure 7.5. With unity recombination probability of Cl on the photoresist, Cl atoms recombine and form molecular chlorine, which does not contribute to the etching of the polysilicon at the right side of the feature. Therefore, polysilicon on the right side was mainly etched by  $\text{Cl}^+$  sputtering, and the etching rate of polysilicon by only  $\text{Cl}^+$  has been measured to be an order magnitude slower than that by  $\text{Cl}^+$  and Cl. As a result, the etching rate of polysilicon at the right side is much smaller than what we measured experimentally. The slight indented, curved structure observed at the top of the right side feature is due to the scattering of atomic chlorine from the right polysilicon sidewall. Again, qualitatively good agreement is observed comparing the simulation results with the experimental measurement, but the simulated etching rate of polysilicon on the right side was much slower than that observed experimentally, leaving more polysilicon remained at the right side at the time when etching was stopped.



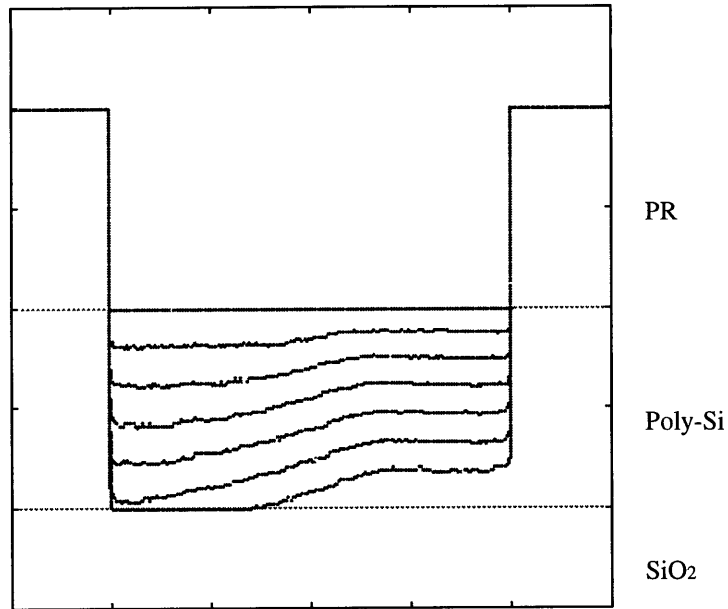


Figure 7.4: Simulation of the profile observed in the shadowed orientation. The photoresist was not etched in the simulation, and chlorine recombination on photoresist surface was not considered. In other words, the recombination probability of Cl on the photoresist surface is assumed zero.

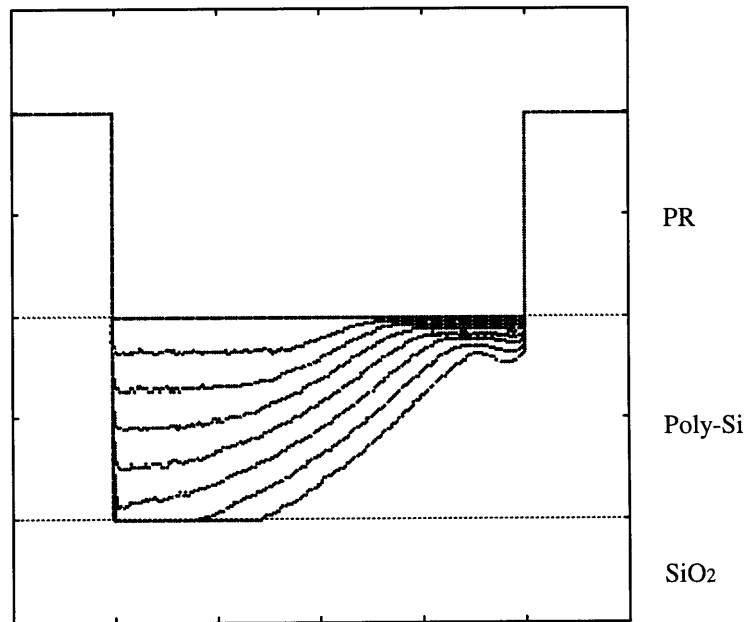


Figure 7.5: Simulation of the profile observed in the shadowed orientation. The photoresist was not etched in the simulation, but a recombination probability of 1.0 for Cl on the photoresist was assumed.

We explored the value for the recombination probability of Cl on the photoresist and found that a probability of 0.5 best represented the measured profile. The simulated result is shown in Figure 7.6. As can be seen from these simulation results, the recombination of Cl on the photoresist can have a significant impact on the profile evolution. Since recombination leads to the reduced Cl concentration within the feature, it can result in reactive-ion-etching lag (RIE lag) or aspect ratio dependent etching (ARDE). Surface recombination is known to reduce the concentration of reactive species within the feature, for example, oxygen atom recombination on the sidewalls has been reported to reduce the reactant flux in the feature during the chemical vapor deposition of SiO<sub>2</sub> [Virmani, 1996]. Since we have neglected the etching of photoresist and assumed the reaction probability of Cl<sub>2</sub> to be zero, the probability of 0.5 does not represent the true recombination coefficient of Cl on a photoresist surface. However, it sheds insight on the importance of the surface recombination effect, and helps determine the critical experiments to be performed in order to quantify this surface reaction.

The quantitatively good agreement between our experimental result and modeling prediction validates the kinetic models we incorporated in the simulator, and further proves the capability of this Monte Carlo based simulation. By comparing the simulation results with our experimental measurement, we identify an important surface reaction that we ignored in our initial assumptions and are able to determine the significance of this surface recombination effect and achieve predictive modeling of the profile evolution.

With the recombination probability of 0.5 for Cl on a photoresist surface, we simulated the profile observed in the unshadowed orientation, shown in Figure 7.7. The photoresist is not etched in the simulation, but a recombination probability of 0.5 for Cl on the photoresist was assumed. No ion scattering was considered in this simulation. Anisotropic etching of the polysilicon sidewalls is observed. The observed faceting of the photoresist and notching at the foot of the polysilicon were not simulated as the proper kinetic coefficients have not yet been implemented.

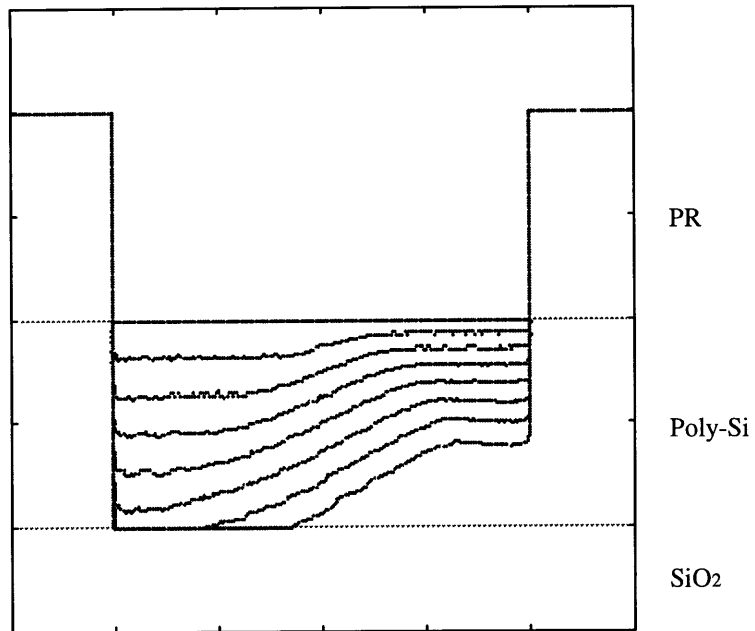


Figure 7.6: Simulation of the profile observed in the shadowed orientation. The photoresist was not etched in the simulation, but a recombination probability of 0.5 for Cl on the photoresist was assumed.

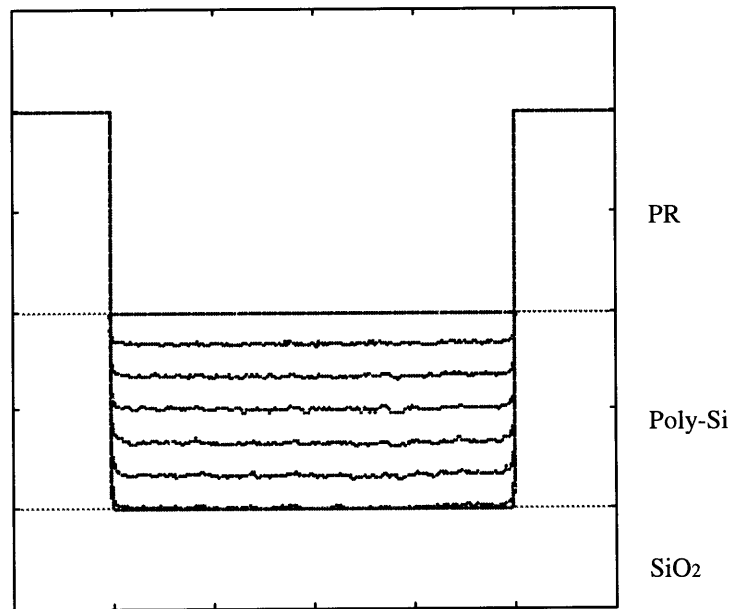


Figure 7.7: Simulation of the profile observed in the unshadowed orientation. The photoresist was not etched in the simulation, but a recombination probability of 0.5 for Cl on the photoresist was assumed. Anisotropic etching of the polysilicon sidewalls was observed.

## 7.5 Generalized Chemistry Model

A generalized chemistry model is constructed to take into account the etching and deposition of carbonaceous species, silicon dioxide, and unsaturated silicon chlorides. The experimental data of etching polysilicon, silicon dioxide and photoresist are reduced into a lumped chemical model in that elemental mass balances are performed to determine the compositions within each cell, and the subsequent etching of each element. The elements we considered include Si, C, Cl and O. Both Si and C are considered as surface lattice elements that provide adsorption sites for Cl or O, and are etched in a similar manner. The sticking probabilities of Si and C are considered constant:  $S_{Si} = S_{Si}^o$ ,  $S_C = S_C^o$ . Both Cl and O are considered as adsorption elements that bond to either Si or C and cause surface chlorination or oxygenation (in a Langmuir-Hinshelwood manner). Upon adsorption, Cl and O occupy one and two reactive sites on the surface, respectively. Chlorine and oxygen are thought to compete for the adsorption sites (Si or C) in each cell. The sticking probabilities of Cl and O are inversely proportional to the surface coverage that is defined in the following:  $S_{Cl} = S_{Cl}^o(1 - \theta_{Cl} - \theta_O)$ ,  $S_O = S_O^o(1 - \theta_{Cl} - \theta_O)$ . The sticking probability of  $\text{SiCl}_2$  is assumed to be a constant, however, once  $\text{SiCl}_2$  deposits on the surface, it will be etched as regular chlorinated silicon.

For simplification, Si and Cl are first considered to illustrate the idea of a generalized chemistry model. Based on our kinetic model, polysilicon is etched by either sputtering or ion-enhanced etching, producing Si and  $\text{SiCl}_x$ , respectively. Notice that the kinetic model developed in chapter 5 ignored the formation of Si as low energy chlorine ions are used. A more general form describing the etching of polysilicon is shown in equation (7.1), where sputtering of silicon is taken into account to properly simulate the etching of polysilicon in high density plasma reactors where higher energy ions are utilized.

$$\begin{aligned}
 Y_{Si} &= c_{sp}(\phi) \cdot Y_{sp} + c_i(\phi) \cdot Y_{i(Cl)} \\
 &= c_{sp}(\phi) \cdot \beta_{sp} \cdot (1 - \theta_{Cl}) + c_i(\phi) \cdot \beta_{i(Cl)} \cdot \theta_{Cl}
 \end{aligned}
 \tag{7.1}$$

$Y_{Si}$ ,  $Y_{sp}$ ,  $Y_{i(Cl)}$  represent total etching yield, sputtering yield, and ion-enhanced (in chlorine) etching yield of polysilicon.  $c_{sp}(\phi)$ ,  $\beta_{sp}$ ,  $c_i(\phi)$ ,  $\beta_{i(Cl)}$  represent angular dependence and reaction probability for sputtering and ion-enhanced (in chlorine) etching of polysilicon.  $\theta_{Cl}$  is the chlorine coverage on a polysilicon surface.

To validate the proposed general chemistry model and the subsequent elemental balance, etching rates of planar polysilicon surfaces are simulated as a function of ion energy and neutral-to-ion flux ratio. The simulated etching yield is shown in Figure 7.8 in comparison to the model fits for chlorine ion-enhanced etching of polysilicon and good agreement is observed. The reproduction of the energy and angular dependencies validates the proposed model and the elemental balance performed.

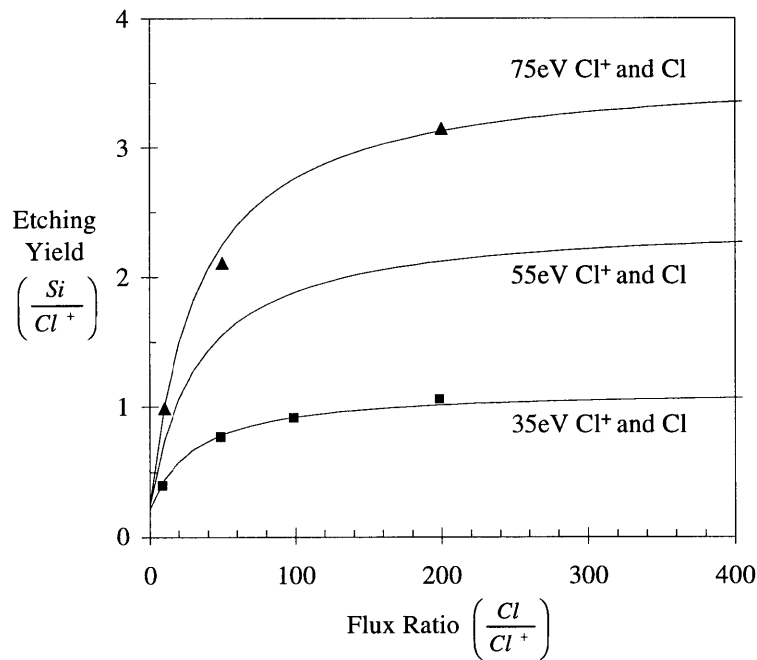


Figure 7.8: Validation of the generalized chemistry model. The simulated etching yields of planar polysilicon surfaces are shown in solid points as a function of ion energy and neutral-to-ion flux ratios. The lines are model fits detailed in chapter 5. Good agreement is observed.

Oxygen from either gas phase or from the presence of silicon dioxide makes the surface kinetics more complicated. Basically oxygen oxidizes the silicon surface and competes with chlorine for adsorption sites on the polysilicon surface. Oxygenation of

the silicon surface reduces the chlorine coverage on the polysilicon surface and also the etching rate of polysilicon. Cheng [Cheng, 1994] reported a reduced etching rate of polysilicon in chlorine plasma upon addition of oxygen, and we have shown etching of silicon dioxide is much slower than that of polysilicon as silicon backbones are occupied by oxygen. A schematic diagram illustrating the general chemistry model, where only Si, Cl and O are considered, is shown in Figure 7.9.

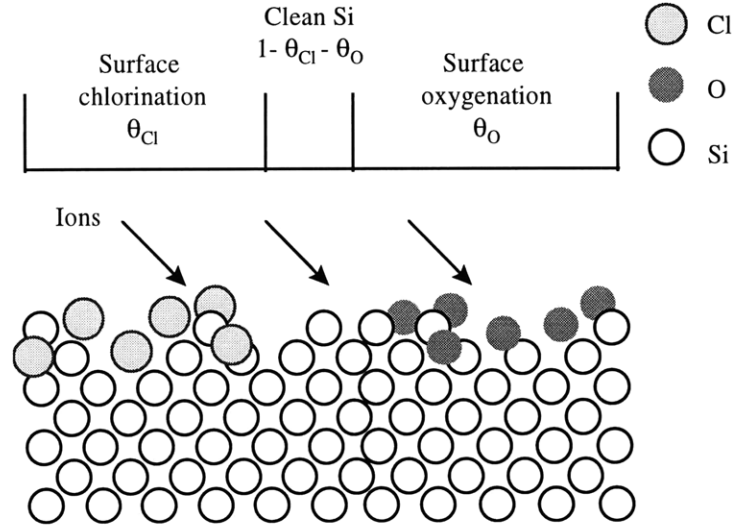


Figure 7.9: Schematic diagram illustrating the surface chemistry model, when only Si, Cl and O are considered.

Figure 7.9 depicted conceptually the polysilicon surface compositions as a function of chlorine and oxygen concentration. As the oxygen concentration increases, the chlorine coverage and the fraction of clean silicon surface decreases. Equation (7.1) is modified to illustrate this effect, where  $\theta_o$  is the oxygen coverage on silicon surface.

$$\begin{aligned}
 Y_{Si} &= c_{sp}(\phi) \cdot Y_{sp} + c_i(\phi) \cdot Y_{i(Cl)} \\
 &= c_{sp}(\phi) \cdot \beta_{sp} \cdot (1 - \theta_{Cl} - \theta_O) + c_i(\phi) \cdot \beta_{i(Cl)} \cdot \theta_{Cl}
 \end{aligned}
 \tag{7.2}$$

Therefore, the total etching yield of silicon is reduced as the oxygen coverage increases.

To include the etching and deposition characteristics of carbon (photoresist), we firstly assumed that the interaction of Cl and/or O to carbon is similar to that of silicon, due to similarity in bonding configuration of silicon and carbon. The assumption also

indicates that etching of Si and C by chlorine and/or oxygen is independent. Therefore, etching of silicon or carbon can be easily calculated if the fractions of Si ( $\psi_{Si}$ ) and C ( $\psi_C$ ) on the surface are known from an elemental balance on the surface, as shown in Figure 7.10.

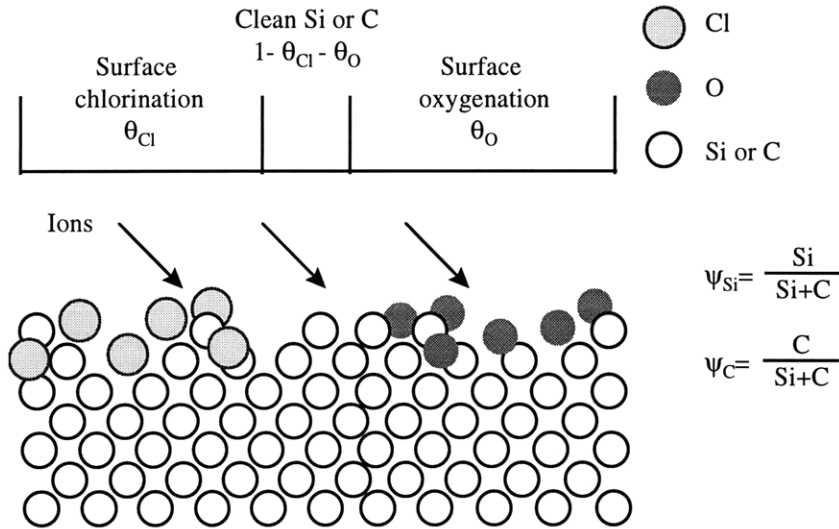


Figure 7.10: Schematic diagram illustrating the surface chemistry model, when Si, C, Cl and O are considered.

However, the etching mechanisms of silicon and carbon are quite different. Silicon is mainly etched by chlorine ion-enhanced mechanism as its angular dependence has suggested, and  $\text{SiCl}_4$  is formed as the etching product in low ion energy regime. Carbon is mainly sputtered as its angular dependence indicated, and C is formed as sputtering product. Carbon can also be chemically etched in chlorine or oxygen plasmas, forming  $\text{CCl}_x$ , CO,  $\text{CO}_2$  as etching products under ion bombardment. Therefore, the etching yield of carbon is given in the following form:

$$\begin{aligned}
 Y_C &= \psi_C \cdot Y_C^o & (7.3) \\
 &= \psi_C \cdot [c_{sp}(\phi) \cdot Y_{sp} + c_i(\phi) \cdot Y_i] \\
 &= \psi_C \cdot [c_{sp}(\phi) \cdot Y_{sp} + c_{i(Cl)}(\phi) \cdot Y_{i(Cl)} + c_{i(O)}(\phi) \cdot Y_{i(O)}] \\
 &= \psi_C \cdot [c_{sp}(\phi) \cdot \beta_{sp} \cdot (1 - \theta_{Cl} - \theta_O) + c_{i(Cl)}(\phi) \cdot \beta_{i(Cl)} \cdot \theta_{Cl} + c_{i(O)}(\phi) \cdot \beta_{i(O)} \cdot \theta_O]
 \end{aligned}$$

$Y_C$ ,  $Y_{sp}$ ,  $Y_{i(Cl)}$ ,  $Y_{i(O)}$  represent total etching yield, sputtering yield, ion-enhanced (in chlorine) etching yield, and ion-enhanced (in oxygen) etching yield of carbon.  $Y_C^0$  represents the etching yield of carbon in the absence of silicon.  $c_{sp}(\phi)$ ,  $\beta_{sp}$ ,  $c_{i(Cl)}(\phi)$ ,  $\beta_{i(Cl)}$ ,  $c_{i(O)}(\phi)$ ,  $\beta_{i(O)}$  represent angular dependence and reaction probability for sputtering, ion-enhanced (in chlorine) etching and ion-enhanced (in oxygen) etching of carbon.

The etching yield of carbon is now scaled with its fraction with respect to silicon on the surface (in a surface cell), and is enhanced by both chlorination and oxygenation of the surface. Equation (7.3) is conceptually simple, but accurate determination of all the reaction probabilities shown in equation (7.3) relies on more detailed characterization of carbon sputtering or etching in chlorine and oxygen plasmas.

## 7.6 Summary

A Direct Simulation Monte Carlo simulator was developed to simulate the profile evolution during the chlorine etching of patterned polysilicon in our beam apparatus and in high density plasma reactors. The DSMC algorithm permitted the incorporation of all the dominant physical and chemical mechanisms of the etching process, such as angle-dependent ion-enhanced etching, physical sputtering, ion scattering, surface recombination, and deposition and redeposition of etching by-products, without encountering numerical difficulties during surface advancement. The simulation results are validated by comparing the simulated profiles with profiles of patterned polysilicon samples etched in the beam apparatus. Quantitatively good agreement was found between the simulated profiles and the measured profiles with one adjustable parameter, the recombination probability of Cl on photoresist.

By emphasizing a few of these mechanisms and implementation of the generalized chemistry model, effects of sidewall passivation, ion scattering, ion directionality, surface recombination and initial mask angle on the profile evolution can be determined. For example, ion scattering within the feature results in trenching and tapering of the sidewall. Therefore, the initial profile of the photoresist or the faceting of



the photoresist during etching can significantly alter the ion trajectory and affect the final etched profile. Recombination of neutral species within the feature has been shown to be significant in providing a loss mechanism for the reactive neutrals, and result in reduced etching rate within the feature.  $\text{SiCl}_2$  deposition from the plasma was determined to be an important factor for the occurrence of two facet angles on photoresist masks commonly seen in experimental profiles, these results will be detailed in a forthcoming paper.



## Chapter 8

### Conclusions

#### 8.1 Conclusions

This work has characterized the chlorine ion-enhanced plasma-surface interactions with polysilicon, silicon dioxide, and photoresist as a function of the plasma compositions ( $\text{Cl}^+$ ,  $\text{Cl}$ ,  $\text{Cl}_2$ ,  $\text{SiCl}_2$ ), ion energy ( $E_{\text{ion}}$ ), ion incident angle ( $\phi_{\text{ion}}$ ) and other important process parameters. A direct beam scattering apparatus capable of generating low energy ions (20-100eV) and reactive neutral species and controlling their flux levels independently was utilized to simulate accurately a high-density plasma environment. Etching of polysilicon, silicon dioxide, and photoresist is quantified to better describe the etching of patterned polysilicon in fabricating the gate electrode of a transistor in the IC manufacturing process. These kinetic measurements facilitate the formulation of surface kinetic models usable in a Monte Carlo based profile simulator, and enable the predictive simulation of feature profiles evolutions.

A multiple molecular beam scattering apparatus which allows the independent variation of the dominant reactive fluxes encountered in a chlorine plasma was utilized to quantify the effect of each individual species. The beam fluxes ( $\text{Ar}^+$ ,  $\text{Cl}^+$ ,  $\text{Cl}$ ,  $\text{Cl}_2$  and  $\text{SiCl}_2$ ) used are of the same order of magnitude as that of a typical plasma reactor and can be controlled independently. This approach enables unambiguous determination of the chemical rate coefficients for ion-enhanced plasma etching of various materials. Etching of polysilicon, silicon dioxide, and photoresist is quantified to better describe the etching of patterned polysilicon in fabricating the gate electrode of a transistor in the IC manufacturing process. This study focuses on the regime of low ion energy (20-100eV) to simulate accurately a high-density plasma environment.

Low energy  $\text{Ar}^+$  ions were utilized with  $\text{Cl}$  and  $\text{Cl}_2$  to measure the ion-enhanced etching yields of polysilicon, silicon dioxide and photoresist. The etching yields of all

three materials exhibit similar dependence on the neutral-to-ion flux ratios, but greatest enhancement is achieved with polysilicon. The order of etching yield enhancement is as following: polysilicon > photoresist > silicon dioxide. This explains the etching selectivity between polysilicon and the other two materials. The etching selectivity of polysilicon with respect to silicon dioxide and photoresist is measured to be 30 and 2.5, respectively. The etching yields were found to scale linearly with  $(E_{ion}^{1/2} - E_{th}^{1/2})$ , where the threshold energies,  $E_{th}$ , are 16 eV and 40 eV for polysilicon and silicon dioxide, respectively. The reactivity of atomic chlorine is found to be greater than that of molecular chlorine and the dissociative adsorption rate of  $Cl_2$  is limited on highly chlorinated surfaces and on silicon dioxide surfaces. The angular dependence of the etching yields indicates that etching of polysilicon in a chlorine environment is a chemical driven process initiated by ion bombardment. However, etching of silicon dioxide in a chlorine chemistry is limited by the physical sputtering of the surface species. Etching of photoresist is strongly dependent upon the heat treatment to the photoresist prior to etching.

A low-energy chlorine ion beam is generated to study the effect of a reactive ion on chlorinating the surface and enhancing the etching yields. Chlorine ions further enhance the etching yield of polysilicon comparing to argon ions, especially at low ion energies and low flux ratios where the chemical reactivity of chlorine ions plays an important role in chlorinating the silicon surface. The effect of deposition from etching products is demonstrated with a  $SiCl_2$  beam. The presence of  $SiCl_2$  significantly suppressed the etching of the polysilicon by both  $Cl^+$  and  $Cl^+$  with  $Cl$ , by almost an order of magnitude. The effect of angular dependence on etching yield is also examined. Maximum etching yield of polysilicon is again observed at normal ion incident angle, indicating the etching reaction is chemically driven in that the ion-induced chlorination compensates for the less efficient momentum transfer to the surface atoms at near normal incident angles.

We demonstrate that the notching formation at the polysilicon/silicon dioxide interface during overetching is in part caused by stress enhanced spontaneous etching and is not solely a result of feature charging. Therefore, notching formation can be reduced

by minimizing the stress within the polysilicon film by annealing or varying the polysilicon deposition conditions. Also the modification of plasma processes to increase the sidewall passivation, e.g. the addition of passivant precursors to the feed gas that blocks spontaneous etching, is an alternative to prevent the spontaneous etching of polysilicon.

Possible reaction pathways are proposed and reduced into kinetic models that are usable in a profile simulator. Patterned polysilicon wafers were etched and investigated by Scanning Electron Microscopy (SEM). Our attempt to etch 0.5  $\mu\text{m}$  and 0.35  $\mu\text{m}$  trenches using  $\text{Cl}^+$  (or  $\text{Ar}^+$ ) and  $\text{Cl}$  beams results in highly directional sidewalls. The topography evolutions of the patterned samples are used to verify the kinetic models and to validate the simulation results.

A Monte Carlo based profile simulator was constructed to simulate feature profile evolution during plasma etching processes. The etching yield models implemented were formulated from our beam scattering studies in which the functional role of  $\text{Cl}^+$ ,  $\text{Cl}$ ,  $\text{Cl}_2$  and  $\text{SiCl}_2$  were characterized, and dominant reaction mechanisms such as surface chlorination under ion bombardment, surface re-emission, and ion reflection were accounted. The profile evolution of patterned samples etched with the combined  $\text{Cl}$  and  $\text{Cl}^+$  beams were simulated to validate the simulation results. Quantitatively good agreement was found between the simulated profiles and the measured profiles with one adjustable parameter, the chlorine recombination probability on photoresist surface.

## 8.2 Suggestions for Future Work

To better quantify the extent of surface chlorination, a detailed angular-resolved XPS analysis should be performed to determine the thickness of the surface chlorination layer as a function of ion energy and neutral-to-ion flux ratios. In addition, laser-induced thermal desorption (LITD) would facilitate measurements of the surface bonding states during etching by ionizing the surface species into gas phase with high energy, high

frequency laser pulses. The surface species can be subsequently analyzed by a mass spectrometer. LITD analysis was initially proposed in this work, but is not carried out due to the time constraint. Combining AR-XPS and LITD analysis would elucidate the extent of surface chlorination and stoichiometry and aid refining of the proposed kinetic models. These analysis are extremely powerful in quantifying surface compositions and bonding states, especially when mixed compositions (Si, C, O, Cl, Br, ... etc.) are present.

The bromine chemistry ( $\text{Br}_2$ , HBr) and its influence on etching anisotropy should be systematically determined with beam scattering experiments, as HBr and  $\text{Br}_2$  are widely used in industry to improve the etching selectivity between polysilicon and silicon dioxide/photoresist. Bromine chemistry is favored especially for etching n-type doped polysilicon as the spontaneous etching rate of polysilicon silicon with Br atoms is lower compared to that with Cl atoms. These kinetic measurements are required to expand the database developed for predictive modeling of the feature profile evolution.

The effects of dopant types, doping levels, surface recombination of various reactive neutrals, and substrate temperature should be addressed. Quantification of the product distribution as a function of neutral-to-ion flux ratio would aid refinement of the kinetic models proposed here. Molecular dynamic simulation would aid determination of the “non-specular” component of an ion scattering event, which plays a dominant role in defining the etched profiles. Molecular dynamic simulation is computationally intensive, but powerful in determining critical kinetic information that is hard to measure experimentally. The effect of feature charging, and model(s) describing the stress-induced spontaneous etching should be included in the profile simulator to accurately model feature profile evolution during overetching of patterned polysilicon.

## Bibliography

- Arnold, J. C. and H. H. Sawin, "Charging of pattern features during plasma etching", J. Appl. Phys. 70(10), 5314 (1991).
- Athavale, S. D. and D. J. Economou, "Molecular dynamics simulation of atomic layer etching of silicon", J. Vac. Sci. Technol. A13, 966 (1995).
- Auciello, O., "Ion interaction with solids: surface texturing, some bulk effect, and their possible applications", J. Vac. Sci. Technol. 19, 841 (1981).
- Baggerman, J. A. G., R. J. Visser and E. J. H. Collart, "Ion-induced etching of organic polymer in argon and oxygen radio-frequency plasmas", J. Appl. Phys. 75(2), 758 (1994).
- Baglee, D. A., "Characteristics and reliability of 100Å oxides", Proc. 22nd IEEE Rel. Phys. Symp. 152 (1984).
- Balooch, M., M. Moalem, W. Wang and A. V. Hamza, "Low-energy Ar ion-induced and chlorine in etching of silicon", J. Vac. Sci. Technol. A 14(1), 229 (1996).
- Barker, R. A., T. M. Mayer and W. C. Pearson, "Surface studies of and a mass balance model for Ar<sup>+</sup> ion-assisted Cl<sub>2</sub> etching of Si", J. Vac. Sci. Technol. B 1(1), 37 (1983).
- Barklund, A. M. and H.-O. Blom, "Influence of polymer formation on the angular dependence of reactive ion beam etching", J. Vac. Sci. Technol. A 10(4), 1212 (1992).
- Barklund, A. M. and H.-O. Blom, "Influence of different etching mechanisms on the angular dependence of silicon nitride etching", J. Vac. Sci. Technol. A 11(4), 1226 (1993).
- Barone, M. E. and D. B. Graves, "Chemical and physical sputtering of fluorinated silicon", J. Appl. Phys. 77(3), 1263 (1995).
- Barone, M. E. and D. B. Graves, "Molecular-dynamics simulations of direct reactive ion etching of silicon by fluorine and chlorine", J. Appl. Phys. 78(11), 6604 (1995).
- Bello, I., W. H. Chang and W. M. Lau, "Mechanism of cleaning and etching Si surfaces with low energy chlorine ion bombardment", J. Appl. Phys. 75(6), 3092 (1994).
- Bird, G. A., *Molecular Gas Dynamics*, London, Oxford University Press (1976).
- Bloem, J., "Nucleation and growth of silicon by CVD", J. Crystal Growth 50, 581 (1980).
- Briggs, D. and M. P. Seah, *Practical Surface Analysis*, New York, John Wiley & Sons (1983)

- Carl, D. A., D. W. Hess and M. A. Lieberman, "Kinetics of photoresist etching in an electron cyclotron resonance plasma", *J. Appl. Phys.* 68(4), 1859 (1990).
- Chapman, B., *Glow Discharge Processes*, New York, John Wiley & Sons (1980).
- Chen, L. D., M. J. Zhang, and S. Zhang, "Determination of bending stress of silicon wafer using concentrated load", *J. Appl. Phys.* 76(3), 1547 (1994).
- Cheng, C. C., K. V. Guinn, V. M. Donnelly and I. P. Herman, "In situ pulsed laser-induced thermal desorption studies of the silicon chloride surface layer during silicon etching in high density plasmas of  $\text{Cl}_2$  and  $\text{Cl}_2/\text{O}_2$  mixtures", *J. Vac. Sci. Technol. A* 12(5), 2630 (1994).
- Chi, K. K., H. S. Shin, W. J. Yoo, C. O. Jung, Y. B. Koh, M. Y. Lee, "Effects of conductivity of polysilicon on profile distortion", *Jpn. J. Appl. Phys.* 35, 2440 (1996).
- Coburn, J. W., "Ion-assisted etching of Si with  $\text{Cl}_2$ : the effect of flux ratio", *J. Vac. Sci. Technol. B* 12(3), 1384 (1994).
- Coburn, J. W. and H. F. Winters, "Ion- and electron-assisted gas-surface chemistry -- an important effect in plasma etching", *J. Appl. Phys.* 50(5), 3189 (1979).
- Coburn, J. W. and H. F. Winters, "The role of energetic ion bombardment in silicon-fluorine chemistry", *Nuclear Instruments and Methods in Physics Research B* 27, 243 (1987).
- Coburn, J. W. and H. F. Winters, "Conductance considerations in the reactive ion etching of high aspect ratio features", *Appl. Phys. Lett.* 55(26), 2730 (1989).
- Cook, J. M. and B. W. Benson, "Application of EPR spectroscopy to oxidative removal of organic materials", *J. Electrochem. Soc.* 130, 2459 (1983).
- Cook, J. M., D. E. Ibbotson, and D. L. Flamm, "Application of a low-pressure radio frequency discharge source to polysilicon gate etching", *J. Vac. Sci. Technol. B* 8(1), 1 (1990).
- Coon, P. A., P. Gupta, M. L. Wise and S. M. George, "Adsorption and desorption kinetics for  $\text{SiH}_2\text{Cl}_2$  on  $\text{Si}(111)7\times 7$ ", *J. Vac. Sci. Technol. A* 10(2), 324 (1991).
- d'Agostino, R., Ed., *Plasma Deposition, Treatment, and Etching of Polymers*, N. Y., Academic (1990).
- Dalton, T. "Pattern dependencies in the plasma etching of polysilicon", Ph.D. Thesis, Massachusetts Institute of Technology, Dept. of Chemical Engineering (1994).



Dane, D. and T. D. Mantei, "Parametric modeling and measurement of silicon etching in a high density chlorine plasma", *Appl. Phys. Lett.* 65(4), 478 (1994).

Deshmukh, S. C. and D. J. Economou, "Remote plasma etching reactors: modeling and experiment", *J. Vac. Sci. Technol. B* 11(2), 206 (1993).

Egitto, F. D., F. Emmi, R. S. Horwith and V. Vukanovic, "Plasma etching of organic materials. I. Polyimide in  $O_2$ - $CF_4$ ", *J. Vac. Sci. Technol. B* 3, 893 (1985).

Fehsenfeld, F. C., K. M. Evenson and H. P. Broida, "Microwave discharge cavities operating at 2450 MHz", *Rev. Sci. Instrum.* 36(3), 294 (1964).

Font, G. I. and I. D. Boyd, "Numerical study of the effects of reactor geometry on a chlorine plasma helicon etch reactor", *J. Vac. Sci. Technol. A* 15(2), 313 (1997).

Fujiwara, N., T. Maruyama, M. Yoneda, "Profile control of polysilicon etching in electron cyclotron resonance plasma", *Jpn. J. Appl. Phys.* 34, 2095 (1995).

Gerlach-Meyer, U., "Ion enhanced gas-surface reactions: a kinetic model for the etching mechanism", *Surf. Sci.* 103, 524 (1981).

Giapis, K. P., T. A. Moore and T. K. Minton, "Hyperthermal neutral beam etching", *J. Vac. Sci. Technol. A* 13(3), 959 (1995).

Gibson, G., "Radial ion transport in a limited axisymmetric ECR plasma", Ph.D. Thesis, Massachusetts Institute of Technology, Dept. of Chemical Engineering (1995).

Gray, D., "Beam simulation studies of plasma-surface interactions in fluorocarbon etching of Si and  $SiO_2$ ", Ph.D. Thesis, Massachusetts Institute of Technology, Dept. of Chemical Engineering (1993).

Gray, D. C. and H. H. Sawin, "Design consideration for high-flux collisionally opaque molecular beams", *J. Vac. Sci. Technol. A* 10(5), 3229 (1992).

Gray, D. C., I. Tepermeister and H. H. Sawin, "Phenomenological modeling of ion-enhanced surface kinetics in fluorine-based plasma etching", *J. Vac. Sci. Technol. B* 11(4), 1243 (1993).

Hamaguchi, S. and M. Dalvie, "Microprofile simulations for plasma etching with surface passivation", *J. Vac. Sci. Technol. A* 12(5), 2745 (1994).

Hanson, D. E., A. F. Voter and J. D. Kress, "Molecular dynamic simulation of reactive ion etching (RIE) of Si by energetic Cl ions", submitted to *J. Appl. Phys.* (1997).

Harper, J. M. E., J. J. Cuomo, P. A. Leary, G. M. Summa, H. R. Kaufman and F. J. Bresnock, "Low energy ion beam etching", *J. Electrochem. Soc.* 128(5), 1077 (1981).

- Hierlemann, M., A. Kersch, C. Werner and H. Schafer, "A gas-phase and surface kinetics model for silicon epitaxial growth with  $\text{SiH}_2\text{Cl}_2$  in an RTCVD reactor", *J. Electrochem. Soc.* 142(1), 259 (1995).
- Houle, F. A., "Laser-induced etching of metals and semiconductors", *J. Vac. Sci. Technol.* 20(3), 790 (1981).
- Houle, F. A., "Photoeffects on the fluorination of silicon. I. Influence of doping on steady-state phenomena", *J. Chem. Phys.* 79(9), 4237 (1983).
- Hsiao, R., K. Yu, L. S. Fan, T. Pandhumsopom, H. Sanitini, S. A. Macdonald et al., "Anisotropic etching of a Novalak-based polymer at cryogenic temperature", *J. Electrochem. Soc.* 144(3), 1008 (1997).
- Hwang, G. S. and K. P. Giapis, "The influence of electron temperature on pattern-dependent charging during etching in high density plasmas", *J. Appl. Phys.* 81(8), 3433 (1997).
- Hwang, G. S. and K. P. Giapis, "On the origin of the notching effect during etching in uniform high density plasmas", *J. Vac. Sci. Technol. B* 15(1), 70 (1997).
- Ishitani, A., "Charge transfer adsorption in silicon vapor phase epitaxial growth", *J. Appl. Phys.* 63(2), 390 (1987).
- Johannes, J., T. Bartel, G. A. Hebner, J. Woodworth and D. Economou, "Direct simulation monte carlo of inductively coupled plasma and comparison with experiments", *J. Electrochem. Soc.* 144(7), 2448 (1997).
- Jorgenson, G. V. and G. K. Wehner, "Sputtering studies of insulators by means of Langmuir probes", *J. Appl. Phys.* 36(9), 2672 (1965).
- Joubert, O., G. S. Oehrlein and M. Surendra, *J. Vac. Sci. Technol. A* 12(3), 665 (1994).
- Kaufman, H. R., J. J. Cuomo and J. M. E. Harper, "Technology and applications of broad-beam ion source used in sputtering. Part I. Ion source technology", *J. Vac. Sci. Technol.* 21(3), 725 (1982).
- Kikuchi, J., S. Fujimura, M. Suzuki and H. Yano, "Effects of  $\text{H}_2\text{O}$  on atomic hydrogen generation in hydrogen plasma", *Jpn. J. Appl. Phys.* 32(6B), 3120 (1993).
- Kinoshita, T., M. Hane, and J. P. McVittie, "Notching as an example of charging in uniform high density plasmas", *J. Vac. Sci. Technol. B* 14(1), 560 (1996).
- Kota, G. P., J. W. Coburn and D. B. Graves, "The recombination of chlorine atoms at surfaces", *J. Vac. Sci. Technol.* (1997).

Layadi, N., V. M. Donnelly and J. T. C. Lee, "Cl<sub>2</sub> plasma etching of Si(100): Nature of the chlorinated surface layer studied by angular resolved x-ray photoelectron spectroscopy", *J. Appl. Phys.* 81(10), 6738 (1997).

Lee, C., D. B. Graves and M. A. Lieberman, "Role of etch products in polysilicon etching in a high-density chlorine discharge", *Plasma Chem. and Plasma Proc.* 16(1), 99 (1996).

Lehmann, H. W., L. Krausbauer and R. Widmer, "Redeposition - A serious problem in rf sputter etching of structures with micronmeter dimensions", *J. Vac. Sci. Technol.* 14(1), 281 (1977).

Levinson, J. A., E. S. G. Shaqfeh, M. Balooch and M. Hamza, "Ion-assisted etching and profile development of silicon in molecular chlorine", *J. Vac. Sci. Technol. A* 15(4), 1902 (1997).

Lii, Y. J. T. and J. Jorne, "Redeposition during deep trench etching", *J. Electrochem. Soc.* 137(9), 2837 (1990).

Maruyama, T., N. Fujiwara, S. Ogino, M. Yoned, "Reduction of charge build-up with high power pulsed electron cyclotron resonance plasma", *Jpn. J. Appl. Phys.* 36, 2526 (1997).

Matsunami, N., Y. Yamamura, Y. Itikawa, N. Itoh, Y. Kazumata, S. Miyagawa, et. al., "A semiempirical formula for the energy dependence of the sputtering yield", *Radiation Effects Letters* 57, 15 (1980)

Matsuo, J., K. Harahashi, A. Sato and S. Hijiya, "Study of chlorine adsorbed silicon surface using soft-X-ray photoemission spectroscopy", *Jpn. J. Appl. Phys.* 31, 2025 (1992).

Mayer, T. M., R. A. Barker and L. J. Whitman, "Investigation of plasma etching mechanisms using beams of reactive gas ions", *J. Vac. Sci. Technol.* 18(2), 349 (1981).

McNevin, S. C. and G. E. Becker, "Investigation of kinetic mechanisms for the ion-assisted etching of Si in Cl<sub>2</sub>", *J. Vac. Sci. Technol. B* 3(2), 485 (1985).

Murakawa, S., S. Fang and J. P. McVittie, "Ion trajectory distortion and profile tilt by surface charging in plasma etching", *Appl. Phys. Lett.* 64(12), 1558 (1994).

Nozawa, T., T. Kinoshita, T. Nishizuka, and A. Narai, "The electron charging effects of plasma on notch profile defects", *Jpn. J. Appl. Phys.* 34, 2107 (1995).

Ogryzlo, E. A., D. E. Ibbotson, D. L. Flamm and J. A. Mucha, "Doping and crystallographic effects in Cl-atom etching of silicon", *J. Appl. Phys.* 67(6), 3115 (1990).

- Okano, H. and T. Horiike, "Si etch rate and etch yield with Ar<sup>+</sup>/Cl<sub>2</sub> system, Jpn. J. Appl. Phys. 20(12), 2429 (1981).
- Oostra, D. J., A. Haring, R. P. v. Ingen and A. E. d. Vries, "Mechanisms of sputtering of Si in a Cl<sub>2</sub> environment by ions with energies down to 75 eV", J. Appl. Phys. 64(1), 315 (1988).
- Oostra, D. J., A. Haring and A. E. d. Vries, "Sputtering of SiO<sub>2</sub> in a XeF<sub>2</sub> and in a Cl<sub>2</sub> atmosphere", J. Vac. Sci. Technol. B 4(6), 1278 (1986).
- Oostra, D. J., R. P. v. Ingen, A. Haring, A. E. d. Vries and G. N. A. v. Veen, "Near threshold sputtering of Si and SiO<sub>2</sub> in a Cl<sub>2</sub> environment", Appl. Phys. Lett. 50(21), 1506 (1987).
- Ramo, S. and J. R. Whinnery, *Fields and Waves in Modern Radio*, New York, Wiley (1953).
- Robinson, R. S. and S. M. Rossnagel, "Ion-beam-induced topography and surface diffusion", J. Vac. Sci. Technol. 21(3), 790 (1982).
- Rossen, R. A., "A molecular beam study of ion-enhanced gas-surface kinetics: the Si/Cl<sub>2</sub>/Ar<sup>+</sup> system", Ph.D. Thesis, Massachusetts Institute of Technology, Dept. of Chemical Engineering (1988).
- Rossen, R. A. and H. H. Sawin, "Time-of-flight and surface residence time measurements for ion-enhanced Si-Cl<sub>2</sub> reaction products", J. Vac. Sci. Technol. A 5(4), 1595 (1987).
- Sanders, F. H. M., A. W. Kolfshoten and J. Dieleman, "Ion-assisted etching of silicon by molecular chlorine", J. Vac. Sci. Technol. A 2(2), 487 (1984).
- Sasaoka, C. and A. Usui, "Self-limiting adsorption of thermally cracked SiH<sub>2</sub>Cl<sub>2</sub> on Si surfaces", Appl. Surf. Sci. 82, 348 (1994).
- Sato, M. and Y. Arita, "Etched profile control of single-crystal silicon in reactive ion etching using chlorine", J. Electrochem. Soc. 134, 2856 (1987).
- Seel, M. and P. S. Bagus, "Ab initio cluster study of the interaction of chlorine and chlorine with the Si(111) surface", Phys. Rev. B 28(4), 2023 (1983).
- Shagfeh, E. S. G. and C. W. Jurgensen, "Simulation of reactive ion etching pattern transfer", J. Appl. Phys. 66(10), 4664 (1989).
- Shen, Y. L., S. Suresh and I. A. Blech, "Stresses, curvatures, and shape change arising from patterned lines of silicon wafers", J. Appl. Phys. 80, 1388 (1996).

- Sigmud, P., "Theory of sputtering. I. Sputtering yield of amorphous and polycrystalline targets", *Phys. Rev.* 184(2), 383 (1969).
- Spence, D. and O. J. Steingraber, "Factors determining dissociation fractions in atomic beams generated by "straight-through" microwave discharge sources", *Rev. Sci. Instrum.* 59(11), 2464 (1988).
- Steinbruchel, C., "Physical and chemical sputtering at very low ion energy: the importance of the sputtering threshold", *Mat. Res. Soc. Symp. Proc.* 129, 477 (1989).
- Szabo, A. and T. Engel, "Etching of Si surfaces with hot chlorine beams: translational and vibrational excitation of the incident chlorine particles", *J. Vac. Sci. Technol. A* 12(3), 648 (1994).
- Szabo, A., P. D. Farrall and T. Engel, "Thermal and direct etching mechanisms of Si(100) with a hyperthermal chlorine beam", *J. Appl. Phys.* 75(7), 3623 (1994).
- Szabo, A., P. D. Farrall and E. T., "Reactions of chlorine with Si(100) and Si(111): adsorption and desorption kinetics", *Surf. Sci.* 312, 284 (1994).
- Sze, S. M., *Physics of Semiconductor Devices*, N. Y., Wiley & Sons (1981).
- Tabara, S., "Notch profile defect in aluminum alloy etching using high density plasma", *Jpn. J. Appl. Phys.* 35, 2456 (1996).
- Tachi, S. and S. Okudaira, "Chemical sputtering of silicon by  $F^+$ ,  $Cl^+$  and  $Br^+$  ions: reactive spot model for reactive ion etching", *J. Vac. Sci. Technol. B* 4(2), 459 (1986).
- Tait, R. N., S. K. Dew, T. Smy and M. J. Brett, "Monte Carlo simulation and measurement of silicon reactive ion etching profiles", *J. Vac. Sci. Technol. A* 12(4), 1085 (1994).
- Teraoka, Y. and I. Nishiyama, "Si(100) etching by translational energy controlled atomic chlorine beams", *J. Appl. Phys.* 79(8), 4397 (1996).
- Thomas III, J. H. and L. H. Hammer, "Native oxide removal during chlorine reactive ion etching of silicon in an rf diode reactor", *J. Appl. Phys.* 68(5), 2400 (1990).
- Tuda, M., K. Ono and K. Nishikawa, "Effects of etch products and surface oxidation on profile evolution during electron cyclotron resonance plasma etching of poly-Si", *J. Vac. Sci. Technol. B* 14(5), 3291 (1996).
- Ulacia F, J. I., C. J. Petti and J. P. McVittie, "Crystal-orientation dependent etch rates and a trench model for dry etching", *J. Electrochem. Soc.* 135(6), 1521 (1988).

Varhue, W. and J. Burroughs, "Electron cyclotron resonance plasma etching of photoresist at cryogenic temperatures", 72(7), 3050 (1992).

Virmani, M., D. A. Levedakis, G. B. Raupp, and T. S. Cale, "Feature scale simulation studies of TEOS-sourced remote microwave plasma-enhanced chemical vapor deposition of silicon dioxide: Role of oxygen atom recombination", J. Vac. Sci. Technol. A 14, 977 (1996).

Wilson, W. D., L. G. Haggmark and J. P. Biersack, "Calculations of nuclear stopping , ranges, and straggling in the low energy region", Phys. Rev. B 15(5), 2458 (1977).

Winters, H. F., "The role of chemisorption in plasma etching", J. Appl. Phys. 49(10), 5165 (1978).

Winters, H. F. and J. W. Coburn, "Surface science aspects of etching reactions", Surf. Sci. Rep. 14, 161 (1992).

Winters, H. F., J. W. Coburn and T. J. Chuang, "Surface processes in plasma-assisted etching environments", J. Vac. Sci. Technol. B 1(2), 469 (1983).

Winters, H. F. and D. Haarer, "Influence of doping on the etching of Si(111)", Phys. Rev. B 36(12), 6613 (1987).

Yu-Jahnes, L. S., W. T. Brogan, A. C. Anderson and M. J. Cima, "A high flux atomic oxygen source for the deposition of high  $T_c$  superconducting films", Rev. Sci. Instrum. 63(9), 4149 (1992).

Zalm, P. C., "Energy dependence of the sputtering yield of silicon bombarded with neon, argon, krypton, and xenon ions", J. Appl. Phys. 54(5), 2660 (1983).

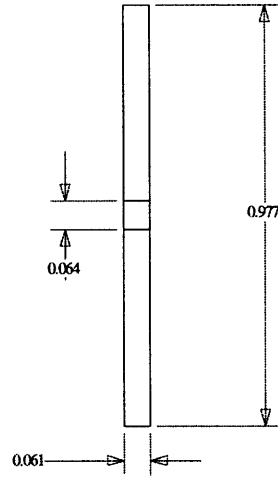
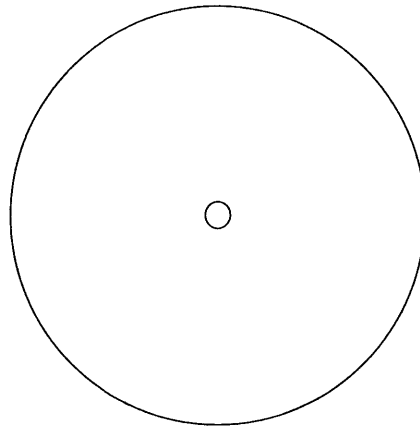
Zau, G., Ph.D. Thesis, Massachusetts Institute of Technology, Dept. of Chemical Engineering (to be published).

## Appendices

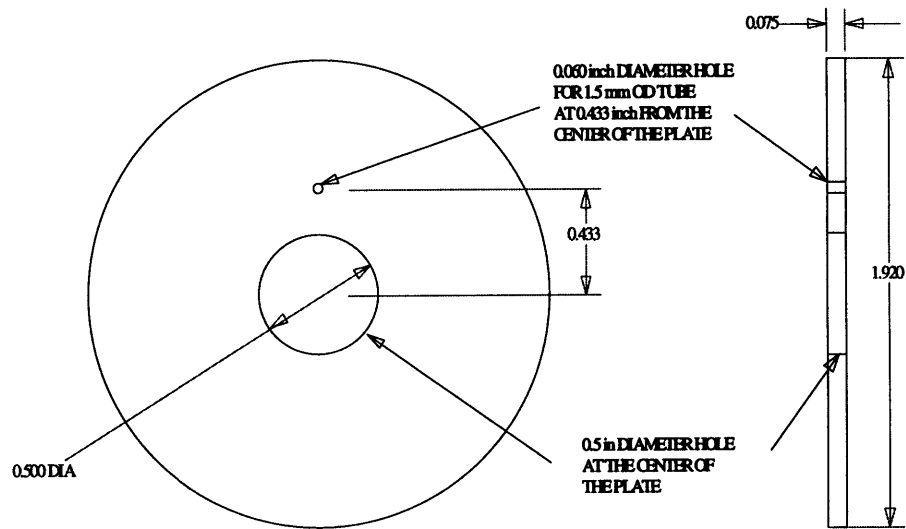
<b>A. Mechanical Drawings</b>	<b>Page</b>
CECR source	
CECR gas diffuser	173
CECR faceplate	174
CECR quartz liner	175
Atom source	
Conflat flange (air side)	176
Outer tube with conflat	177
Air side end of the outer tube	178
Threads on air side end of the outer tube	179
Position of roughing holes on the outer tube	180
Outer conductor tube only showing but in vacuum end	181
Vacuum end of the outer tube	182
Tuning slug	183
Collar	184
Center conductor	185
Center conductor tip	186
Holder	187
Holder showing cooling water circulation holes	188
Holder with cooling water holes hidden	189
Holder and outer tube welded	190
Clamp for holder	191
Gas line	192
Water line	193
Type N connector holder	194
Teflon seal	195
Quartz ampoule	196
Photo of the 3-beam chamber	197
Diagnostic probe mounting system (second setup)	198
Probe mounting assembly	199
Holder for ion energy analyzer	200
Pitot tube support clamp	201
Sample mounting system	
Sample mounting assembly	202
Pin for sample holder	203
Pitot Tube	204

Ion Energy Analyzer	
Ground enclosure	205
Electron repeller plate	206
Ion collector plate	207
Base enclosure with microdot electrical connector	208
Feedthrough (Microdot to BNC)	209
Sample Holder	
30 degree off normal	210
45 degree off normal	211
60 degree off normal	212





<b>Massachusetts Institute of Technology</b>			
<b>Department of Chemical Engineering</b>			
<b>Part</b>	<b>ECR gas diffuser</b>		
<b>Filename</b>			
<b>Designer</b>	<b>Jane Chang</b>	<b>Date</b>	<b>5/11/95</b>
<b>Contractor</b>	<b>G. Finkenbeiner</b>	<b>Date</b>	
<b>Scale</b>		<b>Unit</b>	<b>Inch</b>
<b>Quantity</b>	<b>5</b>	<b>Material</b>	<b>Quartz</b>
<b>Tolerance</b>	<b>+/- 0.005 if not specified</b>		
<b>Comments</b>			

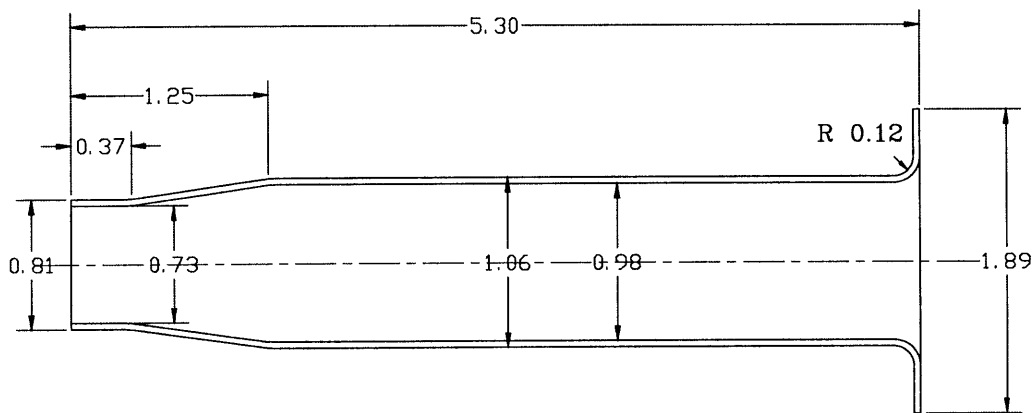


A 0.75"x0.75" stainless steel mesh is spot-welded on the nickel (or stainless steel plate), covering the 0.5" hole in the center. Conductive composite (Dupont) is applied to the mesh where it is not covering the hole to improve thermal contact.

The Stainless steel mesh is manufactured by Buckbee-Mears St. Paul:

304 Stainless Steel  
 Thickness: 0.002"  
 Hole size: 0.003" (Cone/grade hole)  
 Pitch: 0.006"  
 Orientation: 60°  
 Opening: 23%

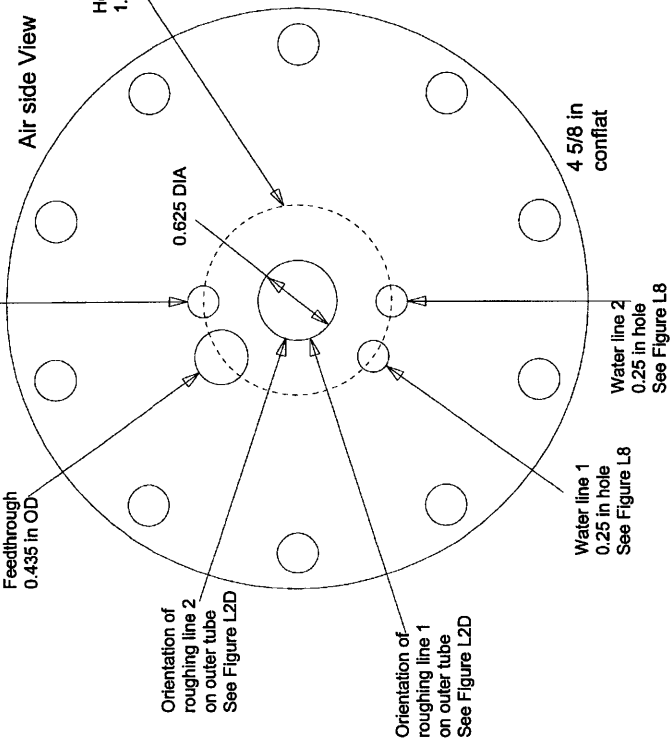
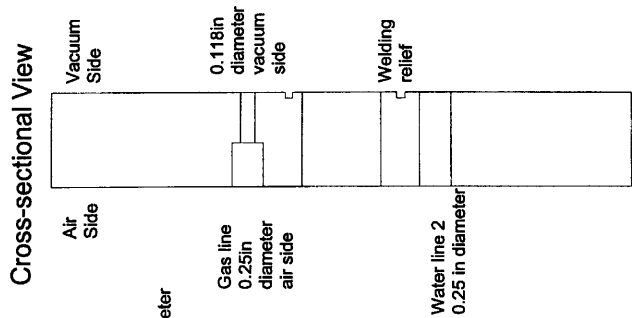
Massachusetts Institute of Technology			
Department of Chemical Engineering			
Part	ECR face plate		
Filename			
Designer	Jane Chang	Date	1/26/96
Contractor	Sharon Vacuum	Date	
Scale		Unit	Inch
Quantity	2	Material	Nickel
Tolerance	+/- 0.005 if not specified		
Comments			



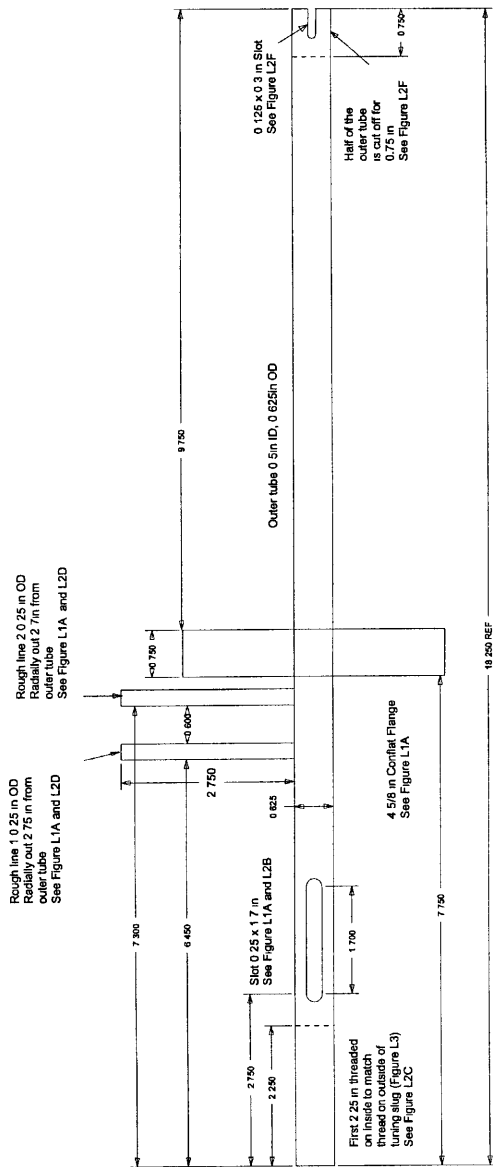
Massachusetts Institute of Technology			
Department of Chemical Engineering			
Part	ECR quartz liner		
Filename	A_LINER.DWG		
Designer	Jane Chang	Date	5/94
Contractor	Finkenbeiner	Date	
Scale	1:1	Unit	inch
Quantity	1	Material	quartz
Tolerance	+/- 0.01 if not specified		
Comments			

Diagram shows orientation of different part of the atom source

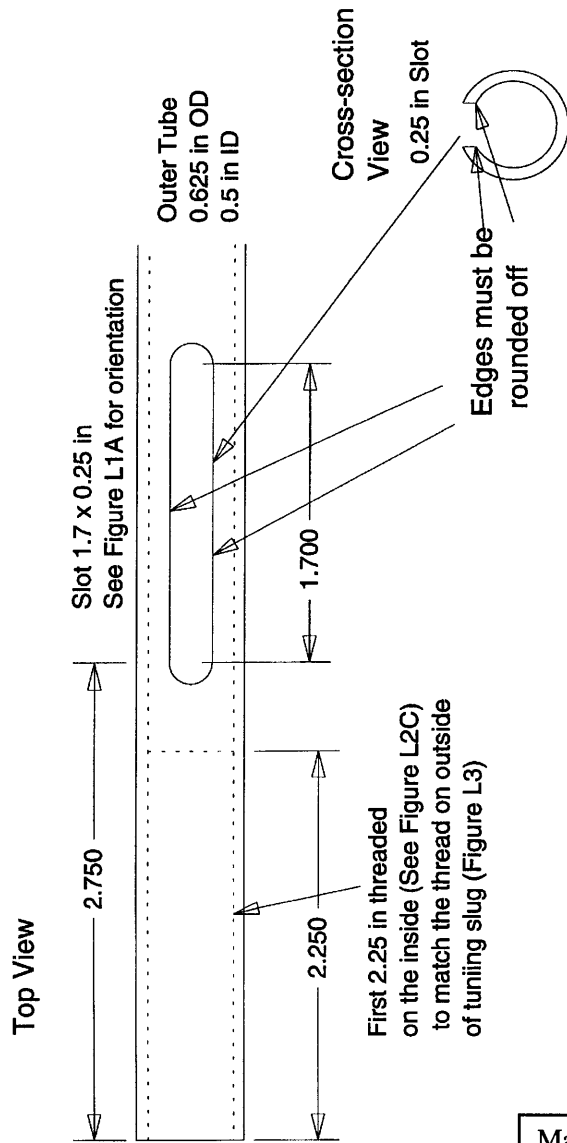
Gas line Air side 0.25 in OD Vacuum side 0.118in OD (FigL7) and Orientation of slot on outer conductor See Fig L2A and L2B



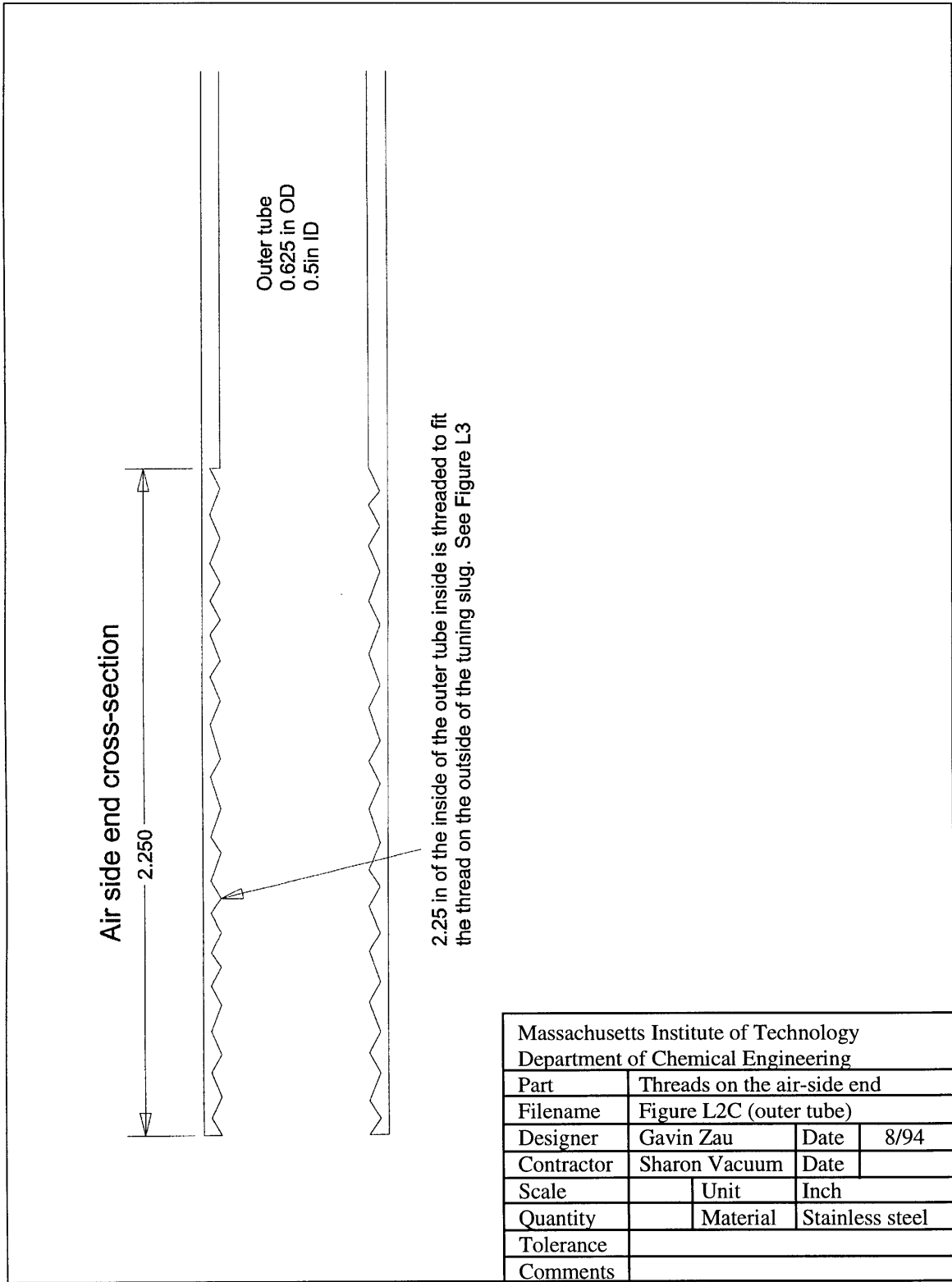
Massachusetts Institute of Technology			
Department of Chemical Engineering			
Part	Conflat flange(air side)		
Filename	Figure L1A		
Designer	Gavin Zau	Date	8/94
Contractor	Sharon Vacuum	Date	
Scale		Unit	Inch
Quantity		Material	Stainless steel
Tolerance			
Comments			

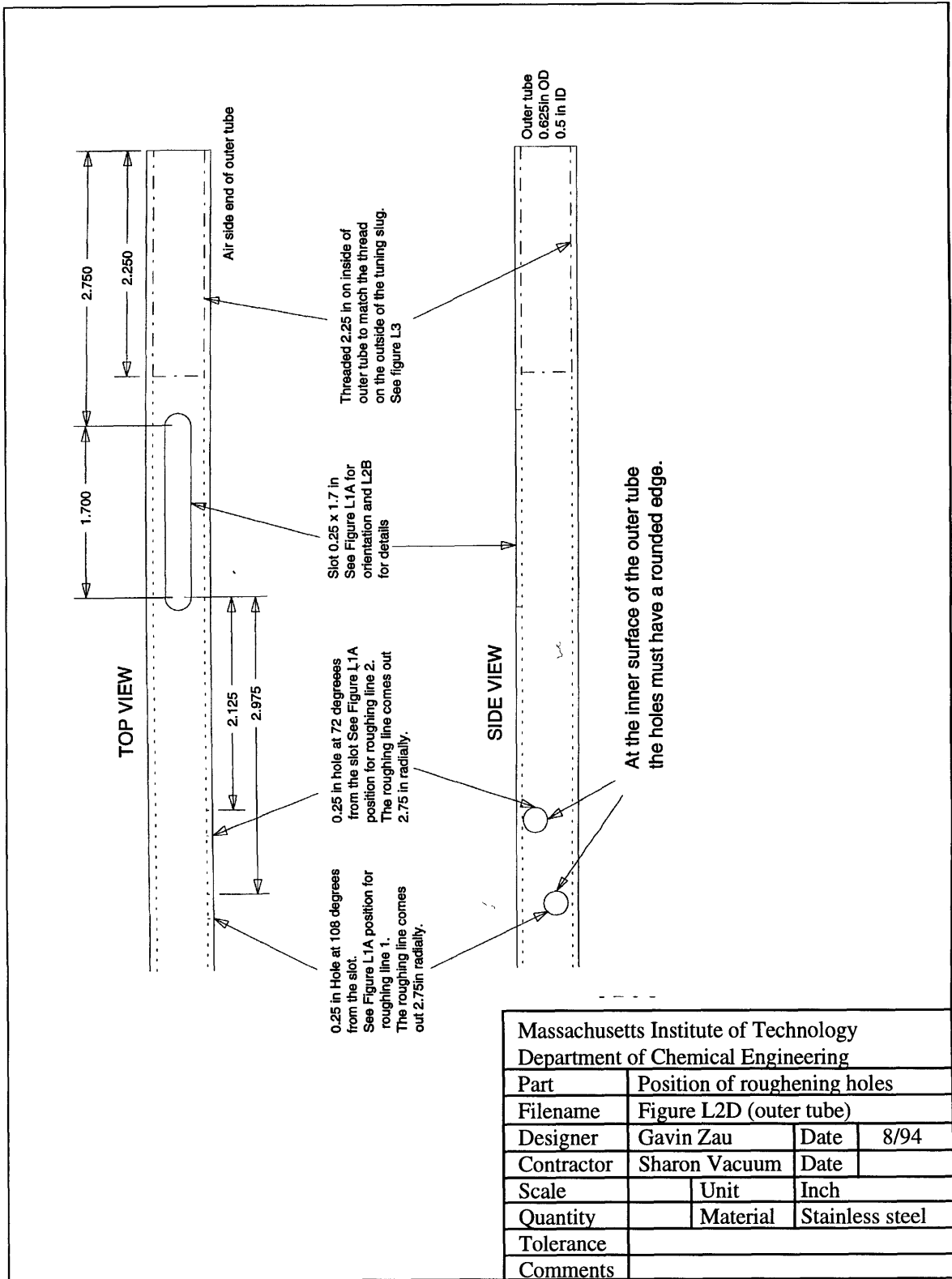


Massachusetts Institute of Technology Department of Chemical Engineering			
Part	Outer tube with conflat		
Filename	Figure L2A		
Designer	Gavin Zau	Date	8/94
Contractor	Sharon Vacuum	Date	
Scale		Unit	Inch
Quantity		Material	Stainless steel
Tolerance			
Comments			



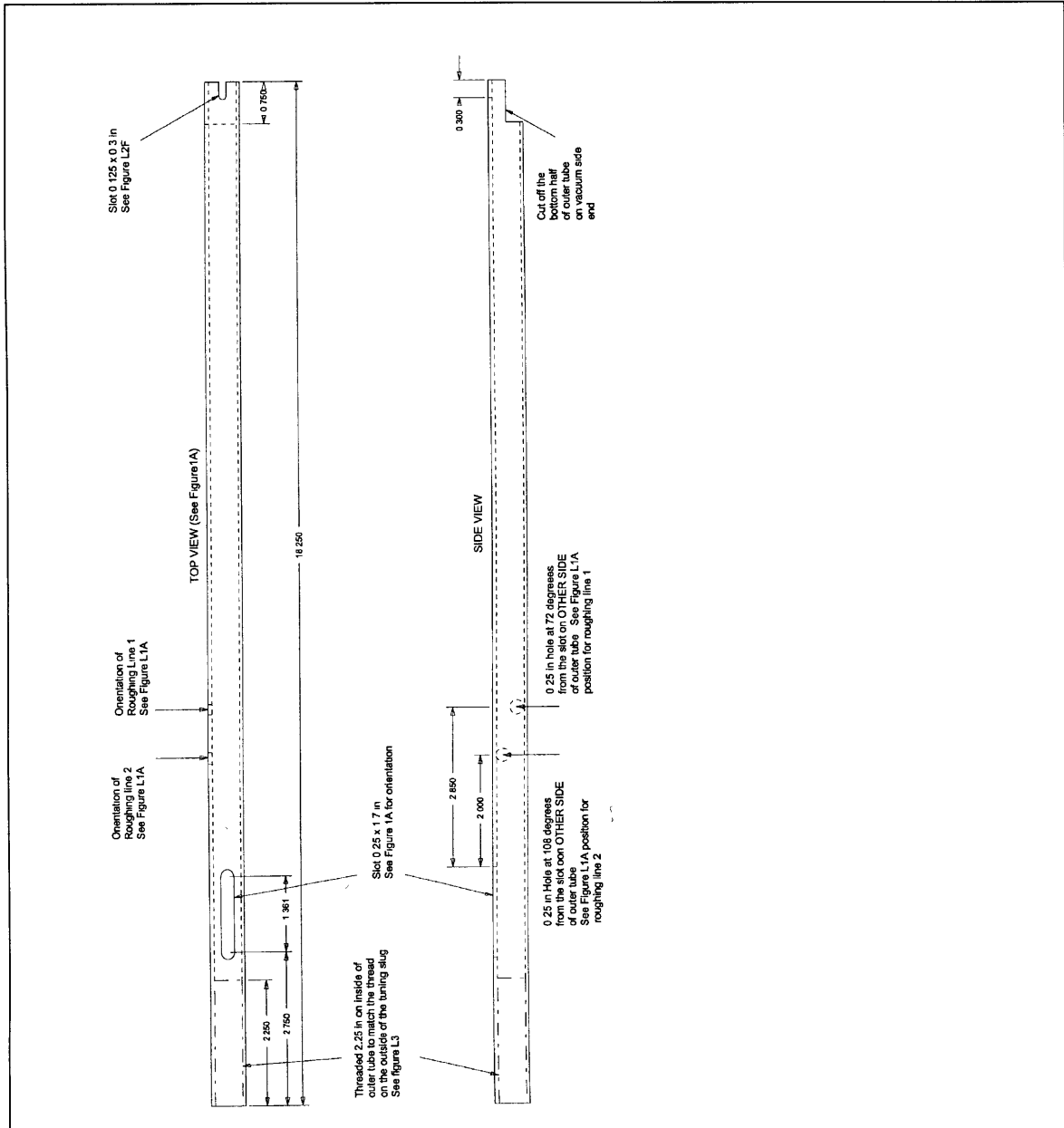
Massachusetts Institute of Technology Department of Chemical Engineering			
Part	Air-side end of outer tube		
Filename	Figure L2B		
Designer	Gavin Zau	Date	8/94
Contractor	Sharon Vacuum	Date	
Scale		Unit	Inch
Quantity		Material	Stainless steel
Tolerance			
Comments			



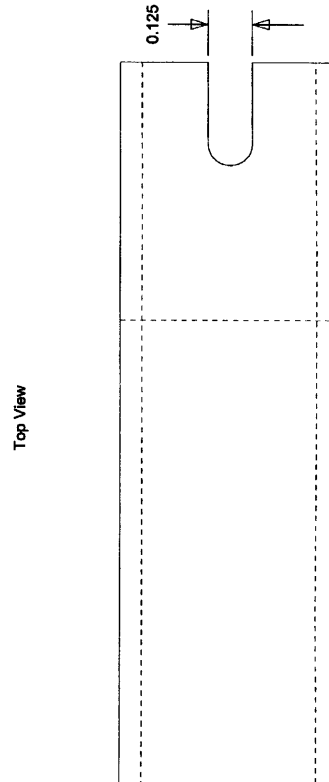
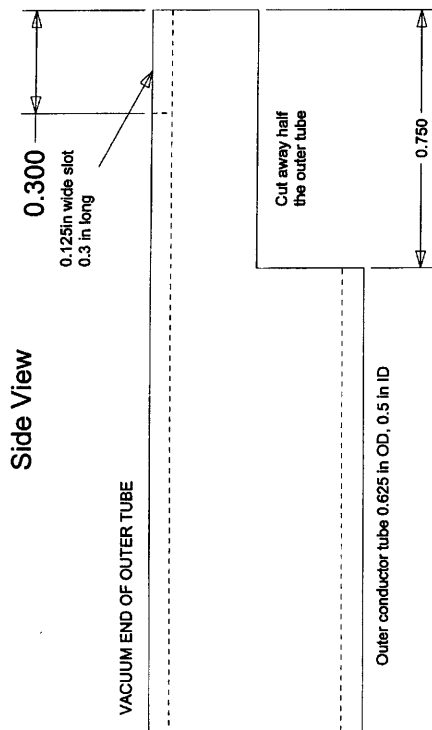


Massachusetts Institute of Technology			
Department of Chemical Engineering			
Part	Position of roughening holes		
Filename	Figure L2D (outer tube)		
Designer	Gavin Zau	Date	8/94
Contractor	Sharon Vacuum	Date	
Scale		Unit	Inch
Quantity		Material	Stainless steel
Tolerance			
Comments			

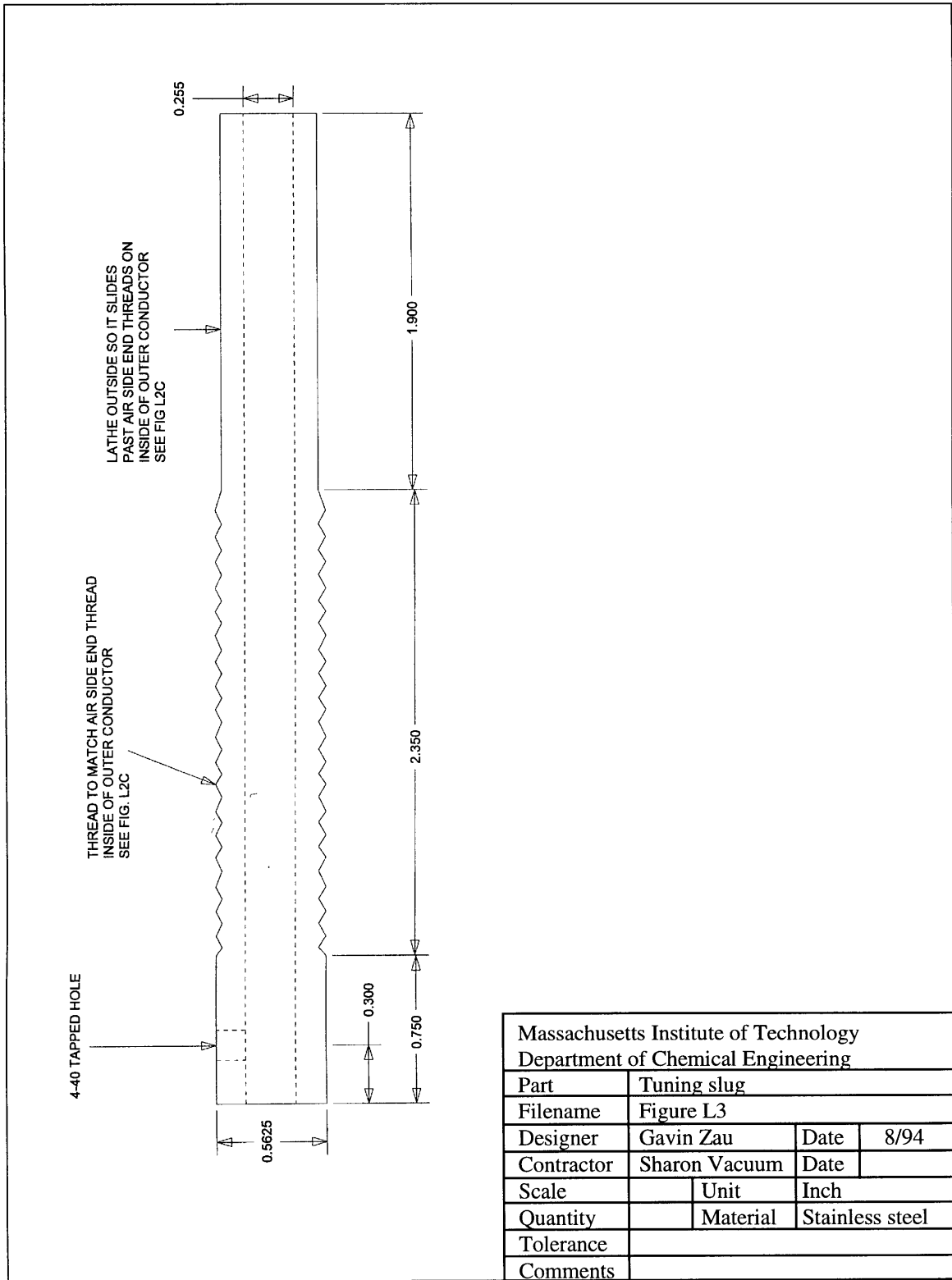


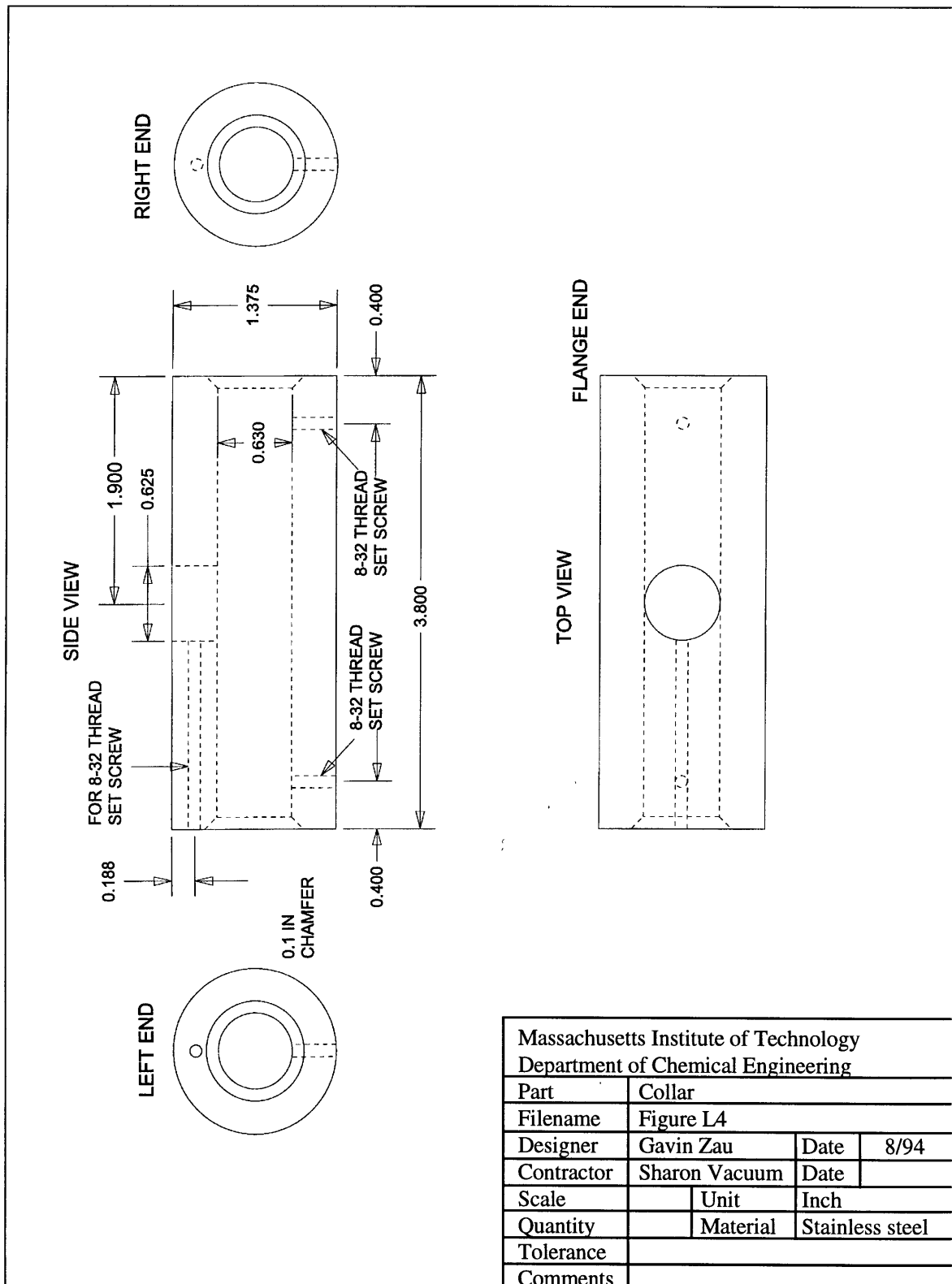


Massachusetts Institute of Technology Department of Chemical Engineering			
Part	Outer tube (vacuum end)		
Filename	Figure L2E		
Designer	Gavin Zau	Date	8/94
Contractor	Sharon Vacuum	Date	
Scale		Unit	Inch
Quantity		Material	Stainless steel
Tolerance			
Comments			

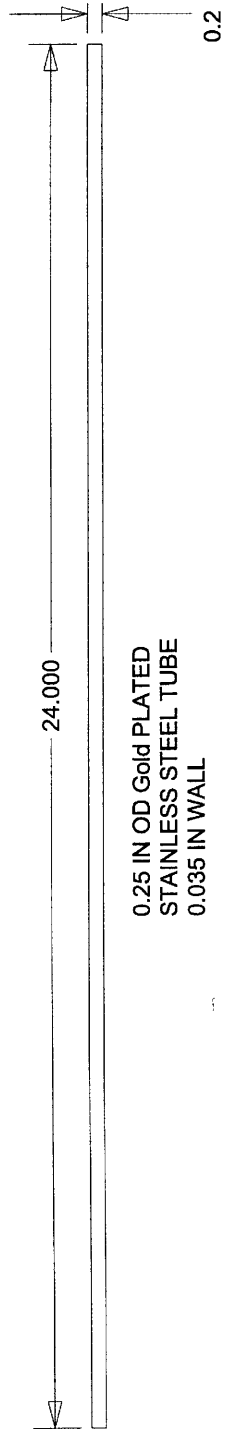


Massachusetts Institute of Technology			
Department of Chemical Engineering			
Part	Outer tube (vacuum end)		
Filename	Figure L2F		
Designer	Gavin Zau	Date	8/94
Contractor	Sharon Vacuum	Date	
Scale		Unit	Inch
Quantity		Material	Stainless steel
Tolerance			
Comments			



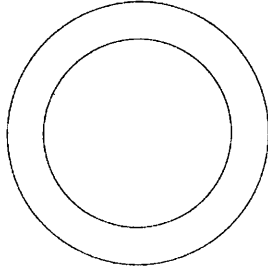


Massachusetts Institute of Technology			
Department of Chemical Engineering			
Part	Collar		
Filename	Figure L4		
Designer	Gavin Zau	Date	8/94
Contractor	Sharon Vacuum	Date	
Scale		Unit	Inch
Quantity		Material	Stainless steel
Tolerance			
Comments			

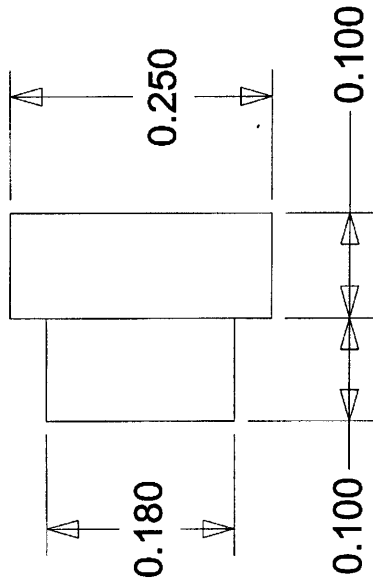


Massachusetts Institute of Technology Department of Chemical Engineering			
Part	Center conductor		
Filename	Figure L5A		
Designer	Gavin Zau	Date	8/94
Contractor	Sharon Vacuum	Date	
Scale		Unit	Inch
Quantity		Material	Stainless steel
Tolerance			
Comments			

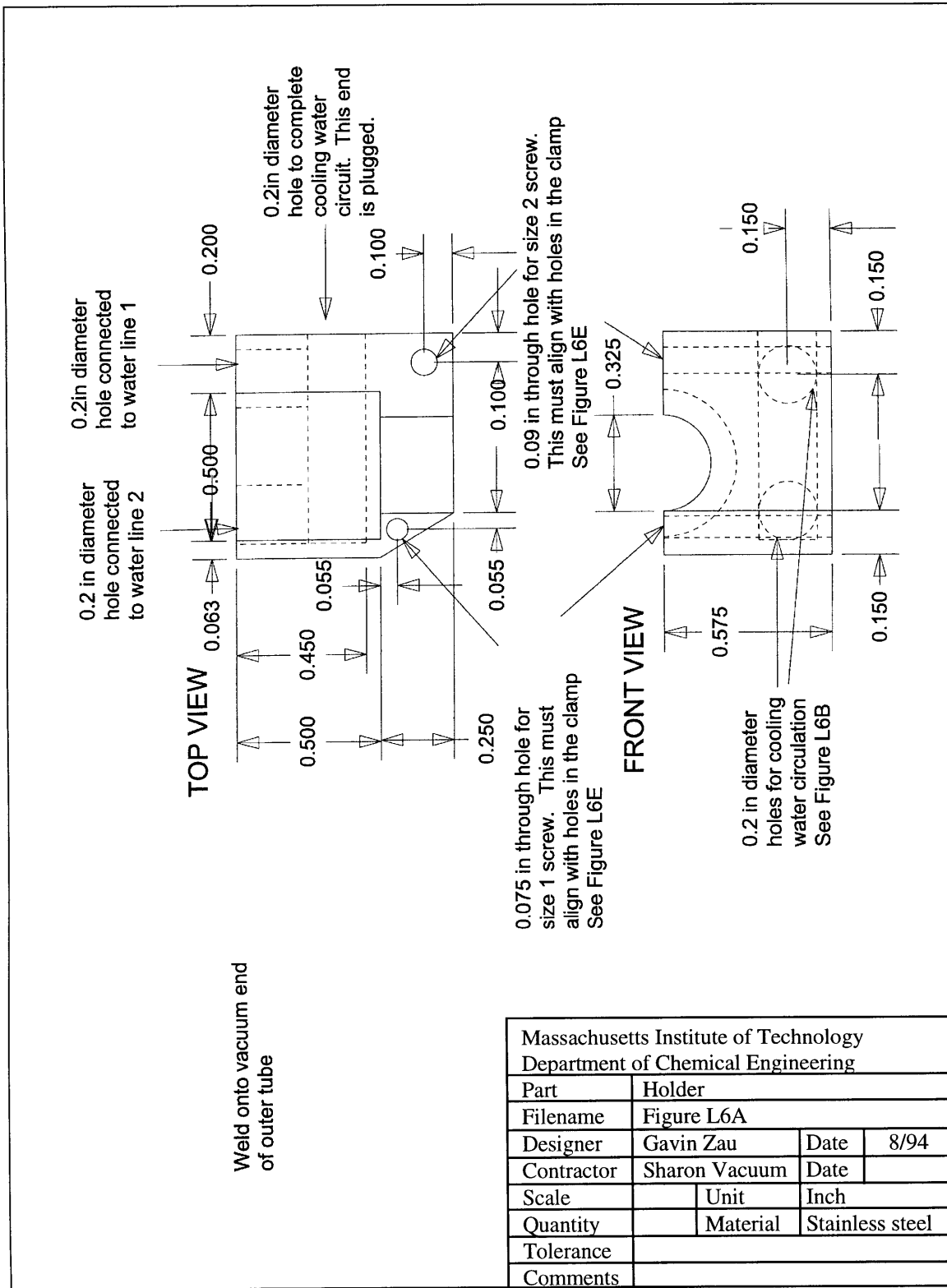
BACK VIEW



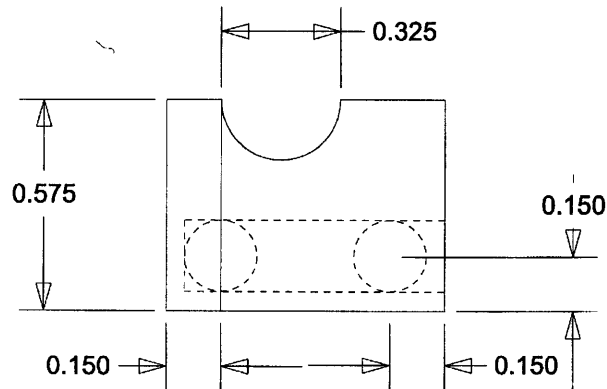
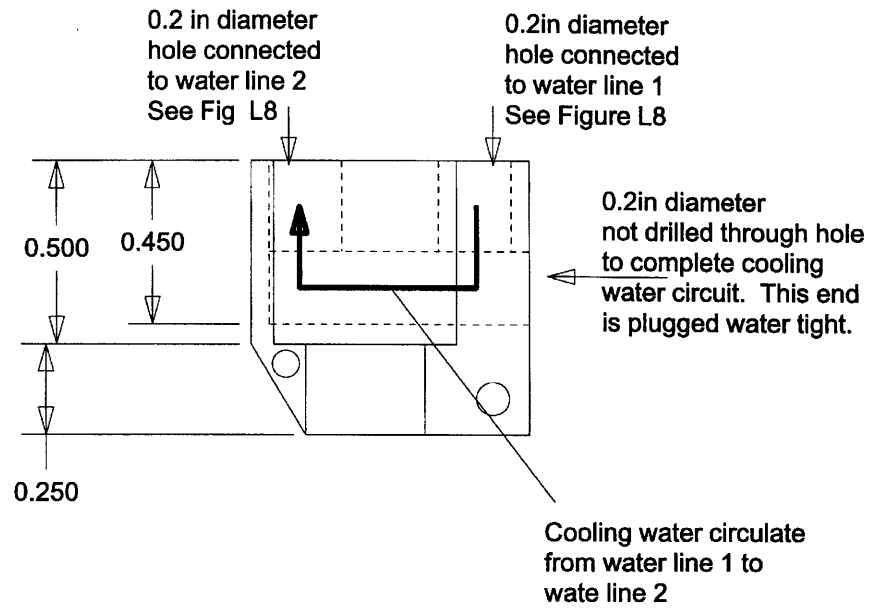
SIDE VIEW



Massachusetts Institute of Technology Department of Chemical Engineering			
Part	Center conductor tip		
Filename	Figure L5B		
Designer	Gavin Zau	Date	8/94
Contractor	Sharon Vacuum	Date	
Scale		Unit	Inch
Quantity		Material	Stainless steel
Tolerance			
Comments			



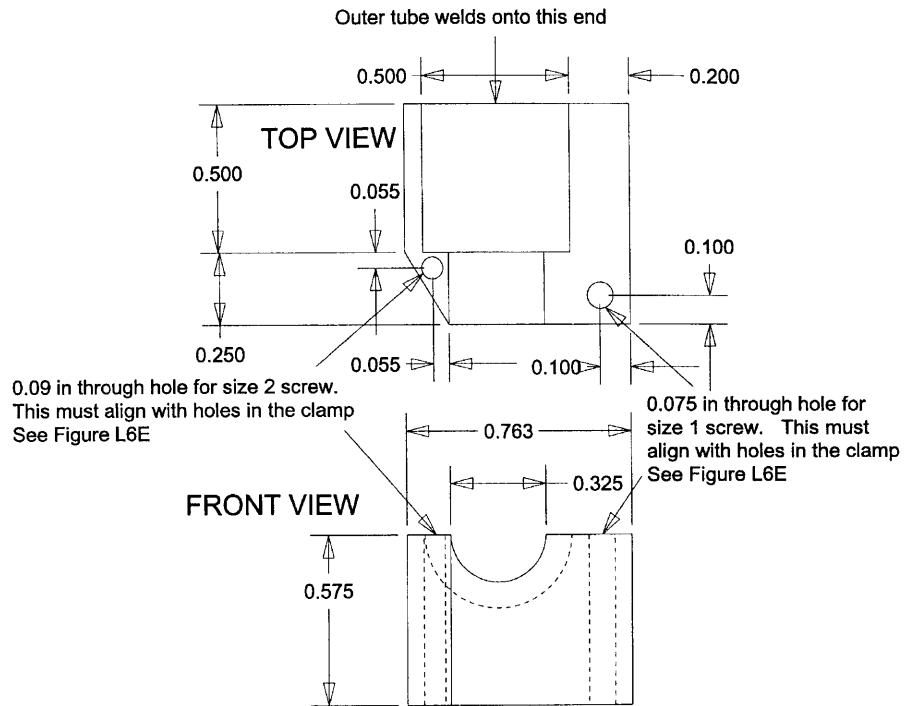
Massachusetts Institute of Technology Department of Chemical Engineering			
Part	Holder		
Filename	Figure L6A		
Designer	Gavin Zau	Date	8/94
Contractor	Sharon Vacuum	Date	
Scale	Unit	Inch	
Quantity	Material	Stainless steel	
Tolerance			
Comments			



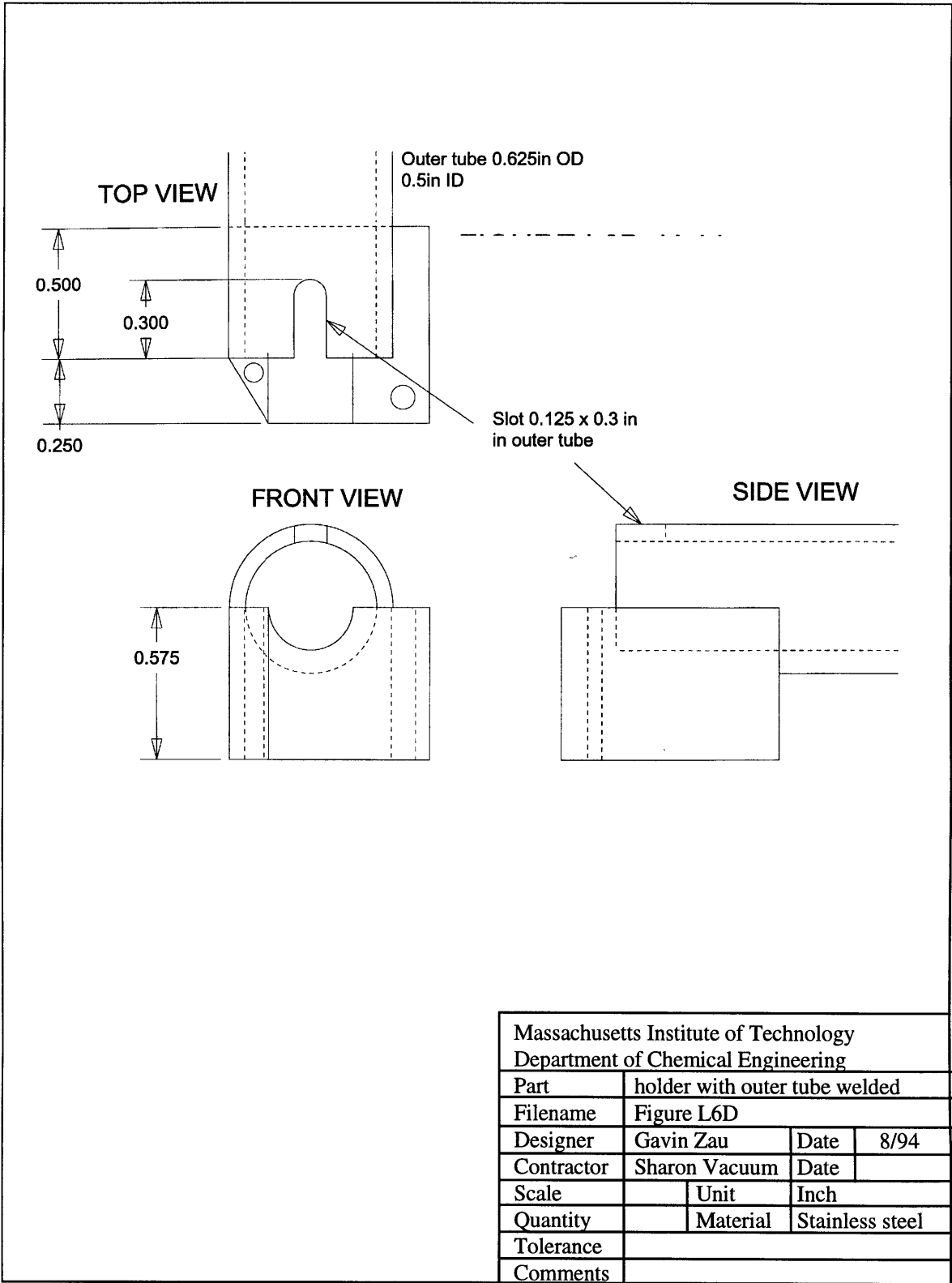
Massachusetts Institute of Technology			
Department of Chemical Engineering			
Part	Colling water circulation holes		
Filename	Figure L6B		
Designer	Gavin Zau	Date	8/94
Contractor	Sharon Vacuum	Date	
Scale		Unit	Inch
Quantity		Material	Stainless steel
Tolerance			
Comments			



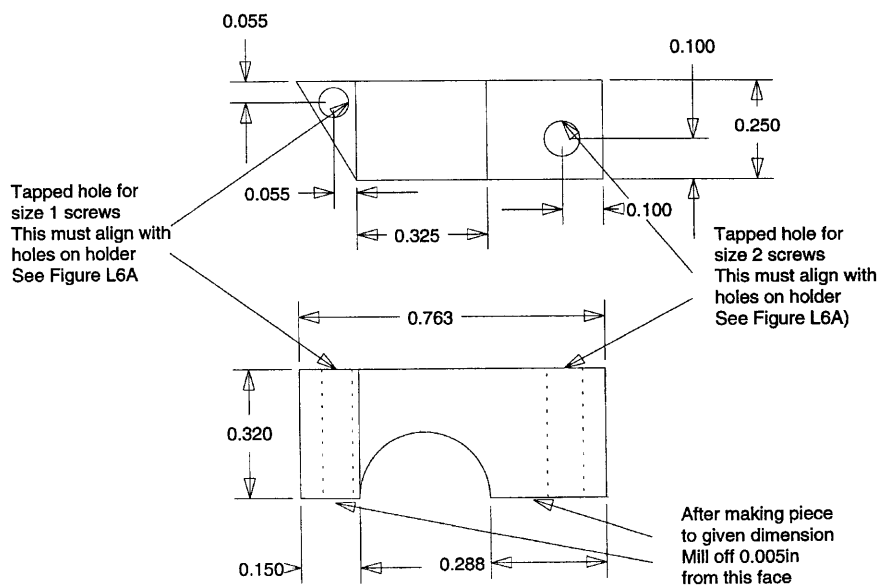
Weld onto vacuum end  
of outer tube



Massachusetts Institute of Technology			
Department of Chemical Engineering			
Part	holder with water holes hidden		
Filename	Figure L6C		
Designer	Gavin Zau	Date	8/94
Contractor	Sharon Vacuum	Date	
Scale		Unit	Inch
Quantity		Material	Stainless steel
Tolerance			
Comments			

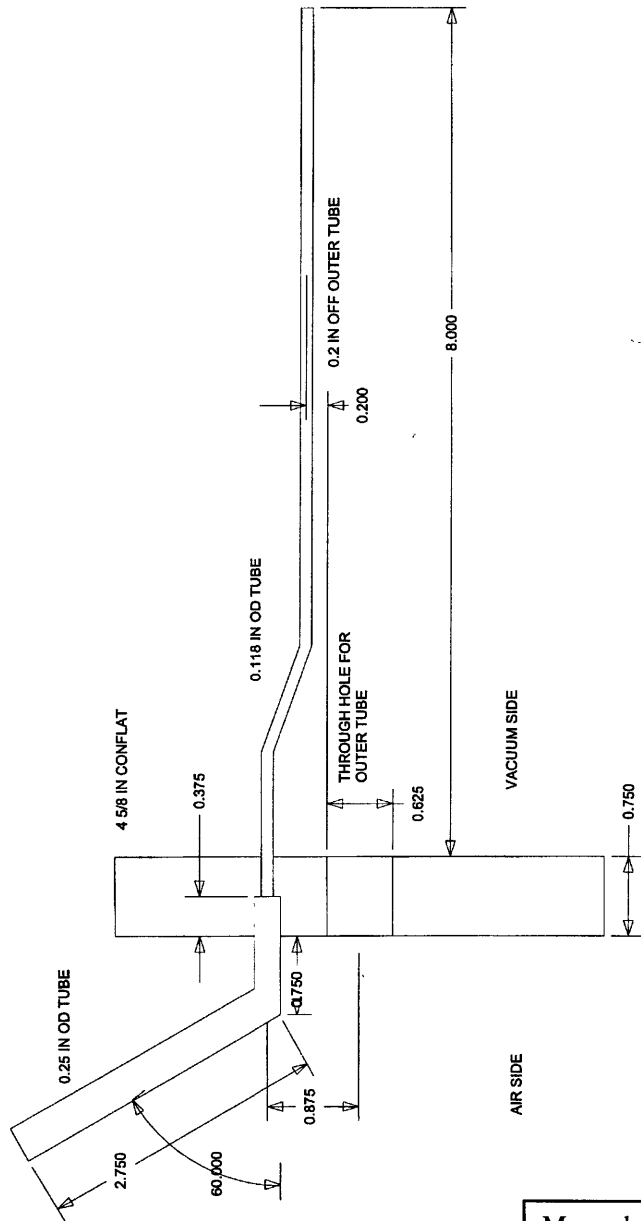


Note the 2 tapped holes are for different size screws and the holes must line up with the through holes in the holder  
See Figure L6A



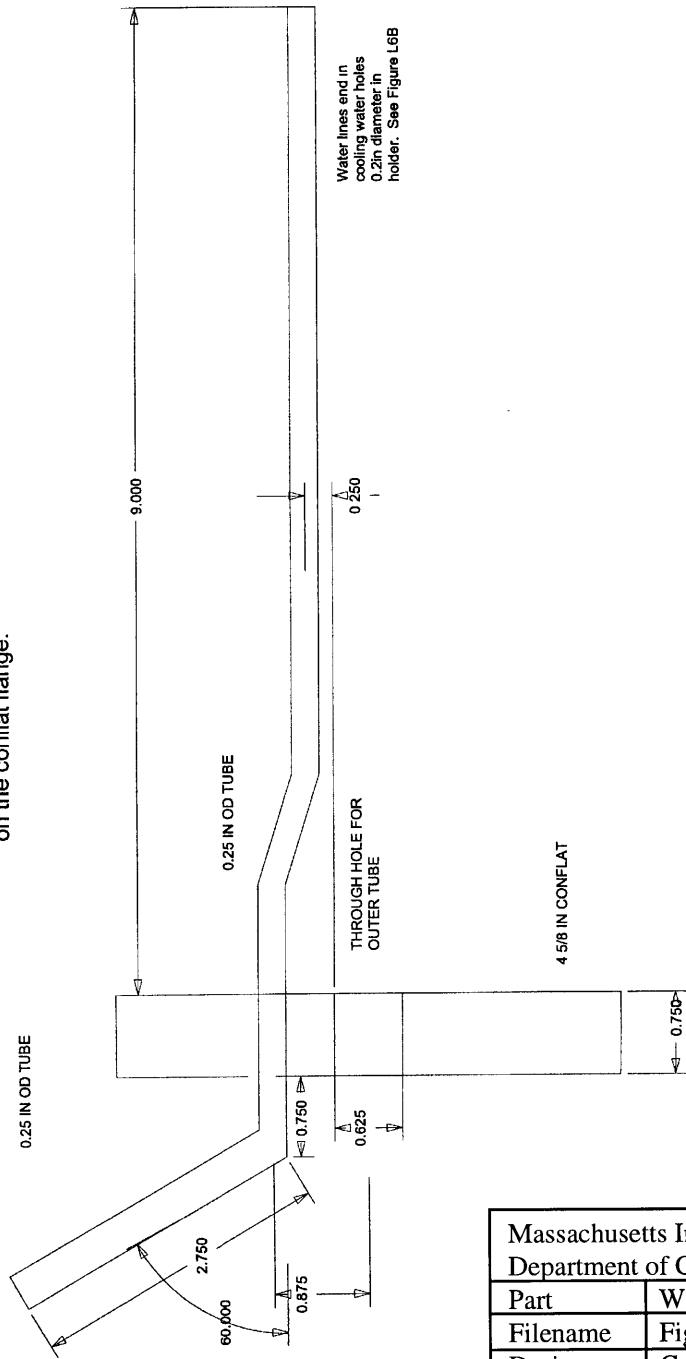
Massachusetts Institute of Technology Department of Chemical Engineering			
Part	Clamp for holder		
Filename	Figure L6E		
Designer	Gavin Zau	Date	8/94
Contractor	Sharon Vacuum	Date	
Scale		Unit	Inch
Quantity		Material	Stainless steel
Tolerance			
Comments			

See Figure L1A for alignment on 4 5/8in flange

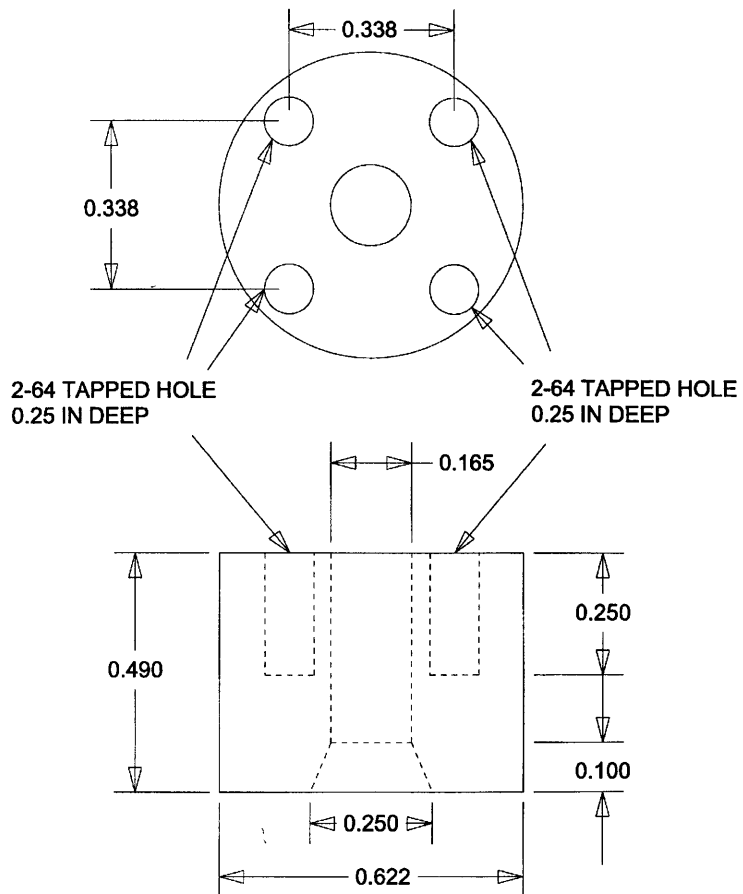


Massachusetts Institute of Technology Department of Chemical Engineering			
Part	Gas line		
Filename	Figure L7		
Designer	Gavin Zau	Date	8/94
Contractor	Sharon Vacuum	Date	
Scale		Unit	Inch
Quantity		Material	Stainless steel
Tolerance			
Comments			

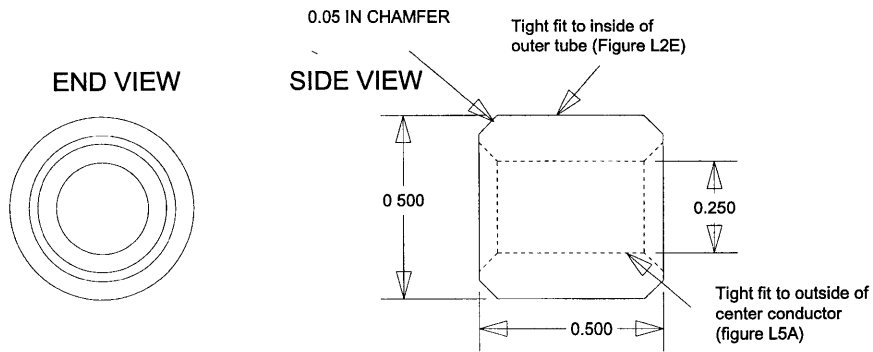
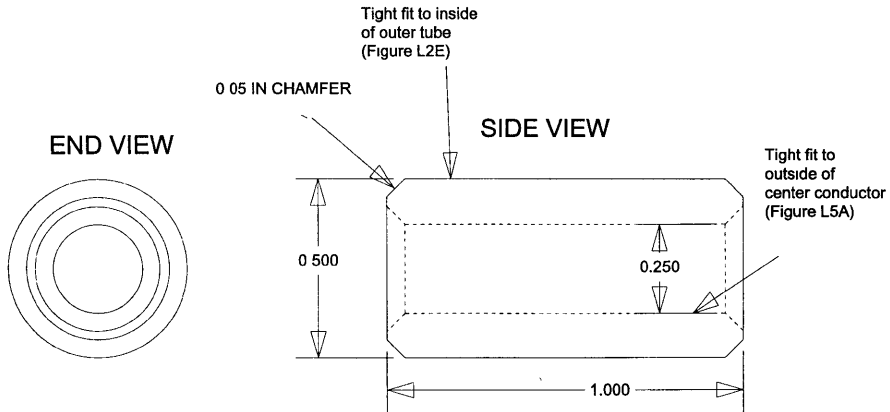
This design applies to both water line 1 and water line 2. See figure L1A for alignment on the conflat flange.



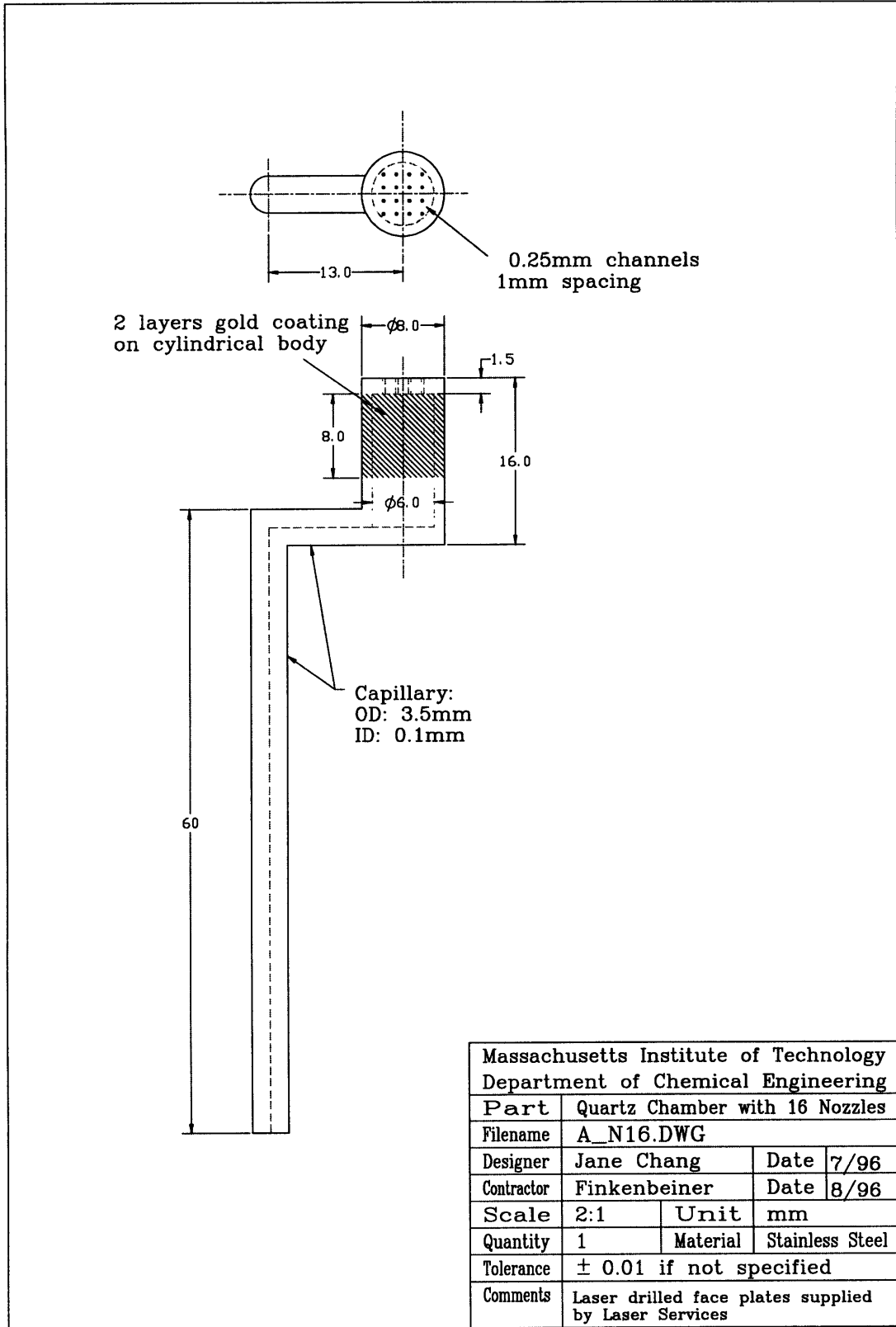
Massachusetts Institute of Technology Department of Chemical Engineering			
Part	Water line		
Filename	Figure L8		
Designer	Gavin Zau	Date	8/94
Contractor	Sharon Vacuum	Date	
Scale		Unit	Inch
Quantity		Material	Stainless steel
Tolerance			
Comments			



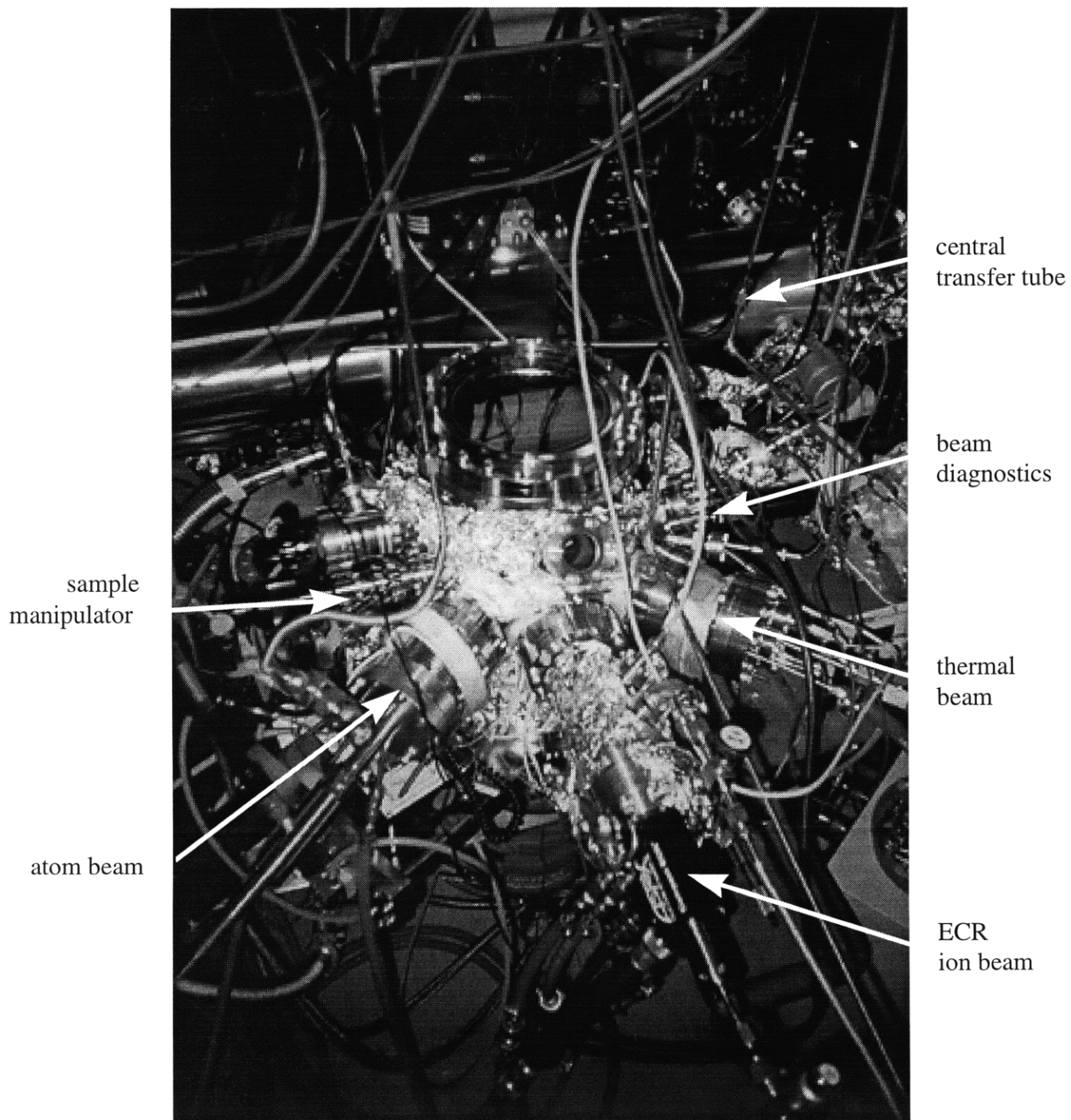
Massachusetts Institute of Technology			
Department of Chemical Engineering			
Part	Type N connector holder		
Filename	Figure L9		
Designer	Gavin Zau	Date	8/94
Contractor	Sharon Vacuum	Date	
Scale		Unit	Inch
Quantity		Material	Stainless steel
Tolerance			
Comments			

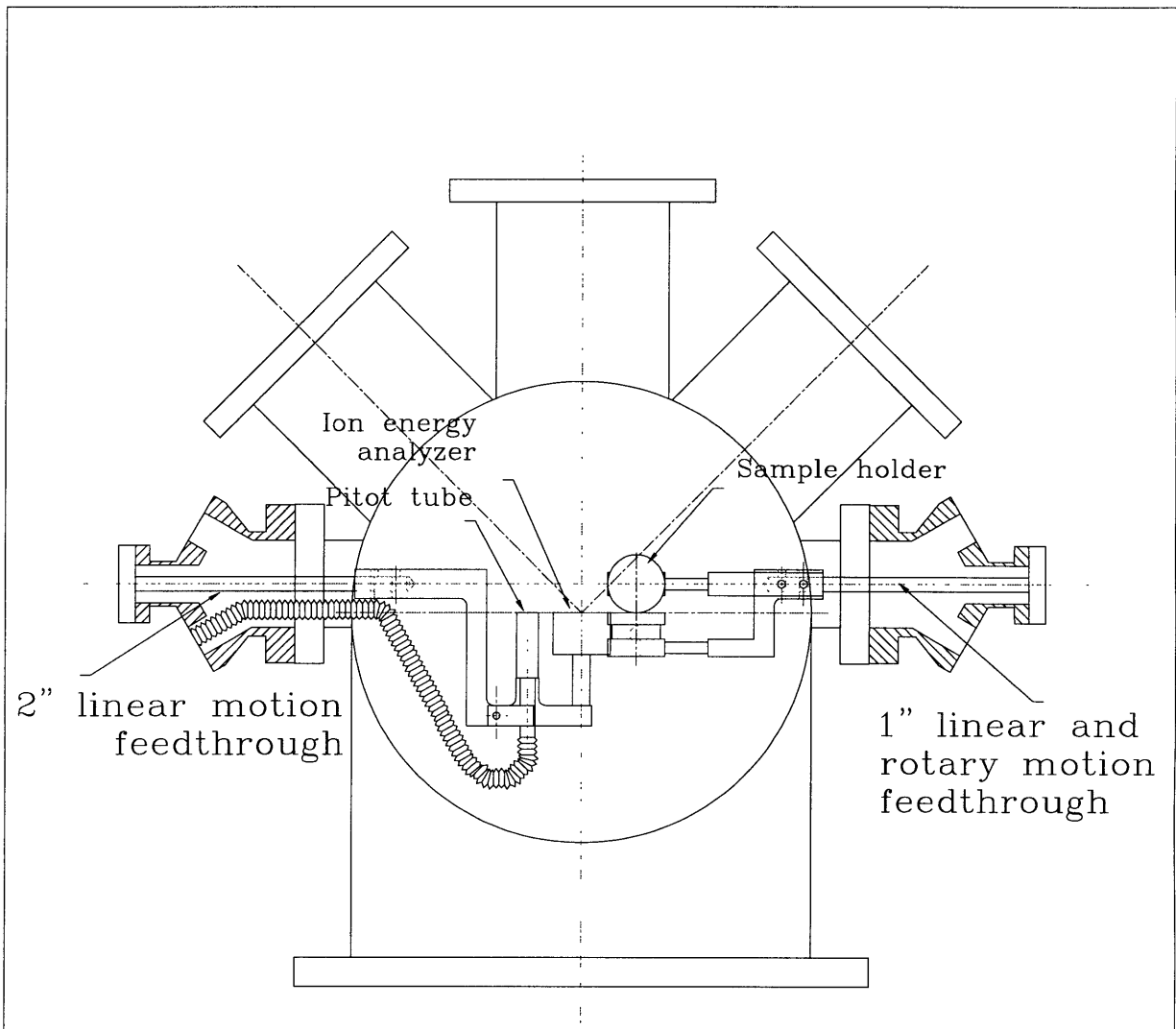


Massachusetts Institute of Technology			
Department of Chemical Engineering			
Part	Teflon seal		
Filename	Figure L10		
Designer	Gavin Zau	Date	8/94
Contractor	Sharon Vacuum	Date	
Scale		Unit	Inch
Quantity		Material	Teflon
Tolerance			
Comments			

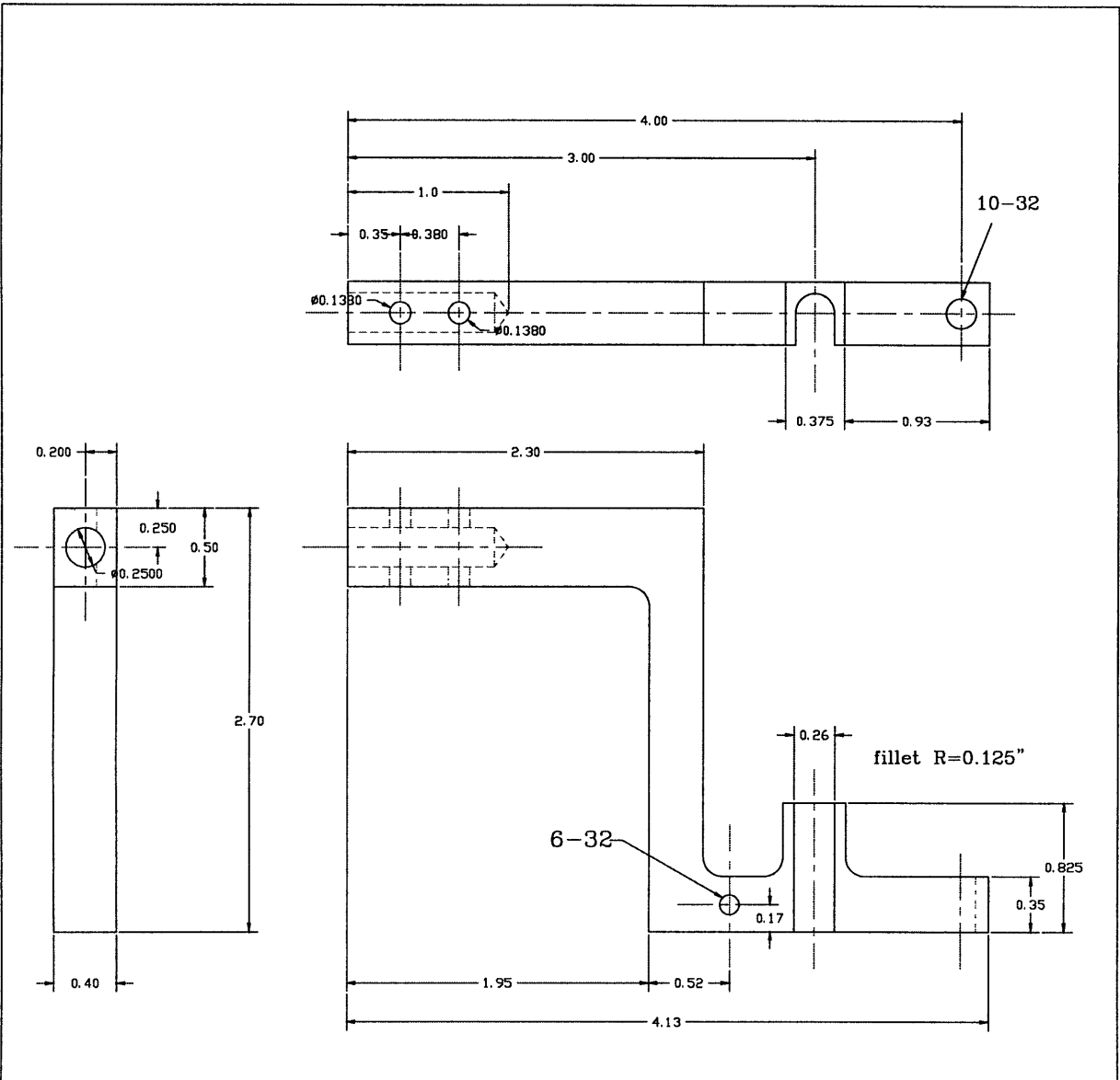




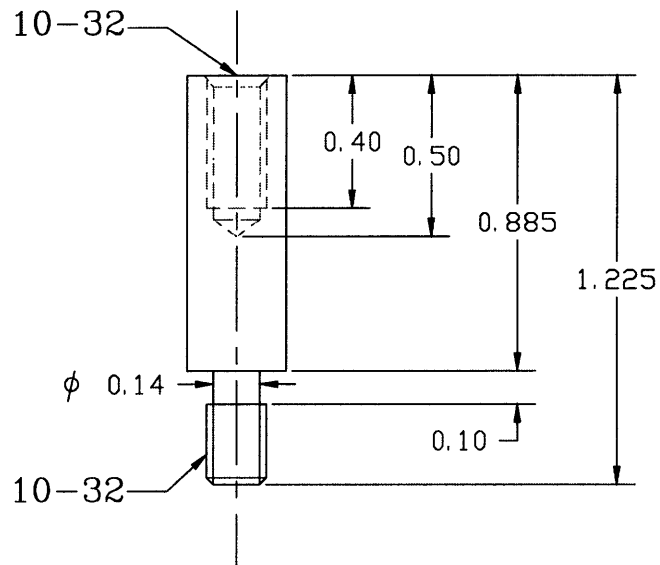
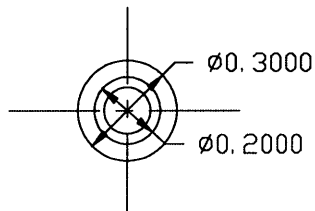




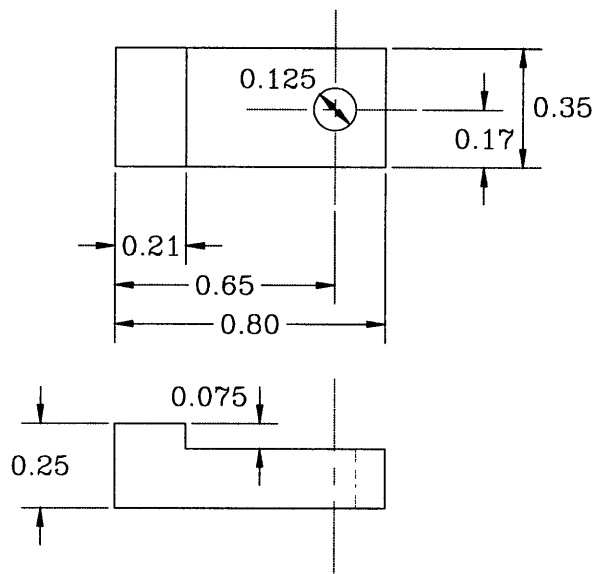
Massachusetts Institute of Technology			
Department of Chemical Engineering			
Part	Probes and sample assembly		
Filename	A_2SETUP.DWG		
Designer	Jane Chang	Date	4/97
Contractor		Date	
Scale		Unit	inch
Quantity	1	Material	Stainless Steel
Tolerance	+/- 0.01 if not specified		
Comments			



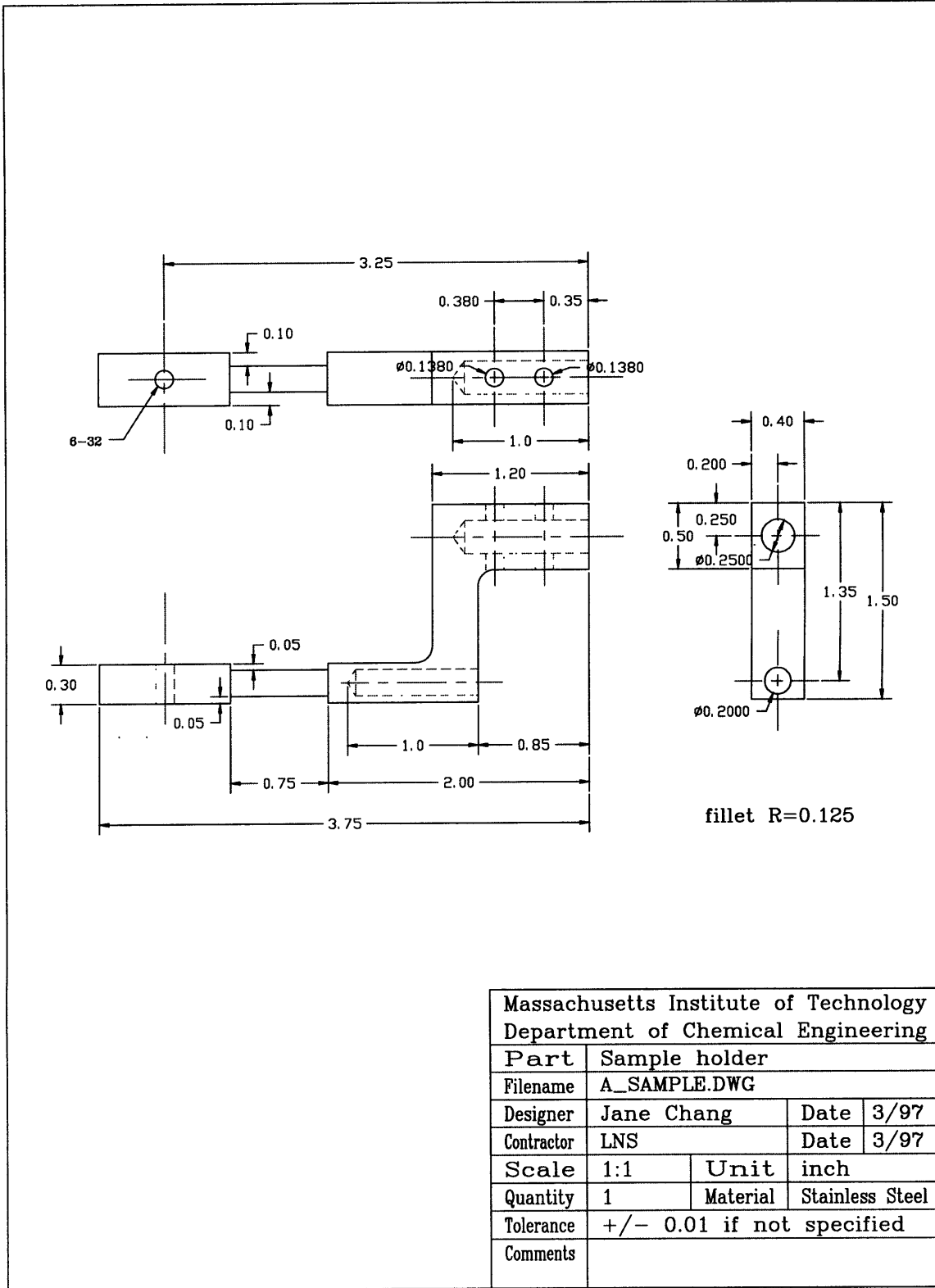
Massachusetts Institute of Technology			
Department of Chemical Engineering			
Part	Probe mount		
Filename	A_DIAG.DWG		
Designer	Jane Chang	Date	3/97
Contractor	LNS	Date	3/97
Scale	1:1	Unit	inch
Quantity	1	Material	Stainless Steel
Tolerance	+/- 0.01 if not specified		
Comments			



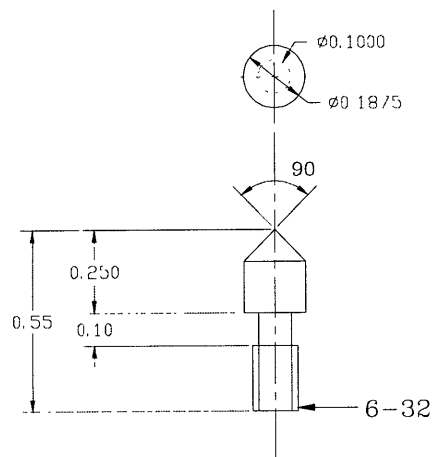
Massachusetts Institute of Technology			
Department of Chemical Engineering			
Part	Holder for ion analyzer		
Filename	A_IEDF.DWG		
Designer	Jane Chang	Date	3/97
Contractor	LNS	Date	3/97
Scale	2:1	Unit	inch
Quantity	1	Material	Stainless Steel
Tolerance	+/- 0.01 if not specified		
Comments			



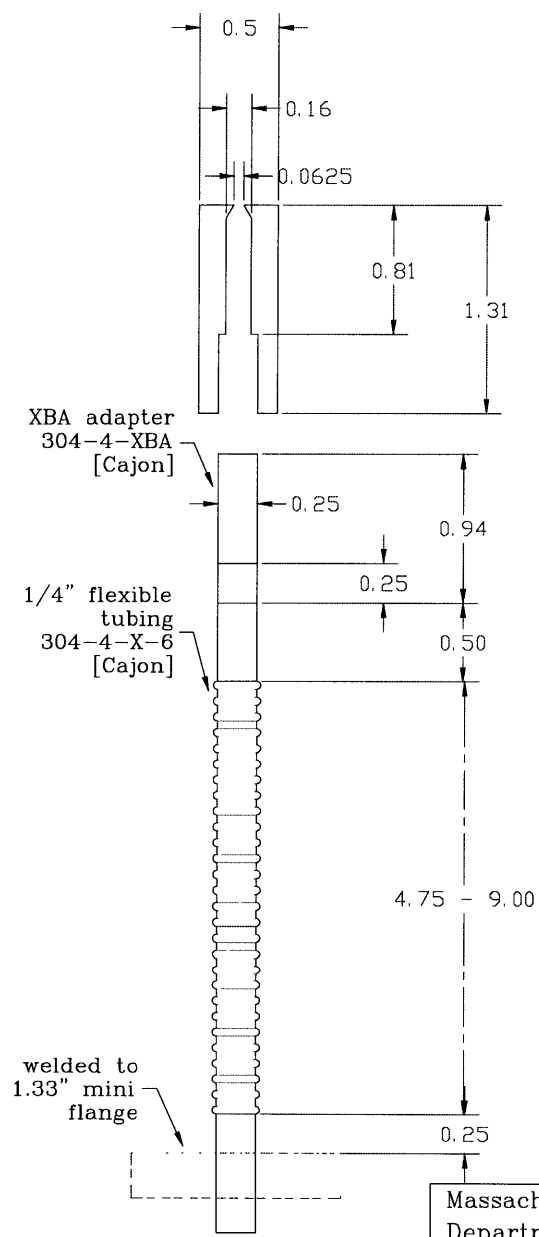
Massachusetts Institute of Technology			
Department of Chemical Engineering			
Part	Clamp		
Filename	A_CLAMP.DWG		
Designer	Jane Chang	Date	3/97
Contractor	LNS	Date	3/97
Scale	2:1	Unit	inch
Quantity	1	Material	Stainless Steel
Tolerance	+/- 0.01 if not specified		
Comments			



Massachusetts Institute of Technology			
Department of Chemical Engineering			
Part	Sample holder		
Filename	A_SAMPLE.DWG		
Designer	Jane Chang	Date	3/97
Contractor	LNS	Date	3/97
Scale	1:1	Unit	inch
Quantity	1	Material	Stainless Steel
Tolerance	+/- 0.01 if not specified		
Comments			

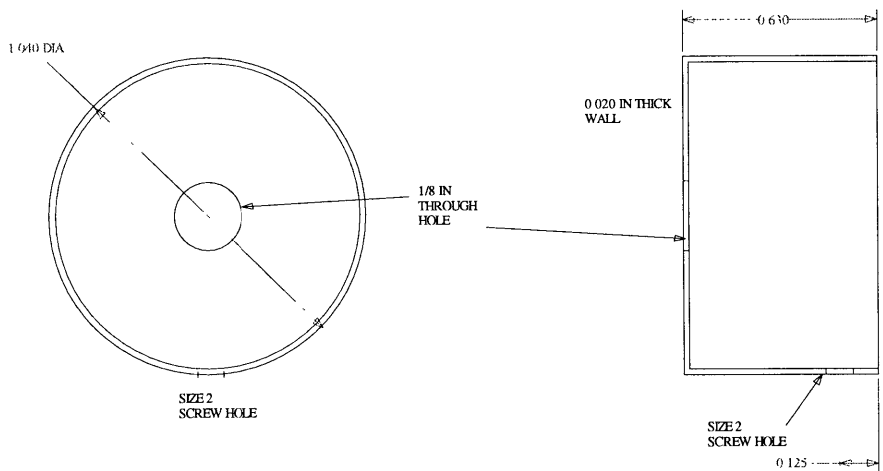


Massachusetts Institute of Technology Department of Chemical Engineering			
Part	Pin for sample holder		
Filename	A_PIN.DWG		
Designer	Jane Chang	Date	3/97
Contractor	LNS	Date	3/97
Scale	2:1	Unit	inch
Quantity	1	Material	Stainless Steel
Tolerance	+/- 0.01 if not specified		
Comments			

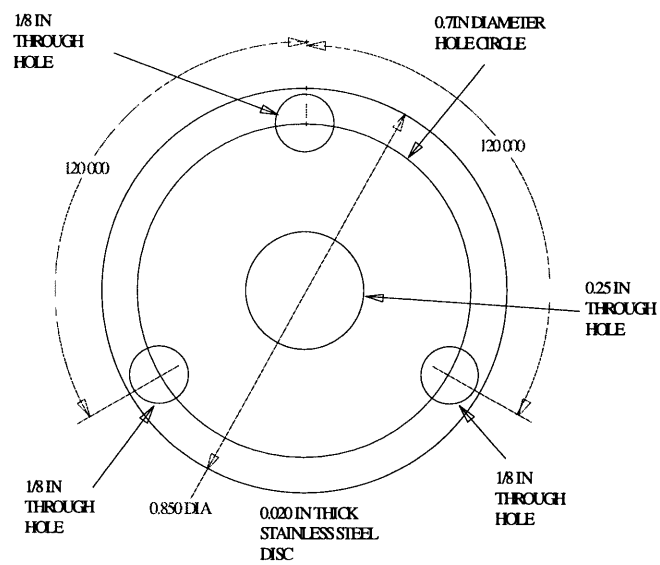


Massachusetts Institute of Technology Department of Chemical Engineering			
Part	Pitot tube		
Filename	A_FLUX.DWG		
Designer	Jane Chang	Date	1/97
Contractor	Sharon Vacuum	Date	1/97
Scale	1:1	Unit	inch
Quantity	1	Material	Stainless Steel
Tolerance	+/- 0.01 if not specified		
Comments			

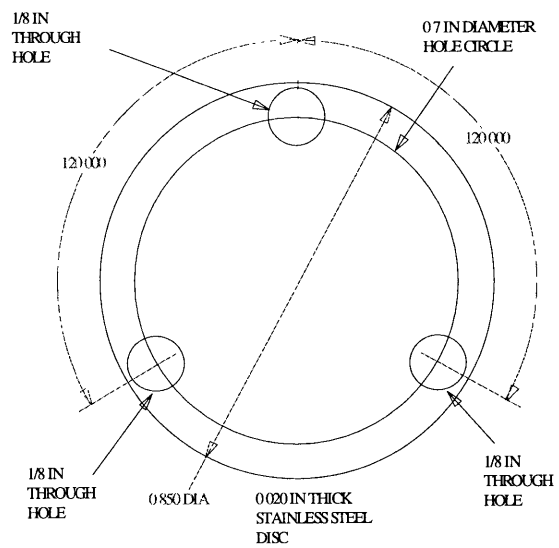




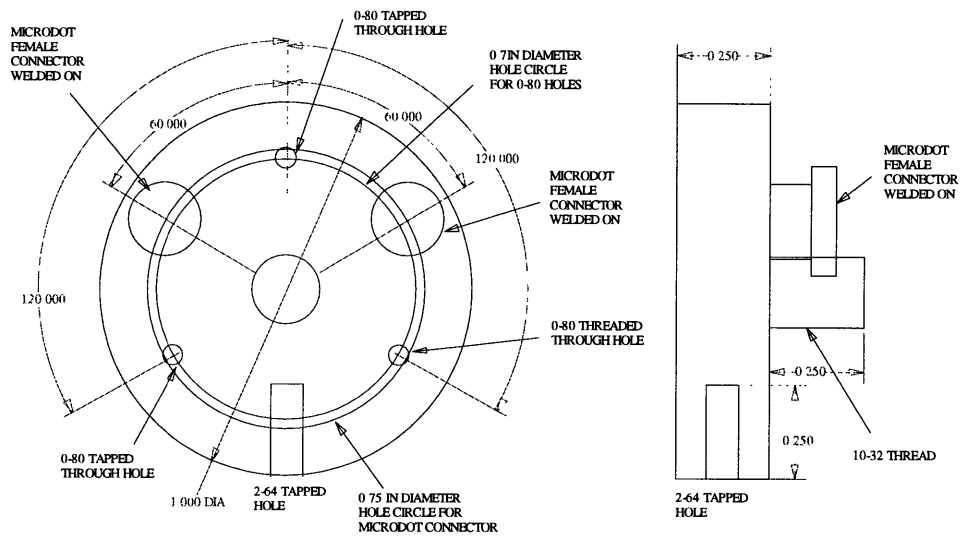
Massachusetts Institute of Technology			
Department of Chemical Engineering			
Part	Ion energy analyzer (1) can		
Filename			
Designer	Jane Chang	Date	4/18/94
Contractor	Sharon Vacuum	Date	
Scale		Unit	Inch
Quantity	1	Material	Stainless steel
Tolerance	+/- 0.005 if not specified		
Comments			



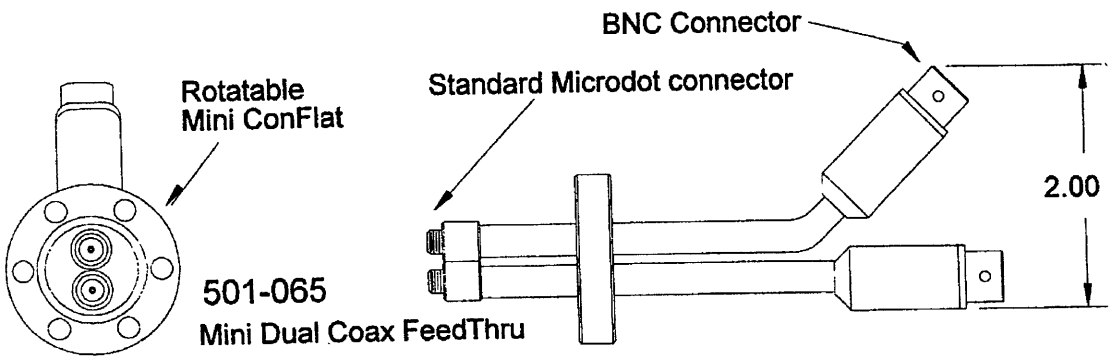
Massachusetts Institute of Technology			
Department of Chemical Engineering			
Part	Ion energy analyzer (2) repeller		
Filename			
Designer	Jane Chang	Date	4/18/94
Contractor	Sharon Vacuum	Date	
Scale		Unit	Inch
Quantity	5	Material	Stainless steel
Tolerance	+/- 0.005 if not specified		
Comments			



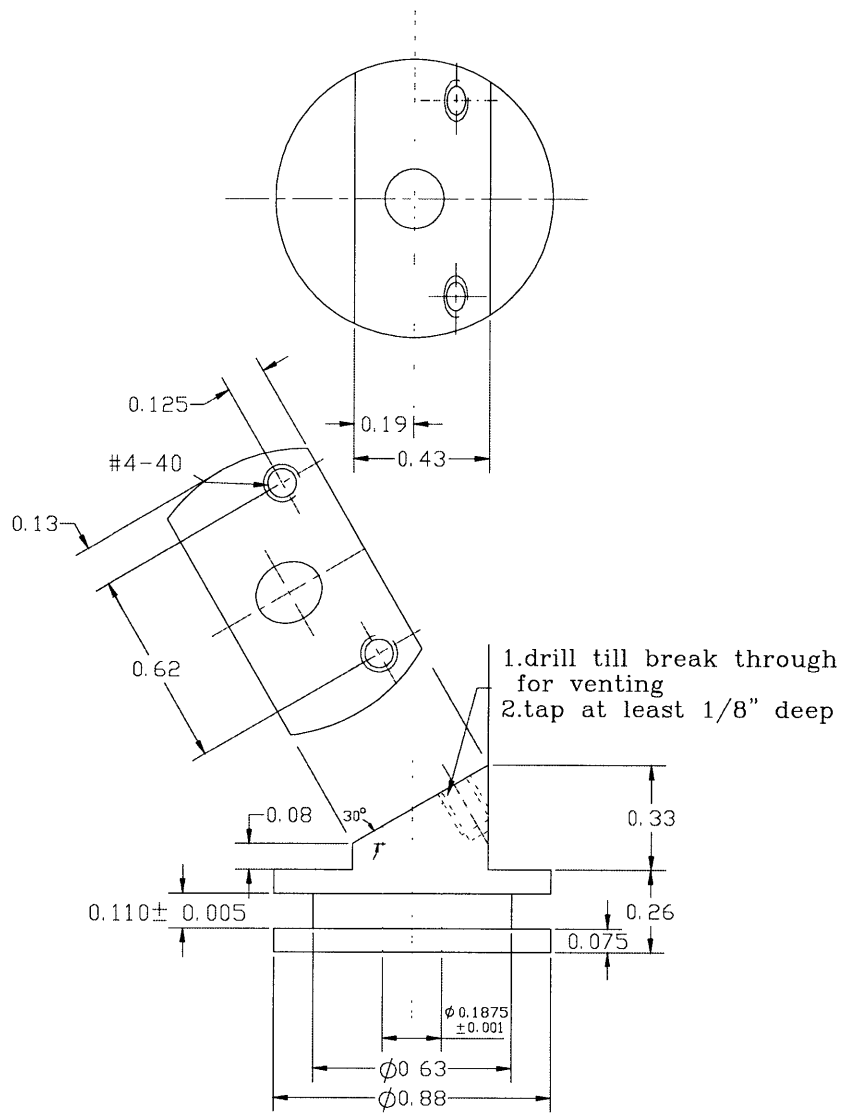
Massachusetts Institute of Technology			
Department of Chemical Engineering			
Part	Ion energy analyzer (3) collector		
Filename			
Designer	Jane Chang	Date	4/18/94
Contractor	Sharon Vacuum	Date	
Scale		Unit	Inch
Quantity	5	Material	Stainless steel
Tolerance	+/- 0.005 if not specified		
Comments			



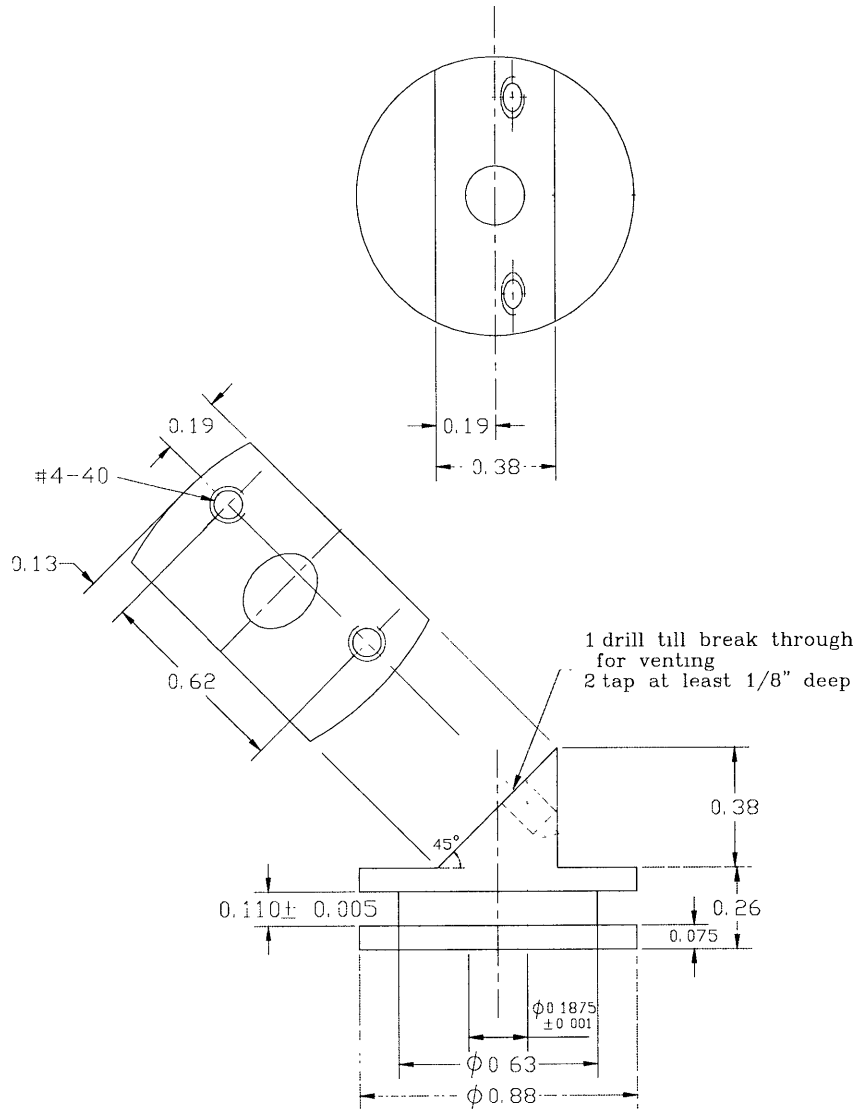
Massachusetts Institute of Technology			
Department of Chemical Engineering			
Part	Ion energy analyzer (4) base		
Filename			
Designer	Jane Chang	Date	4/18/94
Contractor	Sharon Vacuum	Date	
Scale		Unit	Inch
Quantity	1	Material	Stainless steel
Tolerance	+/- 0.005 if not specified		
Comments			



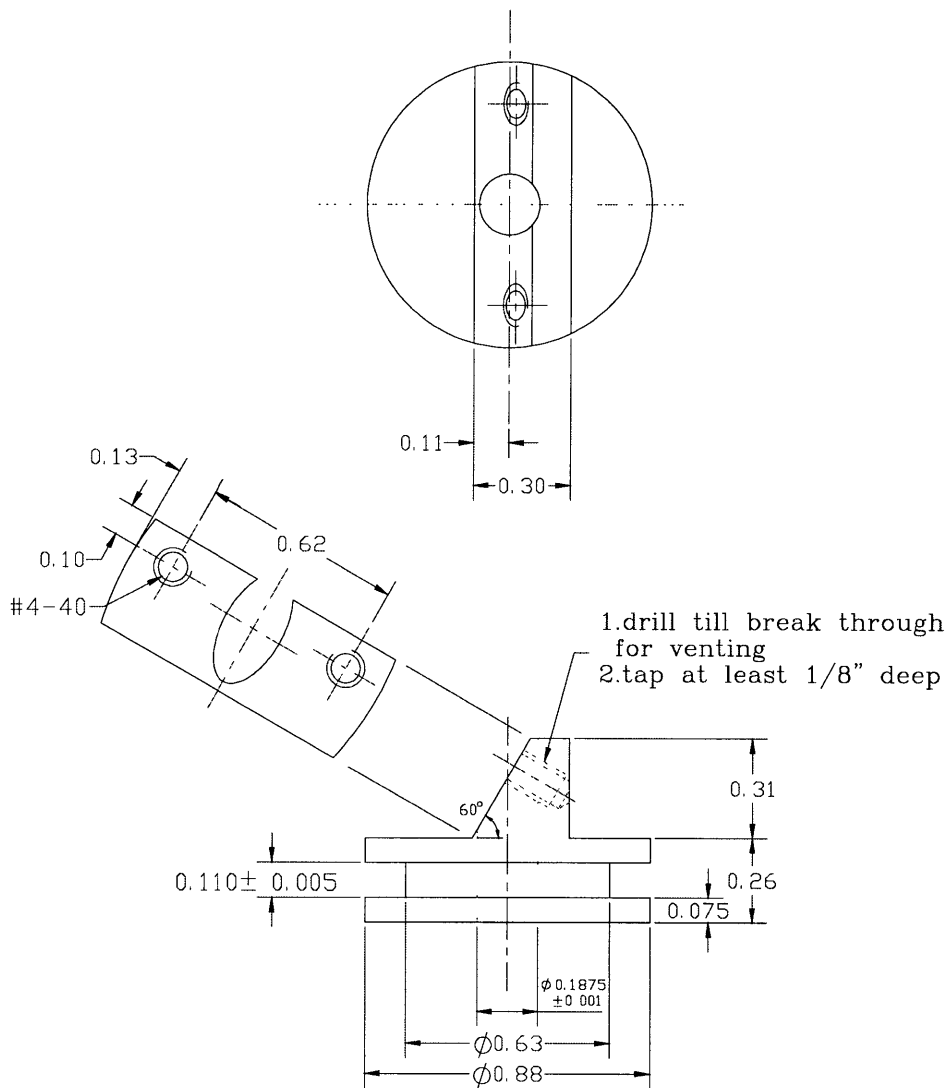
Massachusetts Institute of Technology			
Department of Chemical Engineering			
Part	Feedthrough (Microdot to BNC)		
Filename			
Designer	Jane Chang	Date	5/94
Contractor	Sycon Instruments		
Scale		Unit	Inch
Quantity		Material	
Tolerance			
Comments			



Massachusetts Institute of Technology			
Department of Chemical Engineering			
Part	30 degree sample holder		
Filename	A_HOLD30.DWG		
Designer	Jane Chang	Date	7/97
Contractor	LNS	Date	7/97
Scale	2:1	Unit	inch
Quantity	1	Material	Stainless Steel
Tolerance	+/- 0.01 if not specified		
Comments			



Massachusetts Institute of Technology			
Department of Chemical Engineering			
Part	45 degree sample holder		
Filename	A_HOLD45.DWG		
Designer	Jane Chang	Date	7/97
Contractor	LNS	Date	7/97
Scale	2:1	Unit	inch
Quantity	1	Material	Stainless Steel
Tolerance	± 0.01 if not specified		
Comments			

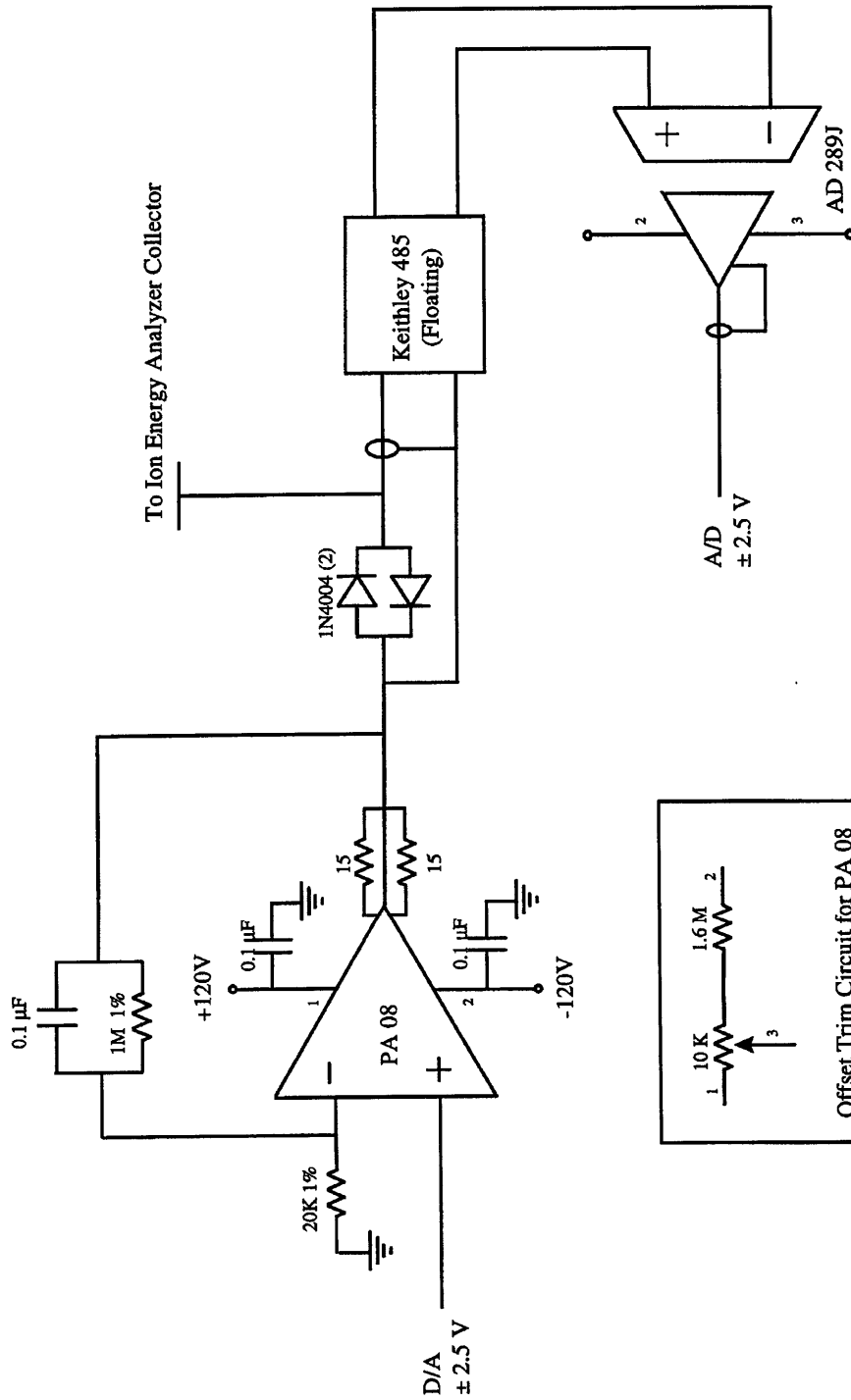


Massachusetts Institute of Technology			
Department of Chemical Engineering			
Part	60 degree sample holder		
Filename	A_HOLD60.DWG		
Designer	Jane Chang	Date	7/97
Contractor	LNS	Date	7/97
Scale	2:1	Unit	inch
Quantity	1	Material	Stainless Steel
Tolerance	+/- 0.01 if not specified		
Comments			

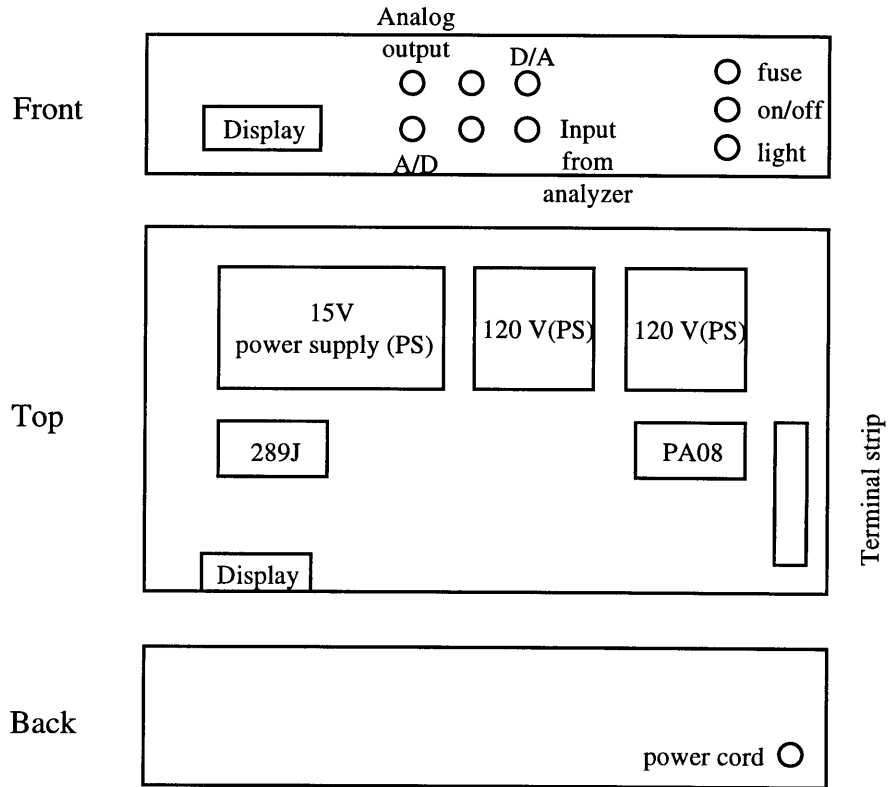


## B. Electrical systems

### 1. Schematic of the circuit diagram for ion energy analyzer



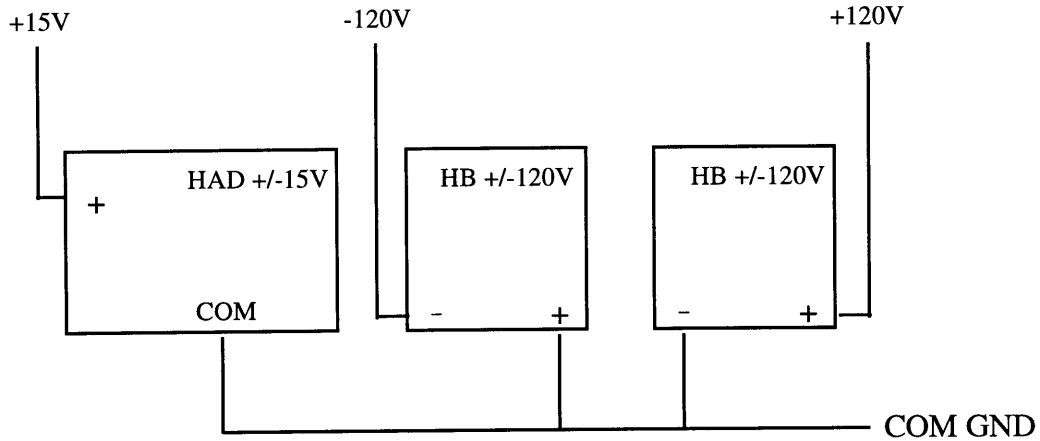
2. Ion energy analyzer (box layout)



Note:  
 Power supplies manufactured by Power One  
 289J manufactured by Analog Devices  
 PA08 manufactured by APEX

### 3. Ion energy analyzer (Power supply and terminal strip interconnections)

(a) Power supply interconnections:



Note: All supplies require 120V AC power

(b) Terminal strip interconnections: power terminal

1		COM GND (green)
2		AC - (black)
3		AC+ (white)
4		Vb/COM (brown)
5		+120V (red)
6		- 120V (purple)
7		
8		
9		
10		
11		

4. Lab-PC+ I/O connector pin assignments (Data acquisition interface)

red	ACH0	1	2	ACH1	green
red	ACH2	3	4	ACH3	green
	ACH4	5	6	ACH5	
	ACH6	7	8	ACH7	
	AISENSE/AIGND	9	10	DAC0 OUT	white
green	AGND	11	12	DAC1 OUT	
	DGND	13	14	PA0	
	PA1	15	16	PA2	
	PA3	17	18	PA4	
	PA5	19	20	PA6	
	PA7	21	22	PB0	
	PB1	23	24	PB2	
	PB3	25	26	PB4	
	PB5	27	28	PB6	
	PB7	29	30	PC0	
	PC1	31	32	PC2	
	PC3	33	34	PC4	
	PC5	35	36	PC6	
	PC7	37	38	EXTTRIG	
	EXTUPDATE*	39	40	EXTCONV*	
	OUTB0	41	42	GATB0	
	COUTB1	43	44	GATB1	
	CCLKB1	45	46	OUTB2	
	GATB2	47	48	CLKB2	
	+5 V	49	50	DGND	

## C. Operating Procedures

- Check chamber base pressure  $\sim 10^{-8}$  torr (after bake overnight)
- Turn on power supplies, allow time for warm-up
- Pump out the mass flow controllers (MFCs) and the gas lines through gas manifold
- Open chlorine gas cylinder to fill the lines with chlorine all the way to the MFCs

### 1. Operating the compact electron cyclotron resonance reactor (CECR)

- Check cooling water is on (for the microwave and the CECR)
- Flow chlorine gas to the CECR source (20 ~ 30 %, 3 sccm MFC )
- Wait till pressure in the main chamber reaches  $\sim 1.5 \times 10^{-6}$  torr (stable)
- Set  $\sim 20$  A to the electromagnets
- Turn on microwave  $\sim 200$  Watts
- Tune the microwave till the reflected power reaches  $\sim 1$ -2 Watts
- Check if there is a glow visible from the window port
- Tune down the gas flow rate to the operating condition, say 7.5 %
- Wait for chamber pressure to stabilize  $\sim 10^{-6}$  torr
- Set acceleration voltage (adjust it before turning it on) and turn it on
- Turn on the neutralizing filament,  $\sim 3$ A (8mil Tungsten)
- Measure the ion current via picoammeter
- Optimize the ion current by varying the current to the magnets and the neutralizing filament simultaneously
- Measure ion energy and ion current with the ion energy analyzer
- Retrieve ion energy analyzer
- Start etching

### 2. Operating the atom source

- Check the cooling water is on (for the microwave and the atom source)
- Check the differential pump valve is open
- Flow 5 % chlorine (3 sccm MFC), wait till the pressure stabilizes  $\sim 4 \times 10^{-6}$  torr
- Turn on microwave  $\sim 40$ Watt
- Touch the high voltage feedthrough with the Tesla coil
- Move the tuning slug till the plasma is stable (Never keep the Tesla coil on for long!!)
- The stable mode is about 40/10
- Start etching

### 3. Regeneration of the Cryogenic pump

- Make sure no one is using the corrosive line for pumping corrosive gases
- Close the gate valve to the main chamber (Keep main chamber at rough vacuum)
- Shut down the compressor
- Open the roughing valve on the pump to the corrosive pumping line

- Wait till pump warms up to room temperature
- Bake the chamber overnight (Set varia to 40 ~ 45 Watt )
- Turn heater off
- Wait till temperature comes down to room temperature  
(NOTE) Check the Helium pressure on the compressor (recharge helium if necessary)
- Close the roughing valve to the corrosive pumping line (make sure it reaches the base pressure)
- Turn on the compressor
- Temperature of the pump should reach 15 K within 2 hrs
- Pump out the main chamber to base pressure and open the gate valve => high vacuum
- Bake the chamber till a base pressure of  $\sim 10^{-8}$  torr is achieved

*Handwritten scribble*